Doctoral theses at NTNU, 2020:249

Ashenafi Lulseged Yifru

Investigation of a screen structure for mitigating debris-flows along coastal roads

Doctoral thesis

Ashenafi Lulseged Yifru

ISBN 978-82-326-4846-7 (printed ver.)
ISBN 978-82-326-4847-4 (electronic ver.)
ISSN 1503-8181

NTNU
Norwegian University of
Science and Technology

NTNU
Norwegian University of Science and Technology
Thesis for the Degree of
Philosophiae Doctor
Faculty of Engineering
Department of Civil and Environmental
Engineering

Doctoral theses at NTNU, 2020:249

NTNU
Norwegian University of
Science and Technology

Ashenafi Lulseged Yifru

Investigation of a screen structure for mitigating debris-flows along coastal roads

Thesis for the Degree of Philosophiae Doctor

Trondheim, October 2020

Norwegian University of Science and Technology
Faculty of Engineering
Department of Civil and Environmental Engineering

NTNU
Norwegian University of
Science and Technology

NTNU
Norwegian University of Science and Technology

Thesis for the Degree of Philosophiae Doctor

Faculty of Engineering
Department of Civil and Environmental Engineering

ISBN 978-82-326-4846-7 (printed ver.)
ISBN 978-82-326-4847-4 (electronic ver.)
ISSN 1503-8181

Doctoral theses at NTNU, 2020:249

Printed by NTNU Grafisk senter

ለእናቴና ለአባቴ

To my Mom and Dad

Preface

This dissertation is submitted to the Norwegian University of Science and Technology (NTNU) in partial fulfillment of the requirements for the degree of philosophiae doctor. The work was carried out at the Geotechnical Division of the Department of Civil and Environmental Engineering at the Faculty of Engineering. A four-month research stay at Polytechnic University of Madrid (Universidad Politécnica de Madrid) in Spain was also completed during the research period.

This Ph.D. study was fully funded by the E39 Ferry Free coastal highway project led by the Norwegian Public Roads Administration (NPRA). It was also conducted in a close cooperation with Center for Research Based Innovation KLIMA2050 project. Professor Vikas Thakur was the main supervisor and Professor Steinar Nordal was the co-supervisor of this Ph.D. study. Samson Abate Degago (Ph.D.) provided the scientific support on behalf of NPRA.

The dissertation was written as a monograph and has a total of eight chapters. During the Ph.D. study period, one journal article and two conference papers were published whose main ideas are included in the body of the dissertation. The published journal article and a draft journal manuscript are included with this dissertation and can be found at the end of the document.

Abstract

Debris-flow is one of the major natural hazards in Norway. The mountainous terrains of Norway are exposed to debris-flow hazards in relation to extreme weather events resulting in intense and prolonged rainfall. This hazard is expected to increase with the changing climate and has been affecting human settlements and damaging infrastructures such as roads, railways, and bridges. The E39 coastal highway is one of the main corridors in the western part of Norway that is exposed to debris-flow hazards. In connection with the long-term goal to upgrade the E39 coastal highway as an improved, continuous, and ferry free coastal highway route, the Norwegian Public Roads Administration (NPRA) sponsored this Ph.D. work to assess countermeasures for the debris-flow mitigation along steep coastal terrains. Based on a broad pilot study, it was decided to focus the work on a screen-type debris-flow countermeasure for its potential to mitigate the debris-flow threats. Moreover, debris-flow mobility and impact behaviors were studied. The study was conducted using a laboratory flume model experiment and a numerical simulation.

This work presents the behavior of debris-flow, performance of a screen-type debris-flow countermeasure in reducing debris-flow mobility and impact force, and performance dependency of the screen in debris-flow composition based on tests conducted on laboratory flume models. A numerical model simulation of the laboratory flume model tests and a real debris-flow case are presented. The work also presents a new method to measure impact force using a pillar (passable structure), a pore-water pressure measuring system, and a mass mixing and releasing cylinder, each of which was designed, developed, and implemented during this study.

The debris-flow behavior study investigated the mobility and impact force dependency on debris-flow composition. Variations in proportions of water content and fines content, along with total flow volume, are seen to affect its behaviors. High water and fines content facilitate debris-flow mobility and result in a relatively longer run-out distance and a faster flow. The change in debris-flow mobility is influenced by the change in water content, more so than the change in the fines content. In investigating effect of debris-flow composition on the dominating stress, it was found that tests conducted by 5.4% fines content with $55\% - 60\%$ solids concentration and tests conducted by 14% fines content with 60% solids concentration exhibited flow regimes dominated by frictional stresses that most real debris-flows probably fall in.

In the tests conducted on screens, the results generally showed that a screen could hinder

the debris-flow mobility and its impact force. Longer screen lengths retain more debris material than shorter counterparts. In contrast, an optimum opening width of screen grids is seen to be related to the mean diameter of the debris material used, d_{50}. In other tests conducted using this optimum opening width, run-up height on a downstream guide-wall of an underpass is more reduced when longer screen lengths are used. Longer screen also reduces the mobility of debris-flows while accumulating more debris on its surface. The debris accumulation decreases when more water and fines contents are used while debris accumulation increases when the total debris volume is increased. The screen potential is also evaluated using the accumulation process by particle image velocimetry (PIV) analyses. The screen working mechanism is observed to be a progressive layer-by-layer accumulation causing the upward shifting of the shearing layer. The speed of this shearing layer shift can describe the rate of accumulation where it is found faster when total volume and water contents are reduced. However, the slower rate of accumulation from large total volume cases is seen to result in maximum final accumulation thicknesses.

The laboratory flume model tests are supplemented with a numerical investigation using a tool called the GeoFlow_SPH-FD numerical model. The model is used, in this study, for simulating the debris-flow behavior and the screen performance along with a simulation of screen application to mitigate a real debris-flow event. The simulations show that the numerical model is capable of capturing and replicating the behaviors of the laboratory tests and a real debris-flow case with proper selection of its governing parameters. The laboratory test simulation results show that the turbulence factor of the Voellmy rheology relates to the solids concentration of the debris-flow. In contrast, the consolidation factor, that controls the evolution of pore-water pressure, relates to the fines content of the debris-flow. However, the basal friction angle of the numerical model is found to be low and could not fit with the conventional friction angle. A low friction angle needed to be used, which is believed to be realistic due to turbulence in mass flows. With these back-calculated parameters, the numerical model simulation is shown to reasonably replicate the performance of screens seen during the laboratory tests.

The numerical model simulation of the real debris-flow event, from the coastal terrains of Norway, is conducted by incorporating the effects of entrainment (erosion) and pore-water pressure evolution. The application of a screen countermeasure is demonstrated by simulating different installation and placement options in the debris-flow channel. Three consecutive screens that are strategically placed in the channel can stop the entire flow according to the numerical simulation. With this the numerical model is seen to be a promising tool in evaluating the performance of the screens in a real debris-flow case.

The E39 coastal highway route and similar roads in steep terrain need effective countermeasures for the debris-flow threats. This study contributes to building insight and

tools necessary to choose debris-flow countermeasures. Both the screen and the numerical model were shown to be promising tools in mitigating areas prone to debris-flows. The screen is shown to potentially reduce the mobility of the debris-flow through laboratory model investigations and numerical simulations. The knowledge obtained from the laboratory investigations, together with the simulation capability of the GeoFlow_SPH-FD numerical model to capture the performance of the screen, is beneficial in debris-flows mitigation works. These knowledge help in scaling-up the size of screens to field level while 50% opening ratio or the d_{50} of the debris material can be used to determine the screen opening width. With this, strategically selected and placed screen(s), and perhaps combined with other countermeasure types, can serve as debris-flows mitigation method for nearby infrastructures and settlements.

In the impact force study, the flow mobility and impact pressure relationship given by the hydro-dynamic power-function between the Froude number, $F_r = v/(\sqrt{gh})$, and the empirical pressure coefficient (normalized impact pressure, $\alpha = F/(A\rho v^2)$), is found to serve as a bridge between real debris-flows ($F_r \leq 3$) and the laboratory flume test results, which typically have $F_r > 3$. Also, it is shown that increasing fines and water contents is seen to increase the flow mobility and to slightly decrease the normalized impact pressure.

The basal pore-water pressure was successfully measured in few tests. The results show that, at peak flow height, the liquefaction level (ratio of pore-water pressure to the total pressure) at basal surface (shearing layer) can reach up to full liquefaction level. Also, the contribution of pore-water pressure to the flow mobility and its prolonged presence in debris deposit long after the debris-flow stops are observed. Moreover, the challenges and limitations of measuring pore-water pressure in an open channel flows are also shown.

Acknowledgements

First, I would like to thank the Geotechnical group and the IBM department for this opportunity and for providing all the assistance for fulfilling the research with theoretical and technical knowledge, and I would like to thank the Norwegian Public Roads Administration (NPRA) for funding the research through the E39-highway project.

I would like to thank my main supervisor, Professor Vikas Thakur, for his continuous guidance throughout this work. I would also like to thank my co-supervisor, Professor Steinar Nordal, for his critical discussions in designing and planning the laboratory tests as well as during articles and paper writings. Also, I am grateful for the contributions of Harald Norem in discussing the work, both during the laboratory testing and article writing stages. Moreover, I am grateful for my colleagues at the Politecnical University of Madrid (Universidad Politécnica de Madrid), and particularly for Professor Manual Pastor (Manolo) and his Ph.D. student at the time, Saeid Moussavi Tayyebi (Ph.D.), for allowing me to use their numerical model and for the thought-provoking discussions.

Special thanks go to Samson Abate Degago (Ph.D.), who went through the draft Ph.D. dissertation and gave critical comments and feedback. I would like to thank him for his invaluable contribution to shaping the dissertation to its final form. Also, I would like to thank his boss, Roald Aabøe, for allowing this contribution to take place. This help came from the NPRA on top of the funding through the E39 Ferry Free project, and so I hope this work will benefit the NPRA in the area.

I would like to thank the Engineers at the Department of Civil and Environmental Engineering, who were the core team of the laboratory test work. Frank Stæhli and Tage Westrum helped in designing and producing the mixing cylinder from our conceptual discussions. Also, they produced every part and small item needed during the model testing, and I'm grateful for that. Next, I would like to thank Per Asbjørn Østensen, who wrote the data acquisition program and produced all the electrical and electronic components and fixing the sensors. Converting the manual operations of debris mixing and releasing into automatic and integrating them in the test procedure was one of the valuable solutions I have gotten for executing tests quicker and with better quality. I would also like to thank Espen Andersen, Karl Ivar V. Kvisvik, and Einar Husby for adding features on flume Model-1, building flume Model-2, bringing tonnes of debris materials, and even helping me with some of the tests. The help and support I received from these staff engineers during this work were invaluable and difficult to put in words. Simply put:

thank you! Last but not least, I would like to thank Geir Tesaker for his help, quick technical solutions, and fixing the physical model during model construction and conducting tests. Throughout this Ph.D. study period, I have worked with a number of Masters degree students in the laboratory and I am grateful for their help, inputs, and contributions.

Further, I would like to thank my Ph.D. colleagues for all of the time we had together. For all of the discussions we have had, whether academic or not, I would like to thank Ivana Anušić and Helene Amundsen especially. I would also like to give a special appreciation to Marit skjåk-Bræk for helping me during my stay at NTNU and also for helping me with administrative issues during and at the final stage of this Ph.D. Also I'm grateful for the support I get from my current colleagues at Sweco Norge AS Trondheim office while finalizing this dissertation.

Finally, I would like to thank my parents, brothers, and sisters for encouraging and supporting me to reach here. I am also grateful for my friends, back in Ethiopia, here in Norway, and elsewhere. Both your in-person and virtual presence has made my journey smooth and easy. I am thankful to have you all in my life!

Takk alle sammen! **ሁላችሁንም አመሰግናለሁ!** Thank you all!

ተመስገን!
ጥቅምት ፫ ፥ ፳፻፲፫ ዓ.ም.

Contents

Preface **i**

Abstract **iii**

Acknowledgements **vii**

Contents **xv**

List of Figures **xvii**

List of Tables **xxvii**

Nomenclature **xxix**

1 Introduction **1**

1.1 Background 1

1.2 Motivation 3

1.3 Research objectives 4

1.4 Research methodology 5

1.5 Scope of the work 5

1.6 Outline of the dissertation 6

1.7 List of publications 7

2 Literature review **11**

2.1 Introduction 11

2.2 Description of debris-flow 11

2.3 Contribution of water and fines to debris-flow mobility 14

2.4 Debris-flow mitigation measures 15

2.4.1 Introduction 15

2.4.2 Non-structural Mitigation Measures 15
2.4.3 Structural Mitigation Measures 16
2.5 Screen-type debris-flow countermeasure 18
2.5.1 Introduction 18
2.5.2 Application and performance 19
2.5.3 Working mechanism of the screen 20
2.5.4 Energy dissipation evaluation 21
2.6 Impact force of debris-flow 22
2.6.1 Introduction 22
2.6.2 Analytical impact force formulas 22
2.6.3 Impact force parts and processes 26
2.7 Physical modeling of debris-flow 27
2.7.1 Introduction 27
2.7.2 Flume modeling and field testing of debris-flows 27
2.7.3 Debris-flows regime characterization 28
2.7.4 Review of the physical modeling study at NTNU 32
2.8 Numerical modeling 33
2.8.1 Introduction 33
2.8.2 Description of available mass flow numerical models 34
2.8.3 The GeoFlow_SPH-FD landslide propagation numerical model . . 35

3 The flume models and the testing procedures 39

3.1 Introduction 39
3.2 Flume Model-1 39
3.2.1 Set-up and instrumentation 40
3.2.2 Testing procedure 42
3.2.3 Set-up of screen-type countermeasure 43

3.2.4 Set-up of the impact force measuring pillar 44
3.2.5 Set-up of pore-water pressure sensors 45
3.2.6 Image analyses methods 45
3.3 Flume Model-2 47
3.3.1 Set-up and instrumentation 47
3.3.2 Testing procedure 49
3.3.3 Set-up of screen-type countermeasure 52
3.3.4 Set-up of the impact force measuring pillar 53
3.3.5 Set-up of pore-water pressure sensors 54
3.3.6 Image analyses methods 56

4 Debris-flow behaviors in the flume models 59
4.1 Introduction 59
4.2 Effect of debris-flow composition on the flow regime 59
4.2.1 Introduction and description of the debris-flow compositions 59
4.2.2 Flow regime determination 62
4.2.3 Summary 65
4.3 The run-out distance 66
4.3.1 Introduction 66
4.3.2 Comparison with an empirical relation 66
4.3.3 Effects of debris-flow composition on the run-out distance 69
4.3.4 Summary 72
4.4 Impact force of debris-flow on passable structures 72
4.4.1 Introduction 72
4.4.2 Impact force on a circular passable structure 72
4.4.3 Impact force on a rectangular passable structure 79
4.4.4 Impact force on varying rectangular pillar width 84

4.4.5 Summary 87
4.5 Pore-water pressure measurements 89
4.5.1 Introduction 89
4.5.2 Pore-water pressure measurement on Model-1 89
4.5.3 Pore-water pressure measurement on Model-2 91
4.5.4 Summary 93

5 Performance of the screen-type debris-flow countermeasure 95
5.1 Introduction 95
5.2 Length and opening width investigation of screen 95
5.2.1 Introduction 95
5.2.2 Model set-up and test plan 96
5.2.3 Test results 99
5.2.4 General observation of the results 100
5.2.5 Run-out distance 101
5.2.6 Flow height, accumulation, and deposition thicknesses 103
5.2.7 Flow velocity and energy dissipation 104
5.2.8 Segregation of the debris material 107
5.2.9 Summary 109
5.3 Combination of screen with guide-wall and underpass 109
5.3.1 Introduction 109
5.3.2 Model set-up and test plan 110
5.3.3 Test results 112
5.3.4 Run-out distance and deposition shape 115
5.3.5 Downstream deposition thickness 118
5.3.6 Accumulation thickness and pattern 119
5.3.7 Run-up height on the guide-wall 121

5.3.8 Impact force of the flow 122
5.3.9 Summary 124
5.4 Working mechanism of screens 125
5.4.1 Introduction 125
5.4.2 Model set-up and test plan 125
5.4.3 Test results 126
5.4.4 Effect of debris-flow composition on the run-out distance 127
5.4.5 Accumulation and downstream deposition thicknesses 128
5.4.6 Impact force of the flow 131
5.4.7 PIV analysis of the flow over the screen 132
5.4.8 Summary 137

6 Numerical study **139**
6.1 Introduction 139
6.2 Model calibration using the physical model tests 139
6.2.1 Introduction and model preparation 139
6.2.2 Back-calculation of parameters based on debris-flow composition . 140
6.2.3 Summary 144
6.3 Simulation of the screen tests 144
6.3.1 Introduction 144
6.3.2 Description of the laboratory test-set and results 144
6.3.3 One-dimensional (1D) Simulation 147
6.3.4 Two-dimensional (2D) simulation 152
6.3.5 Summary 155
6.4 Real debris-flow case 156
6.4.1 Description of the debris-flow case 156
6.4.2 Geology and Geo-hazard levels 156

6.4.3 Terrain model preparation 158
6.4.4 Back-calculation of the debris-flow case 160
6.4.5 Evaluation of the countermeasures 162
Embankment walls 162
Screen-type countermeasures 164
6.4.6 Summary 169

7 Summary and conclusions **171**

8 Recommendation for future work **177**

References **178**

Papers **i**

Paper I iii
Laboratory investigation of performance of a screen type debris-flow countermeasure - HKIE Transactions iii
Paper II xxvii
Two-phase SPH-FD depth integrated model for debris flows: application to basal grid brakes - Submitted to *Géotechnique* xxvii

Appendices **i**

Appendix A **iii**

A1 Additional results from screen and underpass tests on Model-1 v
A2 All impact force measurement plots for V1C1, V2C2, and V3C3 vi
A3 Pore-water pressure measured on Model-1 x

Appendix B **xiii**

B1 Full result of the dimensionless analyses of the Model-2 debris-flow characterization tests xv

B2 Result plots of dimensionless numbers from Table B1 xvii

Appendix C **xix**

C1 1D sensitivity simulation result from V1 xxi

Appendix D **xxiii**

D1 The working drawing of Model-2 xxv

Appendix E **xxvii**

E1 Raw data plots of the Model-2 debris-flow tests xxix

E2 Sequential PIV simulation pictures from G1V1C1_50-2 test xxxix

E3 Sequential PIV simulation pictures from G1V1C2_50-2 test xliii

E4 Sequential PIV simulation pictures from G1V2C1_50-2 test xlvii

E5 Sequential PIV simulation pictures from G1V3C1_50-2 test li

Appendix F **lv**

F1 Instrument specification of the flow height sensor lvii

F2 Instrument specification of the pore-water pressure sensor lxi

F3 Instrument specification of the load cell lxvii

List of Figures

1.1 Example of coastal debris-flow: Mjåland, Norway (02.06.2016). A Firetruck is circled for scale. [Photo: NPRA and Multiconsult] 1

1.2 Maps showing: (a) the E39 highway with landslide susceptible areas, and (b) a closer look at landslide susceptible locations that are potential debris-flow starting zones along the E39 highway (NVE 2014) 3

1.3 The work flow describing the research methodology used in this study . . 6

2.1 Classification of mass movements on steep slopes as a function of solid fraction and material type, Adopted from Coussot and Meunier (1996) . . 12

2.2 Categories of dynamic debris-flows (Takahashi 2009) 12

2.3 debris-flow surge diagram from Pierson (1986) as referred by Hungr (2005) 13

2.4 Commonly used structural countermeasures 17

2.5 Countermeasures that are often used in Norway for different kinds of landslides, flood, and snow avalanche as given in yearly reports of NVE (NVE 2017; 2018, and NVE 2019a) 18

2.6 The screen: (a) before a debris-flow event giving its schematic representation, and (b) after a debris-flow event showing the material depositions (Yifru et al. 2018) 19

2.7 Pore-water pressure development during debris-flow and its dissipation when it hits a screen-type countermeasure: (a) A Schematic representation of a debris-flow on a solid surface and on a screen. (b) Total normal stress components and distribution in the debris-flow mixture: section A is over a solid surface, and section B is over a screen (Yifru et al. 2018). . 20

2.8 Wide range relationship between F_r and impact force normalized by the kinetic force expression (Faug 2015) 25

2.9 Simplification of impact process of debris-flow. Part (1) and (2) representing the head impact and the body impact of the debris-flow, respectively. (Cui et al. 2015) 26

2.10 (a) The initial and deformed configuration of a column of the landslide mass and (b) the reference system and notations (Pastor et al. 2015). . . . 38

3.1 Schematic representation of the flume Model-1: side and plan views. (All linear dimensions are in meters) 40

3.2 Two types of pore-water pressure measuring sensors: a flat and perpendicular one 41

3.3 The assembly process and placement of the $50cm$ long metal grid screen on Model-1 43

3.4 Configuration and installation of the force measuring circular pillar: (a) schematic representation of the front and side view, and (b) Photo of the pillar installation (view from the releasing area towards the deposition area). ($L = 0.45m$, $w = 0.30m$, $W = 0.6m$, and $H = 0.22m$) 44

3.5 The two pore-water pressure sensors (flat and perpendicular) arrangement complemented with sketch showing their dimensions and installation position. 46

3.6 Estimation of front-flow velocity from the recorded video using the Tracker software 47

3.7 Schematic representation of the flume Model-2: side and plan views. (All linear dimensions are in meters) 48

3.8 The schematic drawing of the mixing-cylinder along with its photo (mirror view) 50

3.9 The assembly process and placement of the $50cm$ long plexiglass grid screen in Model-2 52

3.10 Configuration and installation of the force measuring rectangular pillar: (a) schematic representation of the front and side views, and (b) Photo of the pillar installation (mirrored view from the side). ($L = 0.45m$, $w = 0.30m$, $W = 0.80m$, and $H = 0.35m$) 53

3.11 Plan view of installed pore-water pressure sensors: (a) in the run-out channel and (b) at the deposition area 54

3.12 Improved pore-water pressure measuring system and its installation as seen from channel bottom 55

3.13 Estimation of front-flow velocity from Cam-1 video using the Tracker software 56

3.14 The PIVLab App of MATLAB being used for determination of flow velocity over the screen (Flow direction is from right to left) 57

4.1 Grain size distribution (GSD) curves of the debris materials (G1, G2, and G3) 60

4.2 Dimensionless numbers variations with GSD and C_s: (a) Savage number, (b) Bagnold number, and (c) friction number 63

4.3 Dimensionless numbers variations with GSD and C_s: (a) mass number, (b) Darcy number, and (c) grain Reynolds number 64

4.4 Photos showing run-out distances of the G1 tests with varying V and C_s (top view of the deposition area, grid size = $0.2m$) 68

4.5 Run-out distance on the fan area, L_{FL} in relation to volume, V (after Rickenmann (1999)) 69

4.6 L_{FL} variations with V and C_s for: (a) G1, (b) G2, and (c) G3 70

4.7 L_{FL} variations with GSD and C_s for: (a) V1, (b) V2, and (c) V3 70

4.8 L_{FL} variations with GSD and V for: (a) C1, (b) C2, and (c) C3 71

4.9 L_{FL} plotted against the recalculated C_s^* for varying: (a) G and C, (b) G and V, and (c) V and C 71

4.10 The flume Model-1 with instrumentation and placement of the circular pillar (all dimensions in m) 73

4.11 Grain size distribution (GSD) of the debris material 74

4.12 The recorded impact forces on the pillar for all the tests grouped by ranges of discharge 75

4.13 The recorded force and upstream flow height for PT3 76

4.14 The maximum impact force (F_{Max}) plotted against the calculated average discharge (Q) 76

4.15 Comparison of the measured F_{Max} with: (a) F_{hd1} and (b) F_{hd2} 78

4.16 Relationship between the F_r and the normalized peak pressure given by α 78

4.17 The flume Model-2 with the rectangular pillar: instrumentation and placement of the rectangular pillar (all dimensions in m) 80

4.18 Typical test result (from G1V1C1) showing flow heights and impact force plots with time 80

4.19 Impact pressure comparison: measured vs calculated by Equation 2.6 (Zanuttigh and Lamberti 2006) based on variations of: (a) GSD, (b) V, and (c) C_s 82

4.20 Impact pressure comparison: measured vs calculated by Equation 2.10 (Mizuyama 1979) based on variations of: (a) GSD, (b) V, and (c) C_s 82

4.21 Froude number Vs empirical coefficient plots based on the variations of (a) GSD, (b) Volume, V, and (c) Solids concentration, C_s 83

4.22 Passable structure width variations represented by varying plate widths . 84

4.23 Impact measurement result using varying width of a passable structure . . 86

4.24 The impact force normalized by the kinetic force expression plotted as a function of F_r (a) data from this study, Cui et al. (2015) and Huebl and Holzinger (2003), (b) close up view of plot (a), and (c) plot from Faug (2015) for comparison. 86

4.25 Measured pore-water pressure along with calculated total normal pressure and hydrostatic pressure of Test V1T1: (a) entire 20 seconds duration and (b) close up look of the first 8 seconds 90

4.26 Measured pore-water pressure, total normal pressure, hydrostatic pore-water pressure using the sensor in: (a) the channel, and (b) the deposition area. Close up views of both measurements are given at their respective right side 92

5.1 Flume Model-1: placement of the screens and instrumentation. All linear dimension were in meters. 96

5.2 Grain size distribution, GSD, of the test material 97

5.3 Measurements of the model and the screen: (a) photo showing details of Model-1 with a $1m$ long screen (photo from Laache (2016)) and (b) schematic detail of screen with $l = 0.5m$ and $1.0m$ and $w = 2mm$, $4mm$, and $6mm$ 98

5.4 Photos showing deposition pattern and run-out distance of selected tests from $0.5m$ long cases (Photos from Laache (2016)). 100

5.5 Run-out distance results: (a) variation due to l and w variations, and (b) percentage reduction from the respective reference tests 101

5.6 Comparison of percentage opening versus percentage run-out distance reductions with data from Kim (2013). 102

5.7 Average flow height variation with time at the upstream of the countermeasures when using: (a) a $0.5m$ long plate and screen, and (b) a $1m$ long plate and screen 103

5.8 Representative plots of the flow front velocities at the left, center, and right sections of the channel 105

5.9 Percentage energy dissipation with respect to: (a) initial energy at start of screen, and (b) energy dissipation by terrain alteration represented by the solid plate 106

5.10 Change in grain size distribution, GSD, of the debris-flow material on the screen and at the deposition area 107

5.11 Flume Model-1 with screens and underpass placement and instrumentation. All linear dimensions are in meters 110

5.12 Plan view photos showing details of placement of: (a) the screen and (b) the guide-wall and underpass. A road and a car representation over the underpass is also given at the top right. 110

5.13 GSD of the crushed aggregate used for this study 111

5.14 The released V and C_s for each test along with the respective starting (initial) V and C_s. 114

5.15 Average run-out distance: (a) without underpass and (b) with underpass. S1 and S2 were reference tests for the respective categories. 115

5.16 Deposition shape of tests without underpass for: (a) V1C1, (b) V2C2, and (c) V3C3. All dimensions are in cm. 116

5.17 Deposition shape of tests with underpass for: (a) V1C1, (b) V2C2, and (c) V3C3. All dimensions are in cm. 116

5.18 V3C3 Deposition shape comparison between the result from: (a) S3-50-2, and (b) S3-25-2. All dimensions are in cm. 117

5.19 V3C3 Deposition shape comparison between the result from: (a) S4-50-2, and (b) S4-25-2. All dimensions are in cm. 117

5.20 Downstream deposition thickness, t_d, variations of each scenario: (a) without underpass and (b) with underpass 118

5.21 Accumulation pattern for V2C2 tests on: (a) $0.5m$ long screen and (b) $0.25m$ long screen. 119

5.22 Accumulation pattern for V3C3 tests on: (a) $0.5m$ long screen and (b) $0.25m$ long screen. 120

5.23 Flow run-up height on the guide-wall of the underpass 121

5.24 Average maximum flow impact force of each scenario (results from tests with underpass). 122

5.25 Flow impact force from three representative reference tests: (a) V1C1, (b) V2C2, and (c) V3C3 123

5.26 Flow impact force V2C2 tests with: (a) reference, (b) $0.25m$ long screen, and (c) $0.5m$ long screen 123

5.27 Flume Model-2 with screen placement and instrumentation. All linear dimension are in meters 125

5.28 The G2 run-out distances along with their percentage run-out reduction with respect to their respective reference tests 127

5.29 Accumulation shape of representative G2V1C1 tests from: (a) $0.5m$ long solid plate and (b) $0.5m$ long screen 128

5.30 Maximum accumulation thicknesses for G2 tests 129

5.31 Downstream deposition thickness, t_d, from G2 tests 130

5.32 The flow impact force for each $0.5m$ long screen G2 test along with the respective reference tests for: (a) variation in C_s, and (b) variation in V. . 131

5.33 The flow impact force for each $0.5m$ long screen G1 test along with the respective reference tests for: (a) variation in C_s, and (b) variation in V. . 132

5.34 PIV analysis of G1V1C1_50-2: (a) velocity profile at a cross-section $0.15cm$ from the end of the screen, and (b) sequential pictures for corresponding time step plots given in (a). 133

5.35 Velocity profile of the tests conducted by the G1 material and V1 = $25L$ volume measured at $15cm$ cross-section from end of the screen: (a) C1 = 60%, and (b) C2 = 55%. 134

5.36 Velocity profile of the tests conducted by the G1 material and C1 = 60% concentration measured at $15cm$ cross-section from end of the screen: (a) V1 = $25L$, (b) V2 = $30L$, and (c) V3 = $35L$. 135

5.37 Shearing layers in G1V1C1_50-2 (a) at different times and (b) at a representative time of $0.25sec$ 136

5.38 Upward shifting of the shearing layer measured at $0.15m$ from the $0.5m$ long screen end for (a) variation in C_s, and (b) variation in V. 136

6.1 The flume Model-2 DTM topography representation for the numerical model simulation. 140

6.2 Starting conditions of the 1D simulation for: (a) total flow height representing a release mass placed on the opened-gate of the mixing cylinder, h $[m]$, (b) $\overline{\Delta P}_{wp}$ [-], and (c) P_{wp}, $[kPa]$ 141

6.3 The simulated run-out distance, L_{FL}, plotted against ξ: (a) for $tan(\phi_b) = 0.27$, (b) for $tan(\phi_b) = 0.36$, and (c) for $tan(\phi_b) = 0.58$ 142

6.4 The simulated and the laboratory run-out distances, L_{FL}, plotted together against ξ and C_s for the case of V1 143

6.5 Deposition shape of: (a) G2V1C1_00-0, (b) G2V1C1_50-0, (c) G2V1C1_50-2, and (d) compiled deposition shapes. (The lines in the photo represent $0.2m$ interval) 145

6.6 Recorded flow heights: (a) for the reference test, (b) when using the $0.5m$ long plate, and (c) when using the $0.5m$ long screen 147

6.7 The flume model DTM topography representation for tests with the screen or the solid plate 147

6.8 Flow heights: laboratory results vs numerical simulation results (a) of the reference test, (b) when using the $0.5m$ long plate, and (c) when using the $0.5m$ long screen 148

6.9 End of simulation for G2V1C1_00-0 at deposition area: (a) relative excess pore-water pressure, $\overline{\Delta P}_{wp}$, [-], (b) Total pore-water pressure at the basal surface, P_{wp}, [kPa], and (c) deposition height, h, $[m]$. 149

6.10 Final flow height simulation result when using (a) the $0.5m$ long solid plate, and (b) the $0.5m$ long screen 150

6.11 Final total basal pore-water pressure, P_{wp}, result when using (a) the $0.5m$ long solid plate, and (b) the $0.5m$ long screen 150

6.12 (a) Relative pore-water pressure, $\overline{\Delta P}_{wp}$, over: (a) the $0.5m$ long solid plate, and (b) the $0.5m$ long screen 151

6.13 Boundary wall representing coordinates to specify plan of the flume model: applicable to the reference, the solid plate, and the screen representation tests. 152

6.14 The starting height condition and cylindrical representation of the release volume: (a) side view and (b) front view 152

6.15 Final deposition shapes of the reference, plate, and screen cases from: (a) the laboratory test results, and (b) the simulation results 153

6.16 Final accumulation and deposition thicknesses of (a) the $0.5m$ long solid plate simulation, and (b) the $0.5m$ long screen simulation. 155

6.17 Geological formation and geological cover map of the Mjåland debris-flow area (from NVE Atlas (2019) 157

6.18 (a) Event map with AMSL elevations and (b) Susceptibility map and slide extent probability areas (from NVE Atlas (2019) 157

6.19 The Mjåland debris-flow: (a) before the slide in 2014 (from norgeibilder.no), (b) after the slide (from Google Earth pro and QGIS), (c) photo of the event (from Multiconsult and NPRA) 158

6.20 The prepared DTMs of (a) the original debris-flow topography, and (b)-(e) different options of screen implementations 160

6.21 Analysis simulation steps of the event using parameters given in Table 6.6 161

6.22 Evaluation of the existing $5m$ tall wall, $90m$ wide embankment wall. (scale in $[m]$). 163

6.23 Simulation result of embankment wall with: (a) $7.5m$ high wall, (b) $7.5m$ high, wide wall, and (c) $10m$ high, wide wall 164

6.24 Proposed locations of screens: (a) for CM-1, CM-2, and CM-3, (b) for CM-4 based on their combinations given in Table 6.7 165

6.25 Simulation results for different combinations options of the screen given in Table 6.7. 166

6.26 Simulation results comparing between (a) the CM-3 screens and (b) the CM-3 topographical change contribution (solid surface) 168

6.27 Screen implementation sketch (a) plan and profile, (b) rectangular cross-section of screen grid with possible clogging, and (c) isosceles trapezoidal cross-section without clogging possibility. 169

A1 All impact force plots from material V1C1 for: (a) reference, (b) 50cm long plate, (c) 25cm long screen, and (d) 50cm long screen tests vii

A2 All impact force plots from material V2C2 for: (a) reference , (b) 50cm long plate , (c) 25cm long screen , and (d) 50cm long screen tests viii

A3 All impact force plots from material V3C3 for: (a) reference, (b) 50cm long plate, (c) 25cm long screen, and (d) 50cm long screen tests ix

A4 Measured pore-water pressures along with calculated total normal stress and hydrostatic pore-water pressure xi

A5 Measured pore-water pressures along with calculated total normal stress and hydrostatic pore-water pressure: With detail at peak flow height and peak pore-water pressure values xii

B1 Dimensionless numbers variations with GSD and C_s from Table B1: (a) Savage number, (b) Bagnold number, and (c) friction number xvii

B2 Dimensionless numbers variations with GSD and C_s from Table B1: (a) mass number, (b) Darcy number, and (c) grain Reynolds number xvii

C1 The simulation run-out distance Vs B_{fact}: (a) for $tan(\phi_b) = 0.27$, (b) for $tan(\phi_b) = 0.36$, and (c)for $tan(\phi_b) = 0.58$ xxii

C2 The simulation run-out distance Vs $tan(\phi_b)$: (a) for $B_{fact} = 1E-4m^2/s$, (b) for $B_{fact} = 1E-3m^2/s$, (c) for $B_{fact} = 5E-3m^2/s$, (d) for $B_{fact} = 1E-2m^2/s$ xxii

D1 Design and working drawing of Model-2 xxv

List of Tables

2.1 Summary of the resulting dimensionless numbers from the ratio of the stress conditions (*NB: the ratio order is that the quantities in row are numerators*) 30

4.1 Important sizes and gradation properties of the debris materials (grain sizes are in mm) 61

4.2 Summary of typical values of physical and dimensionless parameters of real and experimental debris-flows including this study 65

4.3 Average run-out distance, L_{FL}, results for each combination of GSD, V, and C_s tests 67

4.4 Summary of analytical impact force equations from Section 2.6 73

4.5 Results of the nine tests conducted on the circular pillar 74

4.6 Results of impact force along with approach flow velocity and flow height 81

4.7 Results showing the impact force tests on varying width of the passable structure 85

4.8 The downstream recorded pore-water pressures along with the respective flow heights for V1C1 91

5.1 Test plan and description of dimensions of the debris-flow screens 98

5.2 Summary of the test results (Based on data from Laache (2016)). 99

5.3 Values of d_{50} for the samples at deposition and on the $0.5m$ long screen . 108

5.4 Test plan describing dimensions of screens and presence of flow impact force measurement 112

5.5 Summary of the test results: run-out distance and maximum flow impact force 113

5.6 Test plan showing list of tests conducted for screen mechanism study . . . 126

5.7 Run-out distances from the screen tests conducted on Model-2 127

6.1 Ranges of parameters of the GeoFlow_SPH-FD model used during the laboratory test simulations 141

6.2 Summary of the run-out distance, L_{FL}, and area depositions of the laboratory test results (given in Figure 6.5), and their respective percentage reductions 146

6.3 Summary of the run-out distances of the laboratory tests and the 1D simulation results along with their respective percentage reductions 150

6.4 Summary of the run-out distances of the laboratory tests and the 2D simulation results along with their respective percentage reductions 154

6.5 Summary of the area depositions of the laboratory test results and the 2D simulation results along with their respective percentage reductions 154

6.6 Back-calculated parameters for the Mjåland, debris-flow 160

6.7 The Screen sizes and implementation locations along with their combination options 164

6.8 Simulation results for different combinations of the screen-type countermeasure 167

A1 Down-stream deposition thickness, t_d, and run-up height results from screen and underpass tests v

B1 Physical and dimensionless parameters for all tests using flow front tracked velocity xv

B2 Physical and dimensionless parameters for all tests using average velocity xvi

Nomenclature

Latin Letters

$\bar{n}$	Depth-averaged porosity, [-]
$\bar{P}$	Averaged total pressure, $[M/LT^2]$
$\bar{v}$	Depth-averaged velocity, $[L/T]$
Δp_{wb}	Excess pore-water pressure at the basal surface, $[M/LT^2]$
$\overline{\Delta P}_{wp}$	Excess pore-water pressure normalized by the effective stress (for GeoFlow model), $\overline{\Delta P}_{wp} = (\Delta P_{wp})/(\bar{\rho}' g h)$ [-]
$\overline{P}_{wp,hyd}$	Hydrostatic water pressure normalized by the effective stress (for GeoFlow model), $\overline{P}_{wp,hyd} = (\bar{\rho_w} g h_{sat})/(\bar{\rho}' g h) = (\bar{\rho_w}/\bar{\rho}')/(h_{sat}/h)$ [-]
A	Area, $[L^2]$
B	Maximum width of the deposition area, $[L]$
b_3	Gravity forces along x_3 axis (for GeoFlow model), $[ML/T^2]$
B_{fact}	GeoFlow_SPH model input parameter controlling the consolidation rate, $C_v \cdot \pi^2/4$, $[L^2/T]$
C	The coarse particle concentration by Volume, also referred to as C_s^* in Chapter 4. [-]
C'	A pure drag coefficient in the impact force dimensionless relation given by Faug (2015).
C_c	Coefficient of curvature, $(d_{30})^2/(d_{10} \times d_{60})$, [-]
C_f	Volume fraction of the pore-fluid in the debris mixture, $(V - V_s)/V$, [-] or [%]
C_s	Volume fraction of the solids in the debris mixture, V_s/V, [-] or [%]
C_u	Coefficient of uniformity, d_{60}/d_{10}, [-]
C_v	Coefficient of consolidation, $[L^2/T]$
C_{fines}	Volume fraction of the fines in the fluid, V_{fines}/V_{fl}, [-]
d_{10}	The grain diameter at 10% passing, $[L]$
d_{30}	The grain diameter at 30% passing, $[L]$
d_{50}	The median grain diameter, $[L]$
d_{60}	The grain diameter at 60% passing, $[L]$
d_{90}	The grain diameter at 90% passing, $[L]$
d_{max}	Maximum grain size of the solids debris material, $[L]$
d_{v0}	Extra volumetric component (for GeoFlow model), [-]
E_D	Energy dissipation factor, [%]
e_R	Entrainment rate (for GeoFlow model), $[L/T]$
E_s	The landslide growth rate, $[1/L]$

F_r	Froude number, [-]
F_{hd1}	The first hydro-dynamic equation
F_{hd2}	The second hydro-dynamic equation
F_{Max}	Maximum flow impact force, $[ML/T^2]$
F_{mixed}	The hydro-static and hydro-dynamic mixed model equation
g	Gravitational acceleration, $[L/T^2]$
h	Total flow height, $[L]$
H_A	Total energy head at the beginning of a screen, $[L]$
H_B	Total energy head at the end of a screen, $[L]$
h_{Max}	Maximum flow height, $[L]$
h_{sat}	Saturated flow height, $[L]$
K	Multiplying factor in hydro-static impact force equation, [-]
k	Hydraulic permeability, $[L^2]$
k	Multiplying factor in hydro-dynamic impact force equation, [-]
K'	Equivalent earth pressure coefficient for impact force dimensionless relation given by Faug (2015).
K^*	Multiplying factor in the improved hydro-static impact force equation of Zanuttigh and Lamberti (2006), [-]
K_v	Elastic volumetric stiffness ratio, $[M/LT^2]$
L	Length of entrainment (erosion) zone, $[L]$
L_{FL}	Run-out distance in the deposition area, L
m	Mass of the soil particles (for GeoFlow model), $[M]$
N	The number of grains with size δ that make up h, h/δ, $[-]$
N_{Bag}	Bagnold number, [-]
N_{Dar}	Darcy number, [-]
N_{mas}	Mass number, [-]
N_{Rey}	Grain Reynolds number, [-]
N_{Sav}	Savage number, [-]
p	Flow impact force per unit width, $[M/T^2]$
p_w	Pore-water pressure, $[M/LT^2]$
P_{Max}	Maximum pressure, F_{Max}/A, $[M/LT^2]$
p_{wb}	Pore-water pressure at basal surface, $[M/LT^2]$
P_{wp}	Total pore-water pressure (for GeoFlow model), $[M/L^2]$
q	Discharge per unit width, $[L^2/T]$
R	Internal force, $[ML/T^2]$
r_u	Pore-water pressure ratio, $P_{wp,Max}/\sigma_{v,Max}$, [-]
S_r	Saturation [-] or [%]
t_d	Downstream deposition thickness, $[L]$
t_u	Maximum accumulation thickness on a screen, $[L]$
V	Total Volume or Volume, $[\mathrm{L}^3]$

v	Flow velocity, $[L/T]$
v_A	Average flow front velocity at the beginning of a screen, $[L/T]$
v_B	Average flow front velocity at the end of a screen, $[L/T]$
V_f	Final volume of a slide after entrainment, $[L^3]$
V_i	Initial volume of a slide, $[L^3]$
V_{fines}	Volume of the fines fraction, $[L^3]$
V_{fl}	Volume of the fluid fraction, $V_w + V_{fines}$, $[L^3]$
V_s	Volume of the solids fraction, $[L^3]$
V_w	Volume of water, $[L^3]$
W	Width of the run-out channel, L
w	Width of a single opening on a screen, L

Greek Letters

α	An empirical coefficient obtained from impact pressure normalized by the dynamic factor (ρv^2), [-]
α	Constitutive coefficient of an oedometeric state (for GeoFlow model), [-]
$\bar{\rho}$	Average density of the solid-liquid mixture (for GeoFlow model), $\bar{\rho}h = (1-n)\rho_s h + n\rho_w h_{sat}$, $[M/L^3]$
$\bar{\rho}'$	Average effective density of the solid-liquid mixture (for GeoFlow model), $\bar{\rho}'h = (1-n)[\rho_s h - \rho_w h_{sat}]$, $[M/L^3]$
β	The least impacting angle between the debris-flow direction and the face of a structure, [°]
δ	Characteristic grain diameter of the debris material approximated by d_{50}, $[L]$
$\dot{\gamma}$	Shear strain rate approximated by v/h, $[1/T]$
μ	Dynamic viscosity of the pore-fluid with suspended fine sediment, $[M/LT]$
ϕ_b	Basal friction angle, [°]
ρ	Mixture density of the solid grains and the intergranular fluid, $[M/L^3]$
ρ_f	Density of the intergranular fluid, $[M/L^3]$
ρ_s	Density of the solid grains, $[M/L^3]$
ρ_w	Density of the liquid, $[M/L^3]$
ρ_w	Density of water, $[M/L^3]$
σ_v	Total normal stress, $\rho \times g \times h$, $[M/LT^2]$
τ_b	Basal shear stress, $[M/LT^2]$
ξ	Turbulence coefficient, $[\mathrm{L/T}^2]$

Abbreviations

1D	One-dimensional
2D	Two-dimensional
3D	Three-dimensional
AMSL	Above mean sea level

DTM	Digital terrain model
EGL	Energy Grade Line
FD	Finite Difference
G1	Original sand material for the laboratory test
G2	Original sand material mixed with 10% additional finer material
G3	Original sand material mixed with 20% additional finer material
GeoFlow_SPH-FD	The GeoFlow smooth particle hydrodynamics - finite difference model
GSD	Grain Size Distribution
NPRA	Norwegian Public Roads Administration
NTNU	Norges teknisk-naturvitenskapelige universitet (Norwegian University of Science and Technology)
NVE	Norges Vassdrags- og Energdirektorat (The Norwegian Water Resources and Energy Directorate)
PIV	Particle Image Velocimetry
quasi-3D	Quasi-three-dimensional

1 Introduction

1.1 Background

Debris-flow is among the major natural hazards in the world. It has been putting human lives, infrastructures, and the natural environment at risk due to its destructive nature and unpredictable occurrence. Debris-flow significantly affects countries like Norway, which have abundant precipitation or water sources and mountainous terrains. Other vulnerable countries include Austria, Canada, Colombia, France, Indonesia, Italy, Japan, Mainland China, Nepal, the Philippines, Taiwan, Switzerland, and Venezuela, as well as all Caribbean countries (Takahashi 2014). Figure 1.1 shows a typical coastal mountainous terrain with a road passing at the foot of the mountain, that is susceptible and affected by a debris-flow. Such steep terrain areas with roads can be characterized by a $25 - 45°$ slope with the steepest part usually found towards the top, with deposition areas that sometimes found to be inhabited, with or without a water body on the other side of the road.

Fig. 1.1: Example of coastal debris-flow: Mjåland, Norway (02.06.2016). A Firetruck is circled for scale. [Photo: NPRA and Multiconsult]

During the period of 1900 to 2010, 1 100 people in Norway have died because of more than 500 registered natural disasters, and, currently, more than 100 000 people are living in

areas prone to such natural hazards (Stortingsmelding_nr.15 2012). It is also mentioned by Stortingsmelding_nr.15 (2012) that from only 1980 to 2010, the cost of damage is estimated to amount to approximately 6.1 Billion Norwegian Kroners. Another study, Frauenfelder et al. (2016) reported that the cost of geohazard impacts on the major roads of Norway is estimated to be around 100 Million Norwegian Kroners per year, 70% of which is associated with road closures. More than 30% of the total length of these roads and railways are exposed to natural hazards like snow avalanches, landslides, rockfalls, and rock slides, where these hazards are unevenly distributed throughout the country based on climate and topographical variation (Frauenfelder et al. 2016). During the last two decades, the change in climate has been associated with an increased frequency of strong precipitations which has led to frequent flooding and landslide events (Frauenfelder et al. 2016). In recent years, the destruction of infrastructures (roads and buildings) by debris-flows in Norway has been growing due to the fast changing climate according to the report by NVE (2011). The report indicated the relationship between the changing climate and an increase in the frequency of debris-flow events. Extreme weather conditions like short, intense rainfall, prolonged ordinary rainfall, and rapid snow melting are attributed as causes of the frequent occurrence of debris-flows, which thereby contribute to the damage of infrastructures (Meyer et al. 2012).

Based on records of previous landslides, precipitation data, slope angle and elevation of the area, preliminary landslide susceptibility regional levels were made by NVE (2014). The South-Western and Northern parts of Norway are designated as highly susceptible regions for debris-flow related hazards as shown by Figure 1.2(a). Figure 1.2(b) shows preliminary landslide susceptible locations near inhabited areas of the South-Western region where the planned E39 highway road passes through. In addition, it can be clearly seen that the planned coastal E39 highway passes through the landslide susceptible zones in South-Western part of Norway. These zones are also designated as potential initiation locations for debris-flows. Therefore, in this region, the threat to human lives, infrastructures, and the interruption of traffic due to debris-flow is high and requires the design and implementation of protective and mitigating measures.

The Norwegian Public Road Administration (NPRA) has been commissioned, with a long-term goal of the state (Storting), to develop the E39 highway as an improved and continuous coastal highway route between Kristiansand and Trondheim. By replacing the ferry crossings with bridges and tunnels while also upgrading the number of road sections inland, the E39 ferry free project aims to reduce the route by about 50km and cut the total travel time by half (NPRA 2019). Moreover, a separate project was established whose aim is to ensure that the improved E39 highway has positive impacts on businesses and individuals as well as helps in finding technological solutions to make the fjord crossings possible with special attention to safety aspects, giving proper attention to the

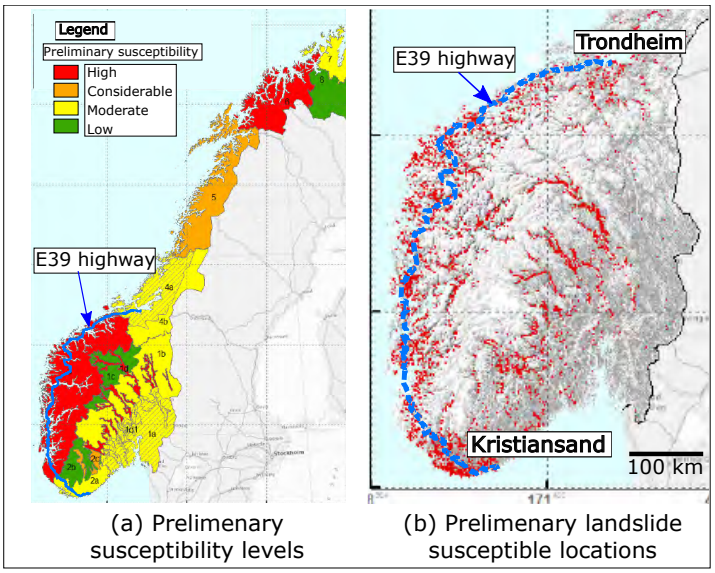

Fig. 1.2: Maps showing: (a) the E39 highway with landslide susceptible areas, and (b) a closer look at landslide susceptible locations that are potential debris-flow starting zones along the E39 highway (NVE 2014)

planning, construction, and use phases of the route (NPRA 2019). This project employed several studies (in Ph.D. and Post-Doctoral levels) on different aspects where route safety and potential protective measures against debris-flows are studied and presented in this dissertation.

The extent of the increased debris-flow threat along this E39 highway can be exemplified by looking at the multiple events that occured on July 30th, 2019. A $20km$ stretch of the highway between Bruland and Ålhus, in Sogn and Fjordane county (kommune), was affected by twelve debris-flows and debris avalanches after an intense precipitation of approximately $107mm/day$. This intensity is found to coincide with the maximum boundary in the absolute threshold ($15-107mm/day$) for debris-flow initiation as reported by Meyer et al. (2012). A parallel regional road in the area (Fv451) was also hit by a large debris avalanche that claimed a person's life. Therefore, the safety and functionality of the existing stretch, its planned improvement, and the new planned stretches should be protected from similar debris-flow threats in the future.

1.2 Motivation

Except some retaining walls and guide walls in a few locations, as reported in NPRA (2014) and NVE (2019b), not many countermeasures are applied in Norway for mitiga-

tion of debris-flow hazards. This Ph.D. study is designed to investigate and assess effective countermeasures for debris-flow threats around and along the E39 highway and for places with similar coastal topographies. The motivation of the study is to understand the behavior of debris-flows in this particular terrain in order to assess effective countermeasure(s) to protect inhabitants, roads users, and road infrastructures. The goal of this study is to assure the functionality of the E39 highway project by providing knowledge for better understanding of debris-flows in steep coastal terrains and by assessing and designing effective debris-flow countermeasures for the area.

Several debris-flows are initiated after excess rainfall or snow melting and their mobility is facilitated mainly by the abundant presence of water and erodible loose material in steep valleys (Breien et al. 2008). In this study, the potential of a screen-type debris-flow countermeasure (hereafter referred to as a *screen*) to serve as an effective mitigating measure by separating water and muddy-slurry from the main body of the sliding mass is investigated. The screen has been implemented in Japan (e.g. ICHARM 2008, Mizuyama 2008, Gonda 2009, and Kim et al. 2012), in the Philippines (e.g. ICHARM 2009 and Atienza and Hipolito 2010), and also in China (e.g. Lien 2003, Xie et al. 2014 and Liu et al. 2017) and has been shown to have been effective by reducing the mobility of debris-flows. In the steeper terrains of coastal Norway, there is lack of space between the infrastructure and sloping valley to place countermeasures like retaining or diversion walls. And so, the motivation to investigate and assess small and effective countermeasures like the screen is clear.

1.3 Research objectives

The following are the objectives of this Ph.D. study.

1. To understand the mobility and impact behavior of debris-flows using a laboratory flume model. In addition, to understand the effects of fines and water contents on behavior and mobility of debris-flows.

2. To investigate the performance and understand the working mechanism of a screen using a laboratory flume model.

3. To investigate the applicability of the screen in the coastal mountainous terrains of Norway, in particular focusing on the majority of the E39 highway section in question. This is done by assessing a suitable numerical model and implementing the countermeasure appropriately.

1.4 Research methodology

The research methodology adopted in this study is given as follows:

1. Literature study on debris-flows and their countermeasures as well as physical and numerical modeling of debris-flow.

2. Site visit on debris-flow event sites and studying the E39 highway area using available landslide maps.

3. A laboratory experiment (physical modelling) study using debris-flow flume models. The study includes investigation of debris-flow behaviors and performance of the screen.

4. Numerical modeling study conducted by back-calculating the laboratory flume tests and a real debris-flow case. The numerical study is also used for back-calculating the performance of the screen in the laboratory scale and up-scaling its performance and evaluating it in the real debris-flow case.

In order to give an overall picture of the research methodology, a work flow chart is presented in Figure 1.3. It demonstrates the relationship between the different research flows and their results.

1.5 Scope of the work

This research is mainly focused on a laboratory investigation of the screen for its suitability and applicability in the Norwegian coastal terrain. The laboratory experiments were conducted using crushed and natural sand aggregates mixed with water as a well-developed debris-flow. These experiments were conducted on two laboratory flume models that have total lengths of $9m$ and $10m$. The models are made from smooth wooden boards that have low friction resistance to the flow. By using these models and the debris-flow material, the debris-flow behavior, its interaction with the screen, and its impact force on vertical passable structures were investigated. In addition, the potential for the screen to reduce the debris-flow mobility and the flow behavior over the screen were studied. This research is complemented by a numerical study which back-calculates the laboratory studies on debris-flows and screen. In addition, a representative debris-flow case from the coastal terrain of Norway was selected and numerically back-calculated. Then, the performance of the screen to mitigate the event was numerically investigated.

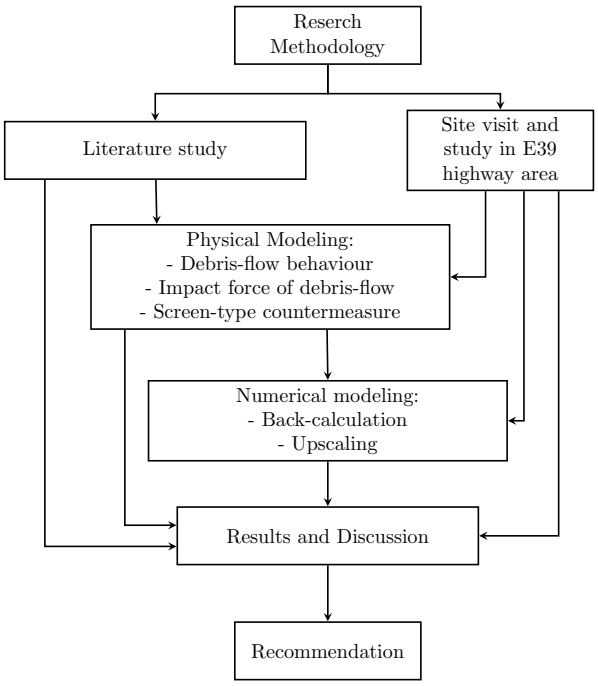

Fig. 1.3: The work flow describing the research methodology used in this study

1.6 Outline of the dissertation

This dissertation has eight chapters including this introductory chapter, which covers the background and motivation of the research, along with its objectives, methodology, and scope. An outline of the other eight chapters is given below.

Chapter 2 is the literature review regarding debris-flow and its flow and impact properties, the common mitigation measures used for debris-flows, physical and numerical modeling, as well as the screen countermeasure. Although a wide range of literature in relation to debris-flow is available, only the relevant topics to this work are selected and presented in this chapter.

Chapter 3 describes the laboratory flume models, their set-up and the methods used for conducting the experiments in this study. It gives a detailed description of the flume models (Model-1 and Model-2), their instrumentation, and the data collection and processing methods implemented. In addition, it explains the different types of screens and the impact force measuring pillars, as well as the set-up of a simple pore-water pressure measuring instrument.

Chapter 4 presents the results of the flume model studies made to evaluate debris-flow behavior, mobility and flow impact force. Debris-flow composition is varied based on water content, fines content, and volume. Effects of debris-flow composition on the flow regime, the run-out distance, and the flow impact force are discussed. In addition, results of the pore-water pressure measurements are presented.

Chapter 5 is entirely dedicated to the study of the screens conducted using both flume models. The first part is a reanalysis of a study made by Laache (2016) and presented in Yifru et al. (2018). In this part, the effects of screen length and opening-width on the flow-mobility are discussed. The second part focuses on the results of investigating the performance of two screen lengths when combined with a down-stream guide wall and underpass. The third part presents effects of varying debris-flow composition in the performance of two screen lengths. In this part, the test is also presented with a close-up study on the working mechanism of the screen.

Chapter 6 covers a numerical modeling study on the flume model tests and a real debris-flow case. A mass flow propagation numerical model called GeoFlow_SPH-FD is used for the numerical simulations. In the first part, results of the numerical simulations of the flume model-2 tests are presented. This includes calibration of the numerical model and evaluating the behavior replication of the flow over the screen. The second part presents the results of the simulation of a real debris-flow case. It covers the results of the back-calculation of the event and an application simulation of the screen to mitigate the event.

Chapter 7 summarizes and concludes the work conducted during this Ph.D. period. The main findings of the individual studies are briefly summarized with concluding remarks.

Chapter 8 gives recommendations and future work. Experiences learned during the laboratory study and numerical simulations as well as works that will be interesting to perform in the future are listed.

1.7 List of publications

This dissertation is presented as a monograph. Two journal articles, one published and one unpublished are also included with the dissertation. The content of the published article is written as a section in the body of the dissertation. The list of conference papers and journal articles are listed below:

- *Paper I*
  Yifru, A. L., Laache, E., Norem, H., Nordal, S., and Thakur, V. (2018). Laborat-

ory investigation of performance of a screen type debris-flow countermeasure. *HKIE Transactions*, 25(2):129–144.

This article is based on the laboratory study conducted by E. Laache and the results presented in her master's thesis. A. L. Yifru contributed in organizing the test and preparing the testing material. A. L. Yifru reanalysed the test results, prepare the figures and plots and wrote the paper. E. Laache contributed in co-authoring by giving feed backs on the draft article. H. Norem, S. Nordal, and V. Thakur contributed in detailed discussions and giving feed backs on the draft article.

- *Paper II*
  Tayyebi, S. M., Pastor, M., Yifru, A. L., Thakur, V., Stickle, M. M. (). Two-phase SPH-FD depth integrated model for debris flows: application to basal grid brakes. *Géotechnique*. Submitted manuscript.

  This article is about the two-phase numerical model and its application to simulate the screen. It uses the laboratory tests made by A. L. Yifru as validating experiment. The article is written by S. M. Tayyebi and M. Pastor with discussion contribution from M. M. Stickle, A. L. Yifru, and V. Thakur.

- *Paper III*
  Yifru, A. L., Pradhan, R. N., Nordal, S., and Thakur, V. (2018). Preliminary study of debris flow impact force on a circular pillar. In McNamara, A., Divall, S., Goodey, R., Taylor, N., Stallebrass, S., and Panchal, J., editors, *Physical Modelling in Geotechnics (ICPMG 2018), Volume 2*, pages 1105–1110, London. CRC Press.

  This paper presents preliminary debris-flow impact force study on a passable structure. The conceptual idea of using a circular pillar as impact force measuring passable structure was first raised by S. Nordal and then designed and implemented by A. L. Yifru. The laboratory experiment was conducted by A. L. Yifru and R. N. Pradhan. The analysis, interpretation of results, and writing of the paper were performed by A. L. Yifru with discussions and inputs from S. Nordal and V. Thakur.

- *Paper IV*
  Yifru, A. L., Vicari, H., Nordal, S., and Thakur, V. (2019). Laboratory investigation of the impact force of debris flow on a passable structure. *In Proceedings of the XVII ECSMGE*, in Reykjavik, Iceland, September 1-6.

  The main idea of the research topic was proposed by A. L. Yifru. This includes the manufacturing of rectangular pillar and variation of the debris-flow composition. The experimental works were done by A. L. Yifru with help from H. Vikari.

The analysis, interpretation of results, and writing of the paper were performed by A. L. Yifru with beneficial feed backs from H. Vikari, S. Nordal, and V. Thakur.

2 Literature review

2.1 Introduction

The literature on debris-flow is a wide subject covering its different aspects. In this review, only important aspects in relation to the studies conducted in this work will be covered. This includes the general description of debris-flow and its mobility dependence on fines and water content, the types and kinds of mitigation measures, and the physical and numerical modeling studies of debris-flow.

2.2 Description of debris-flow

Definitions:
Debris-flow is defined as a very rapid to extremely rapid flow of saturated, non-plastic debris in a steep channel (Jakob and Hungr 2005). Another definition by Coussot and Meunier (1996) states that debris-flow is a peculiar event during which a large volume of a highly concentrated viscous water-debris mixture flows through a stream channel. Besides their rapid mobility, the above definitions state that these flows occur in a defined channel with a possibility for recurrence.

Classifications:
Based on the fraction of solids within the total volume (solids fraction) and the material type, Coussot and Meunier (1996) classified mass movement (as seen in Figure 2.1) and described debris-flow as an intermediate phenomena between hyper-concentrated flows (intense bed load transport) and landslides where the sharp transitions can be identified by flow characteristics like celerity, nature of deposition, and flow type. This qualitative and conceptual classification can be backed by a quantitative value describing the amount of solids in the moving mass. In distinguishing debris-flow from both hyper-concentrated flow and landslide, critical solid fraction (volume concentration) values can be used (Coussot and Meunier 1996). Based on the coarse particle concentration by volume, C and on the basis of *Reynolds number, Bagnold number*, and relative flow depth (h/d), Takahashi (2009) and Takahashi (2014) categorized debris-flows' flow characteristics. Mixtures with $C \geq 0.56$ are referred to as rigid while quasi-static motion is found to have a grain concentration of $0.5 < C < 0.56$. The dynamic debris-flow, which specifically has coarse particle concentration, $C \leq 0.5$ (Takahashi 2014), includes the three types of debris-flows referred to as stony, muddy and viscous, as shown in Figure 2.2, where τ_t, τ_v, τ_c, and τ are the turbulent mixing, viscoplastic, inter-particle collision, and total shear stresses, respectively. In Figure 2.2, the dominant stress is given along with the debris-flow types.

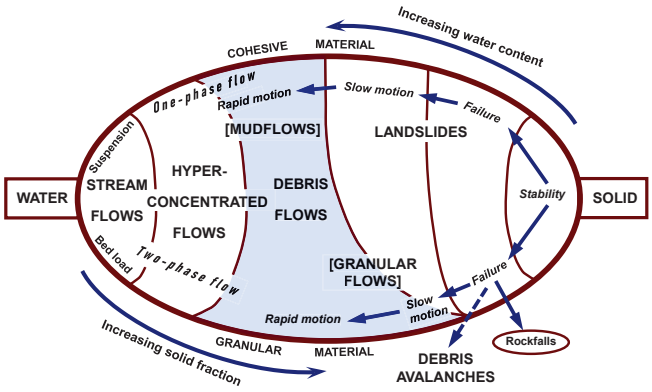

Fig. 2.1: Classification of mass movements on steep slopes as a function of solid fraction and material type, Adopted from Coussot and Meunier (1996)

The debris-flow is called *stony* when the particle collision stress dominates; or, it is called *turbulent-muddy* if the dominant stress is turbulent mixing shear stress; or, it is called *viscous debris-flow* when viscoplastic stresses dominate (Takahashi 2009).

The ratios of these three stresses; τ_t/τ_v, τ_t/τ_c, and τ_c/τ_v give *Reynolds number,* h/d, and

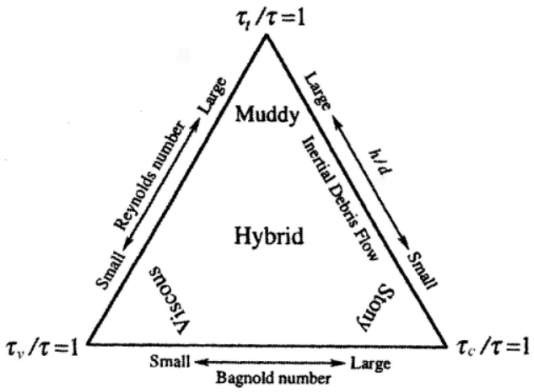

Fig. 2.2: Categories of dynamic debris-flows (Takahashi 2009)

Bagnold number, respectively. These dimensionless parameters can be used to indicate the dominant stress in a given flow type. Stony debris-flows may be characterized by larger *Bagnold number* and smaller flow depth to mean grain diameter ratio (h/d) while viscous debris-flow can be characterized by smaller *Bagnold* and *Reynolds number* (Takahashi 2014). Similarly, Muddy debris flows may occur in region where both *Reynolds number* and h/d are larger while the center region where the flow is not dominated by

either of the stresses may be called hybrid-type debris flow (Takahashi 2014). Debris-flow regime characterization based on dominant internal stresses is explained in more detail in Section 2.7.3.

Parts of a debris-flow:
A typical debris-flow has three zones and can be named as: initiation, transport or deposition zones (Hungr 2005). These zones are explained as follows in Hungr (2005): the initiation zone (source area) is the part where the initial slide, slope failure or erosion happens. In general, this zone is characterized by a steep slope ranging between 20° and 45°. The transport (transition) zone is a down-sloping channel or path, through which the already initiated slide usually gains additional sediment (volume) and mobility. Peak velocity of flow mostly occurs in this flow zone. The deposition zone is the area found at the foot of the steep-sloped transportation zone. This area can easily be distinguished by its relatively flat terrain. It can also be the bottom of a valley. Most infrastructures and human settlements are located in this flatter terrain where debris-flows make debris or colluvial fans. The flow decreases its speed and stops with a considerable damaging force on the settlements and infrastructures nearby.

Debris-flows, usually, have several surges. However, each surge can be characterized by a flow having a flow front, a flow body and a tail, as shown in Figure 2.3. The flow

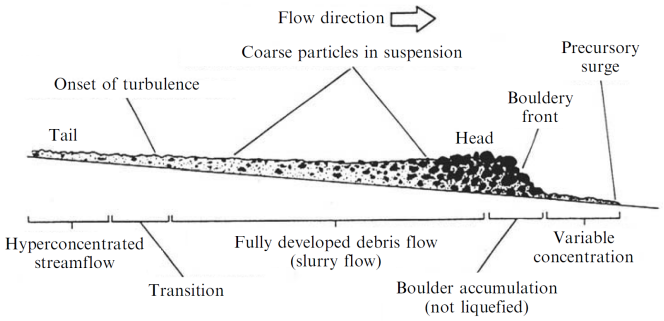

Fig. 2.3: debris-flow surge diagram from Pierson (1986) as referred by Hungr (2005)

front is usually characterized by a part containing boulders and coarser sediments pushed by the more continuous looking flow body which itself mainly contains finer masses of liquefied debris (Hungr 2005). The tail mainly contains sediment-charged water with a turbulent flow behavior. In general, debris-flow contains almost all sorts of earth and organic material: from big boulders to small grained soil with less than 80% sand and fines fraction (Varnes 1978). In forests and vegetated locations, logs of trees and organic matter can also be found within the debris-flow.

Common causes of debris-flow:
Debris-flows could occur in any region with steep terrain and which has at least occasional rainfall Jakob and Hungr (2005). This occasional rainfall contributes water that is sufficient for saturating unstable slopes and mobility after these slopes fail. Debris-flows can be initiated (triggered) by an erosion of a stream bed, form a small landslide on an unstable steep slope, or from pyroclastic flows (Jakob and Hungr 2005, Takahashi 2014, and NPRA 2016). The stream bed erosion and the slope failure are factors that are strongly associated with heavy or intense rainfall or quick snow melting. The extra water could create strong eroding floods in a stream or could saturate an unstable slope and weaken the failure surface even more. In addition, volcanic eruptions, earthquakes and the disruption of lakes or artificial debris dams can be the prior events for the triggering of debris-flows (Jakob and Hungr 2005).

2.3 Contribution of water and fines to debris-flow mobility

The role of water and fines content in debris-flow behavior has caught many researchers' attention (among others, eg. Savage and Iverson 2003, McArdell et al. 2007, Wang and Sassa 2007, Gonda 2009, Kim et al. 2012, and Cascini et al. 2016). Presence of water plays a vital role in the initiation and transportation zones of debris-flow. The majority of debris-flow triggering factors involve the presence of water. Intense rainfall within a short duration or a prolonged precipitation makes unstable soil masses heavier, while also decreasing the friction capacity of week failure surfaces as a result of pore-water pressure development in the presence of fines. Melting of snow or ice can result in creating a similar effect. Water that sometimes percolates underneath a relatively thin soil cover that rests on rock slopes could trigger surface (translational) slides that eventually grow to become debris-flows while traveling through a stream path with an erodible bed.

The body of a debris-flow surge consists of a water-saturated, muddy, granular slurry, liquefied by high pore-water pressure, whereas the front of a debris-flow surge consists of unsaturated, coarse-grained, granular rubble that is pushed from behind by the liquefied slurry (Iverson 1997). Several experimental studies were conducted to measure the basal pore-water pressure in debris-flows. These include, among others, Major and Iverson (1999), McArdell et al. (2007), Wang and Sassa (2007), and Kaitna et al. (2016). These studies gave insights on the pore-water pressure proportion in relation to the total normal stress, the pore-water pressure dissipation, and the decaying behavior on debris-flow deposition. The high pore-water pressure in excess of the hydrostatic water pressure facilitates the high mobility of the debris-flow and is maintained through the entire course of the flow. Once a debris-flow is triggered, the fines in the moving mass would maintain the developed pore-water pressure and reduce the contact friction between grains, and easily floating them over an arbitrary shearing layer. This liquefied mass flow usually stops or reduces its speed mainly because of the topographic features and external res-

isting factors. Widespread natural decay of pore-water pressure in the flow margin does not contribute to debris-flow deposition, rather it is the grain-contact friction and bed friction concentrations that contribute (Major and Iverson 1999).

In addition to the excess water that contributes to pore-water pressure development in the soil mass, the amount of the soil's fines content has its own significant effect. Variations of fines content (10%, 20%, and 30% loess) in pore-water pressure build-up was observed to show no significant difference in the failure while resulting in remarkable variation in the flow behavior afterwards (Wang and Sassa 2007). The mobility of the debris-flow is observed to increase with increasing fines content. This suggests that fines content provides a mechanism for maintaining the already generated pore-water pressure in the motion by keeping the particles floating for longer durations easily (Wang and Sassa 2007). In addition, a study conducted by Chen et al. (2010) showed that clay content variation could contribute to the soil mass failure when the clay content is varied in the ranges below 10%. The 5-10% clay content cases resulted in debris-flows that were triggered by slide failures due to pore-water pressure build-up, whereas the cases with clay contents larger than 10% resulted in debris-flows from the top surface erosion. Low clay contents below 5% resulted either in no failure or took long time to fail by exhibiting only surface erosion.

2.4 Debris-flow mitigation measures

2.4.1 Introduction

The common debris-flow triggering factors in Norway are intense and prolonged rainfall and the rapid melting of snow (Sandersen 1997) resulting in high soil saturation and severe surface runoff (Meyer et al. 2012). The frequency of occurrence of debris-flows has increased with the increased events of intense rainfall and quick snow melting in connection to the changing climate (NVE 2011). As a result, there is a growing need for methods to predict and prevent the debris-flow hazards. Prevention (mitigation measures) can be made either by keeping infrastructures and settlements away from the expected hazard or by constructing preventive structures. Debris-flow mitigation measures are those implemented to reduce the existing risk to an acceptable level of residual risk; generally, it is classified in two main categories: active, and passive (Huebl and Fiebiger 2005). These two can, sometimes, be referred to as structural and non-structural mitigation measures, respectively.

2.4.2 Non-structural Mitigation Measures

Non-structural (passive) mitigation measures focus on the reduction of the potential loss that could result from potential debris-flows by setting up early warning systems, mapping

the hazard zones, and establishing land-use zones. Providing information and education about the hazards within specific areas, setting up disaster management protocols and specifying construction rules are a few of the passive mitigation measures which can be taken *prior* to a debris-flow occurrence. On the other hand, providing information and closing traffic, giving warnings, facilitating evacuations, and technical assistance are some tactics which are considered as passive mitigation *after* a debris-flow happens.

In Norway, debris-flow hazard (susceptibility) mapping has been given attention, and Stalsberg et al. (2012) presents a description of how the susceptibility mapping is done at the national level. A report from the Norwegian Water Resources and Energy Directorate, (NVE 2014), presents this preliminary regionalization of Norway for the purpose to be used in the landslide early warning system or in related investigation projects for mitigation provisions.

2.4.3 Structural Mitigation Measures

Structural mitigation measures, equally referred to as structural countermeasures, focus mainly on reducing the debris-flow magnitude and frequency characteristics by affecting its initiation, transportation, or deposition processes (Huebl and Fiebiger 2005). The selection and application of a structural countermeasure should be made with consideration that to which extent that it is effective, dependable, inexpensive, and easy to install. Some of the structural mitigation measures include, as given in Figure 2.4, open and closed check dams (sabo dams) (Jaeggi and Pellandini 1997, Wu and Chang 2003, Mizuyama 2008, Maricar et al. 2011, and Armanini et al. 2014), flexible barriers (Wendeler et al. 2006, Volkwien et al. 2011, Bugnion et al. 2012, Canelli et al. 2012, Wendeler and Volkwein 2015, Ashwood and Hungr 2016, and Song et al. 2018), baffles(Choi et al. 2014, and Ng et al. 2014), deflection walls (VanDine 1996, Huebl and Fiebiger 2005, and Le et al. 2016), debris-flow screens (breakers) (Ishikawa et al. 1994, Nisimoto et al. 1994, Mizuyama 2008, and Gonda 2009), channel side walls (Huebl and Fiebiger 2005, and VanDine 1996), and deformable geosynthetics-reinforced barriers (DGRB) (Cuomo et al. 2019; 2020b, and Cuomo et al. 2020a).

Not many of these countermeasures have been applied in Norway for the purpose of mitigating debris-flows. The mitigation measures given in Figure 2.5 are a few representative examples that are in use for protecting settlements, roads, and some factory buildings from snow avalanches, quick clay slides, floods, earth- and debris-flows, as well as rockfalls. In addition, as an immediate mitigation measure, an embankment wall with a storage basin is used to protect a road after a recent debris-flow event in Mjåland, Norway.

Deflection walls and protective walls are mainly used to mitigate snow avalanches, rockfalls, and earth-flows (as seen in Figures 2.5(b), (d), and (f)). Screens of metal grids

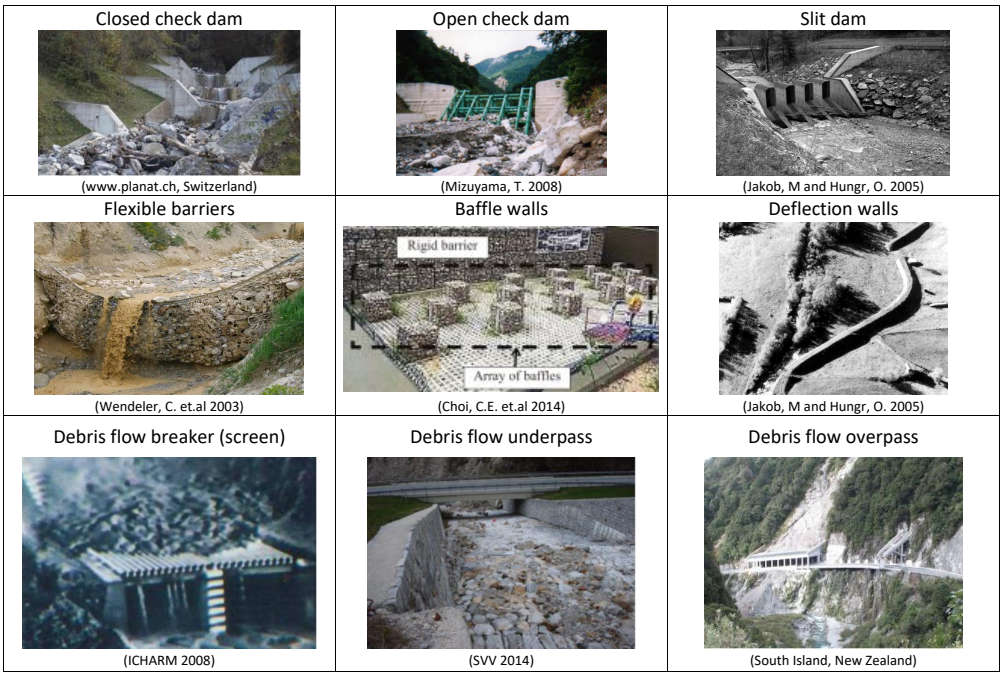

Fig. 2.4: Commonly used structural countermeasures

are used for collecting and reducing flow velocity of snow avalanches (as seen in Figures 2.5(a)) and a small screen in a small stream with a debris collecting basin is used for mitigating erosion and possible earth-flow (as seen in Figures 2.5(c)). The widely used securing or protecting method used is erosion protection along streams and rivers in quick-clay deposit zones (as seen in Figures 2.5(e)). Earth mounds are also being used in connection with deflection walls to mitigate settlement that is exposed to snow avalanches and rockfalls (as seen in Figures 2.5(f)). In this particular case, it is also reported that some of the houses are moved to different place as part of the mitigating process to protect human lives. In addition to these, flexible barriers have been used to mitigate rockfalls in some parts of Norway but not typically for debris-flows.

To fill the knowledge and experience gap in mitigating debris-flows in Norway, several studies have been conducted using the NTNU flume models. Check dams and baffle walls were studied by Fiskum (2012), and deflection and channel walls were studied for debris-flow mitigating application and reported in Le et al. (2016). In general, NPRA (2014) and NPRA (2016) suggests various countermeasures to mitigate debris-flow hazards with general guidelines in their applications at the source, transportation and deposition areas of debris-flows. As given in Figure 2.5, some of the countermeasures have been applied

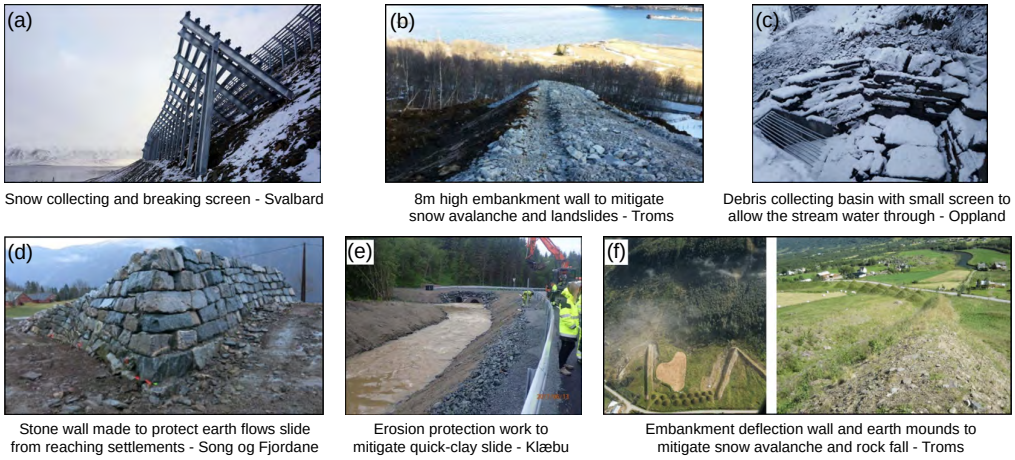

Fig. 2.5: Countermeasures that are often used in Norway for different kinds of landslides, flood, and snow avalanche as given in yearly reports of NVE (NVE 2017; 2018, and NVE 2019a)

in Norway, except the debris-flow screens. Therefore, the screens are investigated in this study for their suitability in mitigating debris-flows in Norway.

Most of the recorded debris-flows in Norway are described to have happened after a considerable amount of rainfall or rapid snow melting. This makes most of the debris-flows in Norway more or less water-based. Separating the water, which is the main mobility facilitator, from the debris-flow might be the first and crucial solution to mitigate its threats. This method of separating the water (fluid part) from the debris-flow can be done by installing the screens in the debris-flow's path. Details of the screen and its working mechanism along with the evaluation methods are described in the following Section 2.5.

2.5 Screen-type debris-flow countermeasure

2.5.1 Introduction

The idea of using screens was conceived in Japan by Professor Noriaki Hashimotoin in the 1950s with the intention to reduce the energy in debris-flows and, thus, contribute to mitigating damage in downstream areas (ICHARM 2008). The main purpose of this screen is to separate water or the fluid from the moving debris. As a result, the pore-water pressure developed inside the debris-flow, particularly in the shearing zone, would dissipate. In return, the debris' solid particles regain their contact friction and thereby increase the shearing resistance of the moving debris (Ochiai et al. 2007, Gonda 2009, and Cascini et al. 2016). A schematic representation of a screen and its before and after debris-flow event is illustrated in Figure 2.6.

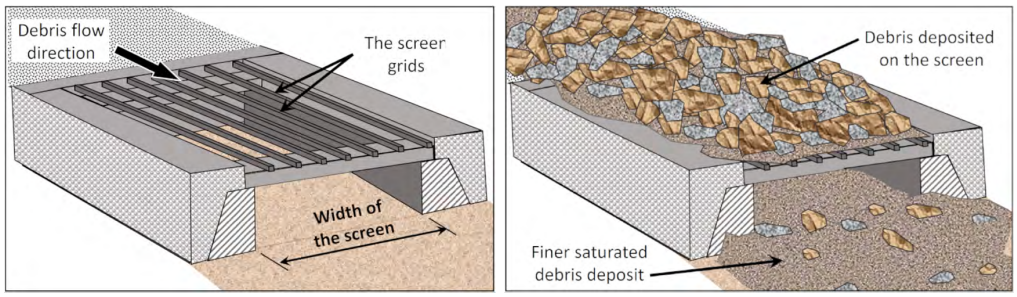

Fig. 2.6: The screen: (a) before a debris-flow event giving its schematic representation, and (b) after a debris-flow event showing the material depositions (Yifru et al. 2018)

2.5.2 Application and performance

A number of studies have investigated the screens, and a field trial in the Kamikami-Horisawa Valley of Japan has also been reported throughout literature (e.g. Mizuyama 2008, Gonda 2009, and Kim 2013). In addition, screen performance, application and some aspects of its design, mostly in Japan, have been communicated in Japanese literature (e.g. Imai et al. 1989, Ishikawa et al. 1994, Nisimoto et al. 1994, Suwa et al. 2009, and Yokota et al. 2012) which is also referred to the screens as debris-flow breakers.

The screen implemented in the Kamikami-Horisawa Valley is studied widely and referred in the above literature. It is $20m$ long and $10m$ wide in which the screen grids are made of $0.2m \times 0.2m$ square steel tubes, that were $8mm$ thick, and are resting on $0.4m \times 0.4m$ wide flange beams. The grids have a spacing of $0.2m$ (Gonda 2009 and Yokota et al. 2012) where the screen opening ratio is 50%. Nisimoto et al. (1994) studied the grain size distribution of the accumulated debris on top of the screen where the size varies between $80mm$ and $1000mm$. In contrast, the maximum grain size of the debris under the screen is around $300mm$ which is slightly more than the opening width. The bigger sized grains ($200mm < d \leq 300mm$) could have passed through the opening width because of their irregular or flat shape. The debris hold back behind the screen due to the damming effect of the accumulated debris on the screen has all range of particle size with maximum $300mm$ and $1000mm$ with respective d_{50} values $60mm$ and $250mm$, the coarser being located closer to the screen.

Due to their simple construction and cost effectiveness, screens have also been implemented and used in other countries, including Mainland China (e.g Lien 2003, Xie et al. 2014, and Liu et al. 2017) and the Philippines (e.g. ICHARM 2008; 2009, and Atienza and Hipolito 2010). In the Philippians, screens have been used to protect mountain roads by installing them in narrow sections of streams where recurrent debris-flows occur.

Performance and effectiveness of screens have been investigated in a small-scale flume model by Gonda (2009). The study was conducted to evaluate the different opening widths of the screens according to the debris-flow run-out distance. Three different uniform-sized materials of $700cm^3$ volume were used. The study found that the reduction in run-out distance increases with an increase in the opening width of up to approximately $2mm$. Kim (2013) investigated three different bed sediments of 13 300 cm^3 in volume with three different blocking and opening widths of screens. The study showed the effect of opening width percentages in reducing the run-out distance. However, the above two studies used the screens as a deposition area and in all the tests, the mass of the debris-flow was retained over the screen. In real debris-flow cases (as shown in Figure 2.6), the entire debris-flow volume might not be deposited on the screen. Therefore, in this study, it was found important to investigate the effects of varying screen lengths on the run-out distance beyond the screen. In addition, the run-out distance and velocity reduction potential of different screen opening widths in combination with the screen length is investigated in this study.

2.5.3 Working mechanism of the screen

The excess pore-water pressure hinders the grain to grain contacts of the solid particles which replaces and overtakes the effective stress part that could mainly contribute to flow resistance. Savage and Iverson (2003) expressed the components of the total normal

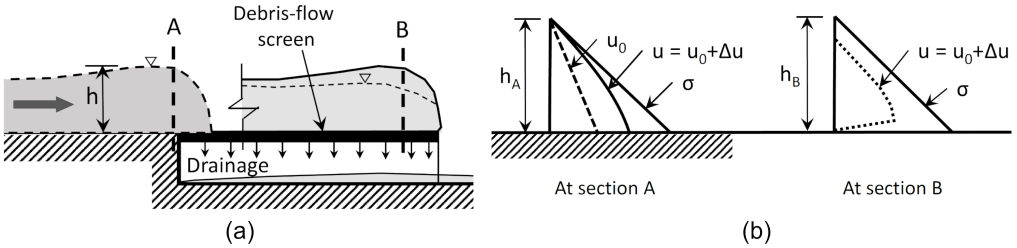

Fig. 2.7: Pore-water pressure development during debris-flow and its dissipation when it hits a screen-type countermeasure: (a) A Schematic representation of a debris-flow on a solid surface and on a screen. (b) Total normal stress components and distribution in the debris-flow mixture: section A is over a solid surface, and section B is over a screen (Yifru et al. 2018).

stress, σ, as a sum of the effective stress generated between grains, the hydrostatic water pressure and the excess pore-water pressure. A schematic representation of this total normal stress components and distribution of debris-flow on a solid surface is seen in Section A of Figure 2.7(b). Major and Iverson (1999) showed that the pore-water pressure persisted until the debris-flow was deposited, and then it dissipated significantly during post-depositional sediment consolidation. Even though it is described that the debris-flow stops in the deposition area before a significant amount of the excess pore-water

pressure is dissipated, one can introduce a screen that helps facilitate the fluid drainage and there by dissipation of pore-water pressure. This results in the increasing of the grain-contact friction and grain-bed friction concentration by the sudden removal of fluids, i.e., dissipation of the pore-water pressure, as schematically shown in Figure 2.7(b) in section B.

2.5.4 Energy dissipation evaluation

Energy grade line (EGL) can be used here for quantifying and evaluating the flow resistance potential resulted from using the screen. In this study, it is used for showing the effectiveness of the type of screen used. The EGL of debris-flow in section A and B of Figure 2.7(a) can be expressed as the total energy in terms of head, H, which can be given by the Bernoulli equation. Considering an open channel flow situation, the Bernoulli equation of debris-flow just before the beginning of the screen, in section A, can be expressed by Equation 2.1:

$$H_A = z_A + h_A + \frac{(v_A)^2}{2g} \tag{2.1}$$

where H_A is the total head in m; z_A is the elevation of a point from a reference datum in m; h_A is the debris-flow pressure head, which is equal to σ_A/γ in m; σ_A is the total normal stress in kN/m^2; γ is the unit weight of the debris kN/m^3; v_A is the flow velocity and g is the gravitational acceleration. Similarly, the energy head at the end of the screen, in section B, can be expressed by Equation 2.2.

$$H_B = z_B + h_B + \frac{(v_B)^2}{2g} \tag{2.2}$$

The effectiveness of screen can be shown by the energy dissipation factor, E_D, which can be expressed by Equation 2.3.

$$E_D = 1 - \frac{H_B}{H_A} \tag{2.3}$$

where $E_D = 0$ represents no energy dissipation, while $E_D = 1$ represents the maximum possible energy dissipation. If the screen is aligned horizontally, as in the case of this study, and with a relatively low pressure head compared to the velocity head, the energy dissipation of the debris-flow when moving from section A to section B can be approximated by the velocity head term only, i.e., $v^2/(2g)$. Then, Equation 2.3 is simplified to become Equation 2.4.

$$E_D \approx 1 - \left(\frac{v_B}{v_A}\right)^2 \tag{2.4}$$

Equation 2.4 is later used for assessing the different screens investigated in this study.

2.6 Impact force of debris-flow

2.6.1 Introduction

In assessing the hazard and damage that results from debris-flow events, impact force is one of the debris-flow characteristics that is considered important. The debris-flow impact force on road structures and settlements, that are situated in debris-flow susceptible areas, need to be taken into consideration. In order to estimate the impact forces, several small- and large scale impact force studies were conducted, with analytical debris-flow impact force estimating formulas, and reported in, among other, (Hungr et al. 1984, Arattano and Franzi 2003, Huebl and Holzinger 2003, Huang et al. 2007, Huebl et al. 2009, Proske et al. 2011, Scheidl et al. 2013, Cui et al. 2015, Vagnon and Segalini 2016, He et al. 2016, and Poudyal et al. 2019). Those that are considered applicable and suitable for dynamic debris-flow behavior are discussed here. In addition, the impact behavior along with its dynamic parts are discussed.

2.6.2 Analytical impact force formulas

Several analytical hydro-static and hydro-dynamic models are reported in, among others (Hungr et al. 1984, Arattano and Franzi 2003, Huebl and Holzinger 2003, Huebl et al. 2009, Proske et al. 2011, and Vagnon and Segalini 2016). The first hydro-static formula is given by Equation 2.5 which gives a basic static pressure equation for estimating the impact force with a multiplying factor K as a compensation for the dynamic behavior.

$$p = K \cdot \rho \cdot g \cdot \frac{h^2}{2} \tag{2.5}$$

where p is impact force per unit width, ρ is the bulk density, g is gravitational acceleration, and h is the impact height. Different values of K are reported in literature given that the flow has smaller flow velocity. These are: for example, the values of K is given as $7-11$ by Lichtenhahn (1973), 9 by Armanini (1997), $5-15$ by Scotton and Deganutti (1997).

Another version of Equation 2.5 is given by Zanuttigh and Lamberti (2006) after studying impact of dry avalanches on structures. The formula is given by Equation 2.6 and it incorporates the dynamic effect by introducing an expression using the Froude number, F_r (i.e. $v/\sqrt{gh}$) and the constant K^* as a factor to account for non-represented flow processes. After the equation was compared with field observation data, the value of K^* was suggested to be 1.0 for stony debris-flows and 1.5 for muddy debris-flows.

$$p = K^* \cdot \frac{(1+\sqrt{2}F_r)^2}{2} \cdot \rho \cdot g \cdot h^2 \tag{2.6}$$

The first hydro-dynamic model equation, F_{hd1}, is derived from conservation of momentum, as stated in Hungr et al. (1984) and is given by Equation 2.7. The effect of impact direction is explicitly incorporated by the impact angle term.

$$F_{hd1} = \rho v^2 A \cdot sin\beta \tag{2.7}$$

where β is the least angle between the face of the structure and the flow direction (Hungr et al. 1984); v is the flow velocity; A is area of impact; g is gravitational acceleration; and h is the impact height.

The second hydro-dynamic model equation, F_{hd2}, is proposed by Huebl and Holzinger (2003) and is given by Equation 2.8. F_{hd2} was obtained by normalizing measured impact pressure with the hydro-dynamic pressure factor (ρv^2), and relating it with the F_r (Huebl et al. 2009, Proske et al. 2011).

$$F_{hd2} = 5\rho v^{0.8}(gh)^{0.6}A \tag{2.8}$$

A mixed model was also given by Arattano and Franzi (2003) and Vagnon and Segalini (2016) after considering both static and dynamic contribution of the flow. The general equation for this mixed model is given by Equation 2.9.

$$F_{mixed} = \frac{1}{2}\rho ghA + \rho v^2 A \tag{2.9}$$

Another version of the hydro-dynamic equation was suggested by Mizuyama (1979) and is given by Equation 2.10. This equation is a version of the first hydro-dynamic equation, F_{hd1}, that was given by Equation 2.7. It replaced the explicitly given impact angle term with a so called correction factor 'k' to serve as an overall term for behaviors that are unaccounted for.

$$p = k \cdot \rho \cdot q \cdot v = k \cdot \rho \cdot h \cdot v^2 \tag{2.10}$$

where k is correction factor (with $k = 1$ from Mizuyama (1979)), q is the discharge per unit width. This relationship is also given in several studies with different k values in which, among others, Daido (1993) gave $5 - 12$, and Armanini (1997) gave $0.7 - 2$.

In order to compare results from laboratory flume tests with debris-flows in nature, similitude for the dimensionless quantities shall be attained. In several impact force studies, two dimensionless parameters, F_r and Reynolds number (Re), were used to compare results of the scaled model with field observations. Wang et al. (2018) reported that dimensionless impact pressure is a power function of F_r for low-viscous debris-flows and of both F_r and Re for high-viscous debris-flows. This is in line with what Huebl et al. (2009) and Armanini et al. (2011) considered F_r as a key dimensionless similarity factor to scale debris-flow impact on structures.

Real debris-flows in nature mostly have velocity v up to $10m/s$ (with some exceptions up to $20m/s$), and flow height h of around $1m - 3m$ (which could go up to $10m$ in some exceptional cases) (Fink et al. 1981, Costa 1984, Iverson 1997, and Iverson and Denlinger 2001); this can give an F_r value up to around 3 where this approximate limiting value is reported also by (e.g., Huebl et al. (2009) and Wendeler and Volkwein (2015)).

A power-function relationship between the dimensionless quantity, F_r and another dimensionless quantity, the empirical coefficient (normalized pressure), α, is reported in Huebl and Holzinger (2003), Huebl et al. (2009), Proske et al. (2011), and Cui et al. (2015), and given by Equation 2.12.

$$P = \frac{F}{A} = \alpha \cdot \rho \cdot v^2 \tag{2.11}$$

$$\alpha = \frac{P}{\rho \cdot v^2} = a \cdot F_r^b \tag{2.12}$$

where a and b are coefficients for the power-function relationship between F_r and α. This relationship is developed by using data from miniaturized tests and field observations found in, among others, Huebl and Holzinger (2003), Tiberghien et al. (2007), Proske et al. (2011), and Scheidl et al. (2013). Values of the power-function coefficients were determined by Cui et al. (2015) after processing 155 data sets where $a = 5.3$ and $b = -1.5$. This relationship has become a robust tool to estimate the impact pressure using F_r in addition to allowing relation between the flume model test results with the field observations.

Faug (2015) presented another dimensionless relationship using compilation of several data spanning a wide range of F_r. Flows with $F_r < 0.1$ are characterized by quasi-static where the normalized force (by gravity force expression), $F/(1/2 \cdot \rho \cdot g \cdot h^2 \cdot w)$, varies between constant boundaries between 1 and 100 while flows with $F_r > 10$ are characterised as very rapid regime flows where the normalized force (by kinetic force expression),

$F/(1/2{\cdot}\rho{\cdot}v^2{\cdot}h{\cdot}w)$, varies between constant boundaries between 1 and 5. The intermediate region between quasi-static and very rapid regime flows, $0.1 < F_r < 10$, is not constant for either of the to normalized relationships, i.e. in this region, neither the quasi-static nor the hydrodynamic dominates the flow and expressed by either h or v (Faug 2015). Based on these two relationships and their boundaries, Faug (2015) proposed two expressions describing each. As the static (quasi-static) contribution of the tests conducted in this study are insignificant compared to the dynamic one, only the dynamic relationship, given by Equation 2.13, and its plot, given seen in Figure 2.8, are given. The intermediate

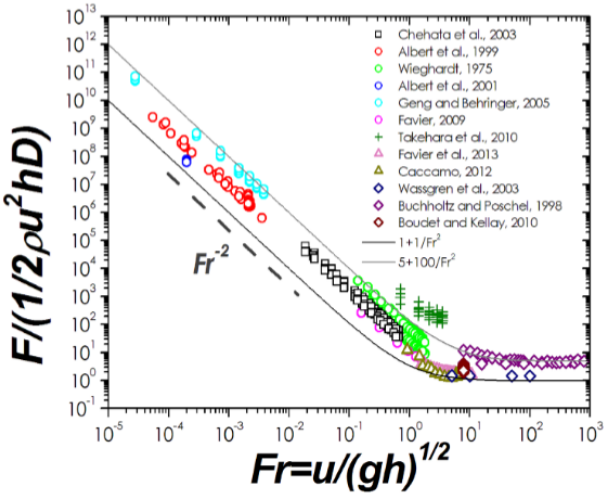

Fig. 2.8: Wide range relationship between F_r and impact force normalized by the kinetic force expression (Faug 2015)

region is where most dynamic debris-flows fall. It is also typical of flows down an inclined plane (Faug 2015) and the lower and upper bounding lines in relating the hydrodynamic expression with the F_r can be given by Equation 2.13.

$$\frac{F_{peak}}{1/2 \cdot \rho \cdot v^2 \cdot h \cdot w} = \frac{K'}{F_r^2} + C' \tag{2.13}$$

where K' and C' are given as 1 and 1 for the lower bound where as for the upper bound it is 100 and 5, respectively. K' and C' are given as an equivalent earth pressure coefficient and a pure drag coefficient, respectively. These coefficients are further explained by anther analytical expressions in Faug (2015) which are found to be beyond the scope of this study and not discussed further here.

2.6.3 Impact force parts and processes

Impact force of debris-flow can be divided into three parts where they are listed by He et al. (2016) as the dynamic pressure provided by the slurry (fines and water), the impact force of coarser particles, and the impact force of boulders. Most of small-scale laboratory tests resulted in impacts forces from the slurry and coarser particles. Some large-scale and field tests were conducted to evaluate the impact force of boulders, among others Huang et al. (2007), He et al. (2016), and Poudyal et al. (2019). It was stated by Poudyal et al. (2019) that boulders can result in sharp impulses that exceed the analytical impact equations. Therefore, a separate assessment and design method is required to address localized damages on structures due to an individual boulder impact, similar to a theoretical impact model proposed by Huang et al. (2007). Impact force of boulders falls out of the scope of this dissertation and it is not discussed further.

According to Cui et al. (2015), the impact process of debris-flow can be roughly divided into two parts based on the variation of impact force signals and the flow regime (as shown by Figure 2.9). The first is the sudden peak impact of the debris-flow front

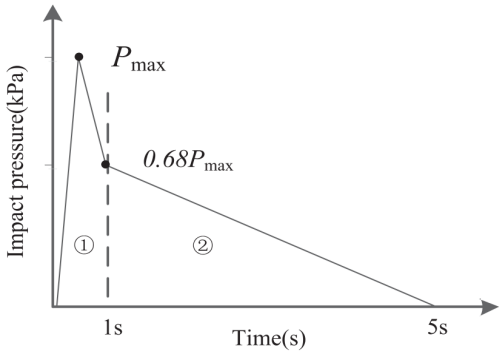

Fig. 2.9: Simplification of impact process of debris-flow. Part (1) and (2) representing the head impact and the body impact of the debris-flow, respectively. (Cui et al. 2015)

which can be characterized by impact of a dry, coarser snout while the second part is the continuously declining dynamic pressure of the subsequent flow behind the front. The second part can be followed, in some cases, by an almost constant static pressure of the tail and possible accumulated mass. Cui et al. (2015) represented the second phase by a duration of 4 seconds in which its peak impact pressure is 68% of the peak of the first phase.

2.7 Physical modeling of debris-flow

2.7.1 Introduction

The necessity to understand the behavior of debris-flow has increased recently in connection with the rapidly changing climate. Several large- and small-scale experimental studies have been employed to understand the debris-flow behavior and its mobility factors. The data from real debris-flow events are mostly estimations made after the events have taken place by observing their extent, trails and depositions. Due to its unpredictable nature and challenges to observe it when it happens, researchers employ physical modelling to study different aspects of debris-flow and ways of mitigation. These physical modelling methods include small- and large-scale flume tests, centrifuge tests, as well as field tests. A summary of large-scale and field tests, as well as centrifuge tests, is given in Section 2.7.2

In employing one of these physical modelling methods, reasonable scaling adjustments need to be made to closely replicate the stress transfer that usually happens in the real debris-flow cases. The debris-flow regime can be distinguished by dimensionless quantities which can be used for estimating the stress transfer in the flow. These dimensionless quantities are explained in Section 2.7.3 and are used for comparing the real and field debris-flow characteristics with the performed laboratory tests in this study. Finally, a short review of the studies made in NTNU's flume model since 2009 is given in Section 2.7.4.

2.7.2 Flume modeling and field testing of debris-flows

In order to compensate for lacking proper real event observations and their valuable data, large-scale debris-flow flume and field tests have been conducted by several researches, (e.g. Iverson et al. 1992, Moriwaki et al. 2004, Ochiai et al. 2004, and Ochiai et al. 2007). They are, generally, built for performing different kinds of tests to study debris-flow behaviors by providing a condition that is very close to the actual events. The field test by Ochiai et al. (2004) investigated the initiation and propagation of landslides in a natural slope induced by an artificial rainfall. This study was then complemented with an almost real-size large-scale flume model test to further investigate the landslide fluidization during excess rainfall events as reported by Ochiai et al. (2007). In these studies, including in Moriwaki et al. (2004), the role of rainfall in initiating landslides was shown when it resulted in an excess overburden load that rapidly loaded the shearing layers to generate excess pore-water pressure and large shearing rates.

In most of the cases, conducting a single test requires the engagement of several skilled professionals with expensive test facility and instrumentation. Such large-scale flume

models might not be the most cost-effective or easiest options when focusing on a single or a couple of debris-flow behaviors with parameter variations in several repetitive tests. For such kinds of tests, researchers use small-scale flume models of different sizes by scaling one or a few more aspects of real debris-flows (e.g. Wang and Sassa 2001, Lien 2003, Tiberghien et al. 2007, Ishikawa et al. 2008, Gonda 2009, Kim et al. 2012, Ng et al. 2014, Xie et al. 2014, Scheidl et al. 2015, Wendeler and Volkwein 2015, Vagnon and Segalini 2016, and Zhou et al. 2019). These small-scale flume tests have been adopted to understand different flow mechanisms and the properties of debris-flow as they are cheaper with respect to both time and resources. Likewise, in the Geotechnical division of NTNU, several debris-flow related studies have been conducted using small-scale flume models since 2009 (e.g. Heller and Jenssen 2009, Fiskum 2012, Christiansen 2013, and Laache 2016). These studies are reviewed in detail in Section 2.7.4.

Few debris-flow studies (e.g. Bowman et al. 2010, Kailey et al. 2011, Song et al. 2017, and Song et al. 2018) were conducted using centrifuges despite the resource and the facility is expensive. These centrifuges allow the use of an even smaller flumes than small-scale laboratory tests. The scaling adjustment is made by using a gravitational force multiplying factor 'N' determined from the centrifuge rotating arm length and rotation speed. A centrifuge debris-flow study model that is used for studying debris-flow characteristics is presented by Bowman et al. (2010). The results were compared with bulk parameters determined in field-scale debris-flow in regard to dimensionless stresses. It is reported that contact-dominated stress behavior and excess pore-water pressure generation are closer to what is observed in the field than results from other $1g$ tests, i.e., laboratory tests. As a continuation of the work by Bowman et al. (2010), Kailey et al. (2011) studied effects of solids and water content in the debris-flow velocity, discharge and run-out distance using centrifuge testing. In addition, Song et al. (2017) addressed the influence of interaction between solid and fluid phases on single-surge debris-flow impacting a rigid barrier using centrifuge testing. Other than the debris-flow behavior studies, hill-slope debris-flow initiation behaviors and characteristics were looked at by Milne et al. (2012). This study showed that sand rich soils with low fines content have a lower excess pore-water pressure threshold before failure. These and similar studies conducted using centrifuges have shown to minimize the scaling issues seen when using small-scale flumes. As a results, the investigated behaviors of debris-flow were reported to exhibit close characteristics with what is observed and estimated in the field.

2.7.3 Debris-flows regime characterization

As highlighted in Section 2.7.2, scaling is an important aspect in debris-flow experimental studies, especially in small-scale laboratory tests. Although it is possible to scale the topography and geometry of the debris-flow, it is challenging to replicate or scale the

internal particle and fluid interaction as well as the resulting stresses at the same time. To analyze the extent of small-scale flume tests in replicating or at least approximating the actual stress conditions of the field-scale debris-flows, dimensionless stress ratios have reportedly been used by researchers. The major and important ones are explained here.

From the dimensional and dimensionless analyses reported in, among others, Iverson (1997; 2015), six dimensionless quantities are used for characterizing the dominant stress conditions (process of momentum transport) in debris-flows. These quantities are Savage Number (N_{Sav}), Bagnold Number (N_{Bag}), Mass Number (N_{mass}), Darcy Number (N_{Dar}), Grain Reynolds Number (N_{Rey}), and Friction Number (N_{fric}). The following five processes of momentum transport in a steady shear flow of idealized mixture of identical grains and water can be distinguished by those quantities.

1. inertial grain collisional stress ($T_{s(i)}$),
2. grain contact frictional stress ($T_{s(q)}$),
3. viscous shear stress ($T_{f(q)}$),
4. inertial (turbulent) fluid velocity fluctuation stress ($T_{f(i)}$), and
5. solid-fluid interaction stress (T_{s-f}).

Assessing the relative importance of these stress generation mechanisms in debris-flows can be accomplished by calculating representative values of the dimensionless parameters. Then, comparing these dimensionless values with those obtained from simpler systems than the process is analogous to assessing open channel water flow on the basis of Froude (F_r) and Reynolds numbers (R_e) (Iverson 1997). These parameters, therefore, are used in characterizing the tests conducted on NTNU flume model-2.

The relationship of the six dimensionless quantities with the five momentum transport processes is summarized and given in Table 2.1. The following is the description of each dimensionless parameter with defining values describing the dominant stress type.

Savage number, N_{Sav}, may be given by the ratio of the inertial grain stress ($T_{s(i)}$) to the quasi-static solid stress ($T_{s(q)}$) associated with the weight and friction of granular mass (Iverson 1997). Iverson and Denlinger (2001) and Iverson and Vallance (2001) also described N_{Sav} as a rough representation of the ratio of grain-collision stresses to gravitational stresses in steady, gravity-driven flows. N_{Sav} is given by Equation 2.14.

$$N_{Sav} = \frac{T_{s(i)}}{T_{s(q)}} \sim \frac{C_s \rho_s \dot{\gamma}^2 \delta^2}{N C_s (\rho_s - \rho_f) g \delta \cdot tan\phi} = \frac{\dot{\gamma}^2 \rho_s \delta}{N(\rho_s - \rho_f) g \cdot tan\phi} \tag{2.14}$$

where C_s is the volume concentration of solids in the mixture, $\dot{\gamma}$ is the shear strain rate averaged by v/h, where h is the flow height, v is the flow velocity, ρ_s is the mass density of the solid grains, and δ is the characteristic grain diameter that can be approximated

Table 2.1: Summary of the resulting dimensionless numbers from the ratio of the stress conditions (*NB: the ratio order is that the quantities in row are numerators*)

			Inertial stress		Quasi-static		Solid-fluid
			solid	fluid	solid stress	fluid stress	interaction stress
			$T_{s(i)}$	$T_{f(i)}$	$T_{s(q)}$	$T_{f(q)}$	T_{s-f}
Inertial stress	solid	$T_{s(i)}$		—	—	—	N_{Dar}
	fluid	$T_{f(i)}$	N_{Mass}		—	—	—
Quasi-static stress	solid	$T_{s(q)}$	N_{Sav}	—		—	—
	fluid	$T_{f(q)}$	N_{Bag}	N_{Rey}	N_{fric}		—
Solid-fluid interaction stress		T_{s-f}	—	—	—	—	

by the d_{50} value of the sediment (Zhou and Ng 2010 and Parsons et al. 2001), $N = h/\delta$ is the number of equivalent grains with average size δ that can make up to the flow height h, ρ_f is the mass density of the intergranular fluid, g is the gravitational acceleration, and ϕ is the friction angle.

After the tests conducted on quartz particles and other geological materials using annular-shear-cell, as a very rough guide, $N_{Sav} >\sim 0.1$ is found to correspond with the *fluidized* state in which collisional interactions dominate over the frictional grain interaction (Savage and Hutter 1989).

Bagnold number, N_{Bag}, may be defined by the ratio of inertial grain stress ($T_{s(i)}$) to viscous shear stress (quasi-static fluid stress, $T_{f(q)}$) and it is given by Equation 2.15.

$$N_{Bag} = \frac{T_{s(i)}}{T_{f(q)}} \sim \frac{C_s \rho_s \dot{\gamma}^2 \delta^2}{C_f \dot{\gamma} \mu} = \frac{C_s}{1 - C_s} \cdot \frac{\rho_s \delta^2 \dot{\gamma}}{\mu} \tag{2.15}$$

where $C_f = (1 - C_s)$ is the volume fraction of the pore fluid in the mixture [$C_s + C_f = 1.0$ in a saturated mixture], μ is dynamic viscosity of the pore liquid with suspended fine sediments in $Pa \cdot s$.

From tests conducted by Bagnold (1954) in neutrally buoyant mixtures of spherical grains

and liquid (in which $\rho_s \approx \rho_f$ resulting $N_{Sav} \to \infty$), collisional stresses dominate viscous stresses if the value of $N_{Bag} >\sim 200$ (Iverson 1997).

Mass number, N_{mass}, is a quantity that describes the ratio between inertial grain stress ($T_{s(i)}$) to fluid inertial stress ($T_{f(i)}$) in the mixture and given by Equation 2.16.

$$N_{mass} = \frac{T_{s(i)}}{T_{f(i)}} \sim \frac{C_s \rho_s \dot{\gamma}^2 \delta^2}{C_f \rho_f \dot{\gamma}^2 \delta^2} = \frac{C_s}{1 - C_s} \cdot \frac{\rho_s}{\rho_f} \tag{2.16}$$

Although there is no experimental data to describe the transition values, N_{mass} can be qualitatively described from its definition: when the grain density or concentration approaches zero, grain inertia becomes unimportant (Iverson 1997). However, in later studies by Iverson and Vallance (2001), it is given that values of $N_{mass} > 1$ imply that momentum transport by solid grains may dominate that of by fluid forces that is seen in the likes of water floods.

Darcy number, N_{Dar}, is the ratio between solid-fluid interaction shear stress (T_{s-f}) to solid inertial stress ($T_{s(i)}$), which describes the tendency for pore-fluid pressure developed between moving grains to buffer grain interaction (Iverson 1997). This dimensionless stress ratio quantity is given by Equation 2.17.

$$N_{Dar} = \frac{T_{s-f}}{T_{s(i)}} \sim \frac{\dot{\gamma} \mu \delta^2 / k}{C_s \rho_s \dot{\gamma}^2 \delta^2} = \frac{\mu}{C_s \rho_s \dot{\gamma} k} \tag{2.17}$$

where k is hydraulic permeability in m^2. High values of N_{Dar}, as reported in Iverson and Lahusen (1989) ranging between 1 000 and 6 000, probably apply for most debris-flows which describes large fluid pressure fluctuations evidenced strong solid-fluid interactions (Iverson 1997).

The two remaining dimensionless parameters can be found by taking ratios of the above dimensionless parameters given in Equation 2.14, 2.15, and 2.16.

Grain Reynolds number, N_{Rey}, can be found by the ratio of N_{Bag} to N_{Mass} which may be given by Equation 2.18. It may also be given by the ratio of fluid inertial stress, $T_{f(i)}$ and quasi-static fluid stress, $T_{f(q)}$. N_{Rey}, which is a function of N_{mass}, greater than unity means that the fluid flow with respect to grains begins to show inertial effects and deviates significantly from ideal viscous behavior (Iverson 1997). For small values of N_{Rey} (<1), the fluid viscous shearing stress dominates solid inertial stress in natural debris-flows as reported by Zhou and Ng (2010) after observations on a real debris-flow case.

$$N_{Rey} = \frac{N_{Bag}}{N_{mass}} = \frac{T_{f(i)}}{T_{f(q)}} \sim \frac{C_f \rho_f \dot{\gamma}^2 \delta^2}{C_f \dot{\gamma} \mu} = \frac{\rho_f \dot{\gamma} \delta^2}{\mu} \tag{2.18}$$

Friction number, N_{fric}, can be obtained by the ratio of N_{Bag} to N_{Sav} and given by Equation 2.19. It may also be given by the ratio of quasi-static solids shear stress, $T_{s(q)}$ and quasi-static fluid stress, $T_{f(q)}$. This dimensionless parameter describes the ratio of shear stress borne by sustained grain contacts to viscous shear stress (Iverson 1997). Large values of N_{fric} ($\gg 1$) are characteristics of many natural debris-flows that imply the solids shear stress from grains contact is larger than the fluid viscous shearing stress (Zhou and Ng 2010).

$$N_{fric} = \frac{N_{Bag}}{N_{Sav}} = \frac{T_{s(q)}}{T_{f(q)}} \sim \frac{NC_s(\rho_s - \rho_f)g\delta \cdot tan\phi}{C_f\dot{\gamma}\mu} = \frac{C_s}{1 - C_s} \cdot \frac{N(\rho_s - \rho_f)g\delta \cdot tan\phi}{\dot{\gamma}\mu} \quad (2.19)$$

In steep terrains where the flows are thin and fast, high shear rates cause N_{Sav} and N_{Bag} to be relatively large, in which collisional stress is expected to dominate; whereas in thicker and slower flows, lower shear rates cause N_{Sav} and N_{Bag} to be relatively small, indicating the dominance of frictional and viscous stresses over collisional stresses Iverson (1997). In the latter case, the flow will probably be dominated by frictional stress if N_{fric} found to be large, whereas viscous drag associated with solid-fluid interactions will likely dominate if small N_{Rey} and large N_{Dar} values are obtained (Iverson 1997).

2.7.4 Review of the physical modeling study at NTNU

The first NTNU flume model was constructed in 2009 with 1:20 geometric scale for an M.Sc. study by Heller and Jenssen (2009). In this first study, guide walls of varying inclination angles with varying opening widths were investigated. In 2012, the same model was improved to have a deposition area. Four countermeasures, namely: a closed check dam, check dams with two and four slits, and breaking mounds, were assessed by Fiskum (2012). The study showed the degree of effectiveness of each countermeasure in reducing the flow velocity and the amount of debris that could be retained. The closed check dam was able to stop almost all of the debris behind it while the four-slit check dam performed better in reducing the flow velocity. The study suggested the use of breaking mounds in two or more rows of staggered spacing than aligning them side-by-side in a single row. In addition, combining breaking mounds with four-slit dam improved the reduction of flow velocity and increased the retention of more mass upstream.

In 2013, Christiansen (2013) studied diversion (side) wall countermeasure using the modified flume model. In this study, the effects of water content of the flowing material, the provision of diversion walls on debris-flow velocity, and extent of the flow were assessed. The debris-flow run-up height on different deflection and inclination angels of the diver-

sion wall were presented in Le et al. (2016). There was a positive correlation between the run-up height and the deflection angle of the wall, while no correlation could be found between the run-up height and the inclination angle of the wall. In 2016, Laache (2016) looked at the effectiveness of screens in reducing the flow velocity and in retaining the debris mass according to grid length and spacing on the flume model. The data of this work was re-analyzed and presented in Yifru et al. (2018) and also discussed in detail in Chapter 5 of this dissertation.

The Norwegian Public Roads Administration (NPRA) is overseeing roads, road structures, and the road users, which sometimes are endangered by the debris-flow hazards. Because of this, there has been a pressing need to understand behaviors of debris-flow in Norwegian terrains and to study several existing countermeasures that can be implemented to mitigate debris-flows. Hence, all of the physical modelling studies at NTNU were performed in collaboration with NPRA. In addition to this collaboration, NPRA presented a general procedure and guideline (NPRA 2014) to secure roads and railways from debris-flow hazards. It suggested different kinds of countermeasures in the three zones of debris-flow (initiation, transportation, and deposition). Restriction and regulation in land use, stabilization of potential slope failure areas, and providing proper drainage and erosion control work are some of the mitigation measures suggested to be use in the potential initiation areas. Flow energy reduction measures and erosion controlling methods along the transportation zone are provided in the same document along with side flow protection methods to hinder the flow from leaving its natural course. Guide walls, underpass bridges, open control dams, embankment walls, and sedimentation basins are suggested to be used in the deposition zones.

2.8 Numerical modeling

2.8.1 Introduction

Several mass flow numerical simulation tools are developed and are used in an attempt to predict debris-flow mobility parameters like: flow velocity, flow height, impact force, run-out distance, and spread of flow. These tools are either one-dimensional (1D) or quasi-three-dimensional (quasi-3D), i.e., two-dimensional (2D) with depth-averaged third dimension, models with different basal rheologies depending on a suitable flow behavior (shear stress versus shear rate). Some of these models are RAMMS::DEBRIS FLOW (Christen et al. 2010), DAN3D (McDougall 2006), Flo-2D (O'Brien et al. 1993), MassMov2D (Beguería et al. 2009), r.avaflow (Mergili et al. 2017), and GeoFlow_SPH (Pastor et al. 2004). As the debris-flow propagation stage is mainly affected by the time-space evolution of the interstitial pore-water pressure (Cascini et al. 2016), and the chosen screen-type debris-flow countermeasure involves the dissipation of pore-water pressure, the choice of numer-

ical tool is based on the model's suitability to capture this debris-flow phenomenon.

2.8.2 Description of available mass flow numerical models

RAMMS::DEBRIS FLOW is a quasi-3D numerical model originally developed for simulating snow avalanches. It uses the Voellmy rheology that has two input friction parameters which are required to determine the shear resistance of a given flow. This model assumes the complex solid grains-liquid mixture as a one-phase viscous liquid in which the basal stresses determine the flow behavior. The model has a feature for the simulation of erosion, but it does not have a pore-fluid pressure propagation simulating feature. Likewise, DAN3D is a quasi-3D dynamic numerical model for run-out analysis of landslides. This numerical model has five different rheologies (namely: Plastic, Bingham, frictional, Voellmy and Newtonian fluid) to select and use for different kinds of flow regimes or mass flow types. Its predecessor DAN has also been used extensively in run-out assessments of landslide hazards (Hungr and McDougall 2009). Although this model is capable of considering erosion, it does not have explicit pore-fluid pressure propagation features.

Flo-2D is a quasi-3D finite difference (FD) model that simulates water and mass flows using quadratic rheological model that is developed from field and laboratory data. This model is suitable for simulating flood hazards and mud-flows which can be up to hyper-concentrated sediment flows (O'Brien et al. 1993). It is mainly applied for simulating the extent of the flooding in alluvial fans (floodplain) by replicating flow and deposition depth as well as flow velocities. The open-source model, r.avaflow is available as a raster module of GRASS GIS. This model is a two-phase model allowing interaction of solids and fluid. The model is also capable of erosion simulation and considers deposition as flow stopping criterion. Another quasi-3D numerical model for mud and debris-flow dynamics is MassMov2D, which is based on depth-averaged motion equation integration using a shallow water approximation (Beguería et al. 2009). This GIS-based open-source model uses one-phase, homogeneous material with rheological properties. A mixed Coulomb frictional-viscous rheological model is used in MassMov2D with an assumed constant pore-fluid pressure throughout the flow described in or lumped with the apparent friction angle calculated by pore-fluid pressure ratio. The lumped expression of pore-fluid pressure, i.e., representing it by a constant value, does not allow pore-fluid propagation simulations during the mass flow.

The GeoFlow_SPH-FD (Pastor et al. 2015) model is a quasi-3D hydro-mechanical coupled SPH (Smooth Particle Hydrodynamics) model for the flow propagation analysis with a 1D vertical FD analysis for the evaluation of pore-fluid pressure along the depth of the flowing mass (Cascini et al. 2016). In this dissertation, it was crucial to choose a numerical model with the capability of capturing the propagation of pore-fluid pressure in

addition to simulating the basic debris-flow behavior. This GeoFlow_SPH-FD debris-flow propagation model is found to be the relevant one due to its capability to simulate the evolution of pore-fluid pressure during flow propagation as demonstrated, among others, by Pastor et al. (2015) and Cascini et al. (2016).

2.8.3 The GeoFlow_SPH-FD landslide propagation numerical model

The GeoFlow_SPH-FD numerical model is developed by the Mathematical group in Universidad Politécnica de Madrid. The first version, GeoFlow_SPH model, was proposed in Pastor et al. (2004) and has been developed further through the years as reported in Pastor et al. (2009) and Pastor et al. (2015). The recent model was shown to be capable of simulating the time-space evolution of the interstitial pore-water pressures in flow propagation steps and upon deposition in Pastor et al. (2015) and Cascini et al. (2016). This makes it a suitable tool to simulate the effect of permeable surfaces like screens in which their purpose is to drain water and dissipating the pore-water pressure in the flowing body. Its main formulations, the rheology and features used in the model are described below.

The GeoFlow_SPH-FD model uses a Lagrangian method that separates the information of the terrain and the fluidized flowing mass. The terrain information can be provided by a digital terrain model (DTM) with specified grid spacing while the flowing mass is represented by meshless Smoothed Particle Hydrodynamics (SPH) points. In this model, the velocity of the solid skeleton and pressure fields are derived as the sum of two components related to propagation and consolidation. Its mathematical model is based on Biot-Zienkiewicz ($u - p_w$) describing the propagation stage. Then, a 1D consolidation model is performed during the propagation stage by assuming the hypothesis that the pore-water pressure dissipation takes place in the normal direction to the ground surface. Finally, these 3D problems are transformed into 2D form by applying a depth-integrated model.

The SPH numerical method is used to transform the problems that are basically in the form of partial differential equations to a form suitable for particle-based simulation. In order to discretize the propagating mass in the SPH method, the first step is to present them as a set of nodes having individual material properties. Then, an interpolation process calculates the relevant properties on each node over neighboring nodes through a kernel function without having to define any element. Finally, the ordinary differential equations of balance of mass and momentum are produced in a discretized form with

respect to time, respectively as given by Equation 2.20 and 2.21.

$$\frac{\bar{d}h_i}{dt} + h_i \sum_{j=1}^{Nh} \frac{m_j}{\rho_j} v_j \cdot gradW_{ij} = \bar{n}_i e_R \tag{2.20}$$

$$\frac{\bar{d}\bar{v}_i}{dt} = -\sum_{j=1}^{Nh} m_j \left(\frac{\bar{P}_i}{h_i^2} + \frac{\bar{P}_j}{h_j^2} \right) gradW_{ij} + b_3 \cdot gradZ_i + \frac{1}{\rho_\alpha h_i} \tau_b + b_3 + \frac{1}{\rho_\alpha} \bar{R}_\alpha - \frac{1}{h_i} \bar{v}_i \bar{n}_i e_R \tag{2.21}$$

Equation 2.20 and Equation 2.21 are completed by appropriate rheological and empirical laws. The selected rheological law determines the basal shear resistance, τ_b, while the empirical law determines the erosion (entrainment) rate, e_R, and the semi-empirical law that determines the basal pore-water pressure propagation, P_{wb}, at each time-space evolution. In this study, the numerical simulations were performed by using Voellmy rheological law which has the same features as the frictional fluid model. Moreover, it implements the effect of pore-water pressure at the basal surface. The Voellmy rheology basal shear resistance, in the case of such frictional mass, is given by Equation 2.22.

$$\tau_b = -\left\{ [(\rho_s - \rho_w)(1-n) \cdot gh - \Delta p_{wb}] \cdot \tan(\phi_b) \cdot \frac{\bar{v}}{||\bar{v}||} + \rho g \frac{||\bar{v}||}{\xi} \bar{v} \right\} \tag{2.22}$$

where ρ_s and ρ_w are densities of solid grains and water, n is porosity, g is acceleration due to gravity, h is flow height, $\bar{v}$ depth-averaged flow velocity, ρ is bulk density, τ_b is the basal shear stress, ϕ_b the basal friction angle, ξ is the turbulence coefficient and Δp_{wb} is the excess pore-water pressure at the basal surface.

To consider bed erosion by the mass flow, the GeoFlow_SPH code uses a parameter called entrainment rate, e_R, which can be formulated by Equation 2.23, which defines the change in the ground level with respect to time.

$$e_R = -\frac{\partial x_3}{\partial t} \tag{2.23}$$

Entrainment rate depends on several conditions like bed slope, bed degree of saturation, and effective stress along the erosion surface. Considering these conditions, several empirical and process-based entrainment laws are given in literature, where three of which are implemented in the GeoFlow_SPH code. Out of these, the Hungr erosion law (Hungr 1995), given by Equation 2.24, is one, and it is based on an algorithm where the total volume of debris increases in accordance with a specified growth rate, E_s.

$$e_R = E_s \cdot h \cdot \bar{v} \tag{2.24}$$

The landslide growth rate, E_s, can be estimated by using Equation 2.25.

$$E_s = ln\frac{V_f}{V_i}\frac{1}{L} \tag{2.25}$$

where V_i is initial volume, and V_f is final volume of the flow of mass that is entering and exiting a specified erodible zone with length L.
In modeling consolidation, similar to the most depth-integrated models, a simple shape function is used by fulfilling the boundary conditions by assuming that the pore-water pressure is zero on the free surface and its derivative is zero at the bottom surface where it is impermeable. Consequently, by considering these assumptions, the vertical distribution of pore-water pressure can be approximated by Equation 2.26.

$$\frac{d\Delta p_{wb}}{dt} = \frac{\pi^2}{4h^2}C_v \cdot \Delta p_{wb\_0} \tag{2.26}$$

where Δp_{wb} is the pore-water pressure at the basal level, C_v is the consolidation coefficient, h is the mobilized soil depth, and Δp_{wb_0} is the initial excess pore-water pressure. Pastor et al. (2015) extended this approach in order to improve the description of the pore water evolution, along the height of the flowing mass, by adding a 1D finite difference grid to each SPH node. One of the advantages of the presented method is its ability to simulate particular cases in which basal pore-water pressures go to zero as a consequence of the flow running over a terrain with very high permeability (or a screen). The equation describing the excess pore-water pressure (Δp_w) evolution along the depth of the flow can be obtained by Equation 2.27.

$$\frac{d\Delta p_w}{dt} = -\rho g\frac{dh}{dt}(1 - \frac{x_3}{h}) - \frac{k_v}{\alpha}d_{v0} + C_v\frac{\partial^2\Delta p_w}{\partial x_3^2} \tag{2.27}$$

where k_v is an elastic volumetric stiffness, α is a constitutive coefficient, d_{v0} is the volumetric component of the rate of deformation tensor. This feature of the model was used by Cascini et al. (2016) to simulate a flume test equipped with a permeable rack (screen) at the end of its channel. In order to solve the above consolidation equation, the landslide mass is decomposed into differential elements of volume in the deformed configuration at time t. Then, the time discretization is carried out with an updated Lagrangian approach as depicted in Figure 2.10(a). For one-phase flow, the second term of Equation 2.27 reduced to be zero in the time step and in the third term the consolidation coefficient, C_v is calculated from the input parameter B_{fact} using the relation given by Equation 2.28.

$$B_{fact} = \frac{\pi^2}{4}C_v \tag{2.28}$$

The continuum flowing body is schematically presented in Figure 2.10(b) along with the assumed coordinate system where the topography is represented by DTM points described

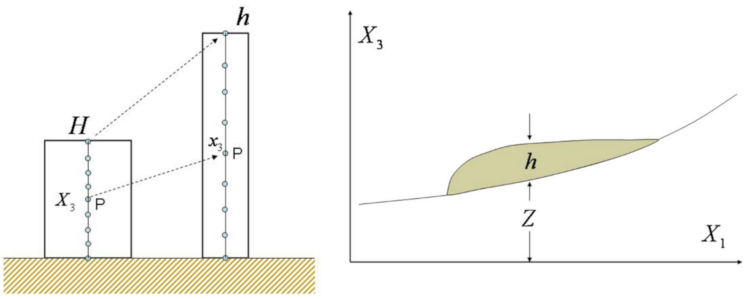

Fig. 2.10: (a) The initial and deformed configuration of a column of the landslide mass and (b) the reference system and notations (Pastor et al. 2015).

by 'Z'. In this model, the discretization and number of particles (SPH points) representing the flowing mass are completely independent from the details and grid discretization (spacing) of the DTM (Cascini et al. 2016). This gives an advantage to refine and increase accuracy of either of the two, independently. It can also be an advantage to choose those combinations with short computation times without compromising output.

3 The flume models and the testing procedures

3.1 Introduction

A laboratory experiment (physical modeling) work using the debris-flow flume model is the main basis for this study. By using physical laboratory modeling, studies to investigate debris-flow behaviors, flow impact force, and performance of the screen-type debris-flow countermeasure (screen) are conducted using two laboratory flume models.

In this chapter, a detailed description of the two NTNU laboratory flume models (Model-1 and Model-2) is given along with the respective test types conducted on them. The description covers the main body of the models, instrumentation, and testing procedures. Specific additional features on the flume models are discussed in their respective result chapters. The screen and the flow force measuring pillar assembly procedure and installation are, however, explained here. Also, the image data analysis methods used in processing videos and photos of the tests are presented.

While conducting tests on both Model-1 and Model-2, the following boundary conditions and assumptions were considered. In the tests, a well-developed debris-flow was simulated in a flume model with a defined run-out channel slope and width as well as a deposition area. The thorough mixing and releasing of the soil-water mixture (at once) resulted in a flow that is assumed to replicate a well-developed (fluidized) debris-flow. The sidewalls and the flow bed of the flume model are smooth. As a result, debris-flow initiation and triggering factors are not considered in the tests. Also, entrainment or resistance to the flow from the surfaces of the model was not considered. The characteristics of the surfaces and rheology of the debris material were assumed to be uniform during testing.

3.2 Flume Model-1

Flume Model-1 was used for studying the debris-flow impact force and the screen by placing a force measuring pillar and a screen in different locations of the run-out channel. Investigation of the screen length and spacing width, debris-flow impact force study, and screen length investigation with and without an underpass were conducted using Model-1.

3.2.1 Set-up and instrumentation

Flume Model-1 was partly constructed in 2009 and got its final shape in the later years to become a $9m$ long flume model, as shown in Figure 3.1. It has two major parts: a run-out channel and a deposition area. The run-out channel has two inclinations: 23° and 14° slopes, and it is $0.6m$ wide and $0.3m$ high. The deposition area is $3.6m$ long and $2.5m$ wide, with a 2° inclination. Figure 3.1 provides a schematic representation of Model-1 with instrumentation and important features. Two identical wooden boxes,

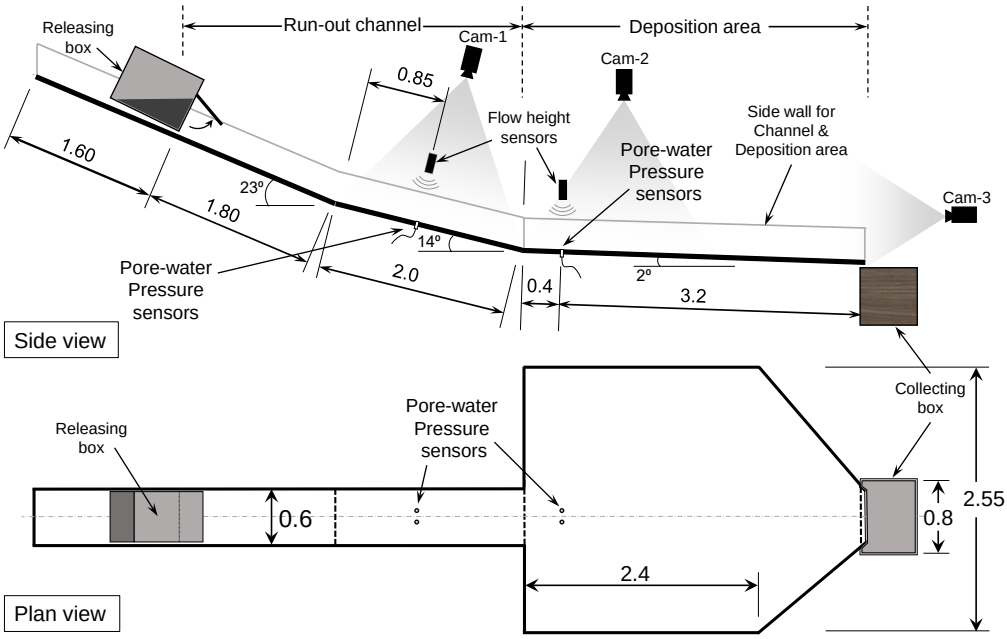

Fig. 3.1: Schematic representation of the flume Model-1: side and plan views. (All linear dimensions are in meters)

measuring $0.9m \times 0.6m \times 0.8m$, were used for measuring, mixing, holding, and collecting the debris solids-water mixture that represents a debris-flow material. The boxes were assigned the titles of Box-A and Box-B with masses of $36.9Kg$ and $38.5Kg$, respectively, and were alternatively used as the releasing box and the collecting box in consecutive tests. This flume model was instrumented with two flow height (MIC+35/IU/TC Ultrasound) sensors. These sensors have measuring range between $65 - 600mm$ with operating range of 350 and transducer frequency of $400kHz$. They are temperature drift compensated with measurement accuracy of $\pm 1\%$ and output response time of $64ms$. Appendix F1 gives the instrument specification where more technical details could be found. The first sensor was used for monitoring the flow in the run-out channel. The second one was placed $40cm$ away from the end of the channel, in the deposition area, to study the de-

position process and to record a representative deposition thickness. Under the shadows of these two flow height sensors, pore-water pressure sensors were also installed in the model bed. Three video cameras (Cam-1, Cam-2, and Cam-3) were used in different locations to capture the flow behavior. Referring to Figure 3.1, Cam-1 was placed to record the flow behavior in the major section of the run-out channel while Cam-2 was placed above the deposition area to record the final deposition process and run-out distance. Cam-3 was placed at the front of the flume model to give a front overview of the debris-flow down the slope. All cameras used in Model-1 tests have a recording capacity of 60fps.

The flow height sensors and the pore-water pressure sensors were connected to a computer with a data acquisition program. This program was custom made (the code is written by NTNU's engineer) using LabVIEW software to get data from the sensors. The rate of data recording was set to be $50Hz$ by taking the average from a $100Hz$ data in order to avoid the interference from noise created by the electricity supply.

The pore-water pressure sensors were produced in NTNU workshop from aluminium metal and brass filter as shown in Figure 3.2. For technical sketch of the sensors and their installation in the model, see Figure 3.5. The pressure sensors 26PCA Type according to the specification and they have measuring capacity up to $1psi$ ($\sim 6.8kPa$). Further details are in Appendix F2. These sensors were used for evaluating the pore-water pressure development during the different tests conducted in this study. In order to evaluate whether the measured values are affected by the flow velocity or not, two types of sensors are manufactured: flat and perpendicular. Both types of sensors are tested in Model-1, while in Model-2 only the flat one is used.

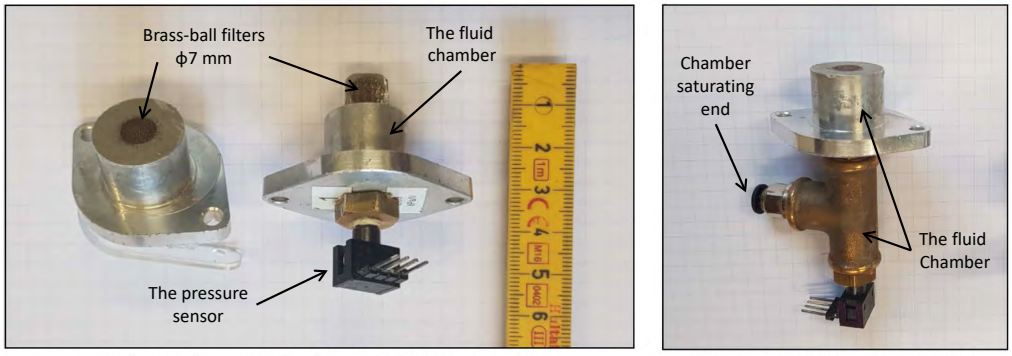

Flat and Perpendicular pore-water pressure sensors used on Model-1

Flat pore-water pressure sensor used on Model-2

Fig. 3.2: Two types of pore-water pressure measuring sensors: a flat and perpendicular one

3.2.2 Testing procedure

To describe the procedure followed in conducting the testing using Model-1, a measured amount of solid debris material and water with a known volume (V) and solids concentration by volume (C_s) were first placed in the releasing box. Then, the box was lifted by a 3 tonne capacity gantry crane in the releasing position shown in Figure 3.1. After placing the releasing box at its location and securing it from its back, the debris material-water mixture in the box was pushed to the front of the box. Then all the cameras were made to start recording and the data acquisition program was calibrated to read zero and made ready to record. After checking that all instrumentation was ready to measure, the debris and water in the box was thoroughly mixed using a hand mixer until a homogeneous mixture was observed. The thorough mixing also helped in minimizing the segregation of the solids as well as in minimizing creation of frozen (saturated chunk) masses upon releasing and during the flow.

After releasing the debris-flow and conducting the given test, the cameras and data acquisition program were stopped. Photos, as well as measurements in different parts of the model, were taken based on the requirements of the given test. Finally, the debris is cleaned from the model into the collecting box to start over with another test. Because of the limited amount of solid material while conducting tests on Model-1, the collected material from each test was used in the next test after proper adjustment for the lost debris mass. Three-fourth of the lost mass is adjusted by water while solids were used for the rest. This was considered as one of the limitations of the tests conducted on Model-1. The error that could be made in reusing and adjusting was well noted and it was dealt with proper considerations to keep it minimal.

Generally, the following steps summarize the sequential procedures taken to conduct a typical test using Model-1:

- An empty box (either Box-A or Box-B) was first placed on a scale with $300Kg$ measuring capacity. The scale was then set to zero.
- A specified mass of debris solids (in this case: crushed sand) and an amount of water, according to a particular test with V and C_s, was added in the box, consequently, by controlling the scale display.
- The box with the debris mixture was lifted by the gantry crane, placed on the channel top at the releasing location, and secured by a cable at its back.
- The debris mixture is pushed to the front of the box at the gate.
- All the cameras were set to start recording, the data acquisition program was set to start registering after ensuring that all instrumentation were working properly.

- The debris mass in the box was thoroughly mixed using a hand-mixer for about a minute. When the debris was in thorough suspension, the front gate was opened to release the debris-flow into the run-out channel.
- After all of the debris-flow movements stopped, the cameras and the data acquisition program were stopped.
- All important observations, measurements, and photos were taken. The releasing box was taken down and weighed to determine the material left inside the box.
- The material left in the releasing box and the deposited debris material on the model were pushed into the collecting box.
- Finally, the collecting box was weighed and adjusted according to the lost solid material and water to make it ready for the next test. The next test follows this procedure from the first step.

3.2.3 Set-up of screen-type countermeasure

In the flume Model-1, metal grids with metal spacers are used for constructing the screens as shown in Figure 3.3. It shows the assembly process and placement of the $0.5m$ long screen in the $0.6m$ wide run-out channel of Model-1. Due to the heavy mass of the result-

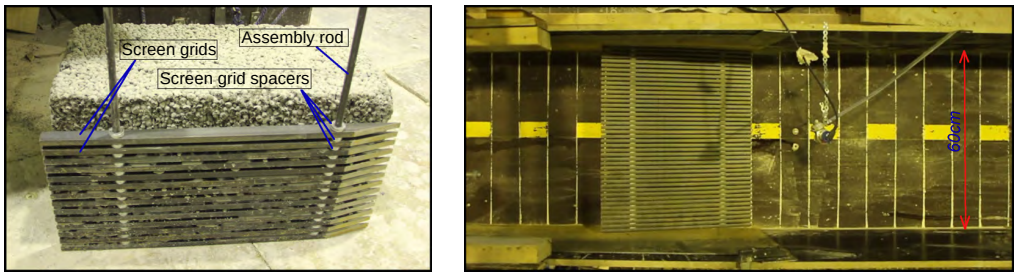

Screen assembly procedure (Laache, E. 2016) A screen installed in Model-1 (plan view)

Fig. 3.3: The assembly process and placement of the $50cm$ long metal grid screen on Model-1

ing screens, the crane was used to lift and put them into place. A supporting metal frame was constructed and installed inside the channel prior to placing the respective screens. Three metal screen lengths were used in this study in different test-sets. These were the $1m$, $0.5m$, and $0.25m$ long screens with a constant channel width of $0.6m$. Their details were given in Section 5.2 and Section 5.3 where their results were presented and discussed.

In addition, in order to study the contribution of the topographical change by the screens, solid plates with equal sizes and shapes of the respective screens were used. The method of installation of these plates in Model-1 was similar to those of the screens. The locations

and placement of these screens depended on the type of test conducted as explained in Section 5.2 and Section 5.3.

3.2.4 Set-up of the impact force measuring pillar

Supplementary to the study of the screen-type countermeasure, flow impact force of the debris-flow was investigated using a circular force measuring pillar on Model-1. The investigation was mainly to evaluate the impact force reduction capacity of the different types of screens implemented. The schematic representations and installations of the pillar on Model-1 is given in Figure 3.4. The pillar had a diameter of $75mm$ and instrumented with a load cell named S2M Force Transducer with measuring capacity up to $1.0kN$ force with 0.02% accuracy. More details can be seen in Appendix F3. The pillar was placed inside the $0.3m$ wide channel for tests presented in Section 4.4.2 and placed at the end of the $0.6m$ wide channel for tests presented in Section 5.3.8. The side view figure shows its installation position inside the run-out channel. The fundamental working principle

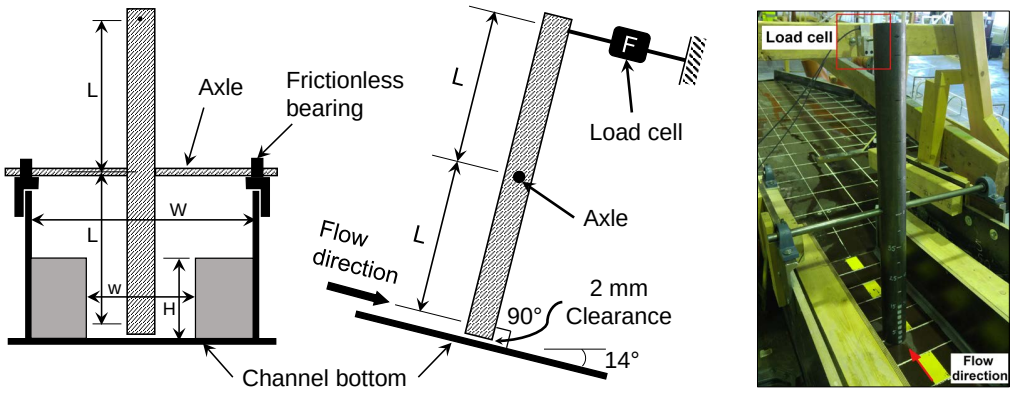

Fig. 3.4: Configuration and installation of the force measuring circular pillar: (a) schematic representation of the front and side view, and (b) Photo of the pillar installation (view from the releasing area towards the deposition area). ($L = 0.45m$, $w = 0.30m$, $W = 0.6m$, and $H = 0.22m$)

of the force measuring pillar is the concept of torque. Torque is a product of force and its perpendicular distance (so called moment-arm) from some rotation axis. The set-up of the pillar in Model-1, as shown in Figure 3.4, was positioned to have a perpendicular impact direction and a perpendicular load-cell attached to the top of the pillar. This moment-arm distance is $L = 0.45m$ in which it is assumed to be equal with the distance of the resultant force point the debris-flow made from the axis. The pillar was hinged

on an axle attached at its mid section where the axle was secured by two frictionless bearing on either sides. In order to avoid any friction against the flow bed, the pillar was given a $2mm$ clearance at its bottom. So, this equal moment-arm configuration allows the application of the principle of torque and allowed for the measurement of the impact forces of debris-flow during specific tests.

3.2.5 Set-up of pore-water pressure sensors

The pore-water pressure measuring instrumentation was produced in the NTNU workshop from aluminum metal with brass-ball filters and pressure measuring sensors connected though a fluid chamber, as seen in Figure 3.5 (top right). In order to evaluate whether what was measure as the basal pore-water pressure was affected by the flow velocity or not, two types are produced: one was flat and leveled with the model surface, whereas the other was set to face the flow perpendicularly. Both are placed in the run-out channel and deposition bed right under the shadows of the flow height sensors (as seen in Figure 3.1 and Figure 3.5), enabling the comparison of the pore-water pressure with the total normal pressure, which can be approximately calculated from the flow height and average bulk unit weight of the debris-water mixture. Before testing, the filter, the fluid chamber inside the instrument (seen in the sketch given in Figure 3.5) and inside the sensor had to be saturated with the fluid. The method for saturating the system is by directly putting the entire assembled instrument in a desiccator with distilled water placed on top. After the saturation and de-airing process were completed, the measuring system was installed on the flume model and the sensors were connected with the data acquisition cable. This saturating procedure was used at the beginning of several tests which added excess time to conduct consecutive tests. This time-consuming process was later replaced by another method which required saturation by the desiccator to be conducted only before the first test of the day. For the consecutive tests, the saturating process was made through the porous filters using a syringe filled with de-aired fluid while the instruments were in the model. Some tests resulted in good measurements after a successful set-up and saturation of the instruments as presented in Section 4.5.2.

3.2.6 Image analyses methods

During the different tests, the recorded videos and photos taken were used to supplement the acquired data using the data acquisition program. The photos taken in different locations of the flume were used as supporting information for the measurements taken. In particular, the overhead photos taken on the deposition area were used for determining the deposition shape, as well as the run-out distance. Some distortions of the pictures, including the perspective feature, were treated by a software called GNU Image manipulation program, or GIMP (The GIMP Development Team 2019) to obtain a perpendicular

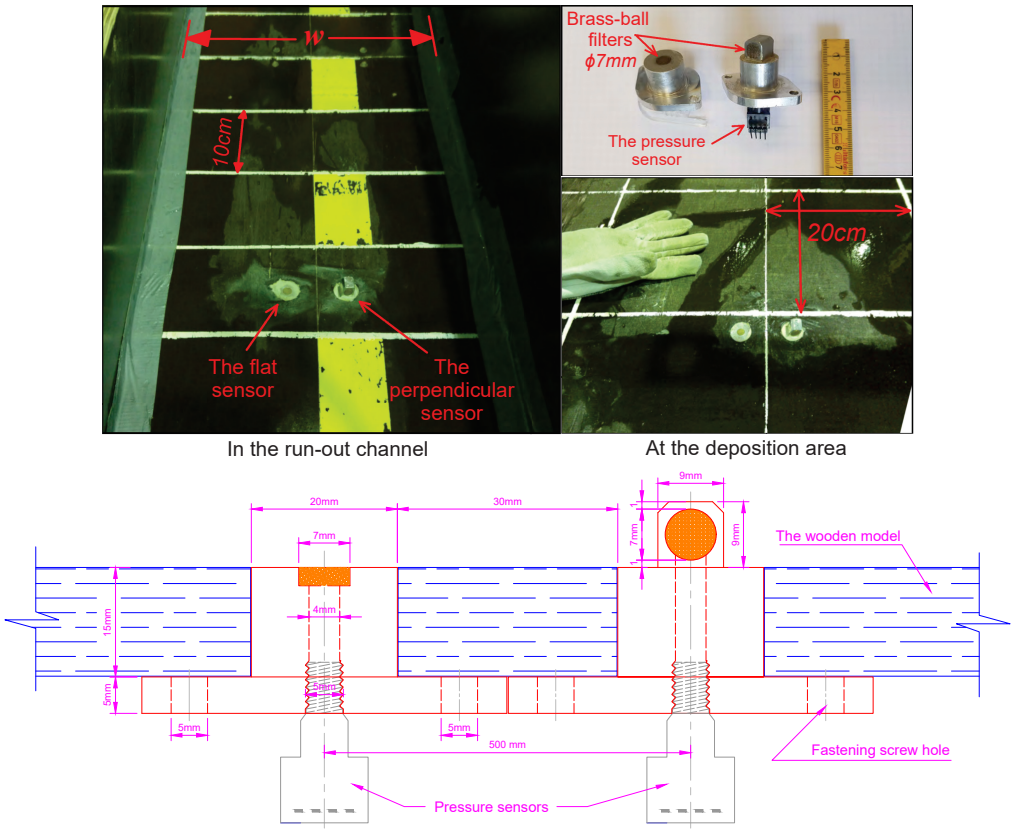

Fig. 3.5: The two pore-water pressure sensors (flat and perpendicular) arrangement complemented with sketch showing their dimensions and installation position.

plan view.

The video recordings from Cam-1 and Cam-2 with capacity of 60fps (as seen in Figure 3.1) were used for analyzing the flow's mobility. The video from Cam-1 was mainly used for estimating the flow velocity and the flow interaction behavior with any structure placed in the run-out channel. For estimating the average velocity of the debris-flow, the movement of the flow front boundary was used, given that the color of the body of the debris-flow is homogeneous due to the use of natural aggregate with its fines. The flow front was tracked by using a software called Tracker (Brown 2019) which is a video analysis and modeling tool (as seen in Figure 3.6). This software is capable of adjusting any perspective and fish-eye distortions of the videos to obtain the right distance scale over the entire flow length. The average flow velocity of the front is determined by considering three front velocities from center, left-, and right-side flows, as shown in Figure 3.6. The

accuracy of the resulting flow front velocity is dependent on the video's frame rate (i.e. 60fps) and the manual selection of the position of the flow front. This flow front velocity

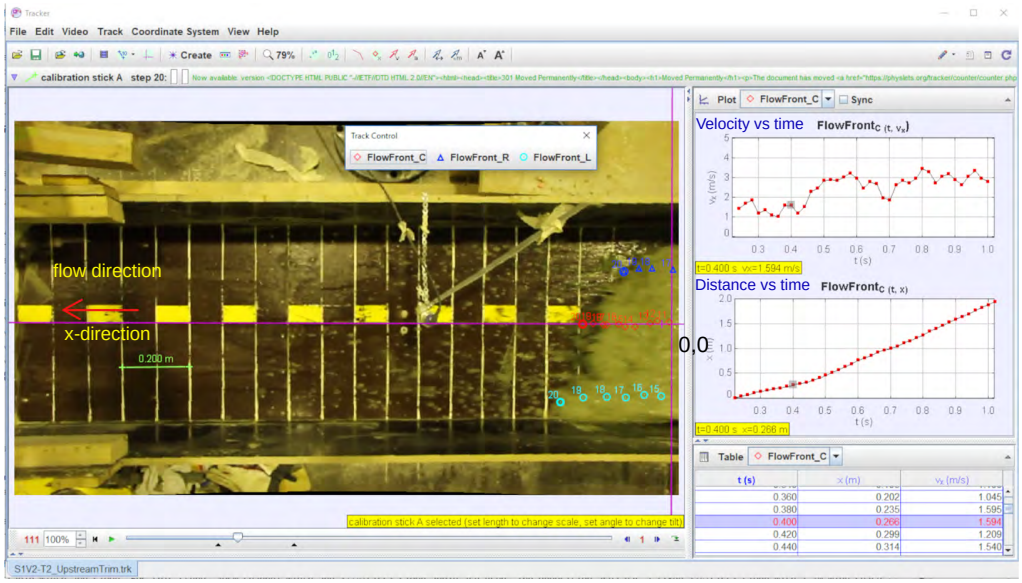

Fig. 3.6: Estimation of front-flow velocity from the recorded video using the Tracker software

obtained using Tracker is used for evaluating the energy dissipation potentials of the different types of screens tested. In addition, it was used for determining the flow impact velocity approaching the force measuring pillar.

3.3 Flume Model-2

3.3.1 Set-up and instrumentation

Flume Model-2 was designed and constructed during this Ph.D. study in order to have a more versatile flume model for the planned tests, and to tackle the limitations of Model-1. The flume model had a total of $10m$ which constitutes a $6m$ long run-out channel and a $4m$ long deposition area as shown in Figure 3.7. The run-out channel had adjustable width and slope. Two channel width possibilities ($0.30m$ and $0.60m$ wide) and five different channel inclination possibilities (varying between 17° and 30°) were included in this model. The channel bottom had a total width of $0.8m$. The detailed design drawing is given in Appendix D1. The deposition area had a fixed 2° slope with $2.2m$ wide space that tapered down near the collecting box. In addition, a mixing-cylinder, which was a new debris-flow mixing and releasing mechanism designed, constructed and implemented along with this model.

One side of the run-out channel wall was constructed by a transparent plexiglass in

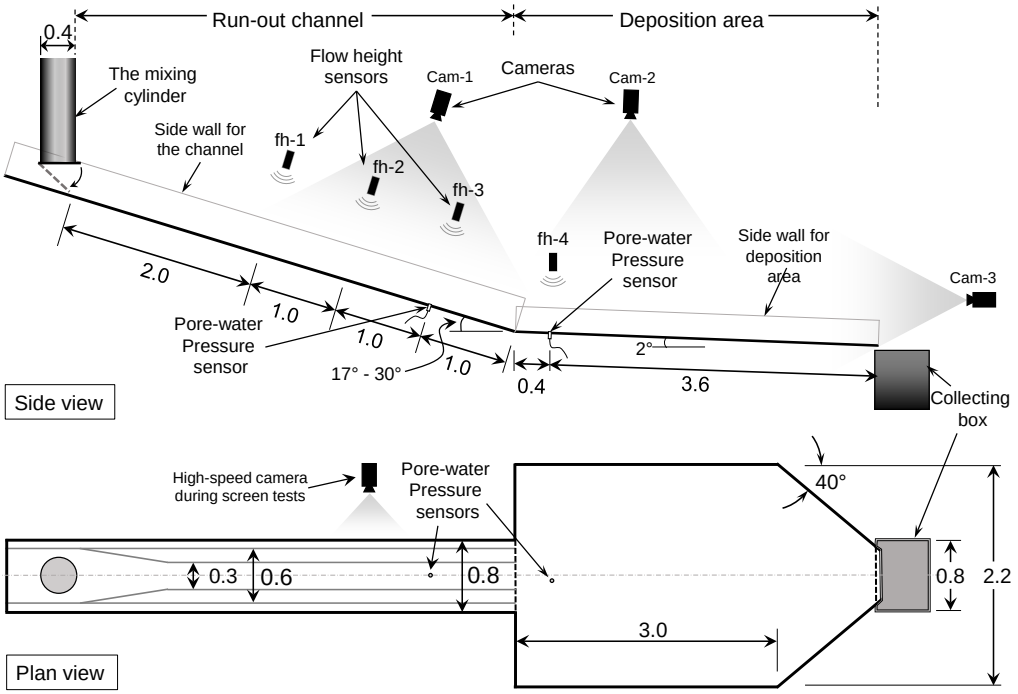

Fig. 3.7: Schematic representation of the flume Model-2: side and plan views. (All linear dimensions are in meters)

order to observe and record video of the debris-flow behavior from the side. Similar to Model-1, Model-2 was also equipped with flow height and pore-water pressure sensors. The number of flow height sensors (fh) was increased to four, where three of which (fh-1, fh-2, and fh-3) were placed in the run-out channel and the last one (fh-4) was placed at the start of the deposition area. In addition, only the flat type pore-water pressure sensors were installed under the shadows of fh-3 and fh-4, as shown in Figure 3.7; this is because the perpendicular (protruded) instrument was observed to show some effect on the flow in Model-1 in addition to the narrower channel width employed in Model-2 tests. The one installed in the deposition area was shifted around $70mm$ from the center because the center line coincided with the main supporting frame beneath the deposition area.

The data acquisition program was the same program described in Section 3.2 with a few adjustments to collect data from and control the additional instruments. The additional instruments were two flow height sensors and a mixing-cylinder. Additional controlling

commands were included in the improved program that replace the mixing initiation, opening the gate of the mixing-cylinder, and stopping the mixing process that were done manually.

In the tests conducted using Model-2, four video cameras are used. Two cameras (Cam-1 and Cam-2) with a recording capacity of 120fps were used in the run-out channel and in the deposition area, while one camera (Cam-3) with a capacity of 60fps was used in front of the model to capture a front-view. The last was a high-speed camera with 12 seconds long, 1000fps recording capacity, and was used for closely studying the debris-flow behavior in different locations of the model. This camera was connected to and controlled from a computer independent of the data acquisition program. The high-speed video also assisted in determining the average front-flow velocity ($\overline{v}$) in the run-out channel with better precision.

Along with the introduction of the mixing-cylinder and construction of Model-2, it was decided to not use the debris material repeatedly. This necessitated bringing several bags (ca. $2m^3$) of natural sand aggregate with known GSD. They are brought from a nearby quarry site called Hofstad in Trondheim. GSD tests were conducted to assure that there is no significant variation between the materials in the bags and previous debris material. This ample amount of natural sand aggregate with similar GSD made it possible for conducting the tests with a new soil mass. When GSD variation was required in a given test, the variation was made by adding the fines extracted from the natural sand aggregate itself. A separate fines deposit with a 30% water content was brought from the same quarry. Proper water content adjustment was made to keep the intended V and C_s of a given test while making the GSD variation.

3.3.2 Testing procedure

Because of the introduction of a new debris-flow mixing and releasing instrument (mixing-cylinder), the procedure of the tests in Model-2 was slightly different from what was followed in Model-1. Before giving the testing procedures followed in Model-2, a brief explanation is given regarding the mixing cylinder below.

The mixing-cylinder is a vertical metal cylinder equipped with a rotating mixing arm powered by a motor. The mechanical details and photo of the mixing-cylinder is given in Figure 3.8. The mixing-cylinder enabled thorough mixing of the debris solid-water mixture inside the cylinder before and upon release. This improved method of mixing and releasing ensured the release of the entire volume of the measured debris-water homogeneous mixture. This helped in studying the influences of different attributes of debris-flow like V, C_s, and the fines content in terms of grain size distribution (GSD). Variations

in V and C_s are, made by controlling the total and relative amounts of solids and water, respectively.

The following steps are instructions and procedures for filling the debris solid and water

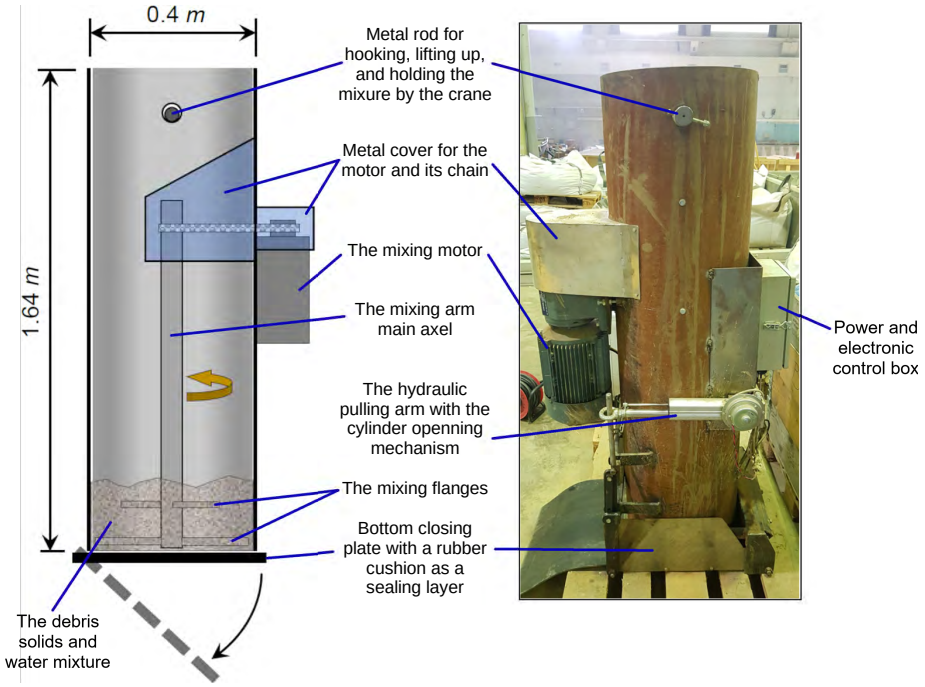

Fig. 3.8: The schematic drawing of the mixing-cylinder along with its photo (mirror view)

into the mixing-cylinder.

- The type of test with a specific V and C_s determines the amount of solids and water. Therefore, the required amount of water was measured and kept in buckets.
- The cleaned and properly closed mixing-cylinder was placed on the $300kg$ capacity scale. The mixing-cylinder weighed around $220kg$, allowing the addition of mass up to $80kg$.
- The scale was set to zero and two or three liters of the measured water was added.
- If the test required the addition of fines, a measured amount of fines was thoroughly mixed with part of the measured water. A hand mixer was used.
- After making sure that there was no lumped solid mass in the mixture, the slurry (fines + water) was poured into the cylinder.

- The debris solid (a natural sand aggregate) was added until the scale reached to the required amount.
- Any debris-solid found on the mixer-chain cover and the hooking-metal-rod was pushed down into the cylinder bottom.
- The rest of the measured water was poured in while washing any debris-solid left down into the cylinder bottom.
- The final mass was cross-checked with the total pre-calculated total mass. The mixing-cylinder was ready to be lifted and placed in the releasing position.

The basic procedure followed to conduct a test on Model-2 was the same as the steps followed on Model-1, except for a few changes made due to the mixing-cylinder. General procedures to conduct tests on Model-2 is given by the following steps:

- After adding the required amount of debris mass and water in the mixing-cylinder, the mixing-cylinder was lifted, hung by the crane, and secured at its back in the releasing position.
- The power and data cables were plugged into the mixing-cylinder. The mixing process was initiated from the data acquisition program.
- While the mixing was occurring, all required sensors were checked and their readings were set to zero on the data acquisition program. The three cameras started recording while the high-speed camera was on standby.
- After a minute of thorough mixing, the command to open the cylinder door was pressed to pull the hydraulic arm and to make the data acquisition program begin recording in unison. The whole homogeneous mixture of debris-flow was released in the run-out channel. The rotating motor was stopped from the program.
- In about five to ten seconds, all of the major flows were completed. About 30-second-long data with a rate of $50Hz$ was saved from all the sensors connected to the data acquisition program. All cameras were set to stop recording.
- All important observations, measurements, and photos were taken. Samples from different locations of the model were taken (whenever they were deemed needed).
- A command was given to push out the hydraulic arm again and the cable connections were removed. The mixing-cylinder was made ready for the next test by being taken off the model and hanged over a debris-waste basin to get properly cleaned by spraying water.

- The debris material on the model was pushed into the collecting box. When the collecting box was full, it was emptied into the debris-waste basin.
- The model was washed by spraying water and dried using a rubber broom so that the model was ready for the next test.
- The next test continued by preparing the required mass of aggregate from the sand bags.

3.3.3 Set-up of screen-type countermeasure

In the flume Model-2, better visibility of the flow interaction with the screen and easy handling of the screen itself were the main requirements. In order to satisfy the requirement, plexiglass grids were used to construct the screen. The plexiglass grids, metal rods, and spacers were used for making the screens as shown in Figure 3.9(a). The transparent grids of the screen in combination with the transparent plexiglass wall allowed for the observation of the flow behaviour and the interaction between the debris-flow and screens. Figure 3.9(b) and (c) shows the close-up front view of the screen and placement of the $0.5m$ long screen inside the $0.3m$ wide run-out channel of flume Model-2, respectively.

The method used for connecting the plexiglass grids to build the screen was similar

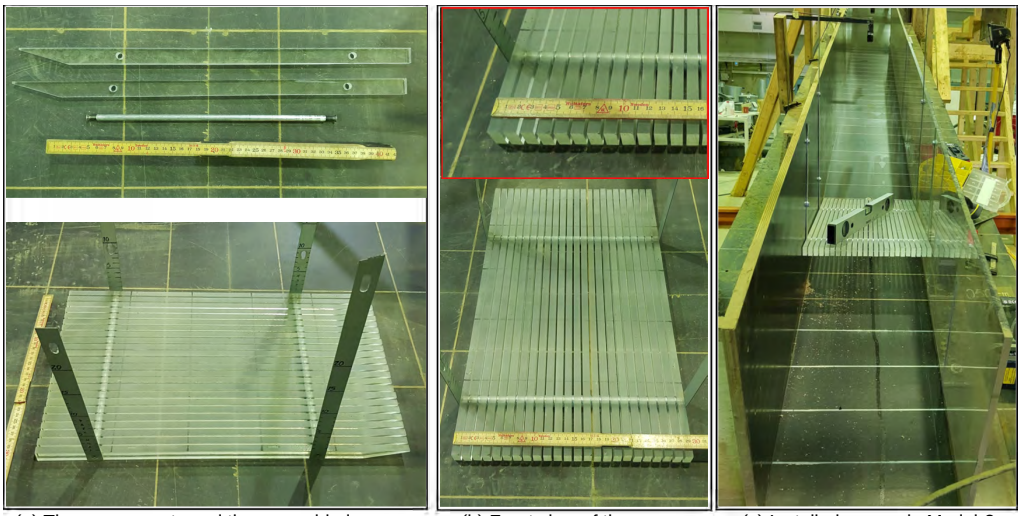

(a) The screen parts and the assembled screen (b) Front view of the screen (c) Installed screen in Model-2

Fig. 3.9: The assembly process and placement of the $50cm$ long plexiglass grid screen in Model-2

to what was used in the case of the metal grid screen. However, the placement of the screen in the channel became simple and used only four flat metal strips to secure it in place thanks to the small width and the lighter mass of the plexiglass screen. The metal

strips also served as a graduated vertical scale to evaluate the amount of accumulated debris over the screens after each test (as seen in Figure 3.9(a)).

Two different lengths of the plexiglass screen ($0.25m$ and $0.5m$ long) with a constant width of $0.3m$ were constructed and used in the tests. Similarly, their respective solid plates that represent the contribution of terrain alteration were made by simply covering their entire screen top surface using duct tape.

3.3.4 Set-up of the impact force measuring pillar

Flow impact force of the debris-flow is also investigated in Model-2. With this model, the pillar is made to have a rectangular section. In addition to investigating the flow reduction potential of the different screens, it was used for evaluating the impact force by varying pillar width. The schematic representation and installation of the force measuring pillar on Model-2 was given by Figure 3.10. This pillar had a width of $25mm$ with a possibility to widen to either $50mm$ or $75mm$ wide.

The torque principle explained for the circular pillar used in Model-1 applies to this

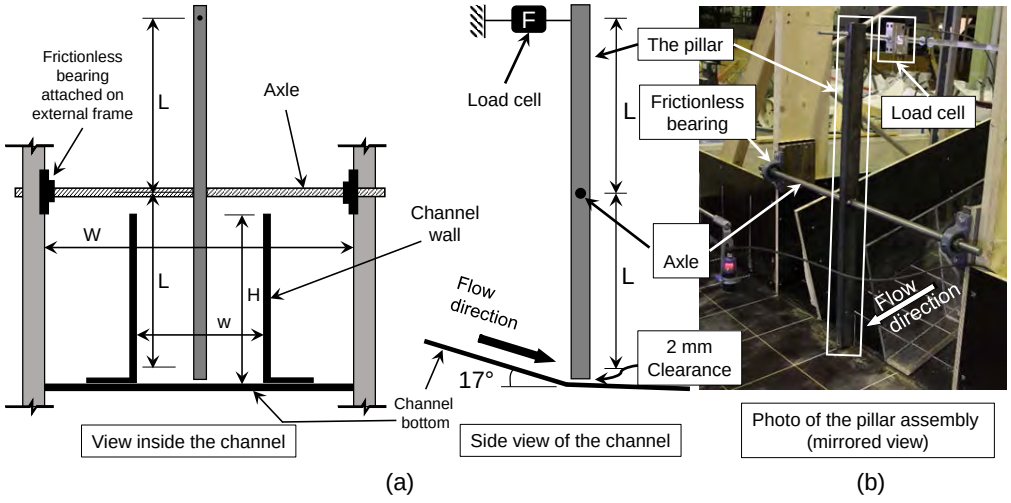

Fig. 3.10: Configuration and installation of the force measuring rectangular pillar: (a) schematic representation of the front and side views, and (b) Photo of the pillar installation (mirrored view from the side). ($L = 0.45m$, $w = 0.30m$, $W = 0.80m$, and $H = 0.35m$)

rectangular force measuring pillar as well. The moment arm length (L) was $0.45m$ measured from the axle to either ends of the pillar. However, the pillar was placed vertically (as seen in Figure 3.10) at the end of the run-out channel where the flow direction and load cell directions were not parallel. Proper adjustment was made for the angled impact

with respect to the perpendicular load-cell installation.

3.3.5 Set-up of pore-water pressure sensors

In the flume Model-2, two pore-water pressure sensors were used; one in the run-out channel and the other in the deposition area. The one in the run-out channel was installed $1m$ before the channel end whereas the other was $0.4m$ away from the end of the run-out channel. These locations are schematically represented in Figure 3.7 and their installation photos are presented in Figure 3.11. In Model-2, only the flat type pore-water pressure instruments were used because of the narrow channel width employed in Model-2, and because the perpendicular (protruded) instrument had been seen to affect the flow during tests in Model-1. In addition, the one installed in the deposition area was shifted around $70mm$ from the center because the center line coincided with the main supporting frame beneath the deposition area.

In order to improve the pore-water pressure measuring method designed and imple-

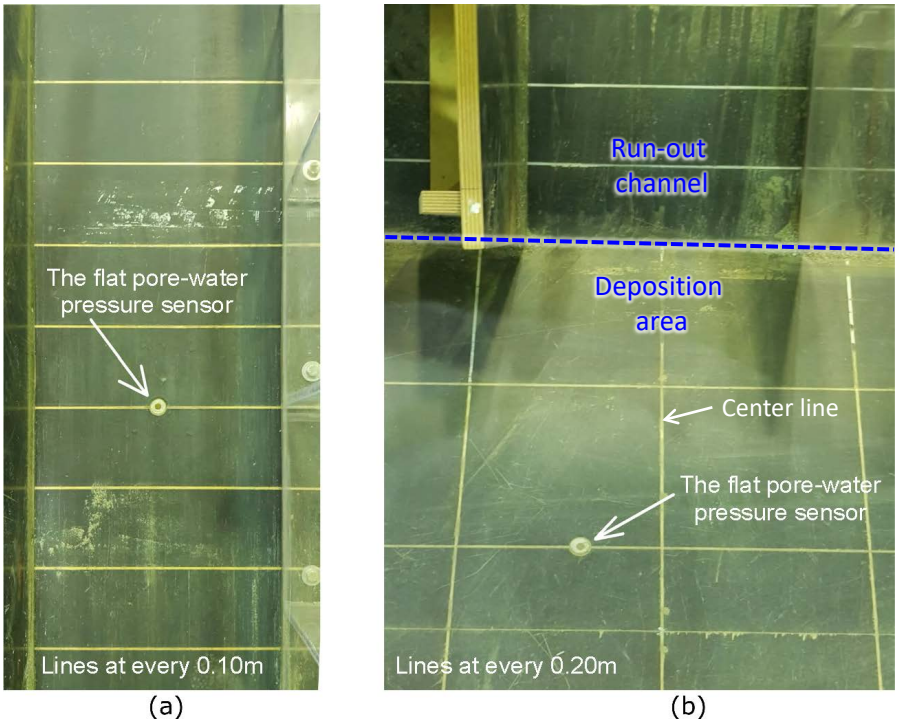

Fig. 3.11: Plan view of installed pore-water pressure sensors: (a) in the run-out channel and (b) at the deposition area

mented in Model-1 during this research period, a better and easier way of saturating the sensors was designed. This method helped solve the challenges of saturating the sensors either by using a desiccator or with a de-aired fluid, while also reducing the time taken to prepare these for a test. Figure 3.12 shows photos of the designed saturating method. The left photo shows the entire saturating system with the sensor while the right two photos show close ups of the sensor along with the cable connecting directly to the computer.

For this saturating method, a de-aired glycerin (using a desiccator) was used as the

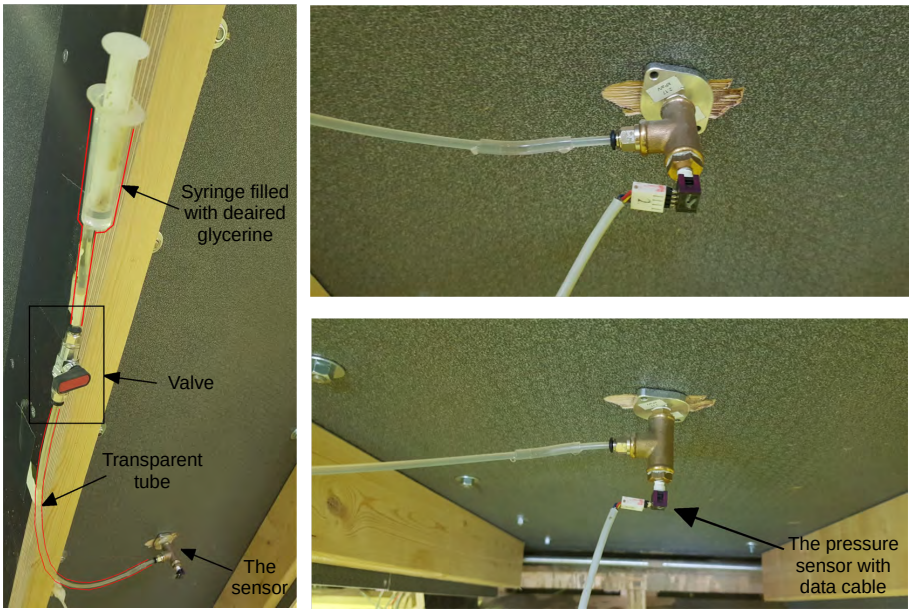

Fig. 3.12: Improved pore-water pressure measuring system and its installation as seen from channel bottom

saturating fluid in order to keep the fluid in the system and to avoid the creation of air bubbles. The pore-water pressure instrument had three ends: the porous filter flushed with the channel surface, the pressure sensor at the bottom, and the inlet for the saturating fluid. The syringe filled with the de-aired glycerin was attached with a valve that was then connected to the inlet tube. Before beginning the test, the valve was opened and the glycerin was slowly pushed using a syringe until air bubbles stop coming through the porous filter. Once this condition was obtained, the valve was closed and the pressure was left for a couple of minutes to stabilized. After getting a stabilized reading of the pressure, the data acquisition program was set to zero.

3.3.6 Image analyses methods

The photos taken and the videos recorded were used as additional sources of information. Like in the case of Model-1, the overhead photos taken on the deposition area were used for determining the deposition shape and run-out distance. For adjusting distorted and perspective views of the photos, the GIMP software (The GIMP Development Team 2019) is used.

The video recordings from Cam-1 is used for estimating the flow velocity and the flow

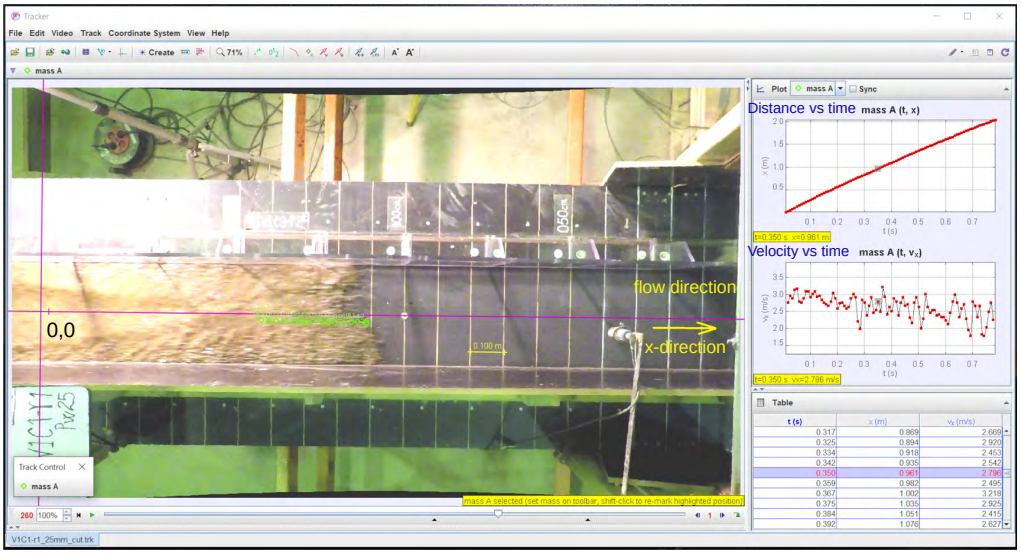

Fig. 3.13: Estimation of front-flow velocity from Cam-1 video using the Tracker software

interaction behavior with the screens and the force measuring pillar. Similar to Model-1, only the flow front is tracked to determine the average velocity of the flow by using the Tracker software (Brown 2019). A representative velocity determination using the Tracker software is given by Figure 3.13. The video used here is from Cam-1.

Adding a high-speed camera with a capacity of 1000fps gave the possibility to closely study the behavior of debris-flow in the run-out channel, while interacting with the screen and the force measuring pillar. In some cases, to obtain a more accurate estimate of the flow velocity, close up videos from the high-speed camera (1000fps) are used, especially in determining impact velocity while the flow approaches the pillar.

Other than the average velocity determination using the Tracker, the close-up video on the side view of the screens allows the conducting of particle image velocimetry (PIV)

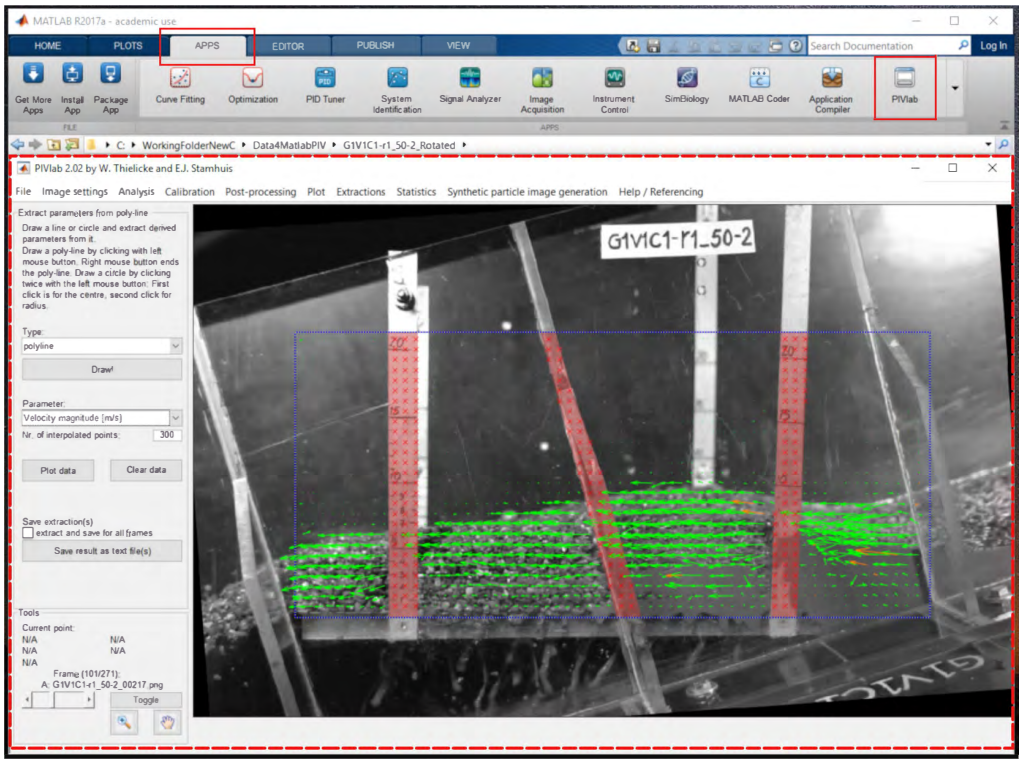

Fig. 3.14: The PIVLab App of MATLAB being used for determination of flow velocity over the screen (Flow direction is from right to left)

analysis to study different velocity layers by tracking the particles of the debris-flow. The PIV analysis was conducted using a MATLAB application named PIVlab, developed by Thielicke and Stamhuis (2014). This application takes sequences of photos that are extracted from a given high-speed video with known time intervals as an input. Figure 3.14 shows the application being used for determining grain velocities of the debris-flows over the $0.5m$ long screen.

4 Debris-flow behaviors in the flume models

4.1 Introduction

This chapter discusses the different behaviors of debris-flow observed in the laboratory tests in light of dimensionless numbers, empirical and analytical relations as well as stress generation characterizing relationships. It only presents the result of tests conducted without countermeasures.

The first part focuses on debris-flow regime characterization using stress generation behavior in regards to the material type (Grain size distribution, GSD), volume (V) of the debris-flow, and the solid concentration by volume (C_s). Using these same tests, the run-out distance (L_{FL}) behavior depending on these attributes of the debris-flow is discussed in the second part. The tests discussed in first and second parts are conducted using flume Model-2. The third part presents results and discussions of studies on debris-flow impact force behavior. In this section, preliminary impact force study on a circular passable structure conducted in flume Model-1 and detailed impact force studies on a rectangular passable structures conducted in flume Model-2 are presented. The detailed impact force study is conducted in relation to varying debris-flow characteristics and varying impact areas of the rectangular pillar. The results are presented and discussed in light of empirical and analytical impact force estimating formulas.

At the end, results from pore-water pressure measurements conducted on some selected tests on both Model-1 and Model-2 are presented. The liquefaction level during the peak excess pore-water pressure, the dissipation time after the debris-flow stopped, and pore-water pressure contribution to the mobility of the debris-flows are discussed.

4.2 Effect of debris-flow composition on the flow regime

4.2.1 Introduction and description of the debris-flow compositions

Based on the dimensionless numbers given in Section 2.7.3, the flume model debris-flow is studied in connection with the resulting flow regime and scaling effect. By using the dimensionless parameter, the flow regimes of the different debris-flow compositions of the flume Model-2 tests are compared with the commonly known flow regime of real debris-

flows.

The different debris-flow compositions were obtained by varying GSD, V, and C_s. These variations were made to see how each variation affects the debris-flow regime and which combinations give a flow that more resembles the common flow regime of real debris-flows. Three variations for each debris-flow characters (GSD, V, and C_s) were selected based on the run-out distance capacity of Model-2 deposition area. The three GSD variations are named G1, G2, and G3, and are given in Figure 4.1. G1 is a natural sand aggregate from Hofstad, Norway, while G2 and G3 are versions of G1 made by replacing 10% and 20% of its total solid mass with its own fines. The fines constitute silt and clay which have sizes $< 0.06mm$. The final fines content in each material is collected from Figure 4.1

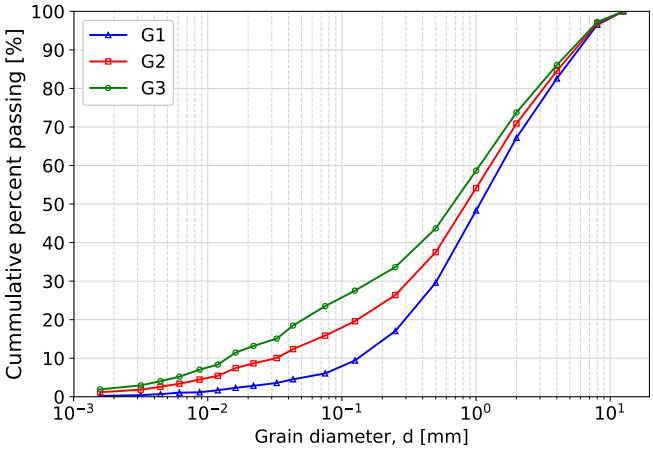

Fig. 4.1: Grain size distribution (GSD) curves of the debris materials (G1, G2, and G3)

and is 5.4% for G1, 14% for G2, and 22.5% for G3.

The three debris materials were chosen in such a way that it helps to study the effects of fines contents in the debris-flow. Gradation indicators for each debris material composition is given in Table 4.1 where the coefficient of uniformity, C_u and coefficient of curvature C_c indicate that the three materials are well-graded.

The three V and C_s respectively are: V1 = $25L$, V2 = $30L$, V3 = $35L$ and C1 = 60%, C2 = 55%, and C3 = 50%. The C_s value given here was what was used for measuring and mixing the debris solid and water at the time of the tests. However, the fines (silt and clay) remained in suspension and acted as part of the fluid (Iverson 1997), and the fluid volume concentration, C_f is given by Equation 4.1 in which the C_s were recalculated for

Table 4.1: Important sizes and gradation properties of the debris materials (grain sizes are in mm)

	G1	G2	G3
d_{10}	0.130	0.036	0.017
d_{30}	0.510	0.340	0.170
d_{50}	1.050	0.850	0.680
d_{60}	1.520	1.270	1.060
d_{max}	8.000	8.000	8.000
C_u	11.69	35.28	62.35
C_c	1.320	2.530	1.600

this dimensionless analyses and referred to as C_s^*.

$$C_f = \frac{V_{fines} + V_w}{V_{fl} + V_s} = \frac{V_{fl}}{V} \tag{4.1}$$

where V_{fines} is volume of fines that can be calculated by $V_{fines} = m_{fines}/\rho_s$ in which the fines grain density is considered as solids grain density (ρ_s), V_w is volume of water, V_{fl} is volume of fluid, V_s is volume of solids, and V is total volume. Although the fluid used in this study is water, the presence of the clay and silt in the suspension gives rise to the need of recalculating the fluid density(ρ_f) by considering the suspension. Equation 4.2 given in Iverson (1997) was used to estimate the fluid density, ρ_f, for each test.

$$\rho_f = \rho_s \cdot C_{fines} + \rho_w(1 - C_{fines}) \tag{4.2}$$

where C_{fines} is the volume concentration of fines that can be given by $V_{fines}/(V_{fines}+V_w)$ and ρ_w is density of water.

For each test, three test repetitions were planned to make up to a total of 81 tests. However, 66 tests were performed systematically without affecting repeatably and representatives. These tests were conducted between February and August 2018 on flume Model-2. The whole result of these tests can be found in Table B2 of Appendix B1, in addition to the raw data plot given in Appendix E1.

As described in Section 4.2, the dimensionless parameters are calculated by the physical parameters of the debris-flow. These physical parameters are: Equivalent grain diameter (δ), flow height (h), flow velocity (v), shear rate ($\dot{\gamma}$), the densities (ρ), fluid viscosity (μ), hydraulic permeability (k), C_s, and friction angle (ϕ). These physical parameters are either calculated or measured except ϕ and k. The ϕ was assumed to be 30° while the k was taken as same as what is typical for well-graded sand (Iverson 1997). However, the k

was varied very slightly between the choices of the three GSD where lesser value is given for G3 while relatively higher value is given for G1 as permeability is facilitated with less fines content.

The h is the maximum flow height registered at the third flow height sensor(fh-3) in the channel (as seen in Figure 3.7 of Section 3.3) while the v is the average velocity calculated between the second (fh-2) and third flow height sensors. These average v values are found to be reasonable estimates of the approach velocities towards fh-3 sensor by comparing them with the flow velocities that are calculated by Tracker software. These velocities are calculated for the purpose of assessing impact velocities (see Section 4.4). The dimensionless numbers calculated by the latter velocities are given in Table B1 of Appendix B1 for reference and comparison purposes.

The fluid viscosity (μ) varies between 0.001 and 0.01 for sand-gravel mixture with water (Iverson 1997), and can goes up to 0.1 for muddy water as given in Iverson and Denlinger (2001) as well us up to 0.5 as reported in Zhou and Ng (2010) for analyzing a natural debris-flow in the Jiangjia Ravine. However, for this study, it is estimated using Equation 4.3 which is an empirical formula given by Thomas, D. G. (1965) developed from experimental data on relative viscosity of suspensions of uniform spherical fines particles.

$$\mu = \mu_w(1 + 2.5C_{fines} + 10.05(C_{fines})^2 + 0.00273e^{(16.6C_{fines})}) \tag{4.3}$$

where μ_w is viscosity of water ($0.001pa.s$ at $20°C$).

4.2.2 Flow regime determination

The first group of dimensionless numbers that distinguish between dominance collisional, viscous, and frictional stresses consist of N_{Sav}, N_{Bag}, and N_{fric}. The GSD and C_s effect on the dimensionless numbers and thereby the type of flow regime is shown in Figure 4.2 (Similar plot with tracker velocity calculated values is given by Figure B1 of Appendix B2).

The $N_{Sav} > 0.1$ indicates that collisional stresses are dominant over frictional stresses (Savage 1984 and Savage and Hutter 1989). Figure 4.2(a) shows that the dominance of collisional stress increases with increasing C_f which is a combined effect of increasing the fines and water contents. In looking at the GSD effect alone, almost all tests conducted using G1 material and G2 material with the lowest water content were seen to be friction dominated while the others exhibited collisional stress dominance.

When comparing the dominance of collisional stress over viscous stress, $N_{Bag} > 200$ is recommended by Bagnold (1954) as an approximate boundary to confirm if the collisional

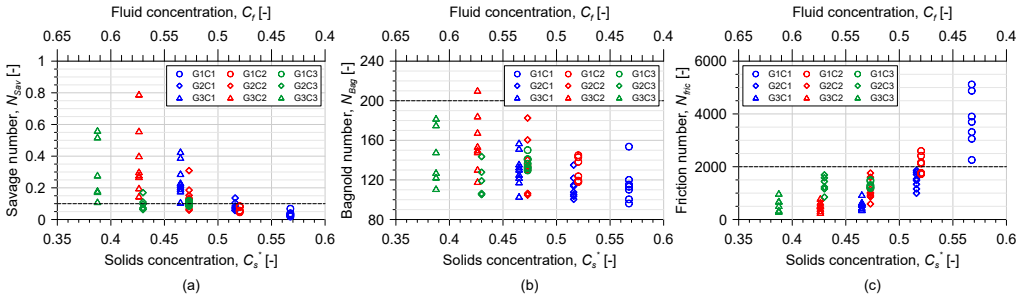

Fig. 4.2: Dimensionless numbers variations with GSD and C_s: (a) Savage number, (b) Bagnold number, and (c) friction number

stresses also dominate viscous stresses like what is seen at larger values of N_{Sav} over the friction stresses. However, almost all tests, except one, were found to have shown viscous stress dominance over the collisional stresses as seen in Figure 4.2(b). Although all fall below the limiting value with few scatters, similar kinds of trends as seen in N_{Sav} plot, can be observed, and the viscous dominance decreases gently with increasing C_f. In addition, comparing the effect of the three GSD with C1, C2, and C3, the fines content increase alone contributed to the increase of N_{Bag}, thus reducing the dominance of viscous stresses.

After studying the N_{Sav} and N_{Bag}, collisional stresses dominated the frictional stresses in major parts of the tests but again collisional stress was seen as completely dominated by viscous stresses. By employing N_{fric} which is the ratio of the N_{Sav} to N_{Bag}, it is possible to see the dominant stress between friction and viscous. Frictional stresses dominate over viscous stresses if $N_{fric} > 2000$ which can be seen on Figure 4.2(c) being fulfilled by G1 materials with the two most lowest C_f. This means that, given these three dimensionless numbers, the $5 - 15\%$ of fines in the debris with $C_f <\sim 0.5$, can give closer behavior to real debris-flows as Iverson and Denlinger (2001) stated, many geophysical flows probably fall within the friction-dominated rather than collision-dominated regime. Tests with less fines material (G1) and less water (C1) resulted with frictional behavior (as seen in Figure 4.2) and exhibited visible grain segregation. Adding more fines and/or more water further than this limits will make the viscous shear stress dominant and reduce grain segregation as Vallance and Savage (2000) indicated that grain size segregation is inhibited in viscous flows.

To further investigate the flow regimes, the remaining three dimensionless numbers, i.e., N_{mass}, N_{Dar}, and N_{Rey} were studied. The resulting plots are given by Figure 4.3 (the corresponding plot from tracker velocity is given by Figure B2 of Appendix B2).

Viscous drag associated with solid-fluid interactions will likely be important if the value

of N_{Rey} is small and the value of N_{Dar} is large (Iverson 1997). Therefore, N_{Rey} and

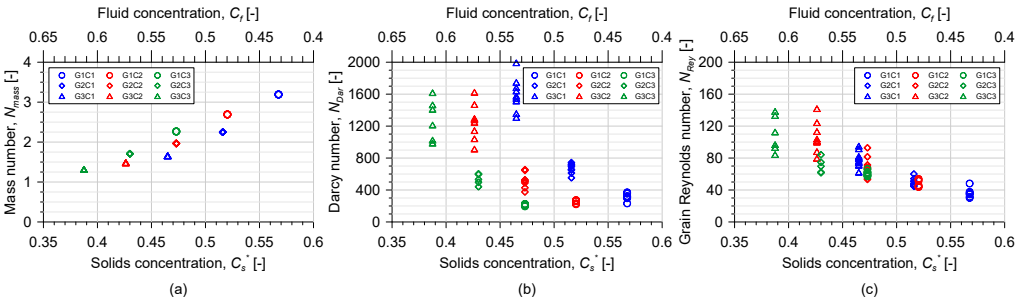

Fig. 4.3: Dimensionless numbers variations with GSD and C_s: (a) mass number, (b) Darcy number, and (c) grain Reynolds number

N_{Dar} are needed to look at the importance of viscous stresses in flows where frictional stresses dominate. For the G1C1 and G1C2 tests that resulted in $N_{fric} > 2000$, the N_{Rey} value is among the smallest from the tests, yet N_{Dar} is not large, rather it is among the smallest. When these values are compared with the values of real debris-flows given in Table 4.2, N_{Rey} is larger and N_{Dar} is smaller. This implies that the solid-fluid interaction in the Model-2 tests might not be important as in many geophysical flows. Therefore, for some tests using G1C1 and G1C2, frictional stress dominates viscous stresses like in real debris-flows, with a possible lack of solid-fluid interaction stresses. For the rest of the tests with relatively higher fines and water contents, the viscous shear stresses dominate the friction and collisional stresses. This may be attributed to the shallow flow depth and relative high flow velocity, resulting in a high shear rate, and the relatively large characteristic grain size compared to flow depth (de Haas et al. 2015).

The value of N_{mass} qualitatively indicates that the grain inertia becomes unimportant when either the ρ_s or C_s become zero (Iverson 1997) which can be quantitatively given by $N_{mass} \leq 1$. Values of $N_{mass} > 1$ imply that momentum transport by solid grains may dominate (Iverson and Vallance 2001) over the momentum transport by the intergranular fluid just like in flood water. From Figure 4.3(a), an increase in C_f generally decreases N_{mass}, thus contributing to the additional influence of the intergranular fluid over the solid grains. Water content variation affects the value more when materials with less fines (G1) are used rather than materials with more fines (G3). In addition, the effect of fines content variation on the N_{mass} value is relatively larger for the lower water content case (C1) than the higher one (C3).

A summary table with maximum and minimum values of the physical and dimensionless parameters along with well documented debris-flow events, and large-scale experiments from literature, is given in Table 4.2.

Table 4.2: Summary of typical values of physical and dimensionless parameters of real and experimental debris-flows including this study

Parameters	Symbol (unit)	This study (small-scale)	USGS Flume debris-flows[a]	Typical ranges in real debris-flows[a,b,c]
Physical parameters				
Characteristic grain diameter	δ (m)	0.00068–0.00105	0.01	0.005–0.5
Flow height	h (m)	0.019–0.040	0.2	1–10
Flow velocity	v (m/s)	2.38–4.17	10	6–20
Flow shear rate	$\dot{\gamma}$ (1/s)	72–197	50	1–10
Solid density	ρ_s (kg/m^3)	2750	2700	2400–2700
Fluid density	ρ_f (kg/m^3)	1090–1450	1000–1100	1000–1200
Fluid viscosity	μ $(Pa \cdot s)$	0.00116–0.00245	0.001–0.1	0.001–0.1(0.5^b)
Hydraulic permeability	k (m^2)	1×10^{-11}–3×10^{-11}	10^{-11}	10^{-12}–10^{-8}
Solids concentration	C_s^* (-)	0.39–0.57	0.6	0.6
Fluid concentration	C_f (-)	0.43–0.61	0.4	0.4
Friction angle	ϕ (deg)	30	28–42	25–50
Dimensionless parameters				
Savage number	N_{Sav}	0.019–0.079	0.2	1×10^{-7}–0.06
Bagnold number	N_{Bag}	96–210	400–6000	0.2–1×10^4
Mass number	N_{mass}	1.0–3.0	4	3.0–4.0
Darcy number	N_{Dar}	195–1995	600	2×10^3–6×10^7
Grain Reynolds number	N_{Rey}	30-140	100–1500	0.01–1.5
Friction number	N_{fric}	250–5200	2000–30000	2×10^4–4×10^5

[a]Data collected from Iverson (1997), Iverson and Denlinger (2001)
[b]Zhou and Ng (2010)
[c]de Haas et al. (2015)

4.2.3 Summary

To determine to what extent the small-scale laboratory experiment replicates the behavior and characteristics of real debris-flows, scale-independent parameters describing debris-flow regimes are utilized. These dimensionless parameters have been used by several researchers to study the flow behavior of debris-flows. Debris-flow physical modeling, be it small- or large-scale, is a time consuming, costly, and labor intensive experiment. Although this study is categorized as a small-scale study, a single test takes between 40 to 60 minutes, and requires at least two people, one of which must has a license to operate a gantry crane. A compromise between time-cost effective methods and representativeness have to be found. This section showed that some of the debris-flow (with specific combinations of GSD, V, and C_s) replicated the flow regimes estimated in real debris-flows. The G1 tests with C1 and C2 solids concentrations showed flow regimes dominated by frictional stresses that most real debris-flows probably fall in. In addition, some of the G2 tests with C1 showed a behavior very similar to frictional stress dominated flows.

4.3 The run-out distance

4.3.1 Introduction

Given that sections of roads and settlements at the foot of mountains are mostly susceptible to debris-flow threats, the debris-flow run-out distance, L_{FL}, along with its lateral spread, is one of the important characteristics of debris-flow that could describe the extent and severity of the damage it results in. Understanding on what factors the L_{FL} depends contributes to the debris-flow mitigation processes. Out of the many factors that affect L_{FL}, GSD, V, and C_s are the three debris-flow attributes chosen to be studied in the flume model study.

Using the same tests presented in Section 4.2 used for debris-flow regime characterisation, effects of varying the attributes (GSD, V, and C_s) of debris-flow on the resulting L_{FL} was studied. The GSD varied from G1 to G3 (as seen in Figure 4.1 and Table 4.1), the values of V are $25L$, $30L$, and $35L$ for V1, V2, and V3 respectively along with variations in C_s as 60%, 55%, and 50% corresponding to C1, C2, and C3.

The variation of these three debris-flow attributes in combination with three test repetitions make up a total of 81 tests. Out of these 81 tests planned, the 27 of them are conducted for measuring the impact force on a rectangular pillar (Section 4.4.3). The average L_{FL} of the other two test repetitions are given in Table 4.3. As it is described in Section 4.2, the C_s can be modified by considering the volume occupied by the fines (V_{fines}) with size $< 0.06mm$ as part of the intergranular fluid (V_{fl}). This will decrease the initial C_s values for all the three materials which is given as C_s^* in Table 4.3. Some of the tests resulted in longer L_{FL} that exceeded the deposition area. Nevertheless, the values were estimated from the decelerating front flow speed.

4.3.2 Comparison with an empirical relation

Empirical and dynamic method solutions have been reported in literature to estimate L_{FL} by comparing it with the physical parameters (like Volume, V) of debris-flow and channel geometry (like channel slope angle and elevation differences, H) (Rickenmann 1999 and D'Agostino et al. 2010). For the empirical relations, data from real debris-flow observations and small and large scale model test results were utilized, as reported by Rickenmann (1999) and further studied by D'Agostino et al. (2010). Both total run-out distance and run-out distance in the deposition area, L_{FL}, were given by two different empirical relations using V and H. Since the run-out distance measured (and given in Table 4.3) was from the deposition area, the comparison was made only using the empirical relation that describe the run-out distance on a fan (Rickenmann 1999) given by Equation 4.4.

Table 4.3: Average run-out distance, L_{FL}, results for each combination of GSD, V, and C_s tests

GSD	Test Name	V $[L]$	C_s [-]	C_s^* [-]	C_f [-]	run-out $[m]$
G1	G1V1C1	25	0.60	0.57	0.43	2.09
	G1V1C2	25	0.55	0.52	0.48	2.72
	G1V1C3	25	0.50	0.47	0.53	3.46
	G1V2C1	30	0.60	0.57	0.43	2.69
	G1V2C2	30	0.55	0.52	0.48	3.72
	G1V2C3	30	0.50	0.47	0.53	3.92
	G1V3C1	35	0.60	0.57	0.43	2.79
	G1V3C2	35	0.55	0.52	0.48	3.84
	G1V3C3	35	0.50	0.47	0.53	4.05
G2	G2V1C1	25	0.60	0.52	0.48	2.28
	G2V1C2	25	0.55	0.47	0.53	3.52
	G2V1C3	25	0.50	0.43	0.57	4.30
	G2V2C1	30	0.60	0.52	0.48	2.41
	G2V2C2	30	0.55	0.47	0.53	3.63
	G2V2C3	30	0.50	0.43	0.57	4.40
	G2V3C1	35	0.60	0.52	0.48	2.68
	G2V3C2	35	0.55	0.47	0.53	4.02
	G2V3C3	35	0.50	0.43	0.57	4.60
G3	G3V1C1	25	0.60	0.47	0.54	2.30
	G3V1C2	25	0.55	0.43	0.57	3.95
	G3V1C3	25	0.50	0.39	0.61	4.70
	G3V2C1	30	0.60	0.47	0.54	2.64
	G3V2C2	30	0.55	0.43	0.57	4.45
	G3V2C3	30	0.50	0.39	0.61	4.80
	G3V3C1	35	0.60	0.47	0.54	3.17
	G3V3C2	35	0.55	0.43	0.57	4.60
	G3V3C3	35	0.50	0.39	0.61	4.99

* recalculated C_s where the solid fines are considered as part of the fluid

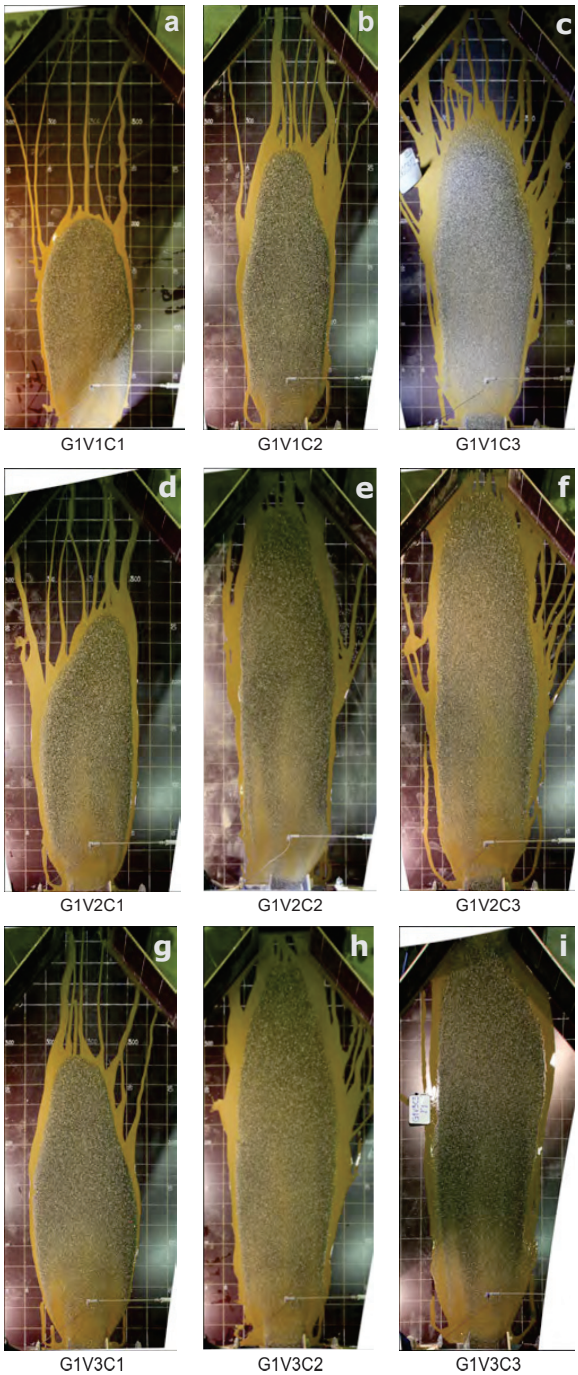

Fig. 4.4: Photos showing run-out distances of the G1 tests with varying V and C_s (top view of the deposition area, grid size = $0.2m$)

$$L_{FL} = 15V^{1/3} \tag{4.4}$$

Figure 4.5 shows the test results in comparison with other field observations, small scale tests, and large scale tests from literature. The empirical relation gives an approximate estimation of the L_{FL} by only considering the V. The dotted line in the plot represents Equation 4.4 and our results fit close to this line as well as the other lab debris-flows results. The color and shape distinctions are given for V1, V2, and V3 variations. As

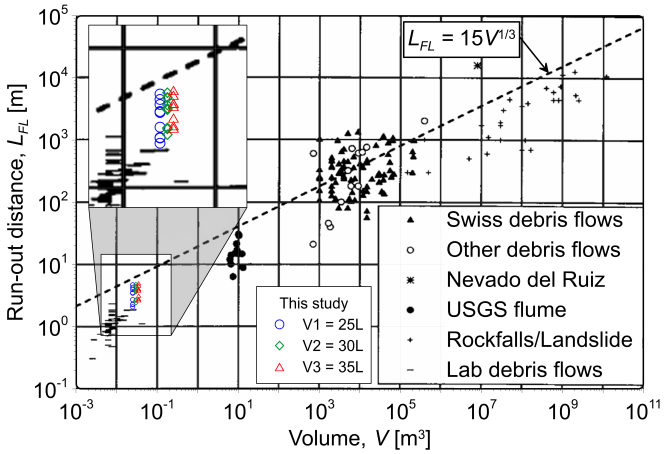

Fig. 4.5: Run-out distance on the fan area, L_{FL} in relation to volume, V (after Rickenmann (1999))

mentioned by Rickenmann (1999), Equation 4.4 is not recommended for practical uses because the L_{FL} is relatively more affected by changes in channel geometry of the fan area and material properties than those that describe the flow as a whole. However, it can be used as a method to roughly assess the expected L_{FL} if the total flow V is known.

4.3.3 Effects of debris-flow composition on the run-out distance

After showing where the test results are generally located in comparison with other lab tests and field observations, the effects and influences of material characteristics (GSD) and two physical parameters (V and C_s) on the L_{FL} behavior of debris-flow was studied. The results given in Table 4.3 were used.

Before discussing the results, representative results with pictorial representation of the run-out distances and deposition patterns from the G1 tests are presented in Figure 4.4. The figure shows the effect of variations in V and C_s. Comparing the rows in Figure 4.4 shows the effect of varying C_s for each V and comparing the columns shows the effect of

varying V for each C_s. The L_{FL} is measured starting from the end of the channel. The deposition area is marked by lines at every $0.20m$ distance to see the debris-flow L_{FL} and lateral its spread width.

From C1 tests, increasing V increases the L_{FL} as well as the lateral spread width to some degrees, due to the least amount of water, the deposition shows an oval shape as the relatively dry front snout hinder the subsequent flows that forces it to spread laterally. In case of C2 and C3, because of the additional water content, the deposition shape is more elongated in the direction of the flow with not much increase in lateral spread from what is seen in C1. Figure 4.6 gives a visual representation of L_{FL} variations

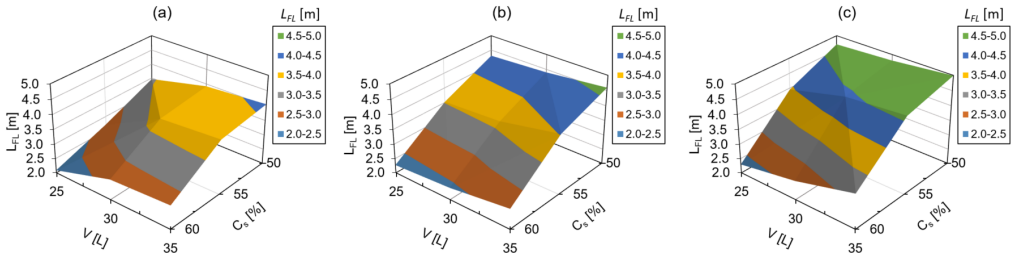

Fig. 4.6: L_{FL} variations with V and C_s for: (a) G1, (b) G2, and (c) G3

based on GSD, V, and C_s. In all G1, G2, and G3 cases, increasing V and/or decreasing C_s contributed to increases in L_{FL} of the flow. In comparing these three plots with one another, increasing the fines content (from G1 to G3) contributed to increases in the L_{FL}.

From Figure 4.6, the effect of reducing the C_s in increasing the L_{FL} is larger than the effect of increasing the V. These effects can be visually described in two other plots that are given for varying V in Figure 4.7 and for varying C_s in Figure 4.8.

In Figure 4.8, the significant effect of C_s variation on affecting the resulting L_{FL} can be

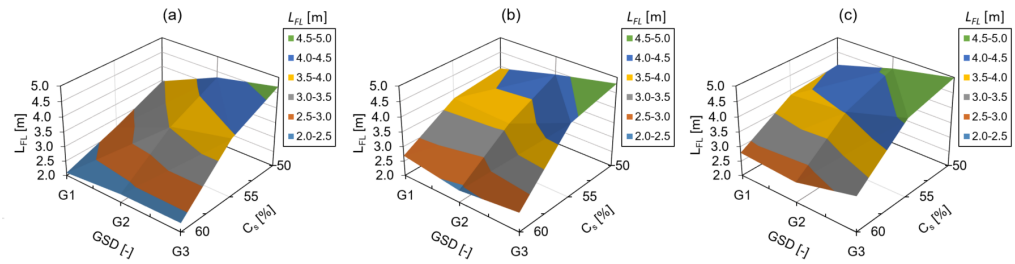

Fig. 4.7: L_{FL} variations with GSD and C_s for: (a) V1, (b) V2, and (c) V3

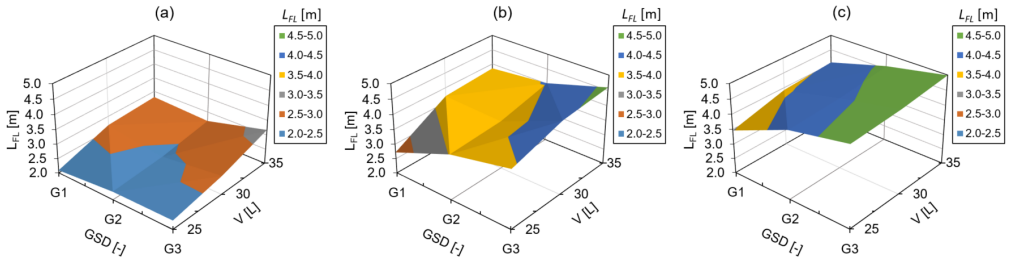

Fig. 4.8: L_{FL} variations with GSD and V for: (a) C1, (b) C2, and (c) C3

clearly seen. These plots are based on the initial solids concentration that considered the entire solids including the fines. However, after considering the fines ($< 0.06mm$ size) as part of intergranular fluid, part of the contribution of varying the GSD will be added to the C_s variation. To observe this effect, the C_s was recalculated as C_s^* and the results are given by three 2D-plots, presented in Figure 4.9.

The contribution to increasing the L_{FL} by varying V, C_s, and GSD can be seen in Figure 4.9(a), (b), and (c), respectively. In Figure 4.9(a), contribution of increasing V to

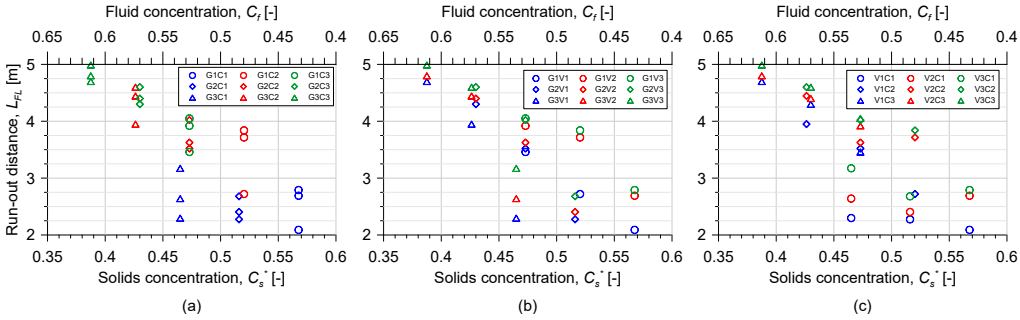

Fig. 4.9: L_{FL} plotted against the recalculated C_s^* for varying: (a) G and C, (b) G and V, and (c) V and C

the increasing of L_{FL} is shown by same shapes and colors data points. The significant contribution of varying C_s is seen on the steeper increases of data points with similar colors and shapes in Figure 4.9(b). Similarly, the moderate contribution to the increase of L_{FL} in varying the GSD is seen on Figure 4.9(c) represented by data points with similar colors and shapes.

4.3.4 Summary

The measurements, generally, show that the L_{FL} is affected more by the variation of C_s than the variation of V. In addition, the contribution of increasing fines content (represented by the varying GSDs) to the increase in L_{FL} is found to be the smallest. The L_{FL} becomes short when the C_s increases (water content decreases) and vice-versa. From the laboratory observations, the higher C_s tests exhibit more viscous and homogeneous flows than those with lower C_s. During the low C_s tests, the flow became less viscous, turbulent and flood-like, where it resembled a hyper-concentrated flow. This may indicate that using C3 = 50% and increasing more water beyond this value will make the flow behave more like a flood with suspended load than like a debris-flow. Therefore, in studying debris-flow, it may be important to consider keeping the C_s between 55% and 60%. This limiting value is also indicated in Section 4.2 where the flow regime resembled what is observed in typical real debris-flows.

4.4 Impact force of debris-flow on passable structures

4.4.1 Introduction

Two sets of tests are conducted to assess the impact force of debris-flows. The first one is conducted using a circular passable structure (pillar) on Model-1 as a preliminary study; later, the circular pillar is employed to evaluate the impact force reduction capacity of the screen-type countermeasures analyzed in Section 5.3.8. The second test set is conducted using Model-2 on a rectangular passable structure (pillar). In this test set, a more detailed assessment of flow impact force behavior is performed. Parallel to the tests conducted and presented in Section 4.2 and Section 4.3, tests with variation of the fines content (GSD), the volume (V), and the solids concentration by volume (C_s) are conducted on a rectangular pillar. Moreover, effect of varying the rectangular pillar impact width is also looked at.

The test results in each section is discussed in light of the existing hydro-static and hydro-dynamic analytical impact force estimating equations that are discussed in detailed in Section 2.6. For a quick reference, the equations are summarized here in Table 4.4.

4.4.2 Impact force on a circular passable structure

Nine tests were conducted as a preliminary study on the debris-flow impact force on a circular pillar using Model-1. The description of Model-1 can be found in Section 3.2 and the modifications for this particular test are presented in Figure 4.10. The flume model is instrumented with two flow height sensors and a rigid circular steel pillar with a load cell at its top. The configuration and placement of the circular pillar for this test setup

Table 4.4: Summary of analytical impact force equations from Section 2.6

Formula	Equation
$p = K \cdot \rho \cdot g \cdot \frac{h^2}{2}$	2.5
$p = K^* \cdot \frac{1}{2} \cdot \left((1 + \sqrt{2}F_r)^2\right) \cdot \rho \cdot g \cdot h^2$	2.6
$F_{hd1} = \rho v^2 A \cdot sin\beta$	2.7
$F_{hd2} = 5\rho v^{0.8}(gh)^{0.6}A$	2.8
$F_{mixed} = \frac{1}{2}\rho ghA + \rho v^2 A$	2.9
$p = k \cdot \rho \cdot q \cdot v = k \cdot \rho \cdot h \cdot v^2$	2.10
$\alpha = P/(\rho \cdot v^2) = a \cdot F_r^b$	2.12
$\frac{F_{peak}}{1/2 \cdot \rho \cdot v^2 \cdot h \cdot w} = \frac{K'}{F_r^2} + C'$	2.13

can be found in Section 3.2.4.

The debris solid material used for this test is the crushed sand aggregate. The grain

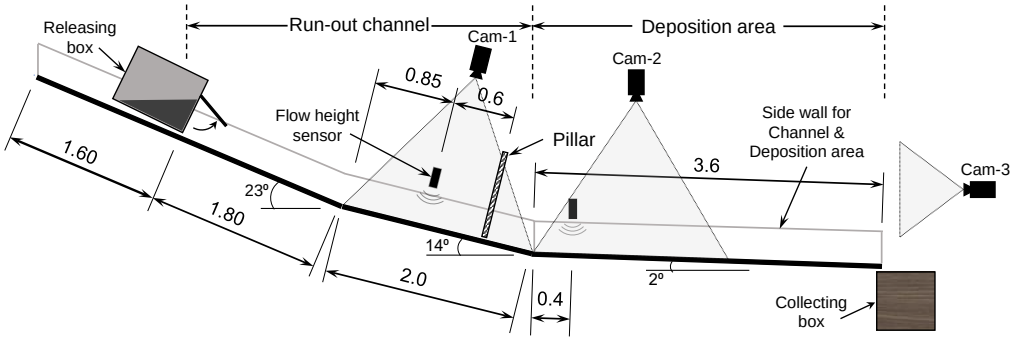

Fig. 4.10: The flume Model-1 with instrumentation and placement of the circular pillar (all dimensions in m)

size distribution, GSD, curve is given by Figure 4.11. Its grain density, ρ_s is $2.72g/cm^3$. The GSD has $d_{max} = 8mm$, $d_{50} = 2.2mm$, and $d_{10} = 0.1mm$ with the resulting coefficient of uniformity $C_u = 26$ which suggests that the material was well-graded.

In order to vary the average flow discharge, three V values ($25L$, $37L$, and $50L$) were

chosen with a constant 60% of C_s. The constant C_s value resulted in a constant bulk

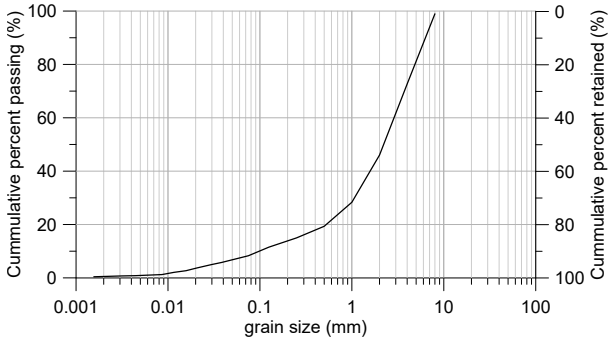

Fig. 4.11: Grain size distribution (GSD) of the debris material

density of $\rho = 2030kg/m^3$ that is calculated by Equation 4.5 given by Iverson (1997).

$$\rho = \rho_s C_s + \rho_w(1 - C_s) \tag{4.5}$$

During tests conducted on Model-1, there was always some amount of unreleased debris in the releasing box. Equation 4.5 was helpful to determine the resulting density from the net released debris-flow volume that hit the pillar. As seen in Table 4.5, the resulting bulk densities of the released volume vary but have not seen significantly deviated from the intended value, $\rho = 2030kg/m^3$.

The recorded forces and flow heights of the nine tests (PT1 - PT9) are presented in Table 4.5. The average discharge, Q values were calculated by computing the flow velo-

Table 4.5: Results of the nine tests conducted on the circular pillar

Test Name	ρ $[kg/m^3]$	v $[m/s]$	h_{Max} $[mm]$	Q $[m^3/s]$	F_{Max} $[N]$
PT1	1940	2.60	13.58	0.0106	18.6
PT2	1960	2.72	15.90	0.0130	16.2
PT3	1920	2.80	16.54	0.0139	12.6
PT4	1960	2.80	19.45	0.0163	24.8
PT5	2000	3.27	17.64	0.0180	19.6
PT6	1950	2.65	22.70	0.0180	17.8
PT7	1940	3.20	32.05	0.0232	28.3
PT8	1960	3.00	35.14	0.0256	27.3
PT9	1990	2.46	31.52	0.0259	27.9

city, v just before hitting the pillar, the maximum flow height h_{Max}, and the total channel width $w = 30cm$. Here, the h_{Max} of the debris-flow, which was recorded at $0.6m$ before the pillar, was considered as the maximum impact height. The v is computed and estimated from the Cam-1 video recorded (as seen in Figure 4.10) with the method explained in Section 3.2.6. Here, it is worth noting that estimating and setting a single value of flow velocity representing the varying velocity distribution across the channel width was challenging. Moreover, tracking the front which was subjected to speed variations due to segregation and a dry snout required averaging of the fluctuating velocity.

Figure 4.12 gives plots of the recorded forces against time in three groups according to the calculated Q. In these plots, the bold lines represent the moving-averages of the

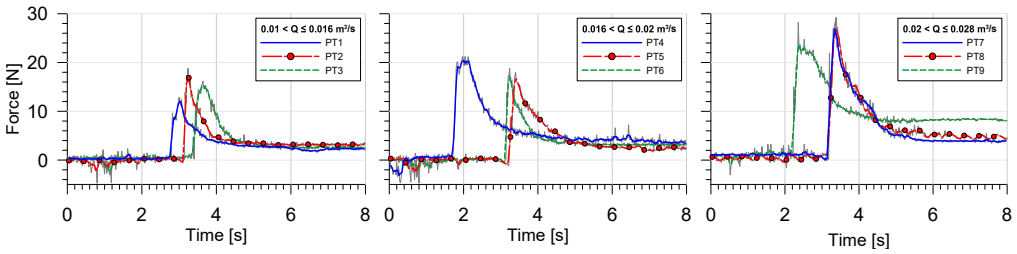

Fig. 4.12: The recorded impact forces on the pillar for all the tests grouped by ranges of discharge

recorded data. The original recorded data are drawn with light gray lines. The initial time $t = 0$ refers to the time at which the data acquisition program was made to start recording just before the release of the material by opening the releasing-box. This is one reason for the varying arrival times at the pillar location with possible additional contribution from the flow velocity variations.

The debris-flow impact force has three parts: the dynamic pressure from the slurry, the impact force of coarse particles, and the impact force of boulders (He et al. 2016). The debris solid material used in this study had a maximum grain size $d_{max} = 8mm$ (as seen in Figure 4.11), where only impact force from the slurry part and coarser particles parts are possible. Due to this, only the slurry impact pressure with a possible influence from the coarse particles was considered when analyzing the test results. The impact from bigger grains and boulders is not considered and falls out of the scope of this study.

The two impact process parts identified by Cui et al. (2015), representing the head and body impacts of debris-flow can be seen on both Figure 4.12 and 4.13 accompanied by the static force from the accumulated mass behind the pillar. Based on the amount (volume, V) of the debris-flow, the duration of the second phase can vary. Cui et al. (2015) repres-

ented this phase by a duration of 4 seconds in which its peak impact pressure is 68% of the peak of the first phase. In this test set, the second phase lasted between $1-2$ seconds where it was challenging to distinguish between the two parts. This led to using the peak impact force value alone representing the test result.

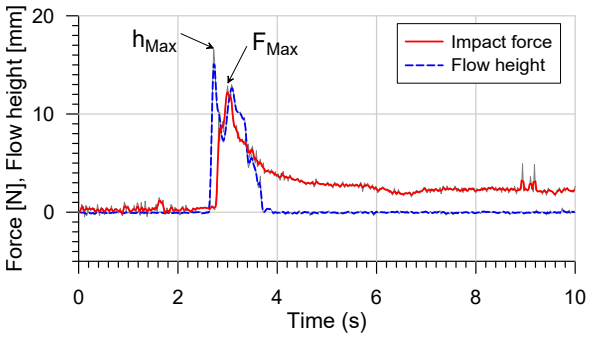

Fig. 4.13: The recorded force and upstream flow height for PT3

In Figure 4.13 the recorded force and flow height from a representative test (PT3) are plotted together. It shows the characteristic values, i.e., F_{Max} and h_{Max} that are given in Table 4.5.In the same figure, there is a 0.27-second lag time between F_{Max} and h_{Max}. This is a result of the $0.6m$ gap between the locations of the pillar and the flow height sensor.

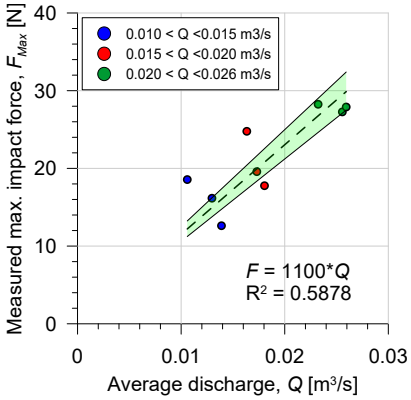

Fig. 4.14: The maximum impact force (F_{Max}) plotted against the calculated average discharge (Q)

According to the result presented in Table 4.5, different analyses are conducted to assess and find correlations between F_{Max} and the other flow parameters. Comparing F_{Max} with Q gave an interesting relationship and is presented in Figure 4.14. The F_{Max} is positively correlated with Q with $R^2 = 0.5878$. This positive correlation can be expressed by the trend line given in equation 4.6.

$$\bar{F} = aQ \tag{4.6}$$

where a is a multiplying factor and $\bar{F}$ is average maximum impact force. From Figure 4.14 and Equation 4.6, a is found to be $1100Ns/m^3$. Here it is worth noting that one may expect different a with a different setup of the flume model, i.e., with change in slope, width and length of run-out channel. In addition, for lower Q values, the scatter from the average line is wider which makes the relationship uncertain for lower discharges. In addition to this relationship that indicated a positive correlation between Q with the resulting impact F_{Max}, other analytical hydro-dynamic models are studied to get a better understanding of the impact force relation with other flow parameters.

The recorded F_{Max} is compared with the available analytical hydro-dynamic and hydro-static models that are presented in Section 2.6 and summarized in Table 4.4. F_{hd1} and F_{hd2}, which are referred to as the first and second hydro-dynamic models, are given by Equation 2.7 and Equation 2.8, respectively. In addition, the mixed model, F_{mixed}, that incorporated contributions of both hydro-static and dynamic effects and given by Equation 2.9, is evaluated with these test results.

Figure 4.15 shows the recorded impact forces along with the two hydro-dynamic impact force equations, F_{hd1} and F_{hd2}. The first hydro-dynamic equation, F_{hd1}, (with impact angle $\beta = 90°$ giving $sin(\beta) = 1.0$) gave slightly higher estimation than the measured F_{Max} values as shown in Figure 4.15(a). However, the F_{hd2} underpredict the measured F_{Max} values. It gives closer predictions for cases with higher flow heights in each Q group, although the measured impact force is not only dependent on the h_{Max} but also on the flow velocity.

When comparing F_{hd1} with F_{mixed}, the only difference is that the mixed model (F_{mixed}) incorporates a static contribution of the flowing debris. Because of the relatively thin flow heights and the pillar, which is a passable structure that does not allow for the progressive accumulation behind it, the static contribution is almost negligible with respect to the dynamic contribution. This indicates that the F_{mixed} model is more suitable for wider structures and thicker flow heights. For passable structures, only the dynamic part that can be expressed by F_{hd1} is seen to give a good estimate of the measured peak impact force.

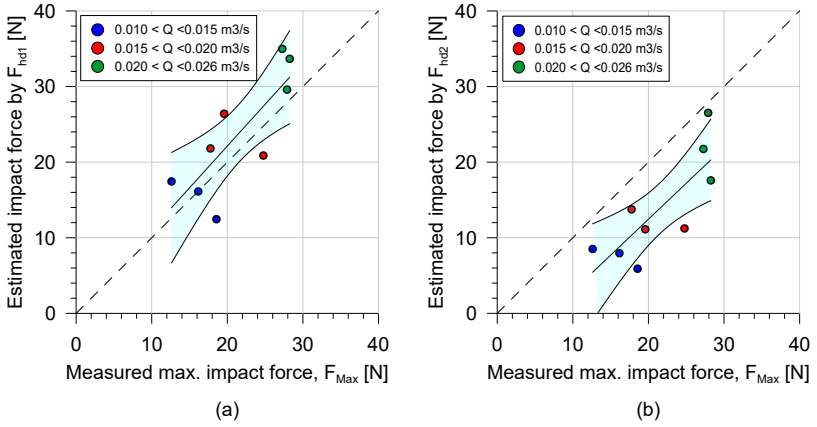

Fig. 4.15: Comparison of the measured F_{Max} with: (a) F_{hd1} and (b) F_{hd2}

Dimensionless relationship between normalized impact pressure, α and Froude number, F_r was reported, among others, in Huebl et al. (2009), Proske et al. (2011), and Cui et al. (2015) and given by Equation 2.12. The resulting F_r values of this test-set, that vary between $4 - 8$, are found to be relatively higher that what commonly estimated in real debris-flows, i.e., $F_r < 3$, which might be attributed to the smooth flow bed of the flume model and the flow viscosity. The desired F_r could possibly be achieved by increasing the flow bed roughness of the flume model and/or by increasing the fines fraction of the debris material, as stated by Iverson et al. (2010), where these two improvements can closely mimic conditions of natural debris-flows. The effect of increasing the fines fraction is studied in the next test-set that is discussed in Section 4.4.3.

The calculated empirical coefficient, α and F_r values are plotted as shown in Figure 4.16. The F_r values of this test-set fall within the range of other flume model tests that exten-

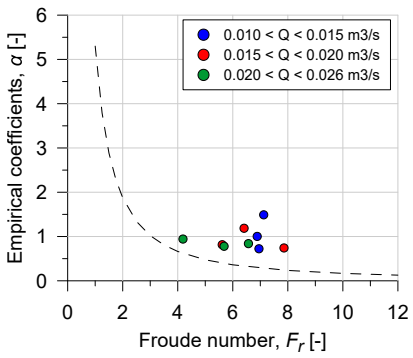

Fig. 4.16: Relationship between the F_r and the normalized peak pressure given by α

ded up to $9 - 11$ (e.g. Huebl et al. 2009 and Cui et al. 2015). However, the calculated α values are seen to be slightly higher than the trend line which might be caused by the method of peaking the F_{Max} values. For this study, only the ultimate peak impact values were picked, while in the other studies like Cui et al. (2015), separation of grain and slurry impact was performed in addition to averaging the impact pressure records of the bottom two pressure sensors. Although there are few data points, the results follow the power function trend line of Huebl et al. (2009) for the empirical coefficient expressed by $\alpha = 5.3F_r^{-1.5}$ which is modified by Cui et al. (2015).

This preliminary study on impact force of a moving debris on a rigid circular passable structure (pillar) showed the potential of this simple method in measuring impact force. It also gave an insight to the missing impact force on passable structures in the literature. The results showed, although with some scatter, that the impact force can be estimated by the hydro-dynamic model, F_{hd1}, developed from conservation of momentum. However, the other hydro-dynamic model, F_{hd2}, underpredicted the measured impact pressure that might be because of its fixed constants and multipliers. The power function relationship between α and F_r was found to give good fit to the data points although the data points have slightly higher α values. Nevertheless, this hydro-dynamic power relationship was found to be very useful as the data follows the trend, as well as it gives better ways to compare and relate laboratory test results with field observations. This simple method of measuring impact force on a pillar representing a passable structure will be studied further with more comprehensive testing with varying material types through fines content (GSD), volume (V), and solids concentrations by volume (C_s) in Section 4.4.3.

4.4.3 Impact force on a rectangular passable structure

This study (test set) extends the preliminary debris-flow impact force assessment conducted on a circular passable structure presented in Section 4.4.2. Flow impact force assessment on a $25mm$ wide rectangular passable structure (pillar) is conducted using all variations of the debris-flow material based on the GSD, V, and C_s on Model-2. The flume Model-2 setup for this test set is given by Figure 4.17 with the vertical force-measuring rectangular pillar placed just at the end of the channel.

The principle of torque as a working mechanism of the pillar explained in Section 3.3.4 is maintained for this test set with proper consideration of the impact angle in the resulting measured impact force. Detailed configuration and setup of the pillar is given in Section 3.3.4.

The recorded flow impact forces, F_{Max} and flow heights, h_{Max} of the 27 tests are collected from their respective time plots and are given in Table 4.6 along with the approach flow

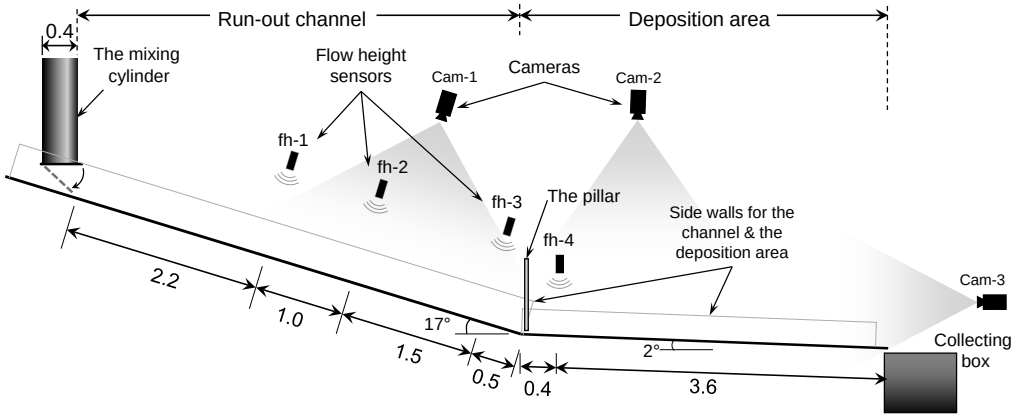

Fig. 4.17: The flume Model-2 with the rectangular pillar: instrumentation and placement of the rectangular pillar (all dimensions in m)

velocity of the debris-flow front. A representative time plot is given by Figure 4.18 as an example from the G1V1C1 test.

The third flow height sensor (fh-3) is situated $0.5m$ before the pillar (as seen in Figure 4.17) and h_{Max}, maximum impact height, is assumed from its peak value. The v is

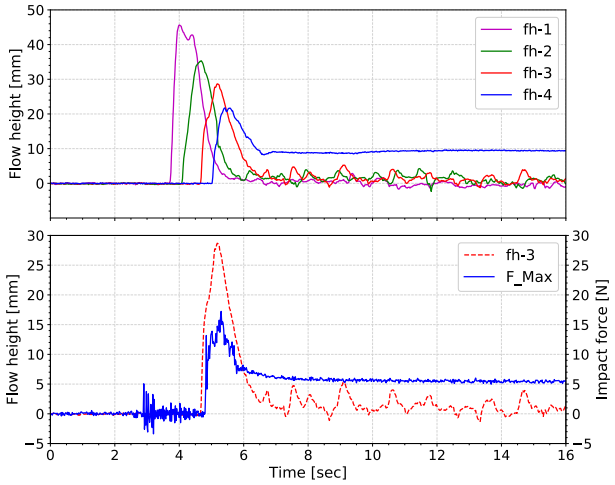

Fig. 4.18: Typical test result (from G1V1C1) showing flow heights and impact force plots with time

estimated from Cam-1 video recording with the method explained in Section 3.3.6.

From the equations listed in Table 4.4, evaluating Equation 2.5 by employing the ρ, v,

and h values listed in Table 4.6 made the K value to be as high as 75 to equate them with the measured force per unit width values. Different K values were proposed in literature;

Table 4.6: Results of impact force along with approach flow velocity and flow height

		G1			**G2**			**G3**		
V & C_s combinations	rho $[g/cm^3]$	v $[m/s]$	h_{Max} $[mm]$	F_{Max} $[N]$	v $[m/s]$	h_{Max} $[mm]$	F_{Max} $[N]$	v $[m/s]$	h_{Max} $[mm]$	F_{Max} $[N]$
V1C1	2.050	2.60	28.7	18.0	2.4	26.8	14.4	3.0	21.6	14.3
V1C2	1.962	3.25	26.0	13.3	2.9	20.7	13.2	3.6	19.1	13.4
V1C3	1.875	3.50	22.2	12.8	4.0	27.1	15.6	4.2	19.2	12.5
V2C1	2.050	3.10	33.6	18.8	2.7	24.4	10.9	3.5	27.4	17.4
V2C2	1.962	3.00	26.2	15.5	4.1	25.7	15.8	3.8	20.7	14.3
V2C3	1.875	3.60	23.8	13.4	4.0	34.1	16.3	4.0	22.4	13.7
V3C1	2.050	3.30	38.5	23.9	3.5	34.5	12.6	3.6	20.5	13.6
V3C2	1.962	3.40	31.8	18.2	3.8	35.2	18.6	3.9	23.9	16.0
V3C3	1.875	3.80	27.1	18.0	4.2	37.0	16.4	4.0	27.5	18.1

for example, $K = 7-11$ Lichtenhahn (1973), $K = 9$ Armanini (1997), $K = 5-15$ Scotton and Deganutti (1997). This shows the limitation of a pure hydro-static equation to be applied for estimating dynamic impact forces of debris-flows, especially on passable structures. The hydro-static impact force estimates (e.g. Equation 2.5) are found unsuitable for these cases of passable structures for two main reasons. First, the impacted structure is a passable one that makes the static contribution from accumulated mass to be very small. Second, this laboratory flume test has a relatively thin flow height that makes the static contribution very negligible when compared to the dynamic one.

Because of the systematic incorporation of the dynamic effect in Equation 2.6, which has a hydro-static basic equation form, the measured impact force per unit width values are seen to fit with the values calculated by Equation 2.6 when taking K^* as 0.85. The equation is developed by Zanuttigh and Lamberti (2006) using dry avalanches and K^* was suggested to be 1.0 for stony debris-flow and 1.5 for muddy debris-flow after the equation is compared with field observation data. The results are presented in Figure 4.19(a), (b), and (c), representing the effect of GSD, V, and C_s variations, respectively.

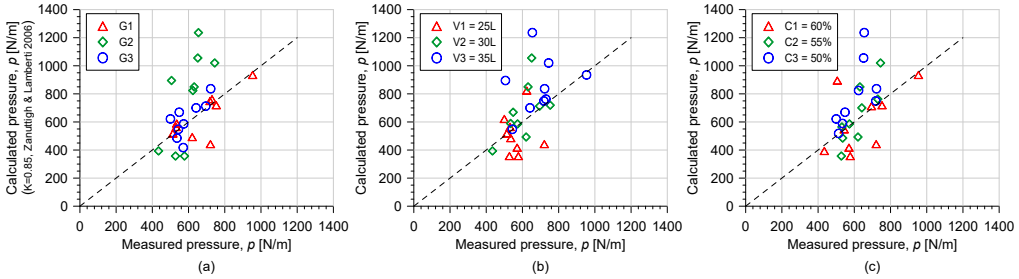

Fig. 4.19: Impact pressure comparison: measured vs calculated by Equation 2.6 (Zanuttigh and Lamberti 2006) based on variations of: (a) GSD, (b) V, and (c) C_s

The impact pressures from G1 and G3 tests fit closely with the vales estimated by Equation 2.6 while the G2 tests are seen to be scattered for few of the data points. In the other two plots, V3 and C3 looked to contribute to the scatter seen in G2 tests. More water (C3) in the debris-flow could be given as one of the reasons for the relatively low impact values measured. These outlier tests behaved and characterized by fast and turbulent flow with possible low impact height that resulted in relatively low impact force.

The hydro-dynamic model proposed by Mizuyama (1979) by considering momentum conservation is given by Equation 2.10. The measured impact force per unit width is

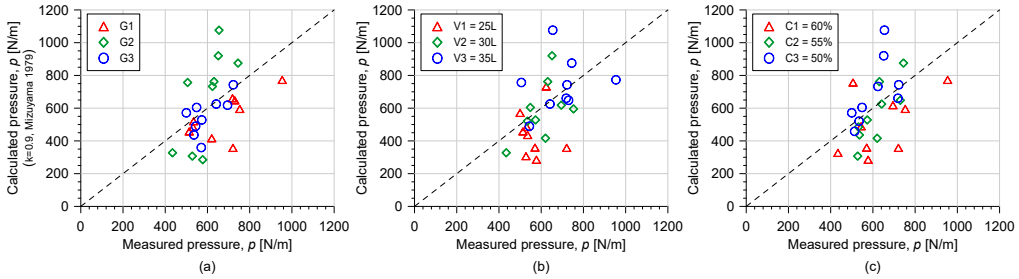

Fig. 4.20: Impact pressure comparison: measured vs calculated by Equation 2.10 (Mizuyama 1979) based on variations of: (a) GSD, (b) V, and (c) C_s

compared with the values estimated by Equation 2.10. when the different GSDs were evaluated, the factor k was found to vary between $0.85 - 1.0$. In general, $k \approx 0.9$ fits for the total data-set, with some G2 outliers, as shown in Figure 4.20. Similarly, not much significant dependence on V and C_s can be seen from Figure 4.20(b) and (c), except the over estimation for few V3 and C3 cases. Observing the overall plots, $k \approx 0.9$ may be considered as a factor for a passable structure when using Equation 2.10.

The dimensionless hydro-dynamic relationship formula that is given by Equation 2.12

is used to compare the laboratory results with other test results and real debris-flows. The data from this study are plotted in the F_r Vs α plot and presented in Figure 4.21. The F_r values of this test-set varied between $4.7 - 9.7$. The figure data includes three plots to show the effect of varying GSD, V and C_s. Data from Huebl and Holzinger (2003) and Cui et al. (2015) are included to show a comparison with other miniaturized model tests.

The α values from this study, generally, are seen to be higher than the trend line of

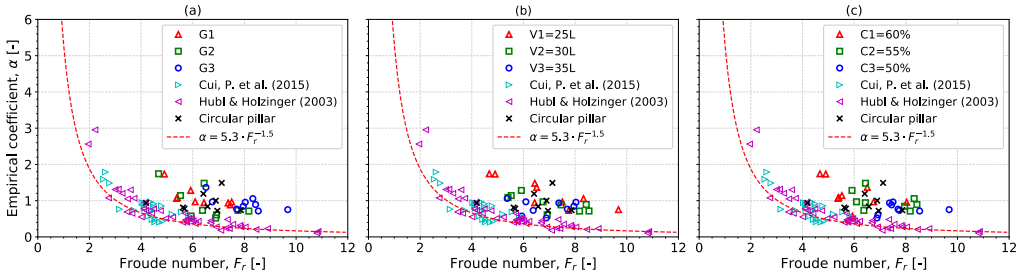

Fig. 4.21: Froude number Vs empirical coefficient plots based on the variations of (a) GSD, (b) Volume, V, and (c) Solids concentration, C_s

the power-function. This shows that the relationship with the selected constants under-predict our measured impact pressure. There might be two main reasons for this. One is that the F_{Max} values peaked from the plots (as seen in Figure 4.18) are the absolute maximum values, as the output is a $50Hz$ data averaged from a 100 samples per seconds of measurement. The other reason might be that in the other data from the literature (e.g. from Cui et al. (2015)), the peak impact pressure is computed from the average of the bottom two sensors (at $1.5cm$ and $4.5cm$), in addition to the process of filtering the impact of slurry from the coarse grains that reduced the peak by about 30%.

In comparing the results among the variations of GSD, V, and C_s, the F_r was seen to be lower for tests with C1 = 60% and higher for tests with C3 = 50%, as shown in Figure 4.21(c). This might be because of the tests with the highest C_s (lowest water content), resulting in a relatively slower flow front towards impacting the structure. This influence of C_s on F_r is also reported by Song et al. (2017).

Increase in fines content is also seen to increase the resulting F_r as the v values recorded for G3 (a material with the largest fraction of fines) are relatively higher. Relatively lower F_r values are observed during the use of G1 and G2. Generally, higher C_s (C1) and lower fines content (G1) resulted in higher α with lower F_r. Data from real debris-flows show low F_r and high α values (Huebl and Holzinger 2003, Huebl et al. 2009, and Proske et al. 2011). This real debris-flow behavior is seen to be approached by the choice of material

G1 and C1=60% as indicated in Section 4.2.

The largest V, V3 = $35L$, is seen to result in lower α with narrower range of F_r values while the smallest V, V1 = $25L$, is seen to result in relatively higher α with a wider range of F_r. Except for the variation in the range of F_r, the choice of V does not show a direct relationship with the resulting F_r value like the choices of C_s and GSD.

The flume model used in this study has a smooth bed and smooth side walls providing minimum friction. This low friction, mainly from the bed, contributed to the high v and low h_{Max}. The high v value contributed to the observed relatively high impact forces that are reflected on the calculated higher F_r and α. Rough bed and significant mud in the debris are stated to closely mimic the natural debris-flow conditions after tests conducted by 20% loam and 80% sand-gravel mixture (Iverson et al. 2010). Although Model-2 bed is smooth, the G1 and G2 tests, with respective 5.4% and 14% fines content, exhibited lower F_r values, i.e., closer to what are seen in real debris-flows while providing additional fines content (as in the case of G3 with 22.5% fines content) gave most of large values of F_r, except when combined with C1=60% case.

4.4.4 Impact force on varying rectangular pillar width

After conducting a series of tests to study the effects of varying GSD, V, and C_s of debris-flow on a rectangular passable structure, further study was conducted to investigate the impact force on varying pillar widths using a selected composition of debris-flow material, G1V1C1. This material combination was selected as it resulted in the lowest F_r which was a closer value to field observations. The test was conducted using Model-2 with model setup given by Figure 4.17. The pillar width variations are given by Figure 4.22.

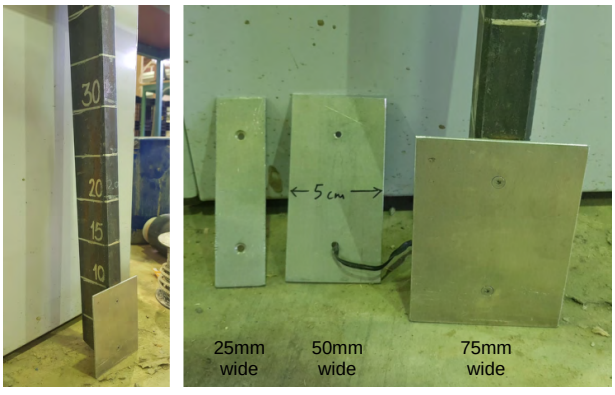

Fig. 4.22: Passable structure width variations represented by varying plate widths

Three widths ($25mm$, $50mm$, and $75mm$) are selected, of which the first is a reference test similar to what is reported in Section 4.4.3. In order to obtain the other two widths, a $10cm$ high, stiff solid metal plate is attached to the bottom section of the rectangular pillar with their corresponding widths (as seen in Figure 4.22). The results along with the calculated impact force estimates are given in Table 4.7. General observation of the

Table 4.7: Results showing the impact force tests on varying width of the passable structure

	Measured values			Calculated values			
Test name	v $[m/s]$	h_{Max} $[mm]$	F_{Max} $[N]$	F_{hd1} $[N]$	p $[N/m]$	F_r [-]	α [-]
V1C1-r1_25mm	2.50	12.4	8.4	4.0	336	7.16	2.11
V1C1-r2_25mm	2.75	14.0	7.7	5.4	308	7.42	1.41
V1C1-r1_50mm	3.30	13.7	12.2	15.3	244	9.00	0.80
V1C1-r2_50mm	3.00	16.0	15.5	14.7	310	7.58	1.05
V1C1-r3_50mm	2.80	13.9	17.8	11.1	356	7.59	1.60
V1C1-r1_75mm	2.20	15.8	19.4	11.7	259	5.60	1.66
V1C1-r2_75mm	2.70	12.6	16.4	14.1	219	7.68	1.16
V1C1-r3_75mm	2.70	15.6	21.5	17.4	287	6.91	1.24

results indicates that it is challenging to obtain consistent results in debris-flow flume studies when estimating the ever changing front flow velocity and flow height. Here, for the same material combination (G1V1C1), approach velocity, v, of the debris-flow front at the pillar location varied between $2.5m/s - 3.3m/s$, while the assumed impact height obtained from fh-3 was observed to vary between $12.4mm - 16mm$. Despite these limitations, the hydro-dynamic models and the power-function relationship of the dimensionless pressure (empirical coefficient) with F_r are calculated and given in Table 4.7.

The results are plotted in Figure 4.23(a) by comparing it with the first hydro-dynamic equation given by Equation 2.7. The first hydro-dynamic equation closely predicts the resulting impact force with the varying impact width. This shows that the F_{hd1} is a robust model that is seen to have estimated, with a close approximation, the circular pillar results, the varying debris material on the rectangular pillar, and this test set made with varying rectangular impacting widths. In addition, no significant change in the resulting impact pressure was observed as the recorded impact force increased with increase of the impact area, although it was not linear.

Again, it can be observed from Table 4.7 and Figure 4.23(b) that the measured impact force (through normalized pressure) is found to be higher than the one that the power-

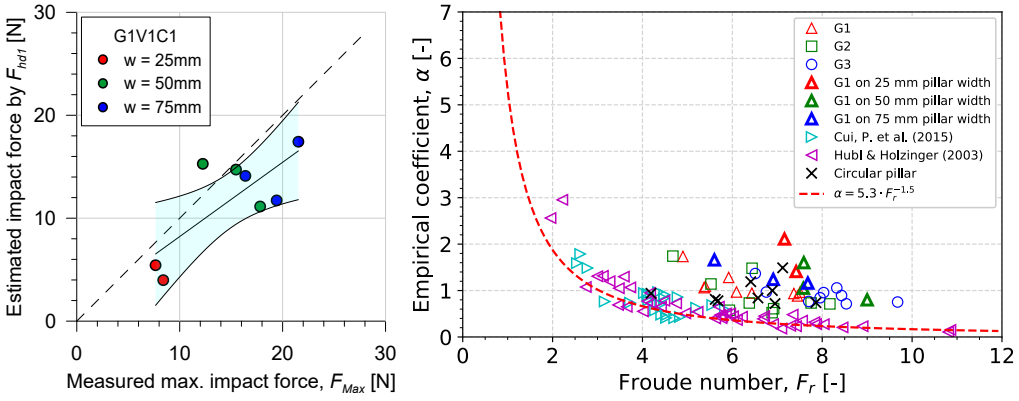

(a) F_{Max} Vs F_{hd1} **(b)** F_r Vs α

Fig. 4.23: Impact measurement result using varying width of a passable structure

function predicts. This might be attributed to the smooth flume bed and the selection of peak impact force as F_{max}. This is explained in Section 4.4.3. However, the dimensionless relationship between α and F_r for impacts on varying widths follows the trend of other tests. This indicates that the model might not be affected by the impact width. This can make it as a suitable model for both passable (thin) structures and impassable (wide) structures. Therefore, Equation 2.12 is an important relationship to estimate and relate impact pressure of debris-flows on different types of structures.

As all data are aggregated in this section, they are plotted according to the dimensionless relationship given by Faug (2015) given as in Equation 2.13. Figure 4.24(a) and (b) gives all data from this study and other data used in the previous section While Figure 4.24(c) shows the original plot from Faug (2015) where the two boundaries are suggested in.

The data from this study fall in the intermediate region between the quasi-static and

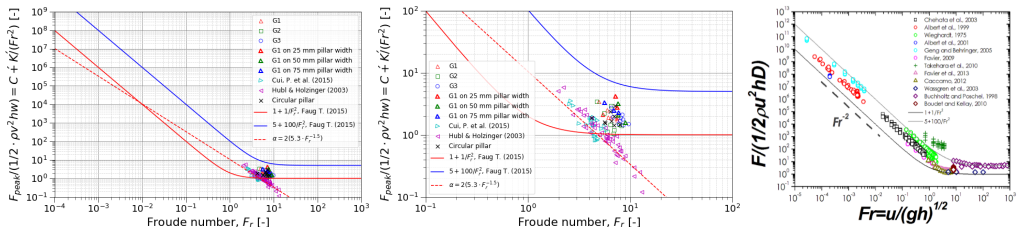

(a) (b) (c)

Fig. 4.24: The impact force normalized by the kinetic force expression plotted as a function of F_r (a) data from this study, Cui et al. (2015) and Huebl and Holzinger (2003), (b) close up view of plot (a), and (c) plot from Faug (2015) for comparison.

very rapid flows in addition to being enclosed between the two boundaries expressed by $1 + 1/F_r^2$ and $5 + 100/F_r^2$, where 1 and 5 are values representing pure drag coefficient, C' while 1 and 100 are values for the earth pressure coefficient, K'. It is challenging to evaluate the results from this study based on the different compositions and water contents because of the wide range of normalized force and F_r used in developing this hydrodynamic relationship. It is However, the hydrodynamic relationship proposed and improved through time by Huebl and Holzinger 2003, Huebl et al. 2009, Proske et al. 2011 and Cui et al. 2015 is shown by the straight line and part of the initial data from Huebl and Holzinger (2003) and few from data Cui et al. (2015) that has values $F_r \geq 6$ are below the lower boundary. Here it is worth noticing that the relationship given by Faug (2015) used granular flow tests while the others are fluidized flows. Therefore it shall be further looked at using data from fluidized flows. Here it is only shown to see its extent and applicability to fluidized flows in inclined planes. It shows promising results for data from this study and where the drag and earth pressure coefficients could be investigated further in the future. For now, the simplified hydrodynamic relationship can help in relating the laboratory scale test results with the real fluidized debris-flows.

4.4.5 Summary

An effort is made to measure the impact force of debris-flow on passable structures using a simple vertical pillar that uses a single force cell. This method avoids direct contact of the debris with the force cell and any other instrumentation. In addition, it can be easily installed on and removed from the model. More importantly, it helps capture the behavior of actual debris-flows in hitting road structures, bridge or underpass pillars, or even houses that can relatively represent or act as passable structures situated in a debris-flow path.

The results are evaluated using the available empirical, semi-empirical and analytical impact force models. The empirical and pure hydro-static models could not fit to the entire data, although they have shown some indications and relationships with single or two flow parameters. These models are not robust enough to work for the major types of debris-flows, as, for example, the pure hydro-static model uses only flow height to calculate the impact force. More specifically, for small scale experiments like this study, the flow height is relatively very thin which reduces the influence of static contribution compared to the dynamic one. Moreover, debris-flows impacting passable structures do not have sufficient width to accumulate debris material behind them where the static contribution becomes comparable to the dynamic one. Therefore, the pure hydro-static and empirical relations might work for specific cases where a multiplying factor is used to compensate the spatial condition and type of debris-flow.

The analytical models are hydro-static and hydro-dynamic models. Some of the semi-empirical and hydro-dynamic models are found to be more robust where they use combination of flow parameters like h and v in combination with dimensionless parameters like F_r. The test results of this study follow the trends with a constant and varying multiplying factors. The semi-empirical models are entirely dependent on a constant multiplying factors applied for some behaviors unaccounted for. Although semi-empirical models demonstrated better agreement with the test results than the pure hydro-static or empirical ones, it also lacked robustness to wide ranges of debris-flow types and scale variations. The hydro-dynamic model with a varying multiplying factor or simply the dimensionless relationship between F_r and normalized pressure term given by the empirical coefficient, α is the robust one which incorporates the debris-flow type in terms of F_r along with α. This dimensionless power-function relationship between F_r and α helps as a bridge between scaled experiments with real debris-flows. The trend of this study found to follow that seen in literature, although the α values are slightly higher. The slight increase in α could be a result of: 1) the smooth beds of the flume models contributing to the recorded higher impact force, 2) or, only peak impact forces are collected in these tests while some of the literature values are reduced either by averaging or by filtering sharp peak values from bigger grains.

The following findings are given as remarks:

- It is observed to be preferable to study the impact force of debris-flow using a passable structure to mimic natural flow and impact behaviors.
- The first hydro-dynamic equation was seen to replicate the trend of the measured impact forces during the use of circular and rectangular passable structures as well as when pillar with is varied, regardless of scatters in the data points.
- The common values of F_r from field observations is not more than 3, while in our tests it ranges between $4.5 - 9.7$.
- Laboratory results and field observation results have gaps due to scaling effects. However, it is shown that it can be bridged by the use of the dimensionless hydro-dynamic power-function relationship between F_r and normalized pressure, α.
- Despite the challenges to evaluate and pick the impact velocity and impact heights from the continuously varying flow front, the dimensionless parameters help in indicating the dependence of debris-flows impact behavior based on its composition.
- Increasing fines content and water content increases the F_r and slightly decreases the normalized pressure, α. The reverse is also true.

- Increasing volume reduces the variation in F_r and reduces the normalized pressure, α. This might be because of relatively consistent flows are obtained during tests with larger V values.
- It is also demonstrated that the power-relationship works for varying impact width as well.
- Low F_r values and high α values are behavior of real debris-flows. Tests with lowest fines content (G1), as well as G2, and Lowest water content (C1) are those which exhibited lower values of F_r and relatively higher α values.

4.5 Pore-water pressure measurements

4.5.1 Introduction

The presence of water is one of the major contributors in the initiation and mobility of debris-flows as explained in Section 2.3. During the movement of debris-flows, along with presence of fines particles, the water may result in excess pore-water pressure that can facilitate the mobility of the debris-flow. During some of the tests conducted in flume Model-1 and Model-2, the flow pore-water pressure was measured in the run-out channel and the deposition area. The results are discussed in regards to the pore-water pressure proportion in relation to the total normal stress, the pore-water pressure dissipation, and its decaying behavior during the deposition process.

4.5.2 Pore-water pressure measurement on Model-1

The pore-water pressure measurement on Model-1 was conducted by two sets of sensors (one set in the run-out channel and one set at the deposition area) that are placed under the shadows of the two flow height sensors, see Section 3.2.1 Figure 3.1. The detailed set-up, instrumentation and working procedures of these sensors are given in Section 3.2.5.

The pore-water pressure measurement is made on the first six reference tests (V1T1 - V1T6) presented in Section 5.3. Due to the challenges in maintaining the pore-water pressure sensors functional (in keeping sensors saturated and making it air free before every test), the pore-water pressure measurements could not be conducted in the other subsequent tests. In addition, the sensors inside the channel were not properly functioning during these tests, and therefore, only the results recorded from the sensors at the deposition area are presented.

A representative result plot from the first test (V1T1) is given in Figure 4.25. The plot includes the two pore-water pressure measurements along with the total normal pressure,

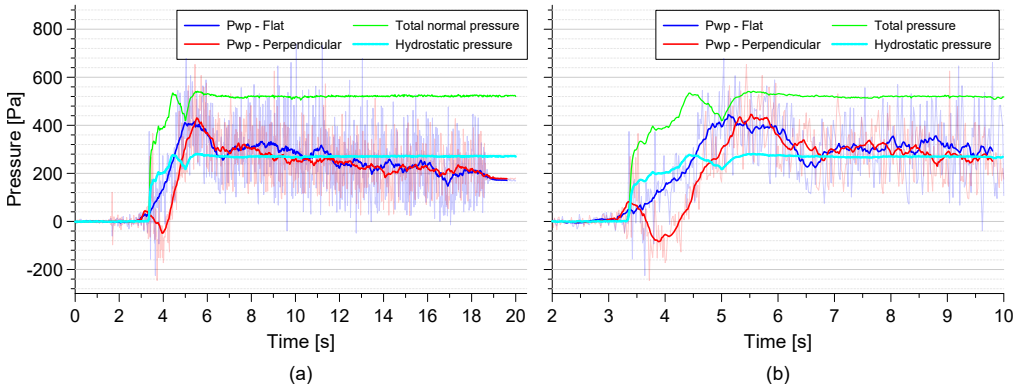

Fig. 4.25: Measured pore-water pressure along with calculated total normal pressure and hydrostatic pressure of Test V1T1: (a) entire 20 seconds duration and (b) close up look of the first 8 seconds

σ_v, and the hydrostatic pressures, $P_{wp,hyd}$, that are calculated by assuming a fully water saturated flow and deposition heights. Plotting hydrostatic pressure helps in indicating the duration of excess pore-water pressure, $P_{wp,excess}$, dissipation. In reality, the total normal pressure and hydrostatic pore-water pressure decrease with the process of water percolating out of the deposit. However, it is challenging to tell when exactly the water height starts to decrease after the deposition process completes. Therefore, until the hydrostatic pressure equals the measured pore-water pressure, it is assumed that the water height and the deposition heights are equal.

The flat and perpendicular pore-water pressure sensors are represented by the blue and red colors, respectively. It is averaged with a moving average window of 21. There is a small-lag between the peak value of flow height, h_{Max}, and the corresponding peak value of pore-water pressure, $P_{wp,Max}$. Both pore-water pressure sensors recorded their peak value between $5.1 - 5.3$ seconds, whereas the peak flow height was first recorded at 4.4^{th} second, giving a lag of almost 1 second. This might be due to a slower response time for the pressure transducer than the flow height ultrasonic sensor.

Around the 10^{th} second, the measured pore-water pressure equals with the hydrostatic one. This marks the end of dissipation of excess pore-water pressure. If we consider the 6^{th} second as the end of the flow where deposition process completed, then it took almost 4 seconds for the excess pore-water pressure to dissipate while the mass deposited. This is in line with what is stated by Major and Iverson (1999), as deposition occurs long before the debris liquefying pore-water pressure fully dissipated from the debris body. Deposition mainly occurred due to grain-contact friction and bed friction concentrated at the dry front and flow margins (Major and Iverson 1999).

The rest of five test results are given in Appendix A3 and their peak values are collected and given in Table 4.8 along with the V1T1 presented in Figure 4.25.

Pore-water pressure ratio, r_u, that indicates the level of pore-water pressure with respect

Table 4.8: The downstream recorded pore-water pressures along with the respective flow heights for V1C1

	Measured values		Calculated values			
Test name	h_{Max} [mm]	$P_{wp,Max}$ [Pa]	$P_{wp,hyd}$ [Pa]	$P_{wp,excess}$ [Pa]	$\sigma_{v,Max}$ [Pa]	r_u [-]
V1T1	29	445	290	155	558.8	0.80
V1T2	25	480	250	230	490.9	0.98
V1T3	20	290	200	90	390.5	0.74
V1T4	52	800	520	280	1027.7	0.78
V1T5	39	700	390	310	773.7	0.90
V1T6	46	750	460	290	914.2	0.82

to the total normal pressure is calculated using Equation 4.7. The values of r_u given in Table 4.8 are those calculated from the peak values (P_{wp} and σ_v). $r_u = 1.0$ represents full liquefaction in the flow (Major and Iverson 1999).

$$r_u = \frac{P_{wp}}{\sigma_v} \tag{4.7}$$

The pore-water pressure and flow height values from V1T4 - V1T6 are higher than the first three, V1T1 - V1T3. This is because of the presence of the underpass and the guide wall that induced additional flow height and deposition thickness at the sensors' location. However, not much difference is observed in the respective r_u values. The r_u values give the total normal stress percentage that is taken over by the pore-water pressure, indicating the proportion of friction force missing in the body of the debris-flow and its contribution in facilitating the debris-flow mobility.

4.5.3 Pore-water pressure measurement on Model-2

The challenges of saturating the pore-water pressure measuring system in Model-1 before every test is explained in Section 3.2.5. In order to minimize the systems preparation time and ensuring proper saturation of the sensor fluid chamber, a separate saturating system is designed and implemented in Model-2. Its set-up and saturating procedure is explained in Section 3.3.5 in addition to the schematic representation of Model-2 with

installation locations on Figure 3.7.

The figure contains the measurements made both in the channel and the deposition area. Figure 4.26(a) shows the measurement in the channel where there is almost no deposition once the flow passed the sensor location. The total normal pressure and the

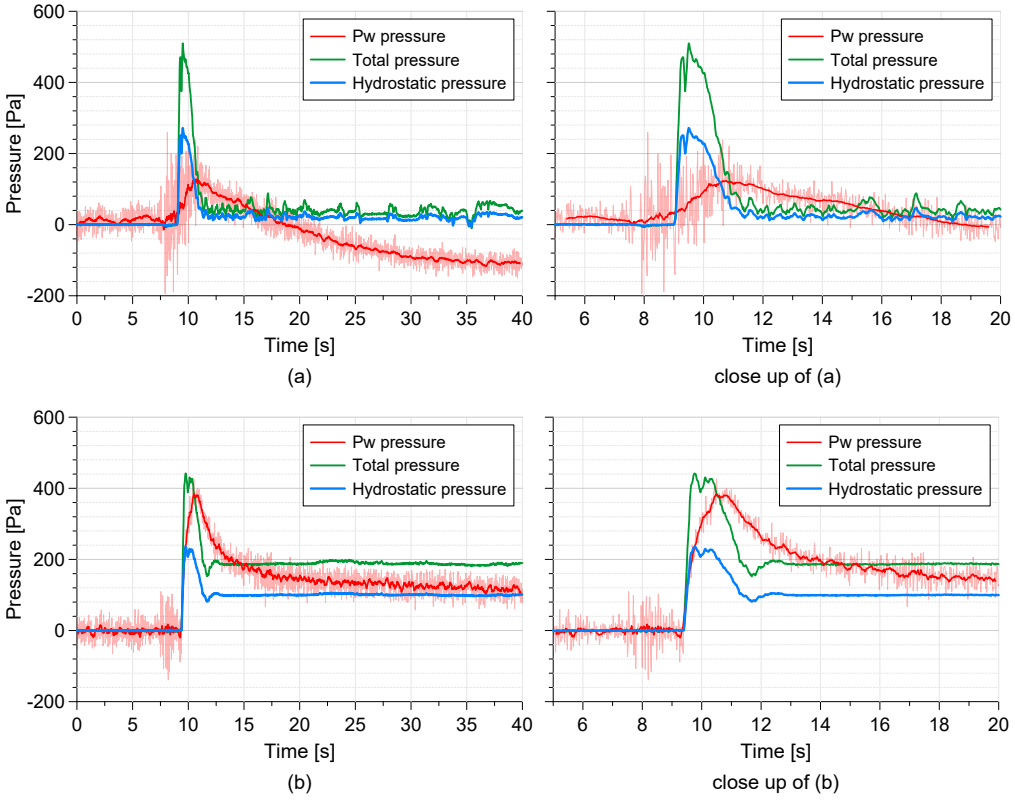

Fig. 4.26: Measured pore-water pressure, total normal pressure, hydrostatic pore-water pressure using the sensor in: (a) the channel, and (b) the deposition area. Close up views of both measurements are given at their respective right side

hydrostatic pressure that are calculated using the recorded flow height gave a near-zero measurement after a three-second long flow. The pore-water pressure line does not show a correct measurement as it gives values less than that of the hydrostatic pressure and goes to negative values once the major part of the flow has passed the sensor location. This is presented here to show one of the challenges in measuring the pore-water pressure.

The measurement in the deposition area (Figure 4.26(b)) gives similar behavior of pore-water pressure dissipation as the measurement on Model-1 (Section 4.5.2). The maximum

pore-water pressure gave an almost liquefied ($r_u \approx 0.9$) flow. However, the pore-water pressure dissipation process is seen to be slower which it looks, resulting in an $r_u > 1.0$. This could be resulted from the naturally slow decaying process of pore-water pressure after deposition. Although it is not as significant as the case here, Major and Iverson (1999) reported that fluid pressure was observed to be slightly higher than the liquefaction level in cases of debris-flows rich in loam (fines particles). This could be a result of the interaction of a drained soil element transferring stresses to adjacent undrained soil element, squeezing it to temporarily increase the pressure level beyond what is expected to have resulted from the loading condition (Major and Iverson 1999).

4.5.4 Summary

In these two models, the pore-water pressure effect in debris-flow mobility is shown. The pore-water pressure was seen to exist after the deposition process had been completed, where the same observation was indicated in Major and Iverson (1999). This indicates that, although pore-water pressure is one of the major contributors to the debris-flow movement, pore-water pressure dissipation is not observed to be the major factor for stopping the flow and facilitating the deposition process. It is rather the geometrical influence of the fan, a relatively slow flow front, which created levee, that could greatly facilitate hindering of the mobility of the debris-flow. Grain-contact friction and bed friction concentrated at flow margins are the main reasons for debris-flow deposition Major and Iverson (1999).

5 Performance of the screen-type debris-flow countermeasure

5.1 Introduction

This chapter presents all of the laboratory test results performed on the screens. The tests were conducted on both Model-1 and Model-2 and the results are presented in three parts in different sections and subsections of this chapter.

The first part presents a study conducted by Laache (2016) in Model-1 that was reanalyzed and published in Yifru et al. (2018). The study investigates the optimal opening width of grids for two different screen lengths. The second part presents other test results after investigating two screen lengths for their performance in combination with an underpass for a road or a bridge placed in the deposition area. This test-set was also conducted in Model-1 by using three different volumes, V, and solids concentrations by volume, C_s. The third part presents a detailed investigation on the effects of variations in V, C_s, along with variations in GSD on the performance of the screens. The study was conducted on Model-2 and two screen lengths were investigated to understand the working mechanism and performance of the screens. A high-speed camera was used to closely study the flow behavior over the screen in which the result was discussed using PIV analysis.

Throughout the section, the tests are discussed based on variations in run-out distance, accumulation thickness on the screen, and deposition thickness and width in the deposition area.

5.2 Length and opening width investigation of screen

5.2.1 Introduction

A study conducted by Laache (2016) in Model-1 that was reanalyzed and published in Yifru et al. (2018), is presented in this section. The study investigates the optimal opening width of grids for two different screen lengths ($0.5m$ and $1.0m$). The opening widths were $2mm$, $4mm$, and $6mm$, where the maximum grain size of the solid material was $8mm$. The test-set constitutes 24 tests that were conducted using debris-flow material with C_s value of 60% and V of $50L$. There were no variations made either on V or C_s values in

this test.

5.2.2 Model set-up and test plan

The main form of Model-1 along with the details and descriptions of dimensions was given in Section 3.2, Figure 3.1. For this study, two types of screens ($0.5m$ and $1.0m$) along with their terrain replicas made from solid plates were manufactured. The placing location and configuration of the screens and plates are shown in Figure 5.1.

The tests were monitored by two flow height sensors and three cameras. The first

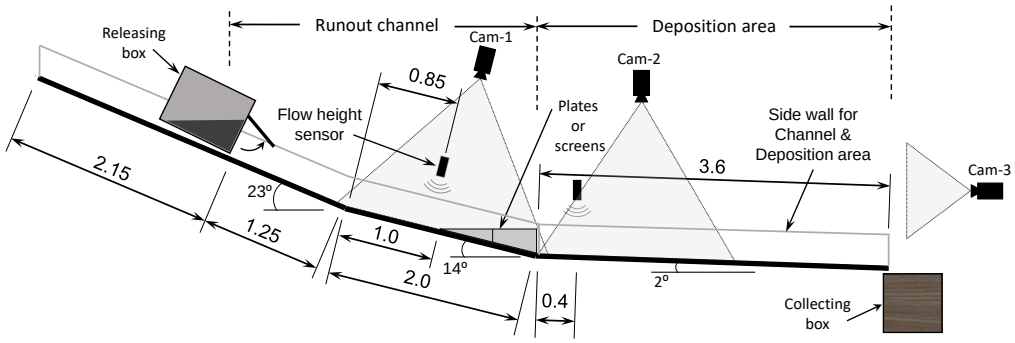

Fig. 5.1: Flume Model-1: placement of the screens and instrumentation. All linear dimension were in meters.

flow height sensor was placed in the run-out channel $85cm$ before the starting end of the screens and the second was placed in the deposition area, $40cm$ after the end of the run-out channel, to monitor the flow after the screens and during the deposition process. The videos recorded by Cam-1 were used in studying the flow front velocity and the behavior of the debris interacting with the screens. The videos from Cam-2 and Cam-3 support the evaluation of each test after the test has been conducted as well as give particular behavior of the debris-flow in the deposition area.

The debris material (solids) used for this test was a sandy soil (crushed aggregate) with a grain size property of $d_{max} = 8.0mm$, $d_{90} = 6.0mm$, $d_{50} = 1.8mm$ and $d_{10} = 0.11mm$. The GSD of the sand is given by Figure 5.2.The coefficient of uniformity was $C_u = 25$, and the coefficient of curvature was $C_c = 1.96$, which indicated that the material is well-graded. The grains density was $2.71g/cm^3$ where, throughout the tests, this value and the GSD were maintained without any significant variations.

A $100kg$ soil-water mixture was prepared by mixing $80kg$ of soil and $20kg$ of water to simulate a saturated debris-flow. The soil-water mixture corresponded to a total of $50L$ ($0.05m^3$) of fully saturated debris material with a C_s of 60%. This saturated debris

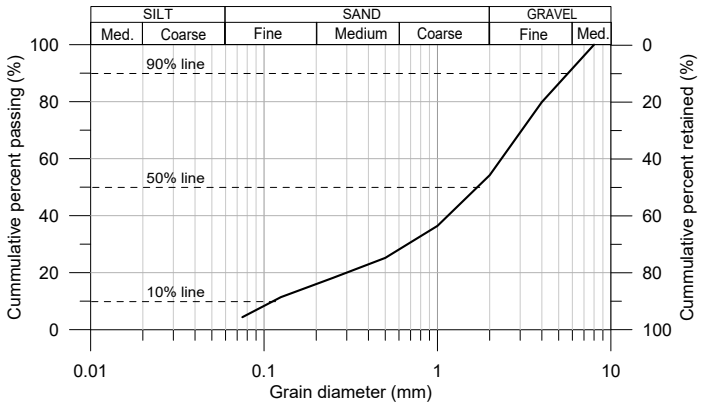

Fig. 5.2: Grain size distribution, GSD, of the test material

represents a well-developed and fast-moving debris-flow material upon release. In the experiments, the releasing mechanism simulated a dam break by releasing the whole mass at once, as the focus of the study was to investigate the behavior of a well-developed debris-flow interaction with different debris-flow screen types.

Two debris-flow screen lengths, l ($0.5m$ and $1.0m$) and three screen grid openings ($2mm$, $4mm$ and $6mm$) were chosen to investigate their respective energy dissipating potentials. The screens were made by the systematic arrangement of rectangular steel rods with a cross-section of $10mm \times 15mm$, using spacers having width, w of $2mm$, $4mm$ and $6mm$. Figure 5.3(a) shows the flume channel with the placement of the screen along with dimensions and important features of this test setup in Model-1.

The starting point of the screens, which was considered as a reference point for measuring the debris-flow's run-out distance, L_{FL}, was $2.25m$ away from the releasing box and $1.0m$ before the start of the deposition area (Figure 5.1). Figure 5.3(b) shows the details of the arrangement of the grids to construct the respective screens. In addition, two scenarios that represent only the terrain alteration of the screens were included and used as reference tests. These were made of $0.5m$ and $1m$ long solid plates in which their opening widths were referred to as zero.

The test plan along with the test names are given in Table 5.1. The 24 tests are named based on the various scenarios and are given the code *'s-l-w-n'*, where s is scenario, l is the length of a screen in m, w is the width of a single opening on a screen in mm, and n is the scenario repetition number. The opening percentage was the ratio of cumulative w to the total width of the screen.

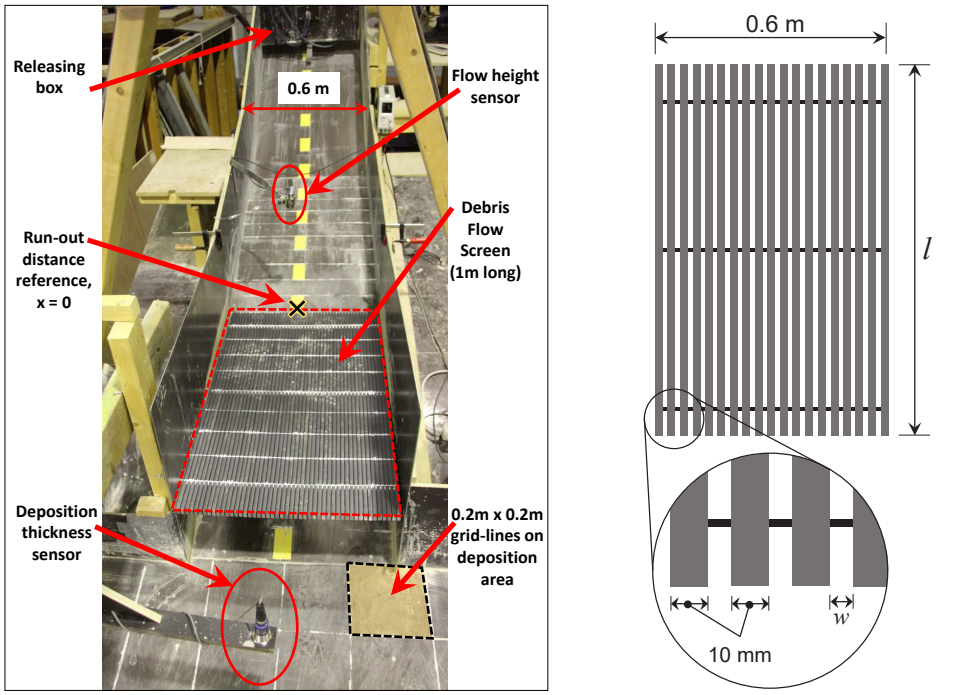

Fig. 5.3: Measurements of the model and the screen: (a) photo showing details of Model-1 with a $1m$ long screen (photo from Laache (2016)) and (b) schematic detail of screen with $l = 0.5m$ and $1.0m$ and $w = 2mm$, $4mm$, and $6mm$

Table 5.1: Test plan and description of dimensions of the debris-flow screens

Test	Test	Screen			Test	Test	Screen		
		length	opening				Length	opening	
Number	Name	[m]	[mm]	[%]	Number	Name	[m]	[mm]	[%]
T1	S-0.5-0-1				T13	S-0.5-4-1			
T2	S-0.5-0-2	0.5	0	0	T14	S-0.5-4-2	0.5	4	29
T3	S-0.5-0-3				T15	S-0.5-4-3			
T4	S-1-0-1				T16	S-1-4-1			
T5	S-1-0-2	1.0	0	0	T17	S-1-4-2	1	4	29
T6	S-1-0-3				T18	S-1-4-3			
T7	S-0.5-2-1				T19	S-0.5-6-1			
T8	S-0.5-2-2	0.5	2	17	T20	S-0.5-6-2	0.5	6	38
T9	S-0.5-2-3				T21	S-0.5-6-3			
T10	S-1-2-1				T22	S-1-6-1			
T11	S-1-2-2	1	2	17	T23	S-1-6-2	1	6	38
T12	S-1-2-3				T24	S-1-6-3			

5.2.3 Test results

For each of the 24 tests, L_{FL}, maximum width of deposition (B), maximum upstream flow height (h_{Max}), maximum accumulation thickness on the screen (t_u) and downstream at the deposition area (t_d), and average front-flow velocity at the beginning (v_A) and the end (v_B) of a screen were recorded and presented in Table 5.2. Tests from T1 to T3

Table 5.2: Summary of the test results (Based on data from Laache (2016)).

Test Number	Test Name	L_{FL} [m]	B [m]	h_{Max} [cm]	t_u [cm]	t_d [cm]	v_A [m/s]	v_B [m/s]
T1	S-0.5-0-1	2.35	0.90	3.20	3.35	1.90	2.63	2.23
T2	S-0.5-0-2	2.60	0.87	3.40	2.49	1.70	2.28	1.73
T3	S-0.5-0-3	3.05	1.12	5.40	1.44	1.60	2.00	1.80
T4	S-1-0-1	2.65	1.08	3.50	4.39	1.00	2.63	1.97
T5	S-1-0-2	2.75	1.08	4.90	2.61	0.90	2.47	1.97
T6	S-1-0-3	2.10	0.98	4.00	3.83	1.40	2.87	2.80
T7	S-0.5-2-1	1.95	0.66	3.50	7.71	1.20	3.13	2.57
T8	S-0.5-2-2	1.80	0.98	4.00	5.64	1.30	2.63	1.65
T9	S-0.5-2-3	2.28	0.90	3.20	3.81	1.30	2.93	2.37
T10	S-1-2-1	0.95	0.60	3.60	6.78	0.80	3.03	0.00
T11	S-1-2-2	0.90	0.60	3.40	5.62	0.30	-	-
T12	S-1-2-3	0.90	0.60	3.70	5.89	0.40	2.67	0.43
T13	S-0.5-4-1	2.25	1.18	3.90	5.20	2.00	3.10	2.27
T14	S-0.5-4-2	2.50	1.08	3.50	3.75	1.70	2.90	2.43
T15	S-0.5-4-3	2.95	1.02	3.90	5.36	1.60	2.77	1.83
T16	S-1-4-1	0.75	0.60	3.70	5.40	0.40	-	-
T17	S-1-4-2	1.00	0.60	3.10	4.22	0.70	2.82	0.57
T18	S-1-4-3	1.00	0.60	3.20	5.07	0.30	3.08	1.10
T19	S-0.5-6-1	2.40	0.85	4.90	6.34	1.20	2.23	1.53
T20	S-0.5-6-2	3.00	1.00	3.60	3.70	1.10	3.20	2.17
T21	S-0.5-6-3	2.50	0.70	3.40	6.17	1.30	2.77	1.63
T22	S-1-6-1	0.90	0.60	4.30	4.86	0.80	2.77	0.10
T23	S-1-6-2	0.90	0.60	3.50	4.39	0.70	2.87	0.40
T24	S-1-6-3	0.90	0.60	4.30	5.85	0.90	2.90	0.50

and T4 to T6 were the reference tests for the screens, where solid plates of $0.5m$ and $1m$ long were used, respectively. The reference tests were used as benchmarks to evaluate the performance of the debris-flow screens. The model geometry was identical in each test. Therefore, changes in the debris-flow run-out distance and flow velocity were considered to be attributed to the debris-flow screens.

Two distinguishing parts of the debris deposit were observed. The first was water mixed with very fines soil particles that continued to flow and ended up in the collecting box. The second was the solid debris that accumulated in the deposition area or on the screen. The L_{FL} and B measurements given in Table 5.2 are for the solid debris. The photos showing the final deposition shape, along with L_{FL} and B of the four representative tests are presented in Figure 5.4. This figure illustrates how the debris material flowed, spread

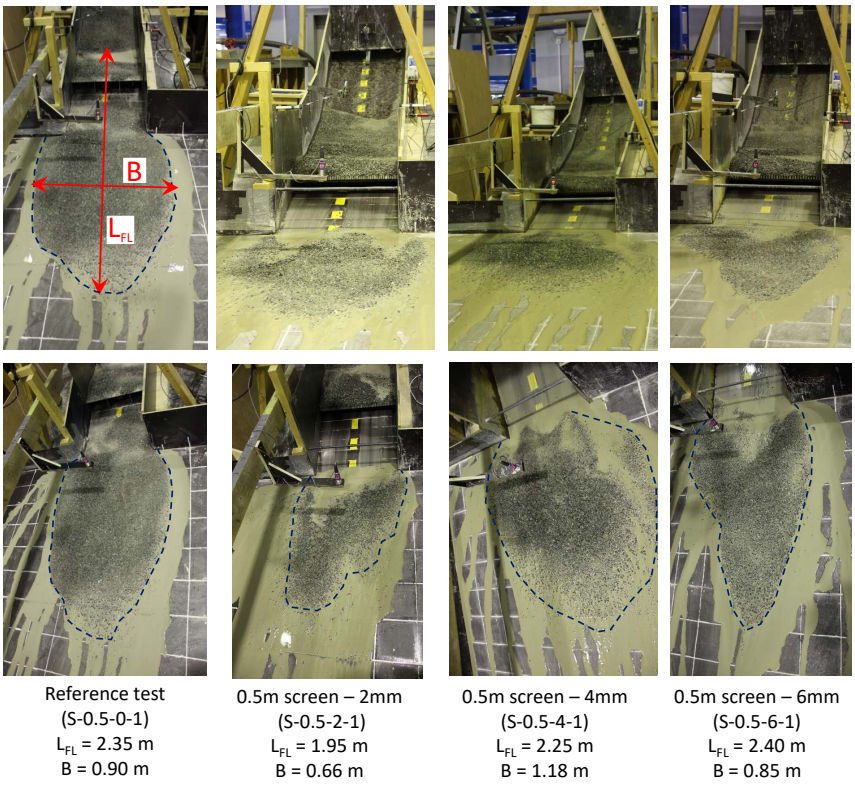

Fig. 5.4: Photos showing deposition pattern and run-out distance of selected tests from $0.5m$ long cases (Photos from Laache (2016)).

and segregated in the deposition area when using the $0.5m$ long plate and screens.

5.2.4 General observation of the results

The reference test results from T1 to T6 will be used as a benchmark for discussing the performance of the debris-flow screens. The average L_{FL} for the $0.5m$ long reference test (T1–T3) was $2.67m$, with a standard deviation of $0.35m$, while for the $1m$ long reference test (T4–T6), the average L_{FL} became $2.5m$, with a standard deviation of $0.35m$. The resulting L_{FL} was found to be shorter for the longer topography-alteration length than for the shorter one.

The average value of the maximum deposition width, B for the $1m$ long reference test, was found to be slightly wider than that of the $0.5m$ long reference test. A wider B value can be an indication of slower flow front in the deposition area, which forced the flow tail to spread sideways, causing a shorter L_{FL}. Similarly, a lower average upstream accumulation, t_u, and a higher average downstream deposition, t_d, were observed in the case of the $0.5m$ long plate than for the $1m$ long plate. The average t_u for both reference tests can be seen in Figure 5.7 between $t = 4s$ and $t = 5s$.

In both cases, the flow velocities were decreased at the end of the plates when compared to the velocity at the beginning of the plates. The average flow front velocity decrease was observed to be in the order of 15%, which can be considered as a channel alteration contribution.

5.2.5 Run-out distance

The recorded L_{FL} were plotted against the opening width of the screen for each length in Figure 5.5(a). The plot shows the average L_{FL} along with the lower- and upper-bound values represented by error bars.

The average L_{FL} when using the $0.5m$ long screen was observed to decrease to $2.01m$

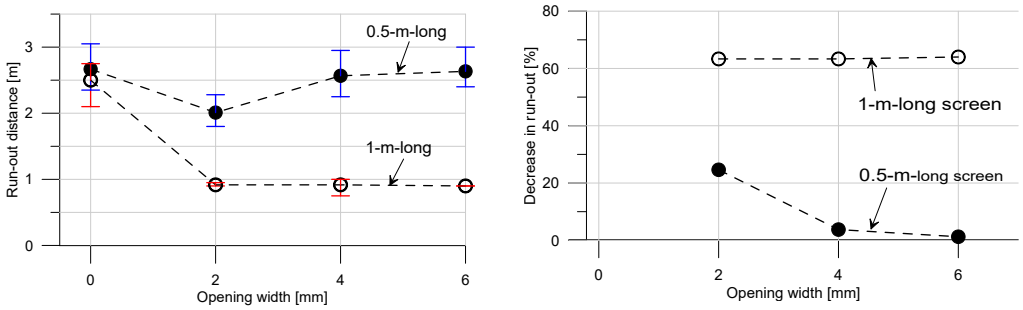

Fig. 5.5: Run-out distance results: (a) variation due to l and w variations, and (b) percentage reduction from the respective reference tests

with the provision of a $2mm$ opening width. However, the average L_{FL} showed no significant change from the reference test when using $4mm$ and $6mm$ screen opening widths (T13–T15 and T19–T21). The respective average L_{FL} were $2.57m$ and $2.63m$, which were not far from the reference average L_{FL} of $2.70m$. One possible reason for these relatively longer L_{FL} was that the sufficiently fast liquid and solid fractions filtered through the wider screen openings mixed with the material that jumped over the screen.

The $1m$ long screen was observed to be just long enough to contain the entire debris-flow volume, as the observed L_{FL} were relatively consistent with an average value of around $0.9m$ for all the three opening widths. All were $\leq 1.0m$, i.e., the total screen length. However, some solid fractions that had filtered through the $4mm$ and $6mm$ screens were observed in the deposition area.

The most effective screen size can be assessed by evaluating the percentage reduction of the L_{FL}, as shown in Figure 5.5(b). This percentage reduction was calculated using the average L_{FL} in comparison with the average L_{FL} of the respective reference test. The $2mm$ opening width reduced the average L_{FL} observed in the reference tests of $1m$ and $0.5m$ by 63% and 25%, respectively. For the $0.5m$ long screen, this was the highest percentage reduction on the L_{FL}. However, the percentage reduction in the average L_{FL} for the $4mm$ and $6mm$ opening widths in the $0.5m$ long screen case were less than 4% and 1.3%, respectively. The reason for these small percentage reductions was the result of the fast-moving water and soil fractions passing through the screen and mixing with the debris that jumped over the screen to travel longer.

For the $1m$ long screen, the percentage reduction remains almost the same for all opening widths. The resulting percentage reduction when using the $2mm$ opening width for both screen lengths was seen to indicate an interesting relationship between the w and the $d_{50} = 1.8mm$ of the testing material used.

A similar experiment done in Kyoto, Japan, by Kim (2013), showed assessment of

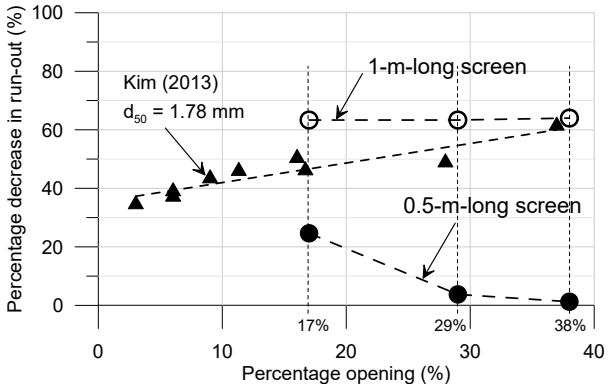

Fig. 5.6: Comparison of percentage opening versus percentage run-out distance reductions with data from Kim (2013).

the effectiveness of the screen-type debris-flow countermeasure based on the percentage

of the ratio between the cumulative opening width and the total width of the screen. The screen was, at the same time, used as a deposition area for the tested material, which makes it suitable to compare it with the $1m$ long screen used in this study. Therefore, the data from Kim (2013) with $d_{50} = 1.78mm$ was plotted against the data from the present study and given in Figure 5.6.

The blocking width of the screens, in this study, was constant ($10mm$ wide) while Kim (2013) varied the blocking width along with the opening width, which might explain the slight variations in the results when it comes to the low-percentage openings of 17% and 29%. The $0.5m$ long screen case was not comparable, as the debris material run beyond the screen.

5.2.6 Flow height, accumulation, and deposition thicknesses

From the upstream flow height sensor, variations in the average flow heights with time, for all the tests, are given in Figure 5.7. For each test, two peak values can be observed from a

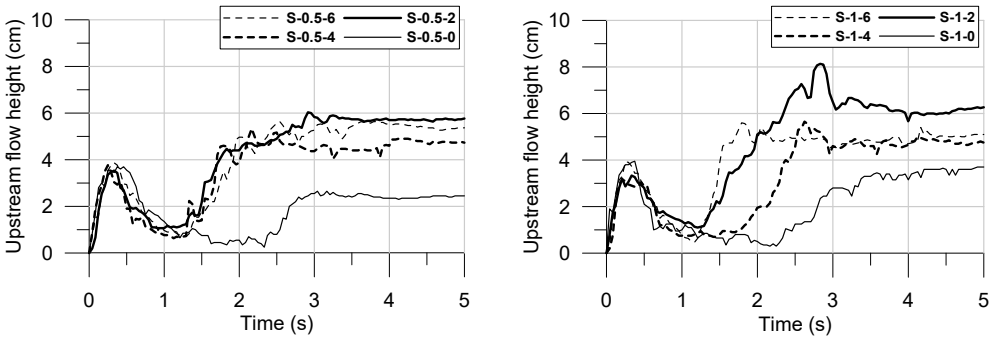

Fig. 5.7: Average flow height variation with time at the upstream of the countermeasures when using: (a) a $0.5m$ long plate and screen, and (b) a $1m$ long plate and screen

respective plot. The first peak represents the h_{Max} while the second, a nearly horizontal line, represents t_u, which are given in Table 5.2. The h_{Max} recorded at the upstream sensor was observed to be uniform. The sensor was placed just before the screen start and the h_{Max} was not affected by the type of countermeasure used. So, the uniformity (with few outliers) indicates that the 24 tests were more or less consistent and give an average h_{Max} value of around $3.5cm$. In some tests, the h_{Max} was found to be high due to some saturated frozen (lumped) masses that were not fully mixed with the rest of the fluidized debris.

In discussing the t_u Figure 5.7 shows that the flow height increases after the $t \approx 1.5s$

mark. This was due to the damming effect from the decelerating flow front. As the flow proceeds, the amount of dry flow front increases, as well as the grains' resistance through grain-contact friction and grain-bed friction, while the flow tail still pushes from behind. However, after a short time ($\sim 1s$), the major part of the flow front stops completely and acts as a dam to halt the entire flow tail, including the remaining liquid. After the debris mass deposited on the debris screen, the liquid held at the back of the debris-dam continued to drain slowly through the mass and the screen. In some tests, a turbulent flow behind the debris-dam was observed, and one of them is visible on the plot of (S-1-2) in Figure 5.7(b).

After the flow ended, the same sensor measured the t_u, which was affected by the performance of the plate/screen. Although this was not a direct measure on the accumulated thickness on the plate/screen, t_u can give an indication of the amount of material that was retained. The resulting average t_u vary between $4.7cm$ and $6.1cm$ for both screen lengths, whereas for the reference tests, the average t_u was recorded as $2.5cm$ and $3.6cm$ for the $0.5m$ and $1m$ long plates, respectively. The average t_u almost doubled from their respective reference test results when using the $2mm$ opening width, while a relatively lesser increase was seen when using $4mm$ and $6mm$ opening widths.

In comparing the observed t_d, the $1m$ long screens gave an average t_d thickness of less than $1cm$, as there was no significant debris mass in the deposition area. When using the $0.5m$ long screen, the lowest average t_d were observed during the $2mm$ and $6mm$ opening widths, while a similar average t_d was recorded as that of the reference test when using the $4mm$ opening width. Measuring t_d only at one location for such wide deposition area might not be represent the entire area. However, it can indicate, to some extent, the amount of material accumulated on the screen indirectly. In general, all opening widths from the $1m$ long screen, and the $2mm$ and $6mm$ opening widths from the $0.5m$ long screen were found to reduce the downstream deposition thickness by up to 33%.

5.2.7 Flow velocity and energy dissipation

The flow front velocity was tracked and measured by analyzing the Cam-1 using the method explained in Section 3.2.6. In many of the test cases, the flow front velocity was non-uniform across the width of the plate or the screens because of flow surges. As a result, the average flow front velocity at any point along the flow direction was calculated by considering velocities at the left, center, and right of the flow as shown in Figure 5.8. These average values are presented as v_A and v_B in Table 5.2 representing the average approach and the average exit-velocities to and from a debris-flow screen, respectively.

These six representative velocity plots are from both lengths of screens and each opening widths. The three velocity profiles of each plot show how the flow front varies across the

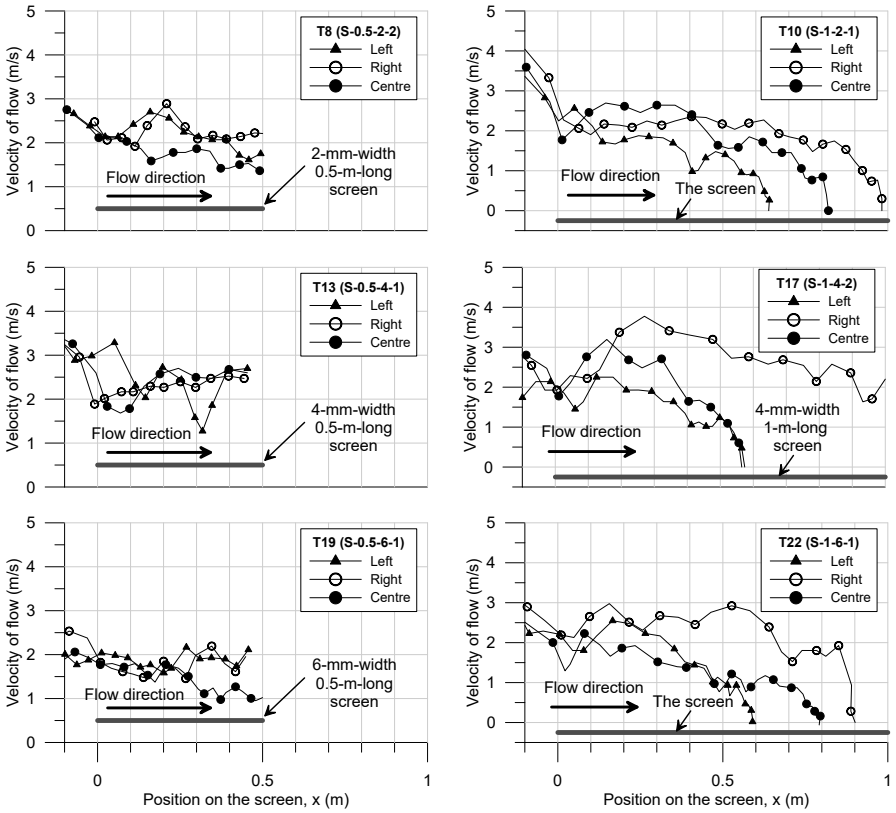

Fig. 5.8: Representative plots of the flow front velocities at the left, center, and right sections of the channel

width of the screens. However, except for such an outlier like in the case of $1m$ long screen with $w = 4mm$, the flow velocity reduction capability of the screens was clearly seen. In the case of $l = 1m$ screen, all velocities, except the outlier, became zero before reaching the end of the screen.

The average flow velocities recorded approaching, v_A, and exiting, v_B, the respective plate or screen are given in Table 5.2. The average v_A was consistent and ranges between $2.65m/s$ and $2.95m/s$, except some outliers observed in T3 and T20 with very low and very high velocities. This variation could be a result of different surges observed in different sections of the flow channel, as shown in Figure 5.8.

Although average velocity reductions were observed due to the terrain alteration in the reference tests and the water-draining effect in the screens, the value of v_B was affected by small surges of highly saturated debris mass. Some of the v_B values of the $1m$ long

screen shown in Table 5.2 are non-zero; this was the effect of a small flow front part, either in the left or right of the channel, which shoots until the end of the screen. In the cases of T17 and T18, the average exit-velocity value was as high as $1.1m/s$. However, the average exit velocities when using $0.5m$ long screen vary, and this variation was analyzed based on the energy dissipation.

Energy dissipation, E_D, was another aspect for evaluating the effectiveness of the screens in mitigating debris-flow. From energy line equation, the energy head between the start and end of the screens were compared. Because of the horizontally aligned provision of the debris-flow screens and an extremely low-pressure head compared to the velocity head, the energy dissipation between the beginning and end of each screen will be assessed only by the velocity head term i.e. $v^2/(2g)$ which gives a simplified relation given in Equation 5.1.

$$E_D \approx 1 - (\frac{v_B}{v_A})^2 \tag{5.1}$$

The results are plotted in Figure 5.9(a) which shows the average percentage energy dissipated in each case. In both the $0.5m$ and $1m$ long screen cases, the major amount of energy was dissipated when using the $2mm$ opening width. When using the $4mm$ and

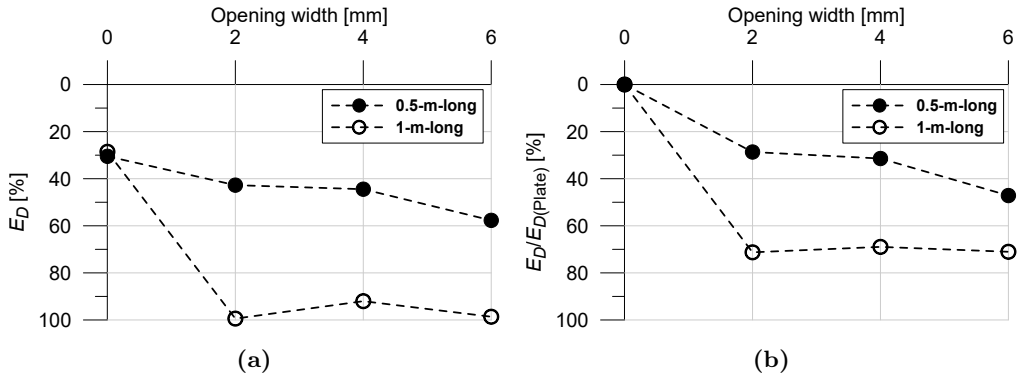

Fig. 5.9: Percentage energy dissipation with respect to: (a) initial energy at start of screen, and (b) energy dissipation by terrain alteration represented by the solid plate

$6mm$ opening widths in the $1m$ long screen, no significant increase in energy dissipation was observed beyond what was obtained by during the $2mm$ opening width. However, a gradual increase in energy dissipation was observed when the $0.5m$ long screen was used. In the case of the $4mm$ opening width and $1m$ long screen, the energy dissipation was seen to be small and out of the data trend. This could mainly be a result of the outlier flow velocity observed on the right side of the screen (as seen in Figure 5.8).

Generally, the average percentage energy dissipation presented in Figure 5.9(b) implies that, the contribution of only filtering out the liquid part in reducing the energy in the $1m$ long debris-flow screen was up to 70%, while in the $0.5m$ long screen, it varies between 25% and 50%.

5.2.8 Segregation of the debris material

Soil samples from the deposition area and from the top of the countermeasures were collected to study the segregation or change in grain size distribution of the original debris-flow material. The selected tests were T7 (S-0.5-2-1), T13 (S-0.5-4-1) and T19 (S-0.5-6-1).

The samples that were taken from the top of the screen were collected from the end of the screens because the material deposited in the middle or at the back of the screen was affected by the debris-tail or subsequent flow surges, while the front deposit was interacted fully with the screen and was considered less affected.

A sample GSD plot (Figure 5.10) from T7 (S-0.5-2-1) shows that the material accumulated on the screen was coarser than the original material, while finer materials were observed in the deposition area. Table 5.3 shows a comparison using the d_{50} values of

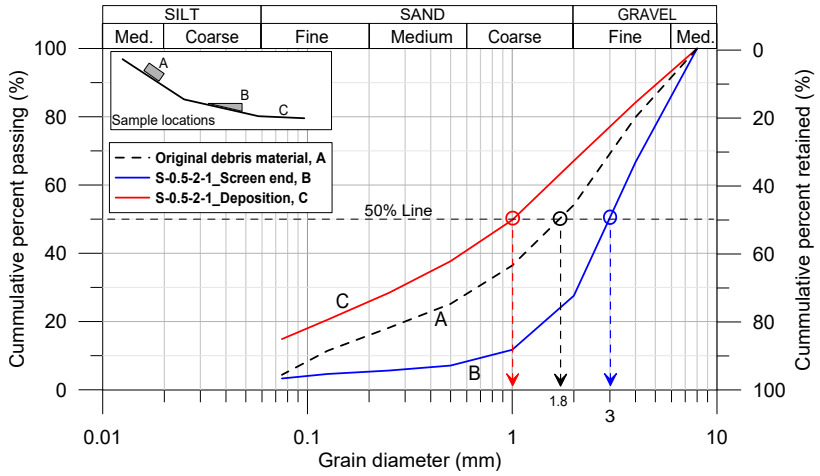

Fig. 5.10: Change in grain size distribution, GSD, of the debris-flow material on the screen and at the deposition area

the tested samples. The values given in the table demonstrate that the screens can retain the major coarse part of the debris-flow. This also shows that debris-flow screens were not only breaking the flow but also have the potential to retain coarser debris that might have significant destructive powers.

Table 5.3: Values of d_{50} for the samples at deposition and on the $0.5m$ long screen

Test number	Scenario	d_{50} screen end $[mm]$	d_{50} deposition area $[mm]$
T7	S-0.5-2-1	3.0	1.0
T13	S-0.5-4-1	4.2	1.4
T19	S-0.5-6-1	2.7	1.6

In general, the performance of the debris-flow screen with respect to the opening width can be discussed in light of the soil material grain size property, d_{50}. The d_{50} of the test material was $1.8mm$. The screens were observed to retain the major part of coarser soil grains that were greater than $d_{50} = 1.8mm$ while the materials in the deposition area exhibit lower values as shown in Table 5.3. In the case of the $4mm$ and $6mm$ opening widths, the d_{50} values in the deposition area were found to be greater than that of the $2mm$ cases. Generally, the d_{50} values in the deposition area increases with increase of the opening width which can be taken as a decrease in performance of retaining the coarser proportion. This can also indicate that the mass in the deposition area was not only the soil that was pushed over the screen but also some soil grains that were filtered through the openings along with the muddy fluid. On the other hand, the samples taken from the screens end show varying d_{50} values although they were all greater than $1.8mm$. The drop in d_{50} value when using the $6mm$ opening width might be resulted from the escaping of soil grains through the opening. This phenomenon was also observed in the case of the $1m$ long screen as well, where some soil grains escaped through the $4mm$ and $6mm$ screens.

If not for the friction between the soil grains, $6mm$ and $4mm$ opening widths could allow 94% and 80% of the debris solids, respectively, while the $2mm$ opening width could allow 54% of the debris solids through the openings of the screen. This gives another perspective on why the first two allowed some soil fractions and were less effective than the latter. This might be one important observation that relates the debris material property, d_{50}, with the opening width on the performance of debris-flow screens. As Nisimoto et al. (1994) reported the grain size distribution of the debris material in the Kamikami Valley screen mitigation work, the d_{50} of the debris material varied between $60mm$ and $250mm$, which can be said that closely related with the opening width of the screen, i.e., $0.2m$. Thus, this observation during the use of the $2mm$ opening width in both screen lengths may contribute to the possible use of d_{50} as a design criterion for the optimal opening width of screens.

5.2.9 Summary

In this section, the effects of the length and opening width of debris-flow screen variation in its performance based on the resulting dissipation of the flow energy was assessed. The tests were conducted using a constant debris-flow volume of $50L$ with solids concentration of 60%. The assessment was done by comparing the screen variations with the resulting run-out distances, flow velocities, flow heights and deposition thicknesses. The $1m$ long debris-flow screen was found to be just long enough to halt the entire debris-flow volume regardless of the opening widths. However, the $4mm$ and $6mm$ opening widths, which were widths greater than the mean grain size, d_{50}, of the debris-flow material, were seen to allow some solid fractions through their openings along with the draining water. Although the $1m$ long screen stopped the entire flow on each case, most debris-flow in nature were continuous mass flows that may not be contained by one screen. Therefore, the results from the $0.5m$ long screen that reduced the mobility of the debris-flow was equally interesting in showing the behavior of screen-type countermeasures. A general observation about the $0.5m$ and $1m$ long debris-flow screens show that the run-out distance and flow velocity decreases with an increase in screen length. However, among the three screen opening widths, the $2mm$ ($\approx d_{50}$) opening width was found to be optimal regarding reducing both the run-out distance and flow velocity of the debris-flow. A further increase in the opening width exhibits a relatively small improvement in the reduction of run-out distance and flow velocity. In addition, higher accumulation thicknesses on the screens and lower deposition thicknesses at the downstream were observed in using the $2mm$ opening width than the other two.

5.3 Combination of screen with guide-wall and underpass

5.3.1 Introduction

This test set was conducted on Model-1 after finding the $2mm$ opening width was the optimal opening for the material with $d_{50} \approx 2mm$. In this test, two screen lengths ($0.25m$ and $0.50m$ long with $2mm$ openings) were evaluated along with their respective topographical contributions represented by solid plates. These two lengths were selected in order to evaluate the flow reduction capacity of screen in a continuous debris-flows after the $1m$ long screen was seen to accumulate almost the entire volume in the previous study in Section 5.2. The screens were also assessed in combination with guide-wall and underpass. The guide-wall and underpass (referred here after as underpass) can be considered as a safe passage for debris-flows under an elevated road near at the foot of a mountain. The test-set was categorized in to two: tests conducted with underpass and tests conducted without underpass. Variations were made on volume, V and solids concentrations by volume, C_s.

5.3.2 Model set-up and test plan

The main form of Model-1 with its plan was given in Section 3.2. For this test, the modified schematic representation of the model is given in Figure 5.11. Impact measuring pillar and the underpass were added. In this section, the comparison of the results will be

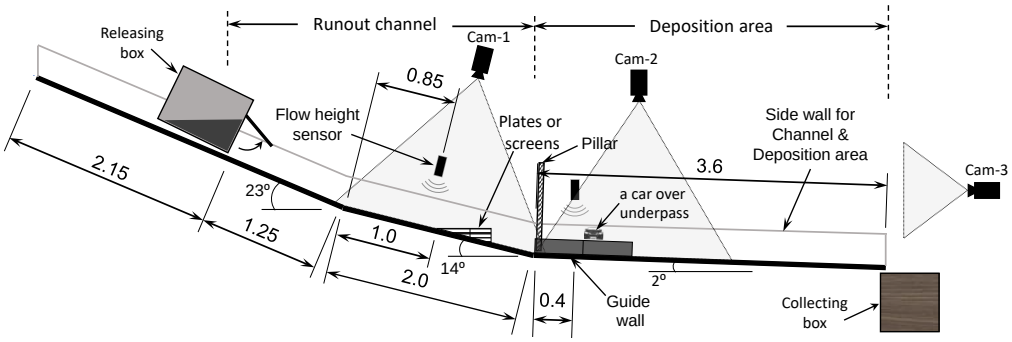

Fig. 5.11: Flume Model-1 with screens and underpass placement and instrumentation. All linear dimensions are in meters

based on the run-out distance, L_{FL}, value measured from the starting of the deposition area unlike the previous study which was started at the beginning of the screen. Details of the placement of the $0.50m$ long screen in the run-out channel and the guide-wall and underpass in the deposition area is given in Figure 5.12. The height of both guide-wall

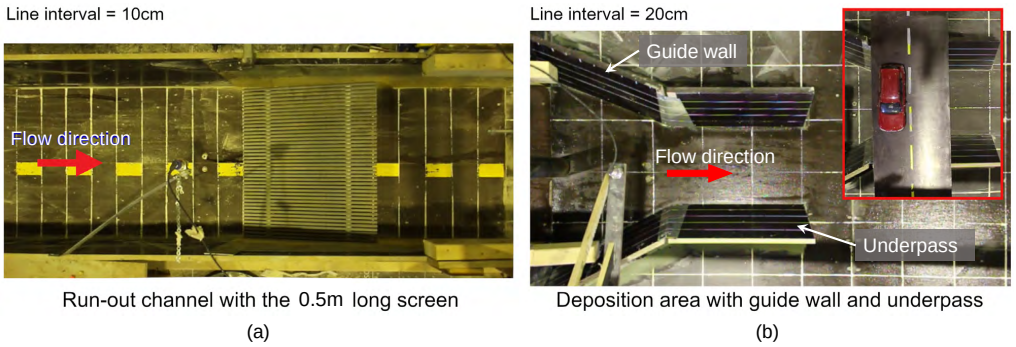

Fig. 5.12: Plan view photos showing details of placement of: (a) the screen and (b) the guide-wall and underpass. A road and a car representation over the underpass is also given at the top right.

and underpass was $0.25m$ with opening width of $0.30m$ for the underpass. As the parts that make up the guide-wall placed on the model, they are placed in such away that they are impermeable for both the fluid and solid parts of the debris-flow using a rubber membrane placed in their bottom while fastening them on the deposition area.

For this study, 72 tests were conducted from June 2017 to October 2017 on Model-1. The debris material, crushed aggregate, was the same as the one described and used in the previous section (Section 5.2.5) with a slight difference in the GSD curve (as seen in Figure 5.13). Due to the limited amount of debris material, it was compulsory to reuse the

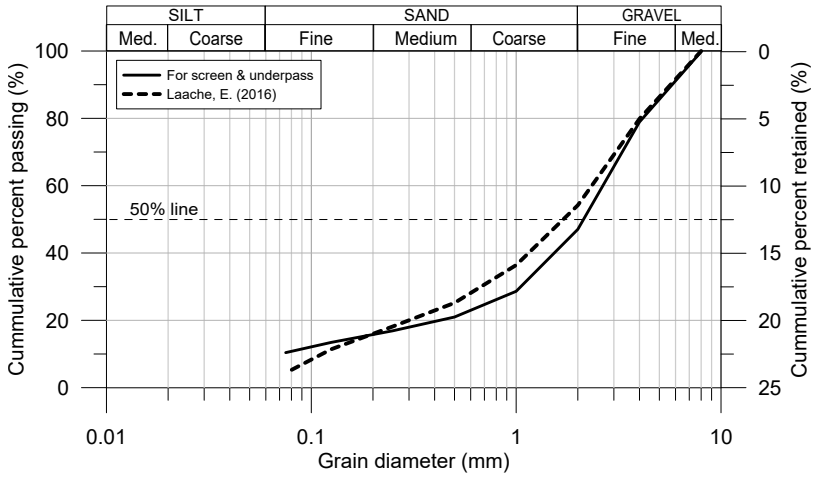

Fig. 5.13: GSD of the crushed aggregate used for this study

collected debris-flow after each test. The detailed test procedure was given in Section 3.2.

The test-set plan is given in Table 5.4. Three combination of V and C_s (i.e. V1C1, V2C2, and V3C3) were used on each category (with or without underpass) which makes a total of 72 tests. The three V values were V1 = $49.4L$, V2 = $40.1L$, and V3 = $29.4L$ along with the three C_s of C1 = 60%, C2 = 55%, and C1 = 50%. For simplicity, we shall refer the three V values as $50L$, $40L$, and $30L$, respectively. Each category has two scenarios: S1 and S3 for tests without underpass, and S2 and S4 for tests with underpass. S1 and S2 were reference tests from each category with which the results of S3 and S4 were compared. Each test can be referred by a test name or a test number. The test number is unique for each test (that uses the combination of V, its index, and sequential numbers) whereas test name, which mainly describes the scenario and topographic condition, is common for the three group of tests with V and C_s variations. The test number and test name are given in the first and second column of Table 5.4, respectively. In numbering the test, only letter 'V' was used without the letter 'C'. This is because there were only three debris-flow variations (V1C1, V2C2 and V3C3) that 'V and 'C' carry same indices. Therefore, V1T1 refers to the first test using V1C1.

Table 5.4: Test plan describing dimensions of screens and presence of flow impact force measurement

Test Number*	Test Name	Underpass	Force pillar	Screen	
				length [cm]	opening [mm]
V#T1	S1_r1	—	—	—	—
V#T2	S1_r2				
V#T3	S1_r3				
V#T4	S2_r1	✓	✓	—	—
V#T5	S2_r2				
V#T6	S2_r3				
V#T7	S3-50-0_r1	—	—	50	0
V#T8	S3-50-0_r2				
V#T9	S3-50-0_r3				
V#T10	S3-25-2_r1	—	✓	25	2
V#T11	S3-25-2_r2				
V#T12	S3-25-2_r3				
V#T13	S3-50-2_r1	—	✓	50	2
V#T14	S3-50-2_r2				
V#T15	S3-50-2_r3				
V#T16	S4-50-0_r1	✓	✓	50	0
V#T17	S4-50-0_r2				
V#T18	S4-50-0_r3				
V#T19	S4-25-2_r1	✓	✓	25	2
V#T20	S4-25-2_r2				
V#T21	S4-25-2_r3				
V#T22	S4-50-2_r1	✓	✓	50	2
V#T23	S4-50-2_r2				
V#T24	S4-50-2_r3				

* The symbol '#' refers to indices used to describe V and C_s

5.3.3 Test results

All of the 72 test results are listed in Table 5.5 with their respective test names. In this table, only L_{FL} and maximum flow impact force, F_{Max} are given. The rest of the results are given in Appendix A1. To ensure repeatability, each scenario with a type of

countermeasure was conducted three times and is described by the repetition references: r1, r2, and r3 as suffixes. In discussing the results, both average values of these three repetitions and representative individual test results are used.

Table 5.5: Summary of the test results: run-out distance and maximum flow impact force

	V1C1			V2C2			V3C3		
Test Name	Test Nr.	L_{FL} [m]	F_{Max} [N]	Test Nr.	L_{FL} [m]	F_{Max} [N]	Test Nr.	L_{FL} [m]	F_{Max} [N]
S1_r1	V1T1	2.28	—*	V2T1	2.90	—	V3T1	2.80	—
S1_r2	V1T2	2.80	—	V2T2	3.20	—	V3T2	3,25	—
S1_r3	V1T3	3.00	—	V2T3	3.60	—	V3T3	3.50	—
S2_r1	V1T4	2.88	17.66	V2T4	2.95	20.50	V3T4	2.50	10.55
S2_r2	V1T5	2.83	20.81	V2T5	3.00	14.13	V3T5	2.40	7.06
S2_r3	V1T6	3.02	17.37	V2T6	3.10	18.08	V3T6	2.20	9.91
S3-50-0_r1	V1T7	1.56	10.84	V2T7	2.30	—	V3T7	2.20	—
S3-50-0_r2	V1T8	1.64	13.83	V2T8	2.30	—	V3T8	2.20	—
S3-50-0_r3	V1T9	1.56	10.31	V2T9	2.40	—	V3T9	1.90	—
S3-25-2_r1	V1T10	1.21	—	V2T10	1.20	2.70	V3T10	1.10	3.06
S3-25-2_r2	V1T11	1.08	6.83	V2T11	1.25	3.59	V3T11	1.30	8.90
S3-25-2_r3	V1T12	0.70	1.02	V2T12	1.30	3.63	V3T12	1.30	5.71
S3-50-2_r1	V1T13	0.70	—	V2T13	0.60	2.26	V3T13	1.40	0.73
S3-50-2_r2	V1T14	0.59	—	V2T14	0.80	1.65	V3T14	1.30	1.40
S3-50-2_r3	V1T15	1.08	—	V2T15	1.00	1.05	V3T15	1.30	0.82
S4-50-0_r1	V1T16	2.06	13.26	V2T16	2.10	13.52	V3T16	1.70	4.76
S4-50-0_r2	V1T17	1.90	28.97	V2T17	2.55	8.71	V3T17	2.00	4.91
S4-50-0_r3	V1T18	2.06	3.41**	V2T18	2.50	12.94	V3T18	2.10	6.47
S4-25-2_r1	V1T19	1.70	23.62†	V2T19	1.45	9.07	V3T19	1.30	3.16
S4-25-2_r2	V1T20	1.82	5.70	V2T20	1.80	5.91	V3T20	1.40	3.84
S4-25-2_r3	V1T21	1.55	6.80	V2T21	1.80	10.67	V3T21	1.30	5.66
S4-50-2_r1	V1T22	1.57	17.66†	V2T22	1.20	1.96	V3T22	2.20	0.64
S4-50-2_r2	V1T23	1.20	6.68	V2T23	1.40	2.60	V3T23	1.80	1.05
S4-50-2_r3	V1T24	1.90	8.76	V2T24	1.60	1.21	V3T24	1.80	0.78

* Tests where flow impact force was not measured.

** The main flow missed the pillar.

†Values from fluidized, fast flows jumping over the countermeasure.

Although the initial V and C_s were carefully controlled and thoroughly mixed before starting each test, there had always been some debris remained in the releasing box with varying amount from test to test. This limitation was found unavoidable regardless of the different mixing technique and hand mixers used. Therefore, the remaining mass from each test was measured and actual released V and C_s were calculated. This was done by measuring the box along with the debris mixture before and after releasing. The average water content of the remained mass in the box was also determined to evaluate the remaining water. Then these remaining solid mass and water masses are subtracted and the actual V and C_s were computed. The following plots in Figure 5.14 give the actual released V and C_s compared with the starting values.

Tests conducted by V1C1 were seen to show bigger variations and larger reduction

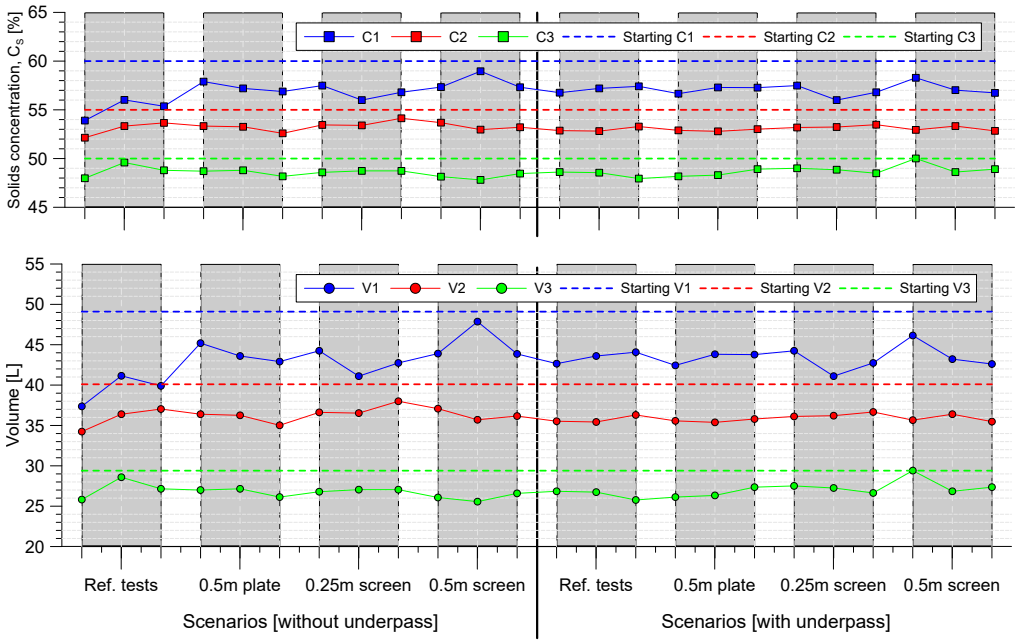

Fig. 5.14: The released V and C_s for each test along with the respective starting (initial) V and C_s.

in the calculated values from the initial V and C_s. This was mainly because of its lowest water content (higher C_s) that made it challenging to keep the entire $50L$ in suspension at a time. However, for V2C2 and V3C3 with relatively higher proportion of water, the resulting V and C_s were deviated uniformly by a relatively uniform amount. One can see that it was easier to handle and work with lower V and C_s during the mixing and releasing which result in the lowest deviation.

5.3.4 Run-out distance and deposition shape

The results are presented based on the two main categories referring the presence and absence of the underpass. The L_{FL} of these two categories are presented in Figure 5.15. In the first category shown in Figure 5.15(a), L_{FL} was seen to decrease with the provision

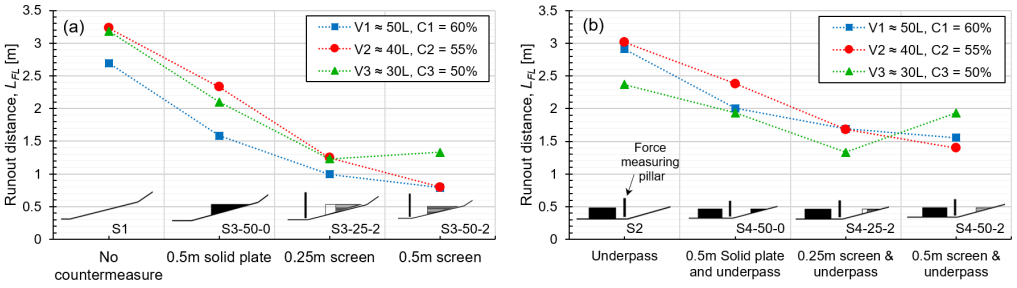

Fig. 5.15: Average run-out distance: (a) without underpass and (b) with underpass. S1 and S2 were reference tests for the respective categories.

of screens and its terrain alteration. The solid plate provision (described here as terrain alteration) has contributed to 45% to 65% of the L_{FL} decrease resulted from the provision of the $0.25m$ long screen. An out-of-trend behavior was seen when a $0.5m$ long screen used during V3C3 where lowest V and C_s were used. The L_{FL} increased due to the water drained through the screen and pushed few soil grains that were jumped over the screen. The deposition shape was witnessed to be very scattered and spread slowly. In addition, despite the long run-out, the deposition thickness was thinner compared to what was seen in the case of the $0.25m$ long screen.

When using the underpass (as seen in Figure 5.15(b)), the corresponding L_{FL} values registered without the underpass were further decreased due to accumulation of the debris material in the underpass and within the guide-walls. In addition, the guide-wall and underpass structures have contributed in the reduction of the debris-flow mobility by reducing the speed and safely guiding it through.

From Figure 5.15 and the comparisons, V2C2 has given the longest run-out in most of the scenarios of each category. In this V and C_s combination, their combined contribution on the resulting L_{FL} was found to be the highest in most of the cases except the V3C3. The L_{FL} was observed to reduce during the use of the lowest amount of V (V3C3) and the lowest water amount (V1C1).

The deposition overview photos were used to plot the deposition shapes. This photos were first corrected by GIMP (The GIMP Development Team 2019) for the perspective distortions and then digitized using Grapher (Golden Software, Inc. 2014). The digitized

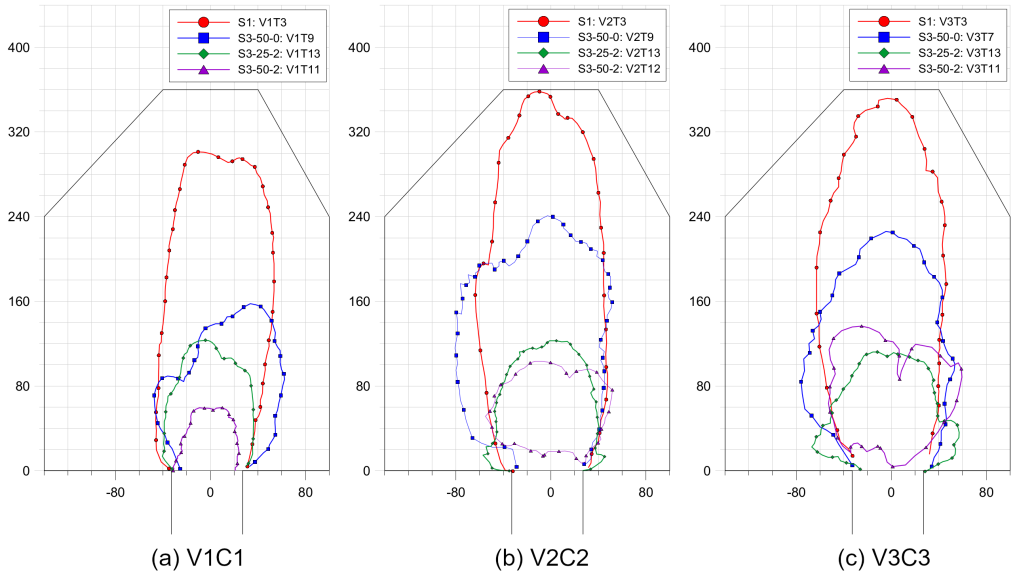

Fig. 5.16: Deposition shape of tests without underpass for: (a) V1C1, (b) V2C2, and (c) V3C3. All dimensions are in *cm*.

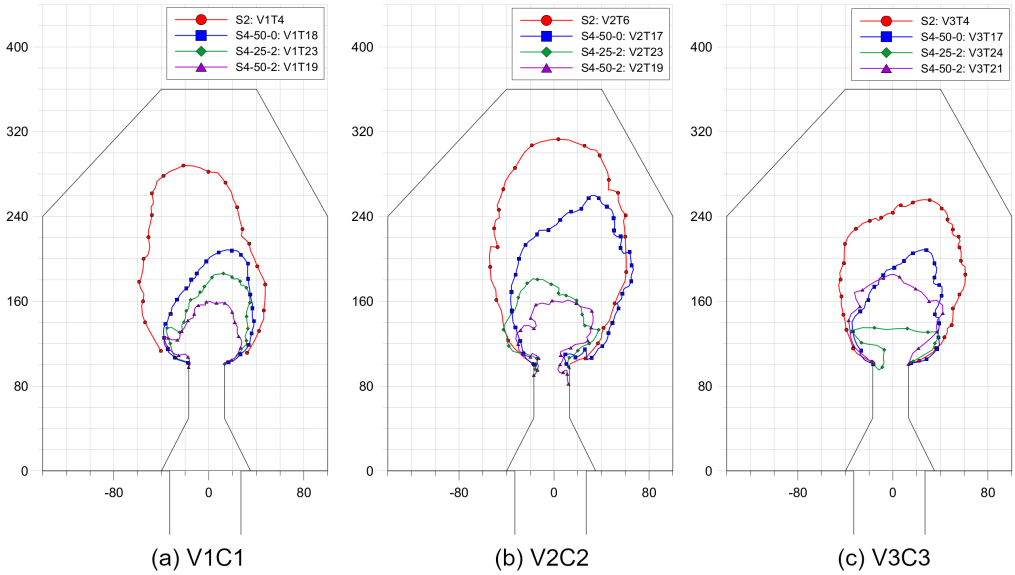

Fig. 5.17: Deposition shape of tests with underpass for: (a) V1C1, (b) V2C2, and (c) V3C3. All dimensions are in *cm*.

deposition shapes are plotted and given by Figure 5.16 and Figure 5.17. Figure 5.16 shows the deposition shape from the tests without the underpass where the deposition shapes when underpass was used is given by Figure 5.17. All scenarios are included in each graph to compare between the types of countermeasures.

In Figure 5.16(c) and Figure 5.17(c), the L_{FL} is observed to be longer when $0.5m$ long screen was used than when $0.25m$ long screen was used in the case of V3C3. In addition, for other cases like in V2C2 with and without underpass (Figure 5.16(b) and Figure 5.17(b)), the additional L_{FL} reduction in using the $0.5m$ long screen is observed to be small when compared with the result of the $0.25m$ long screen. However, there was a significant deposition thickness difference. Although the L_{FL} looks longer and the deposition spread looks wider in case of $0.5m$ long screen, the deposition thickness was much thinner than in the case of the $0.25m$ long screen (Figure 5.18 and 5.19).

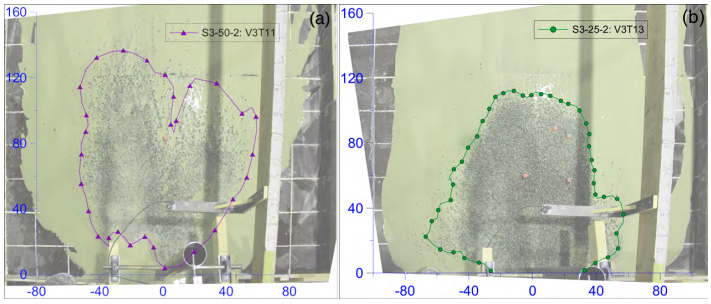

Fig. 5.18: V3C3 Deposition shape comparison between the result from: (a) S3-50-2, and (b) S3-25-2. All dimensions are in *cm*.

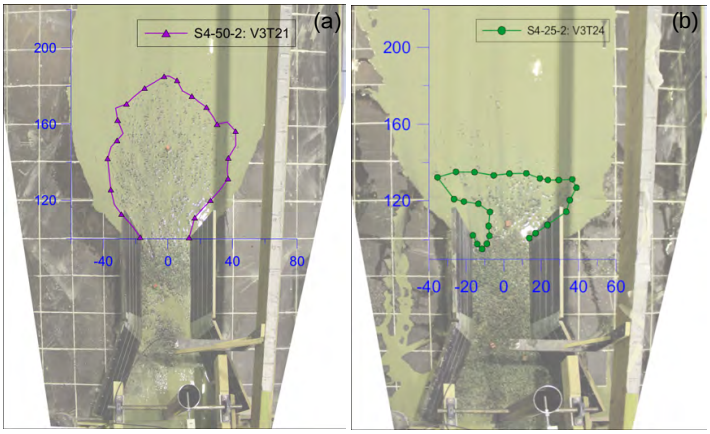

Fig. 5.19: V3C3 Deposition shape comparison between the result from: (a) S4-50-2, and (b) S4-25-2. All dimensions are in *cm*.

During the use of the $0.5m$ long screen, it was observed that small amount of material jumped over the screen and was washed and pushed further by the percolating water in the deposition area. On the other hand, more debris material jumped over in the case of the $0.25m$ long screen which can reduce the pushing energy of the subsequent water. Figure 5.18 and 5.19 can also explain the out-of-trend data points observed in the L_{FL} plots given in Figure 5.15(a) and (b) when using V3C3.

5.3.5 Downstream deposition thickness

The downstream deposition thickness, t_d, was measured by the downstream flow height sensor. The location of this sensor falls inside the guide-wall of the underpass for scenarios S2 and S4. The t_d generally decreases with an increase in C_s. The only outlier case was

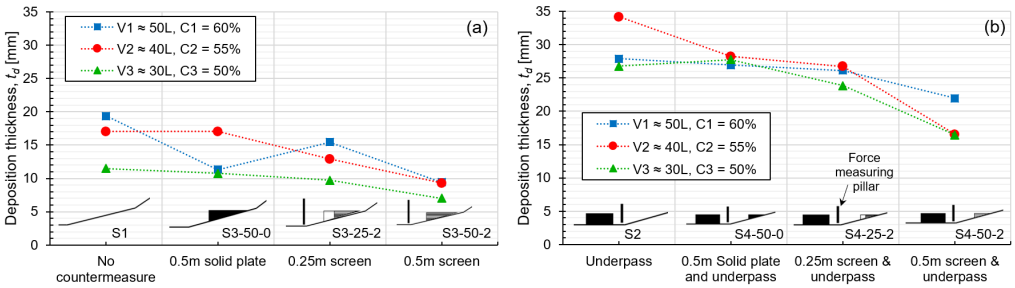

Fig. 5.20: Downstream deposition thickness, t_d, variations of each scenario: (a) without underpass and (b) with underpass

the test by $0.5m$ solid plate and V1C1 (as seen in Figure 5.20(a)) that was affected by the use of force measuring pillar unlike in the other two cases (V2C2 and V3C3). This resulted in a lower thickness reading as the flow height sensor was situated next to the pillar along the flow direction.

In the first category (as seen in Figure 5.20(a)), the main cause of t_d decrease was seen to be the provision of the type of countermeasure. As more and more debris retained over a given countermeasure provided in the channel, fewer material crosses the channel resulting in thinner deposition. Although the measurement was taken in a single point, it shows the debris reducing effect of the screen in a similar way as the L_{FL} reduction. As a result of longer L_{FL}s and larger deposition shapes for this category, the t_d was thinner and varies between $7mm$ and $20mm$. Highest C_s with the help of the largest V value, resulted in a relatively thicker deposits for each scenario followed by V2C2 and V3C3, respectively.

In the second category (as seen in Figure 5.20(b)), the underpass which has a guide-wall significantly influenced the resulting t_d values. The guide-wall prohibited the side way spread of material that forced deposition of at least $15mm$ thick. Because of this,

the t_d was seen to show almost no variation based on C_s and V except one outlier case for V2C2 of scenario S2 that was affected by lumps of debris in two of the three repetition tests. However, the trend of decreasing the t_d from no use of countermeasure in the channel to using plate, $0.25m$ long screen, and $0.5m$ long screen can be seen. In general, the t_d varies between $16mm$ and $34mm$ when using the underpass.

5.3.6 Accumulation thickness and pattern

The accumulation thickness on a screen varies widely based on its length as well as the V-C_s used. Generally, the accumulation thickness was higher in the mid and tail sections of the screen while it was lower near its front end. In the case of V1C1, the maximum accumulation thickness was recorded anywhere on the screen while the accumulation pattern at the mid-way of the screen across the channel was recorded in the cases of V2C2 and V3C3. Since the screen was situated before the underpass, the accumulation thickness was not affected by the use of underpass and therefore the result is not discussed based on the two categories.

For V1C1, the maximum accumulation thickness was recorded to be between $3cm$ and $4.5cm$ for the solid plate case, between $6.5cm$ and $8.5cm$ for $0.25m$ long screen, and between $7.5cm$–$10cm$ for $0.5m$ long screen test cases. The maximum accumulation thickness was increased up to 3 times than the maximum thickness seen in the reference test for $0.5m$ long screen case whereas it was increased around 2.5 times for the $0.25m$ long screen.

In V2C2 tests (as seen in Figure 5.21(a)), the accumulation thickness on the $0.5m$ long screen was not uniform across its width for some of the tests. However, due to the shorter

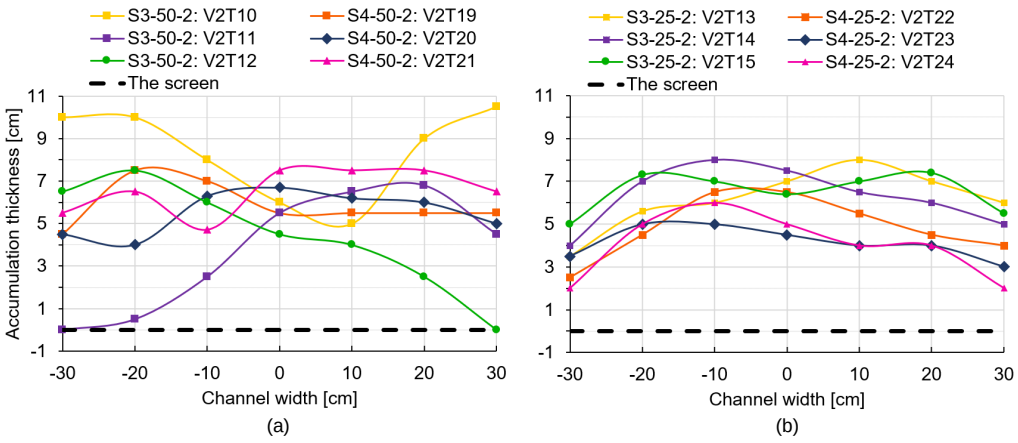

Fig. 5.21: Accumulation pattern for V2C2 tests on: (a) $0.5m$ long screen and (b) $0.25m$ long screen.

screen length of the $0.25m$ long screen, the flow could not get much interruption across the width that resulted in a nearly uniform accumulation thickness (as seen in Figure 5.21(b)).

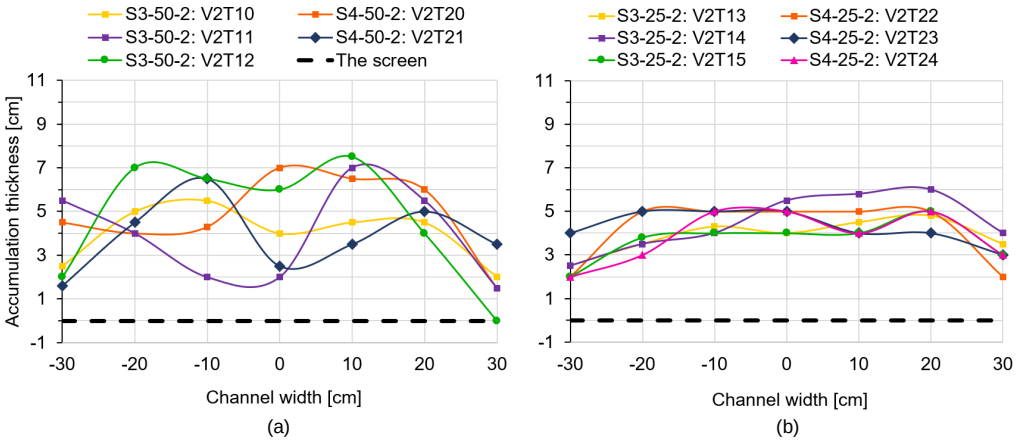

Fig. 5.22: Accumulation pattern for V3C3 tests on: (a) $0.5m$ long screen and (b) $0.25m$ long screen.

In the reference tests made with a solid plate, the accumulation thickness varied between $2.5cm$–$3cm$. Comparing the maximum thicknesses with the thickness of the reference tests, it showed an increase up to 4 times during the use of $0.5m$ long screen. When using the $0.25m$ long screen, the maximum increase was observed to be around 3 times higher than what is seen during the reference tests.

For V3C3 tests (as seen in Figure 5.22), similar, non-uniform accumulation, pattern was observed across the width when using the $0.5m$ long screen while uniform accumulation thickness was seen for $0.25m$ screen cases. Generally, the accumulation thicknesses were lower than what were seen in the cases of V2C2 which can be attributed to the presence of more water (high C_s) and smaller starting V. In addition, the small amount of V made the flow concentrate in one part of the channel where it resulted in large variation in accumulation pattern in case of $0.5m$ long screen. When the maximum thickness increase was evaluated using values of the reference tests that vary between $2cm - 3.5cm$, the $0.25m$ and $0.5m$ long screens resulted in 3 and 3.5 times thicker accumulations, respectively.

In the case of the $0.5m$ long screen, a relatively unsaturated portion of the flow was observed to slow down over the screen giving thicker accumulation while a water rich portion flow with a relatively faster speed giving thinner accumulations. However, in the case of $0.25m$ long screen, a more uniform depositions were observed as the major portion (both saturated or unsaturated) of the flow continue over it due to its shorter screen length.

An observation of the maximum accumulation thickness for all the three cases show that the peak accumulation decreases with a decrease in both V and C_s. More material was accumulated over the screen when high C_s and larger V were used. The individual contribution of V and C_s on the accumulation thickness over a given screen will be looked at in Section 5.4.

5.3.7 Run-up height on the guide-wall

The guide-wall which was the extension of the $0.30m$ wide underpass has a total height of $0.25m$. The maximum run-up height of the flow on this guide-wall was measured for all the four scenarios. A compiled plot of the run-up heights is presented in Figure 5.23. The

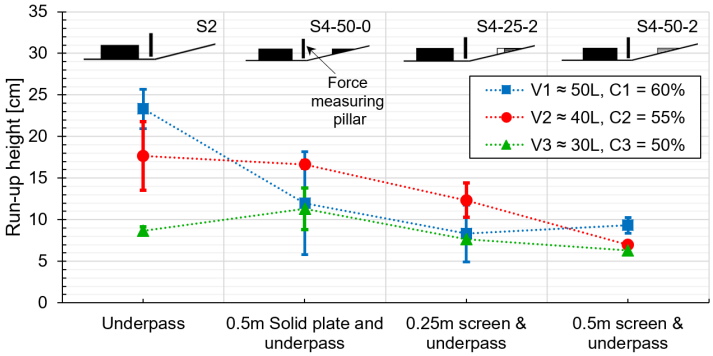

Fig. 5.23: Flow run-up height on the guide-wall of the underpass

plot gives the average values along with the standard deviations from the test repetitions.

The run-up height is, generally, seen to get reduced based on the scenario changes from solid plate to the $0.25m$ long screen, and from the $0.25m$ long screen to the $0.5m$ long screen as shown in Figure 5.23. The force measuring pillar that was placed at the beginning of the guide-wall was seen to have minor contribution on the run-up height. This effect was not looked at separately, and because the pillar was used for all the tests, the run-up height is discussed based on only the scenarios and the V-C_s variations.

The high run-up heights in V1C1 and V2C2 tests at the reference tests (S2) were seen to get reduced consecutively by the solid plate, the $0.25m$ long screen, and the $0.50m$ long screen. In V1C1, although the V was the highest, the run-up was seen to considerably decreased by the countermeasures due to its low water content (high C_s). In the case of the $0.50m$ long screen, the slight increase in the average run-up was due to the turbulent flow created by the percolated water and the material jumped over the screen near the guide-wall. In the case of V2C2, the run-up height decrease was gentler manner than V1C1 case in regard to the three scenarios. However, the jumping over the plate and the

0.25m long screen was seen to affect the run-up height.

During V3C3 tests, the relative decrease in V gives the flow a less energy to interact with the guide-wall. The low run-up height during the reference test can be seen as example. However, when the solid plate was introduced, the flow jump produced a relatively higher run-up height on the guide-wall. This behavior was also observed in V2C2.

The run-up height on the guide-wall was seen to increase with increase of V and C_s when we look at the reference tests (S2) only. However, when the countermeasures were used, the determining debris-flow characteristic looks like the C_s with a possible contribution from the V. Tests with more water (C_s less than or equal to 55%) could not significantly lower the run-up height observed in their respective S2 tests. This could be attributed to the turbulence created after the debris material jumps over the given countermeasure in addition to getting mixed with the percolated water in the cases of the screens.

5.3.8 Impact force of the flow

The flow impact force was measured by the circular pillar that was placed at the end of the run-out channel (as seen in Figure 5.11). This study plans to investigate the potential and performance of screens in reducing the impact force of the debris-flow. At the same time, the flow impact force dependence on $V - C_s$ variation is looked at. The measured impact forces from the three repetitions of each test were averaged and presented in the plot that is given by Figure 5.24. The presence or absence of the underpass has no or

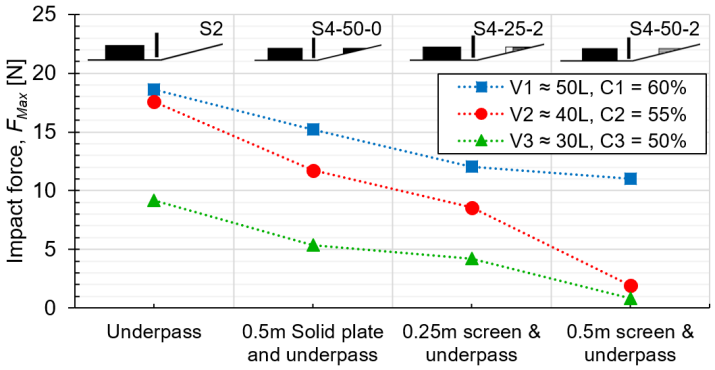

Fig. 5.24: Average maximum flow impact force of each scenario (results from tests with underpass).

minimal effect on the measured force as the pillar was situated before the underpass. However, as given in Table 5.5, impact measurement was not conducted in some of the tests where the underpass was not used and therefore, only the results from the tests with

underpass are plotted in Figure 5.24.

Maximum impact forces that were recorded in each respective $V - C_s$ tests were observed to be the highest. On each case, this maximum impact force was observed to decrease progressively with the provision of plate, $0.25m$ long screen, and $0.5m$ long screen. Despite some high values (as seen in Table 5.5) in some of the tests, the average impact force show the trend of increased flow hindering potentials of the screens used. The case during the use of $0.5m$ long screen in V1C1 test showed high average value which was affected by a single test that resulted in 3 times higher value.

The magnitude of the recorded force was seen to be affected by $V - C_s$ variation as well. The case where large V with high C_s (V1C1) results in the highest flow impact force in each scenario and vice versa. This indicates that both increase in V and decrease in water content, with more viscous type flow characteristic, may result in higher impact force.

Another perspective to see the contribution of $V - C_s$ variation on the resulting impact

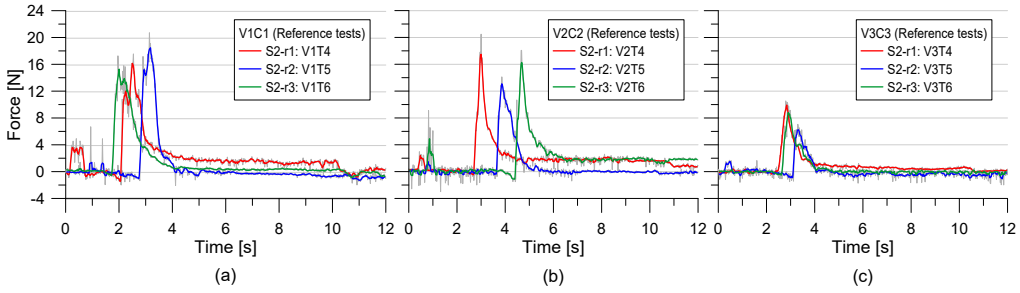

Fig. 5.25: Flow impact force from three representative reference tests: (a) V1C1, (b) V2C2, and (c) V3C3

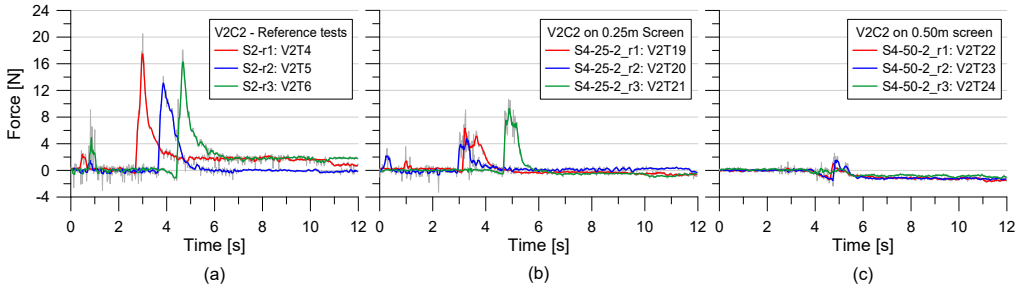

Fig. 5.26: Flow impact force V2C2 tests with: (a) reference, (b) $0.25m$ long screen, and (c) $0.5m$ long screen

force was by plotting the individual impact force measurements. Three representative plots are selected and presented from the two reference tests (S1 and S2) in Figure 5.25. The slight decrease in the average impact force with the decrease from V1C1 to V2C2 and the significant decrease with decrease from V1C1 to V3C3 is also seen in this plot.

To show the effect of providing screens for reducing the mobility of debris-flow through the measured flow impact force, Figure 5.26 is provided for comparing the results from V2C2 representative tests. The three plots represent results conducted in the reference, $0.25m$ long screen, and $0.5m$ long screen tests. It shows the progressive reduction of the flow impact force because of the types of countermeasures used. The entire results from V1C1, V2C2, and V3C3 that included the terrain contribution is given in Appendix A2.

5.3.9 Summary

In this section, the effect of screen length variation along with $V - C_s$ variations were studied in two categories based on an underpass presence. Providing a screen was seen to reduce all the adverse characteristics of the debris-flow in all $V - C_s$ variations with the effect being pronounced when using $0.5m$ long than $0.25m$ long screen. Run-out distance, downstream depositions thickness, run-up height on the guide-wall, and flow impact force were reduced with increasing screen length. This was accompanied by the retention of more debris material behind and on a screen, that was seen in the increasing accumulation thicknesses with increase in screen length.

As the changes in V and C_s were applied simultaneously in this study, only their combined effects on the debris-flow behavior was looked at. These effects were shown during the reference tests and the varying interaction behavior of the debris-flow with the screens and the guide-wall. The run-out distance, downstream deposition thickness, and run-up height values were seen to be affected by both V and C_s of debris-flow in $V - C_s$ variations. These characteristics could result in lower values when V decreases. However, the V decrease was accompanied by C_s decrease (increase of water), which result in the debris-flow mobility increase and the values of the results. In many of the tests, V2C2 was seen to result in the highest mobility. This might indicate that debris-flows with $C_s \approx 55\%$ were more mobile. On the other hand, the impact force was seen to decrease with decrease of V and C_s, and vice versa. In addition, for each $V - C_s$ variation, these debris-flow characteristics, generally, have decreasing trends with increasing screen length which shows the potential of a screen in reducing debris-flow mobility.

In this study, the use and performance of underpass in safely guiding the debris-flow was shown by the deposition shape and run-up height. Some of the run-up heights were seen to hit the entire guide-wall height. For such cases and areas with large debris-flows

where the design might require big underpasses for the elevated road or any infrastructure, the advantage of installing screens in the debris-flow path in reducing the resulting impact force and run-up height was also demonstrated.

5.4 Working mechanism of screens

5.4.1 Introduction

The study in this section looks at the working mechanism of screens on Model-2 along with evaluating variations in screen length and debris-flow parameters. Plexi-glass channel wall and plexi-glass screens were used while the flow was closely monitored using a high-speed camera. In this section, only the screen was investigated as a countermeasure without the underpass. From the debris-flow regime study conducted on Model-2 (as given in Section 4.2), selected combinations of GSD, V, and C_s that exhibit close flow regime behavior with real debris-flows were used for conducting the tests on two screen lengths ($0.25m$ and $0.50m$ long with $2mm$ opening width). The results are evaluated using image analysis techniques in addition to the comparisons made on the run-out distance, downstream deposition and accumulation thicknesses.

5.4.2 Model set-up and test plan

The model set-up given in Figure 5.27 shows flume Model-2 after it was modified for this test set. The rectangular impact measuring pillar was installed as shown in the figure whenever it was needed. All the basic details of Model-2 including the rectangular impact measuring pillar can be referred from Section 3.3.

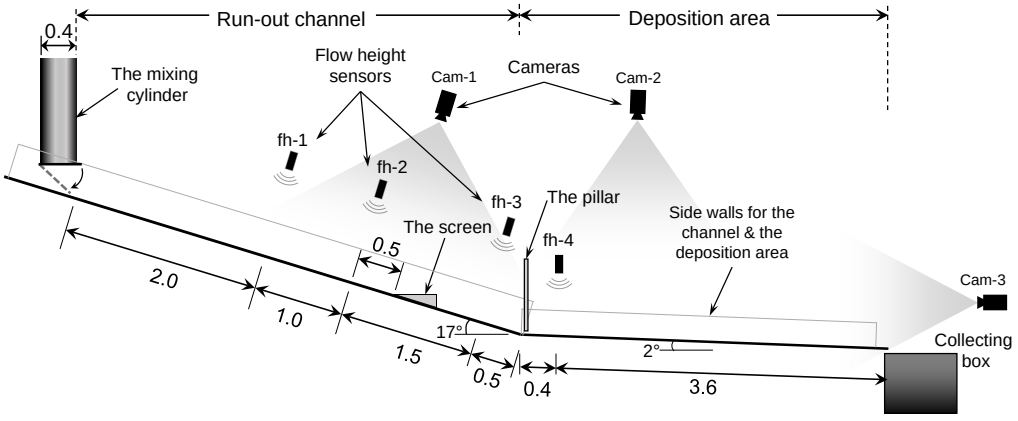

Fig. 5.27: Flume Model-2 with screen placement and instrumentation. All linear dimension are in meters

For this test-set, the selected GSDs were G1 and G2, with different combinations of V and C_s as given in Table 5.6. A total of 38 tests were conducted between July and August of 2018. Out of these test, 13 of those were repetition and impact force determination tests that are not shown in Table 5.6. In this study, in addition to investigating the screen working mechanism and screen length, it was attempted to show the effect of cross-combination of V and C_s that could not be shown in the previous Section 5.3. In these tests, the values of V were: V1 = $25L$, V2 = $30L$, and V3 = $35L$. Similarly, the values of C_s were given as C1 = 60%, C2 = 55%, and C3 = 50%.

Flow impact force measurement was also taken using a $25mm$ wide rectangular pillar for

Table 5.6: Test plan showing list of tests conducted for screen mechanism study

	Test scenario (Screen length - Screen opening width)				
Material Type	Reference 00-0	$0.25m$ plate 25-0	$0.25m$ screen 25-2	$0.5m$ plate 50-0	$0.5m$ screen 50-2
G1V1C1	✓	—	—	—	✓
G1V1C2	✓	—	—	—	✓
G1V2C1	✓	—	—	—	✓
G1V3C1	✓	—	—	—	✓
G2V1C1	✓	✓	✓	✓	✓
G2V1C2	✓	✓	✓	✓	✓
G2V1C3	—	—	—	—	✓
G2V2C1	✓	✓	✓	✓	✓
G2V3C1	—	—	—	—	✓

each test scenario. Identical but separate tests were conducted to measure impact force as the pillar affects the L_{FL} measurements. The L_{FL}, downstream deposition thickness, t_d, and accumulation thicknesses on the screens were also recorded.

5.4.3 Test results

The resulting L_{FL} for both G1 and G2 tests were presented in Table 5.7. Recall that G2 has 10% more fines by weight than G1. General comparison between each scenario on the resulting L_{FL} show that having less finer materials has resulted in comparably shorter L_{FL}. The percentage reduction in L_{FL} when compared with the respective reference test conducted with no countermeasures ranges between 55% and 70% for increasing V while the minimum value reduces even further to 50% when C_s decreases to C2 = 55%. The maximum percentage reduction in L_{FL} from G2 tests was around 47% which shows that the screen performs most effectively in debris-flows with lower fines content. The screen performance for higher fines content is discussed below through G2 tests.

Table 5.7: Run-out distances from the screen tests conducted on Model-2

Material	Run-out distance, L_{FL} [m]					Reduction w.r.t 00-0 [%]			
Type	00-0	25-0	25-2	50-0	50-2	25-0	25-2	50-0	50-2
G1V1C1	2.09	—	—	—	0.95	—	—	—	54.5
G1V1C2	2.72	—	—	—	1.35	—	—	—	50.4
G1V2C1	2.69	—	—	—	0.90	—	—	—	66.5
G1V3C1	2.79	—	—	—	0.84	—	—	—	70.0
G2V1C1	2.86	2.59	2.18	2.10	1.61	9.4	23.8	26.6	43.7
G2V1C2	3.94	3.40	2.99	2.73	2.43	13.7	24.1	30.7	38.3
G2V1C3	—	—	—	—	2.78	—	—	—	—
G2V2C1	3.35	2.83	2.40	2.12	1.76	15.5	28.4	36.7	47.5
G2V3C1	—	—	—	—	2.35	—	—	—	—

5.4.4 Effect of debris-flow composition on the run-out distance

To compare between the tests conducted using the G2 material, the L_{FL} corresponding to each scenario is plotted and given in Figure 5.28. This L_{FL} plot is given along with

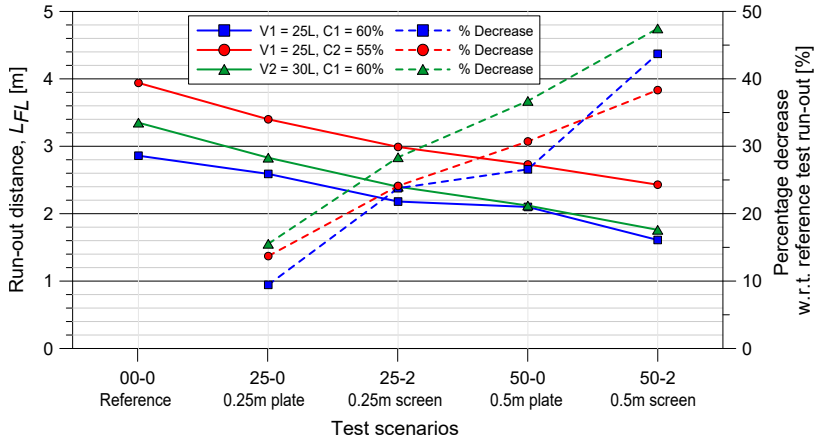

Fig. 5.28: The G2 run-out distances along with their percentage run-out reduction with respect to their respective reference tests

the percentage reduction with respect to the reference test for each test. The L_{FL} was seen to vary based on the water content (C_S) more than on the V. This can be seen by comparing G2V1C1 test set with the other two. When C2 was used (decrease in C_s) without changing V, the L_{FL} has increased by almost twice of the increase when V2 was used (increase in V) at constant C_s. This tends to show that the C_s was the major contributor of the merged effect of $V - C_s$ on the L_{FL} of tests conducted using Model-1

presented in Section 5.3.4.

The percentage reduction with respect to the respective reference test gives an interesting relationship between the use of screens and water content of the debris-flow. Although a decrease in C_s resulted in a larger increase in L_{FL} than an increase in V, the calculated run-out percentage reduction in decreasing C_s from C1 to C2 has remained almost the same. However, in increasing V from V1 to V2, the run-out percentage reduction was found to increase in almost all scenarios of screens. Therefore, for an increase in V, the screens were seen to reduce more percentage of the reference L_{FL} than for a decrease in C_s. It was also observed that the water percolating through the screens has contributed to the increase in L_{FL} when high water content (low C_s) was used.

5.4.5 Accumulation and downstream deposition thicknesses

The accumulation thickness can be another measure to evaluate the performance of screen-type countermeasures and can be used as a validating figure to the L_{FL} results discussed in Section 5.4.4. Although the accumulation thickness varies in different sections of the screens, accumulation shapes along a section profile parallel to the flow direction were found to be similar and a representative photo is given in Figure 5.29. It has more or

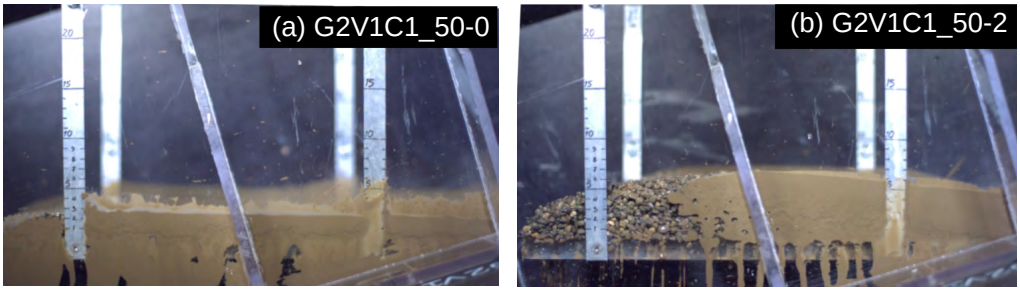

Fig. 5.29: Accumulation shape of representative G2V1C1 tests from: (a) $0.5m$ long solid plate and (b) $0.5m$ long screen

less uniform maximum accumulation on most of the screen section and behind it over the inclined channel section while it has a rapidly decreasing shape on the front part of the screen. Therefore, the maximum accumulation thickness value was collected and discussed in relation to GSD, V, and C_s variation for different screen scenarios. The accumulation shape will be discussed in detail along with the PIV analyses of velocity profile over the screen in Section 5.4.7.

From the uniform accumulation area, maximum accumulation thicknesses from the G2 tests were collected and plotted in Figure 5.30. The accumulation thicknesses recorded in the G2V1C1 tests were considered as reference to evaluate the effect of increasing the

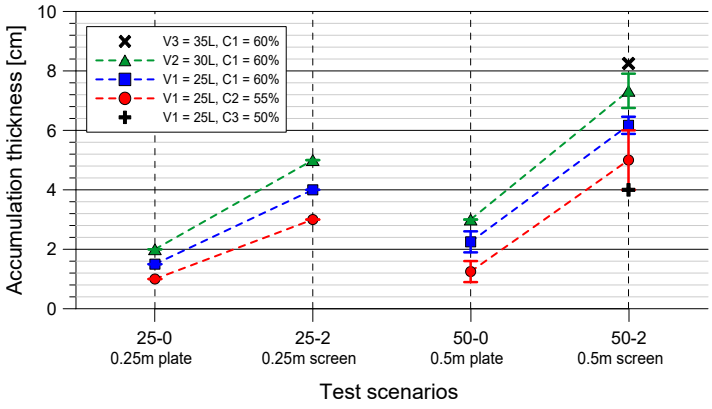

Fig. 5.30: Maximum accumulation thicknesses for G2 tests

V and decreasing C_s. The accumulation thickness increases with increase in V and it decreases with decrease in C_s. In decreasing C_s, the addition of more water makes the flow more mobile giving the debris relatively less time to interact with the screen. In addition, the subsequent water rich flow (surge) was seen to eroding the slowed down and accumulated mass contributing to the decrease in the final thicknesses. These increase and decrease in accumulation thicknesses with respective increase in V and decrease C_s were found to be analogous to the decrease and the increase in L_{FL} shown in the previous section (as seen in Figure 5.28).

From the additional tests conducted on the $0.5m$ long screen using G2V1C3 and G2V3C1, further increase only in V (G2V3C1) increases the resulting accumulation thickness to $8.25cm$. Similarly, further decreasing only in C_s (G2V1C3) (addition more water) decreases the accumulation thickness to a value around $4cm$. The reference test selected, i.e. G2V1C1, has accumulation thickness of around $6cm$ as shown in Figure 5.30. In comparing the accumulation thickness within each individual debris composition selected, the amount of change in accumulation thickness as a result of change in V was less than the amount of change due to change in C_s. This can be shown by the percentage increase in thickness with reference to the thicknesses on the respective solid plates. In G2V1C1 and G2V2C1, 64% and 60% more mass accumulated over the screen than on the solid plate, respectively. However, in G2V1C2, up to 75% more mass was observed to get retained on the screen than the respective solid plate. This relative higher percentage increase was contributed from the very small accumulation thickness in the reference test.

The downstream deposition thickness, t_d was measured at a single point using flow height sensor (fh-4) $40cm$ away from the end of the channel (as seen in Figure 5.27). The sensor measurement gives the final t_d at a single point that might not be a representative thick-

ness to the entire deposition area. However, it can gave some indications when it was looked along with the L_{FL}. The collected measurements are plotted in Figure 5.31 com-

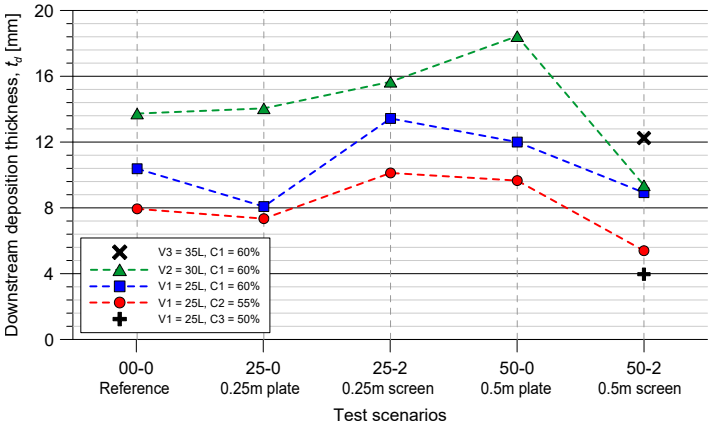

Fig. 5.31: Downstream deposition thickness, t_d, from G2 tests

paring the different scenarios with variation in V and C_s.

The presence of additional water facilitated easy spread and fast movement of the debris that resulted in thinner t_d. The additional tests conducted on the $0.5m$ long screen are also plotted in Figure 5.31. Effect of further increase in V (G2V3C1) seen to increase the t_d while further water content increase (decrease in C_s) results in thin t_d.

The effect of the scenario variation on the t_d is discussed along with the corresponding L_{FL} results given in Figure 5.28. The $0.25m$ long plate was seen to result in almost similar thicknesses as the reference tests. This was because of the low flow breaking potential of the $0.25m$ long plate that result in a similar flow behavior of in the deposition area. On the other hand, the $0.25m$ long screen and $0.5m$ long solid plate were seen to reduce the flow mobility which result in the deposition of the material that has passed over them near the end of the run-out channel. The deposited debris show short L_{FL} that resulted in a thicker deposition around the sensor location. In the last scenario where the $0.5m$ long screen was used, the t_d was seen to decrease along with a reduction of L_{FL}. Although there was some debris material jump over the screen like the other cases, the amount was small and was washed by the percolating water from the sensor location. In addition, it was shown that relatively thicker debris was accumulated over the $0.5m$ long screen in each debris-flow composition case that resulted in a thinner t_d when compared with its corresponding scenarios.

While conducting consecutive tests on screens, the whole model had to be cleaned in-

cluding the screen and its opening. During this cleaning process, it was observed that the debris grains that were stuck in the opening gap of the screen grids required extra effort to get removed. This is due to the rectangular grid shape that left uniform opening width throughout the screen thickness. In order to avoid such clogging by grains, that have almost equal sizes as of the screen opening, it is recommended to use grids with isosceles trapezoidal cross-sectional shape where the narrow edge is placed in the bottom. This shall help grains with sizes less than that of the top opening width to fall through the gap while the bigger grains remain on the screen to get cleaned after the test. This shape is also suggested by Ishikawa et al. (1994), in a real scale screen study, to avoid boulders clogging. The solution will contribute to making a once used screen ready and available in short duration by easy cleaning and debris removing procedure.

5.4.6 Impact force of the flow

Similar to L_{FL}, t_d, and accumulation thickness, effect of individual variations in V and C_s on flow impact force was studied in Model-2. For this study, the flow impact force was measured on each $0.5m$ long screen test and on the corresponding reference tests. There was no any countermeasure in the run-out channel during the reference tests. The results are plotted in Figure 5.32 and Figure 5.33.

Figure 5.32 gives the results from the G2 test set. To see the results clearly, the variation in V and C_S are given in two plots. In both cases, the maximum impact force recorded

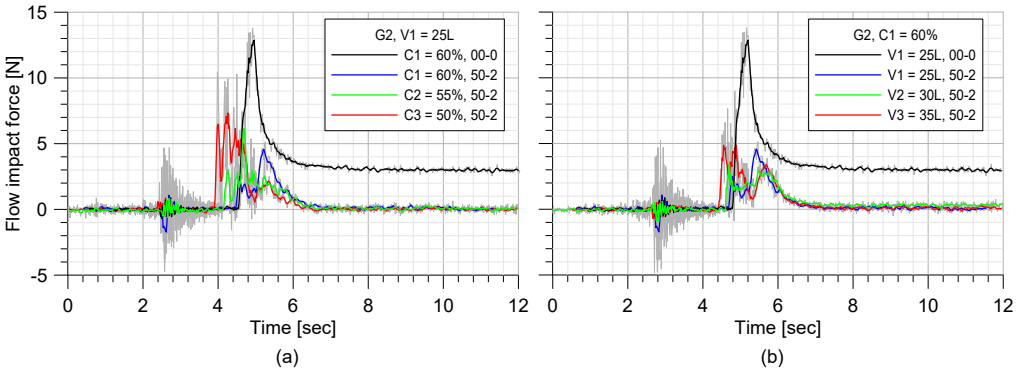

Fig. 5.32: The flow impact force for each $0.5m$ long screen G2 test along with the respective reference tests for: (a) variation in C_s, and (b) variation in V.

in the reference test was almost reduced by half when the $0.5m$ long screen was used. When comparing the individual tests where the $0.5m$ long screen was used, consecutive increase in impact force was observed for the respective decrease in C_s (increase in water content), as seen in Figure 5.32(a). Similarly, for constant C_s, increasing V results in gradual increase in the maximum impact force. However, this measurement was also

affected by the unpredictable behavior of the flow after it passes the screen. This can be seen by the second peak impact force on each case resulted from second surge which was made from combination of the percolated fluid part and the debris briefly stopped after jumping over the screen.

The effect of fines content through the GSD variation was also studied using the representative tests conducted using G1 material. A considerable amount of impact force measured on the reference test was seen to be reduced by using the $0.5m$ long screen as seen on both Figure 5.33(a) and (b). However, not a significant distinction was seen on

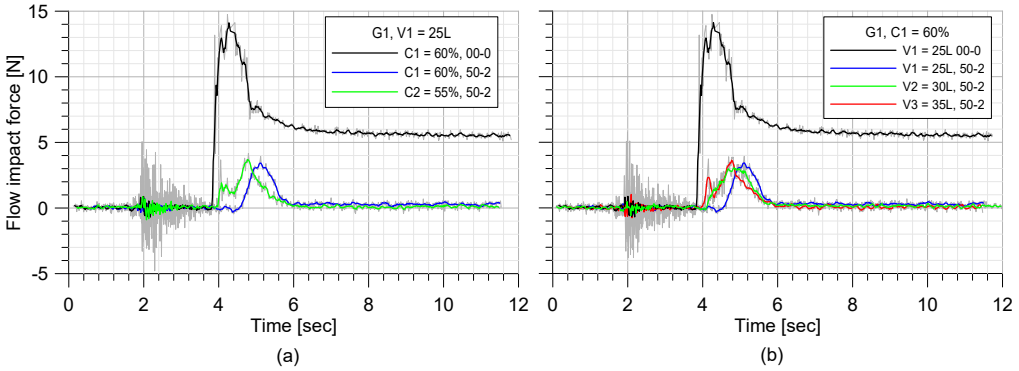

Fig. 5.33: The flow impact force for each $0.5m$ long screen G1 test along with the respective reference tests for: (a) variation in C_s, and (b) variation in V.

the reduction of flow impact in variations of V and C_s. This was mainly attributed to the effectiveness of the screen in stopping the debris material with lesser fines content.

In general, change in GSD of the debris material has effect on the resulting flow impact force. The G2 tests show relatively higher values than the G1 forces. The introduction of additional fines content resulted in higher mobility of the debris-flow which was the main contributor of the resulting higher impact forces. This behavior was discussed in more detail in Section 4.4.3.

5.4.7 PIV analysis of the flow over the screen

To study the mechanism and process of accumulation over the screen, Particle Image Velocimetry (PIV) was conducted using MATLAB application named PIVlab developed by Thielicke and Stamhuis (2014). Consecutive images of the tests were obtained from the $1000fps$ videos recorded using a high-speed camera. This high-speed camera was situated on the side of the channel where it was possible to see the horizontal motion and partial deposition of the debris over the screen. In this PIV analysis, only G1 (the soil which has the least fines content) tests were used because of its better particle movement

visibility through the plexi-glass channel wall.

The flow velocity profile of G1V1C1_50-2 test was extracted at a cross-section $0.15cm$ from the end of the screen and is given in Figure 5.34(a). The sequential photos showing the velocity vectors at each time is also given in Figure 5.34(b) (a more detailed sequential photos can be seen in Appendix E2). The vertical cross-section where the velocity profile was taken from is drawn on the first photo (at $t = 0.0sec$). The time measurement starts when the flow front reaches the beginning of the screen. The flow and accumulation pro-

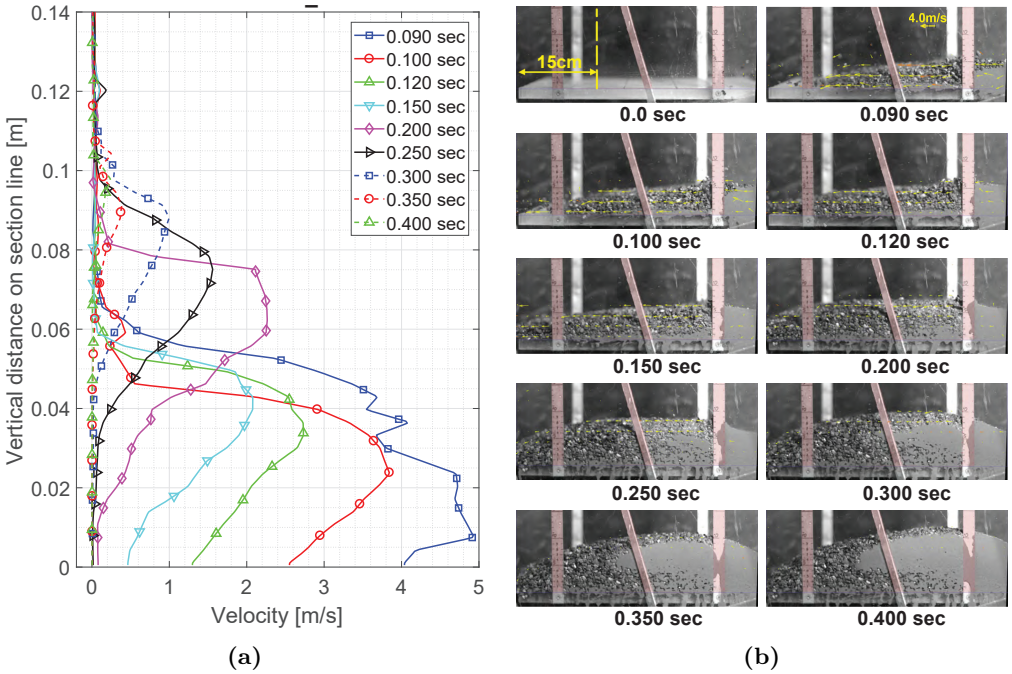

Fig. 5.34: PIV analysis of G1V1C1_50-2: (a) velocity profile at a cross-section $0.15cm$ from the end of the screen, and (b) sequential pictures for corresponding time step plots given in (a).

cess over the screen took nearly 0.4 seconds in total. The first rapid flow (at $t = 0.090sec$) looks like it has thicker flow height (ca. $5cm$) than the subsequent ones. However, this was not the true height of the debris mass, rather it was a result of the front, bigger grains scattered and flying over the screen. The real front flow height should be around $3cm$ at this time. Then most of the first flow surge cover the entire $0.5m$ long screen at around $0.12sec$. This flow height has been maintained until the $0.15sec$ while the effect of draining the fluid part out of the debris starts to have an effect. While the fluid draining effect starts to work, the flow continues as a second surge on top of the partially slowed front and it can be seen by the plot of $0.20sec$.

After observing the high-speed video, $0.5m/s$ speed was selected to represent the flow boundary layer (shearing layer) between the accumulated and the moving mass. This value was selected due to the analysis that was affected by every pixel color change which results in non-zero value even if the entire mass has stopped. Therefore, at $0.20sec$, we can see that almost $3cm$ thickness of the flow has stopped while the whole flow height was nearly $8cm$. After this stage both the damming effect and filtering the liquid part were acting to accumulate additional thickness and to reduce the flow velocity. This process continued until the whole mass stopped over the screen and resulted in maximum accumulation of around $9cm$ at this profile cross-section (as seen in Figure 5.34(a)). The maximum accumulation thickness was seen to be around $13cm$ from the entire screen length (as seen in Figure 5.34(b)).

Similar analyses were performed on the rest of G1 tests. In few of the cases, the muddy part (water-fine mixture) blocked part of the view and made it challenging to perform the analysis (sequential photos can be seen in Appendix E3). However, the representative results that can show the effects of variation in V and C_s were presented. The two plots

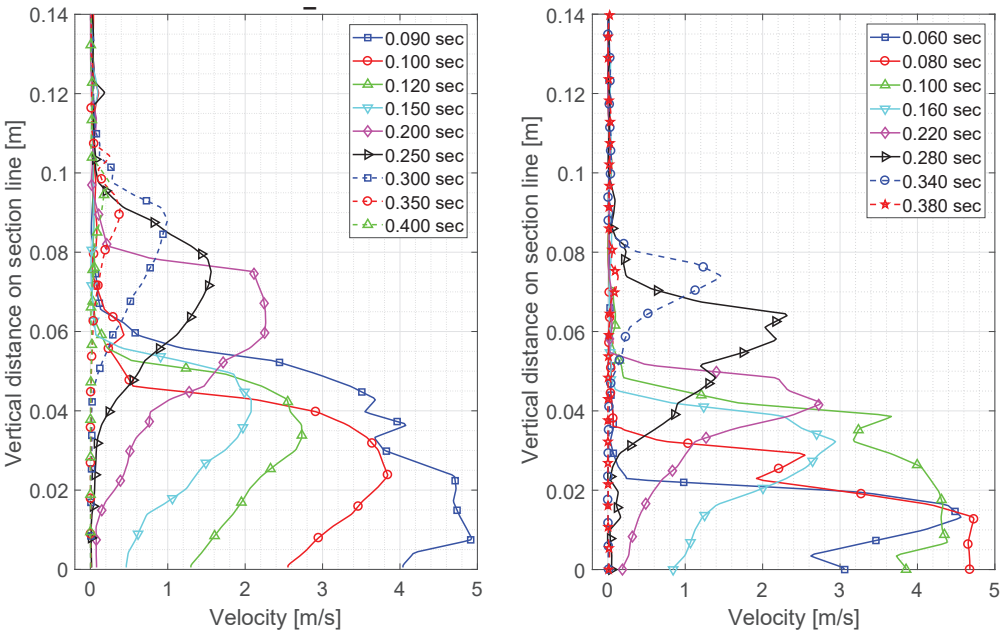

Fig. 5.35: Velocity profile of the tests conducted by the G1 material and V1 = $25L$ volume measured at $15cm$ cross-section from end of the screen: (a) C1 = 60%, and (b) C2 = 55%.

shown in Figure 5.35 are given to compared the variation in C_s for a constant V of $25L$.

The additional water content in C2 gives the flow faster and made it relatively turbulent as the flow front reaches the profile section $0.03sec$ earlier and the velocity profiles were not smooth like the C1 case. The main homogeneous mass arrived at $0.10sec$ with around $3.8m/s$ speed for C1 while it arrives slightly early at $0.08sec$ with higher speed of around $4.7m/s$ for C2 test. Although the final accumulation thickness at this section was lower in C2, the time it takes to fully accumulate their respective thicknesses were almost the same. This can be attributed to the similar V value used.

In addition, the effect of increasing V on the resulting velocity profile was compared by plotting the three V variation tests (the sequential photos for the G1V2C1_50-2 and G1V3C1_50-2 are given in Appendix E4 and Appendix E5). The plots are given in Figure 5.36. The total accumulation thickness and the time of accumulation increase with

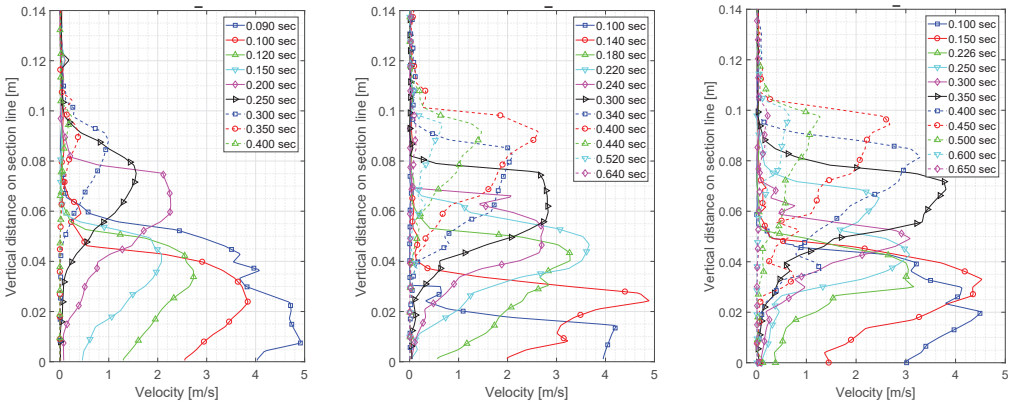

(a) **(b)** **(c)**

Fig. 5.36: Velocity profile of the tests conducted by the G1 material and C1 = 60% concentration measured at $15cm$ cross-section from end of the screen: (a) V1 = $25L$, (b) V2 = $30L$, and (c) V3 = $35L$.

increase in V. The final accumulation height at this section was found to be $9.5cm$, $10cm$, and $10.5cm$ for V1 = $25L$, V2 = $30L$, and V3 = $35L$, respectively. In the cases of V2 and V3, the initial flow front was found to be similar with the case of V1 as the flow front was heavily affected by the dry snout, scattered, and colliding grains. In addition, the arrival time of the scattered snout was found to be the same for all the three cases. The homogeneous flow front for V2 and V3 cases were seen to give a velocity more than $4.5m/s$. In addition, the increase in V resulted in multiple surges that flow layer-by-layer. It took around 0.5 and 0.6 seconds to accumulate almost the entire thickness for the V2 and V3 tests, respectively. Therefore, increasing in V increases the accumulation time, accumulation thickness, and it results in many layer-by-layer surge flows.

The layer-by-layer flow and accumulation process over the given screen was better visualized by plotting the rate of accumulation. As mentioned above, $0.5m/sec$ was considered as velocity to indicate the shearing layer over the screen. This shearing layer level for each velocity profile was collected along with the time. An example from the first test G1V1C1_50-2 is presented in Figure 5.37 to show the shearing layer movement on the entire length of the screen. For the rest of the tests, the shearing level and its corresponding time were collected and plotted in Figure 5.38 to determine the rate of accumulation (shearing-layer upward shift) in each case. The average rate of accumulation (shearing-

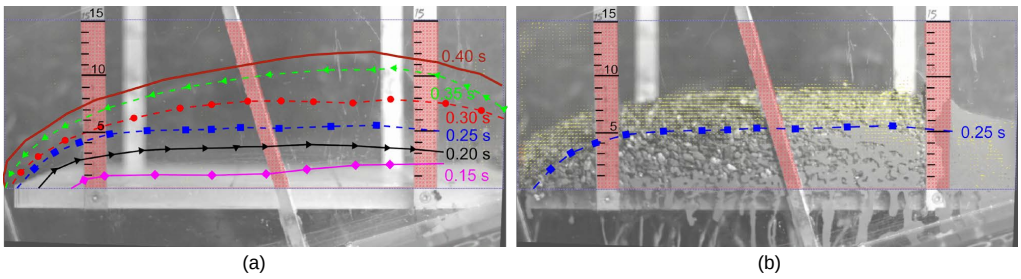

Fig. 5.37: Shearing layers in G1V1C1_50-2 (a) at different times and (b) at a representative time of $0.25sec$

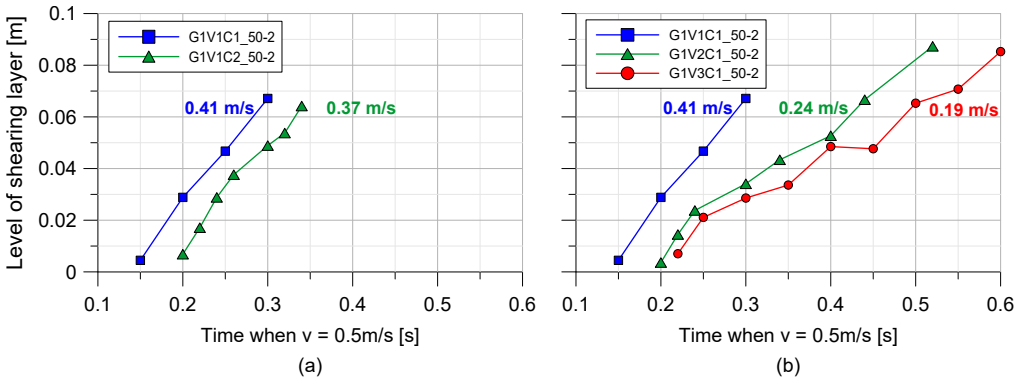

Fig. 5.38: Upward shifting of the shearing layer measured at $0.15m$ from the $0.5m$ long screen end for (a) variation in C_s, and (b) variation in V.

layer upward shift) was faster when the V was small where as it takes longer duration to accumulate same thickness when larger V were used (as seen in Figure 5.38(b)). Although the shearing layer shift gets slower with increase in V, the amount of accumulation thickness increases with increase in V. In addition, a slight decrease in the rate of accumulation was seen when decreasing C_s as shown in Figure 5.38(a).

5.4.8 Summary

In this section, a closer look in the working mechanism of screen along with the effects of varying individual debris-flow composition parameters (GSD, V, and C_s) on its performance were investigated. In addition, this study shows the individual effects of V and C_s, which gives better insight for the results reported in Section 5.3 where the effects of varying $V - C_s$ simultaneously was looked.

The GSD variation effect on the performance of screen was seen by the corresponding effects on the L_{FL}, impact force, and amount of debris accumulated. The performance of screen was seen to increase in G1 tests where it has 10% less fines particle proportion than G2 tests. Shorter L_{FL}, relatively lower impact force, and more accumulation thickness on the screen were observed during G1 tests. In investigating the effect of variations in V and C_s in G2 tests only, decreasing C_s (increasing water content) was found to increase the L_{FL} and impact force more than increasing V. Likewise, the accumulation thickness increases with increase in V and decreases with decreasing C_s (increasing water content). However, the percentage change from their respective reference tests was higher when C_s changes than V changes. The overall result tends to show that additional fines content, water content, or volume could result in additional mobility of debris-flow. These factors were seen to affect the resulting performance of the screen.

From the PIV analyses of the G1 tests conducted on the $0.5m$ long screen, it was shown that the accumulation mechanism was a layer-by-layer deposition step where the rate of accumulation was demonstrated using the upward shift of shearing layer. This shearing layer was forced to shift upward first due to the filtering of the fluid part and then the filtering and damming effect from the already deposited debris. The rate of accumulation was faster for small V and higher C_s case while it was seen to reduce for increasing V. The slow rates of accumulation during the big V cases were accompanied with thicker accumulation thicknesses. on the other hand, decreasing in C_s shows a gradual decrease in both the rate of accumulation and accumulation thickness.

6 Numerical study

6.1 Introduction

This chapter covers the numerical study conducted concerning debris-flow, its interaction with the screen, and the screen countermeasure application. In doing so, a numerical study was performed on the physical model tests and a real debris-flow case.

The GeoFlow_SPH-FD numerical model was used in this study for various reasons explained in Section 2.8. Although both one-phase and two-phase flow models were evaluated, only the one-phase flow model results are presented as the two-phase flow model was not fully functional for screen simulation during the research visit. The model was firstly assessed for its governing parameters as well as parameters of the chosen Voellmy rheology by back-calculating various laboratory tests conducted in the flume Model-2. The various laboratory tests were selected based on variations of GSD (variation in fines content), C_s (variation in water content), and V. The numerical back-calculations were performed based on replicating the run-out distance and the flow velocity. Sensitivity analyses and the back-calculations were majorly conducted using one-dimensional (1D) simulation of the laboratory tests. The second part of this chapter evaluates the numerical model for its simulation potential of the screen performances seen in the laboratory tests. The calibrated governing parameters of the numerical model were used in this part, and the model simulation was evaluated based on the run-out distance, deposition area, flow heights, and flow velocity. The analysis in this part was conducted in both 1D and Two-dimensional (2D) simulations.

In the third and last part of this chapter, a real debris-flow case from Norway, particularly from the coastal terrain, was selected for back-calculation using the numerical model. After calibrating the model parameters for the debris-flow case, the existing countermeasure (embankment wall) built after the event and application of screen-type debris-flow countermeasures were evaluated for their performances and effectiveness to mitigate similar future events.

6.2 Model calibration using the physical model tests

6.2.1 Introduction and model preparation

The GeoFlow_SPH-FD model calibration was made by conducting a sensitivity analysis of its governing parameters. The debris-flow composition varying characteristics from the

laboratory test were compared with the governing parameters of the numerical model. The run-out distance, L_{FL}, was used for comparing the simulation result with what observed in the laboratory.

The GeoFlow_SPH-FD model requires a digital terrain model (DTM) and release volume

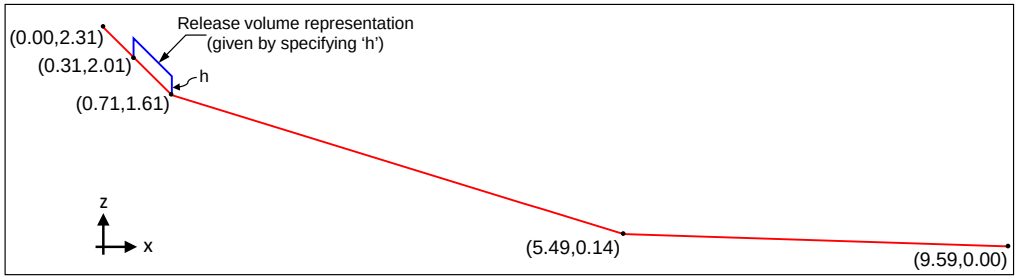

Fig. 6.1: The flume Model-2 DTM topography representation for the numerical model simulation.

represented by SPH points. The 1D DTM topography was prepared to represent flume Model-2 without any obstacles (either the pillar or the screen/plate) and is given by Figure 6.1. The coordinate points that define the DTM along with the mesh-spacing were given as inputs in addition to the rheological parameters.

The starting volumes: V1, V2, and V3 that were $25L$, $30L$, and $35L$, respectively, were represented as 1D trapezoidal sections distinguished by starting height, h. This shape was representing the opened position of the cylinder over the flume channel. The model only uses h, along with two boundary coordinate points, to define the flow source area using the SPH points. The h value was taken from the height of the actual cylindrical volume with a diameter of $0.4m$. The corresponding h values were $0.2m$, $0.24m$, and $0.28m$, respectively.

The parameters of GeoFlow_SPH-FD numerical model and the selected Voellmy rheology, that are given in Table 6.1, were used in the calibration and back-calculation simulations of the laboratory tests.

6.2.2 Back-calculation of parameters based on debris-flow composition

The debris-flow composition variation that was used for the numerical model calibration study was given and described in detail in Chapter 4. However, it is briefly described here for a recap. The three solid material variations were represented by the variation in Grain size distribution (GSD) as G1, G2, and G3, where the fines content ($<0.06mm$) were 5.4%, 14%, and 22.5%, respectively. The solids concentration by volume (C_s) referred to as C1, C2, and C3 that was varied by changing the amount of water have values of 60%, 55%, and 50%, respectively. These two debris-flow composition determinants

Table 6.1: Ranges of parameters of the GeoFlow_SPH-FD model used during the laboratory test simulations

Material and Rheological parameters	Unit	Range of values
Turbulence coefficient, ξ	m/s^2	$100 - 1000$
Friction angle, ϕ_b	$^\circ$	$15 - 30$
$B_{fact} = \pi^2 C_v/4$	m^2/s	$1E-4 - 1E-2$
Erosion growth factor, E_s	m^{-1}	not considered
Specific gravity of solids, ρ_s	kg/m^3	2750
Solids concentration, C_s	%	$50 - 60$
Saturation, S_r	%	100
Porosity, n	%	$40 - 50$
Total average density, $\bar{\rho}$	kg/m^3	$1875 - 2050$

were compared and matched with the GeoFlow_SPH-FD model governing parameters for a given V of debris-flow. The governing parameters of the GeoFlow_SPH-FD model and its Voellmy rheology were the turbulence coefficient, ξ, the basal friction angle, ϕ_b, and the consolidation coefficient described by B_{fact}.

During the laboratory study, every test was made to replicate a well-developed (and fully liquefied) debris-flow in a defined sloped channel by releasing the mass while mixing. The triggering mechanism and initiation phase of real debris-flows were not part of the laboratory tests. The flume surfaces were smooth that makes the bed friction very small. In addition, entrainment characteristic that was usually seen in real debris-flow cases was not considered. The 1D representation of the event simplifies some features of the laboratory test. For example; a trapezoidal shaped area with unit width represents the cylindrical release volume (as seen in Figure 6.2). The lateral interaction of the flow

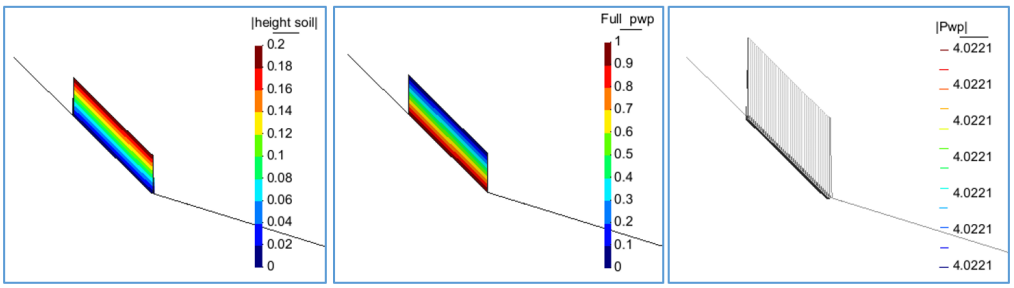

Fig. 6.2: Starting conditions of the 1D simulation for: (a) total flow height representing a release mass placed on the opened-gate of the mixing cylinder, h $[m]$, (b) $\overline{\Delta P}_{wp}$ [-], and (c) P_{wp}, $[kPa]$

within itself and against the wall was not considered. These assumptions were considered in the numerical calibration simulations.

The starting condition for V1 case is given in Figure 6.2. The releasing flow height was $0.2m$ high trapezoidal mass on an opened position of the releasing cylinder gate. The GeoFlow_SPH-FD model allows to see how the relative excess pore-water pressure (excess pore-water pressure normalized by the corresponding effective stress), $\overline{\Delta P}_{wp}$, change along the flow depth and/or the total pore-water pressure at the basal surface, P_{wp}, (in kPa). At the start, full liquefaction was assumed that makes $\overline{\Delta P}_{wp} = 1.0$. A full liquefaction was assumed upon releasing of the debris mass to replicate the simultaneous mass mixing and releasing process in the laboratory tests. This fully liquefied start has a maximum basal pore-water pressure, P_{wp}, that can be calculated by Equation 6.1.

$$P_{wp} = \rho_w g h_{sat} + \bar{\rho'} g h \cdot \overline{\Delta P}_{wp} \tag{6.1}$$

$$\bar{\rho'} \cdot h = (1 - n)[\rho_s h - \rho_w h_{sat}] \tag{6.2}$$

where $\bar{\rho'}$ is the average effective density of the solid-water mixture that was calculated from $C_s = 60\%$ value and $\rho_s = 2750kg/m^3$, $n = (100 - C_s)/100$ and $h_{sat} = h$ for the full saturation. As a result, the maximum P_{wp} at start was $4.022kPa$ for V1 (as seen in Figure 6.2(c)). Similarly, for V2 and V3 cases, the fully liquefied starting maximum P_{wp} were $4.826kPa$ and $5.631kPa$ respectively.

Several simulations were conducted to determine the governing parameters for the range of L_{FL} recorded in the laboratory tests with variations of GSD, V and C_s. The result for V1 is given in the sensitivity analysis plots in Figure 6.3. Each plot in the figure shows

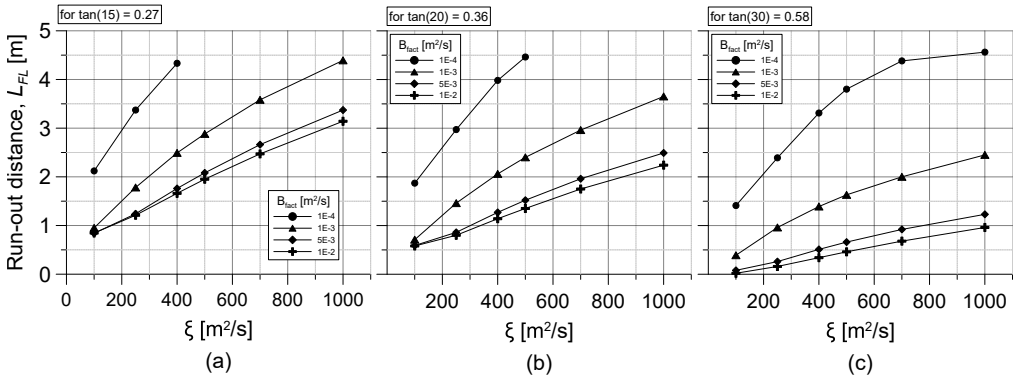

Fig. 6.3: The simulated run-out distance, L_{FL}, plotted against ξ: (a) for $tan(\phi_b) = 0.27$, (b) for $tan(\phi_b) = 0.36$, and (c) for $tan(\phi_b) = 0.58$

the L_{FL} dependence on varying ξ for a given $tan(\phi_b)$ variation. In addition, Appendix C1 shows the L_{FL} dependence on varying B_{fact} and varying $tan(\phi_b)$.

After trying to match the laboratory L_{FL} results with the resulting plots presented in Figure 6.3 and with those presented in Appendix C1, the numerical parameter $tan(\phi_b) = 0.27$ tends to fit best with most of the data when used with the other governing parameters. This means the basal friction angle was $\phi_b = 15°$. However, when the friction angle assumed for this material in Chapter 4, $\phi = 30°$, was used, the flow was resulted in relatively slow flows with shorter L_{FL} as this friction angle commonly relates with the static nature of the debris material. The low value of $_b$ can be considered as a result of the effect of turbulence in the flow. As a result, the L_{FL} of V1 from the laboratory tests and the numerical simulations conducted by $tan(\phi_b) = 0.27$ were compared. The suitable laboratory test result values were collected from Table 4.3 in Chapter 4 and are plotted together with the simulation results as shown in Figure 6.4.

The B_{fact}, which is a function of C_v (Equation 2.28), was seen to have related with the GSD variation made by using fines content. In the laboratory test observation, the

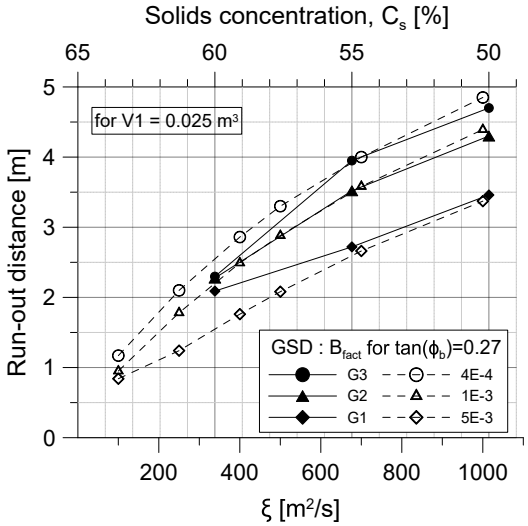

Fig. 6.4: The simulated and the laboratory run-out distances, L_{FL}, plotted together against ξ and C_s for the case of V1

more the fines content (in cases of G2 and G3), the longer it takes for the water to separate from the mass, especially after deposition. This behavior can explain the relationship that an increase in fines content (from G1 to G3) has with the decrease in consolidation coefficient (through B_{fact}). Moreover, the ξ was seen to have related with C_s that was

attained by water content variation. The laboratory tests were observed to have turbulent flow when using higher water contents (resulting in lower C_s) which might explain the curve fitting with the numerical parameter ξ.

6.2.3 Summary

This calibration simulation of the GeoFlow_SPH-FD numerical model using the laboratory flume tests indicates that two of its governing parameters (ξ and B_{fact}) can be related with the debris-flow composition characteristics (C_s and GSD). However, the ϕ_b parameter used in the Voellmy rheology of the numerical model was seen to differ and not to relate with the debris materials friction angle, ϕ. With fixed representation of V and $tan(\phi_b)$, ξ was seen to relate with the C_s while B_{fact} relates with GSD variations. This tends to show that the flow turbulence behavior could, majorly, be controlled by the amount of water a debris-flow has (ξ and C_s) while its rate of consolidation (pore-water pressure evolution) could, majorly, be affected by the fines content (B_{fact} and GSD). Therefore, these back-calculated parameters are used in the subsequent investigations of the screen tests conducted by debris-flow compositions with V1 and C1.

6.3 Simulation of the screen tests

6.3.1 Introduction

Following the back-calculation of governing parameters of the GeoFlow_SPH-FD model for the different GSD and C_s, assessment of the numerical model for replicating the laboratory performance of the screen was conducted. For this simulation study, the back-calculated values of the governing parameters and a representative test-set, G2V1C1 were used. The three tests from G2V1C1 constitutes a reference test with no countermeasure, a test conducted by $0.5m$ long plate, and another test conducted by $0.5m$ long screen. These tests were first compared based on L_{FL}, depositional area coverage, accumulation thickness, and flow height (h). The simulation study is, then, conducted using 1D and 2D DTM of Model-2. In the 1D simulation, the numerical parameters are evaluated based on the L_{FL}, h, accumulation thickness on the solid plate and screen. Same is done in the 2D simulation in addition to considering the deposition area as criteria for checking the governing numerical parameters.

6.3.2 Description of the laboratory test-set and results

The selected representative test-set was conducted by a debris-flow composition with V1 = $25L$ and C1 = 60%. The test-set was comprised of three tests which has different scenarios. The first scenario was the reference test that was conducted without any countermeasure and is referred to as G2V1C1_00-0. The second scenario was the test

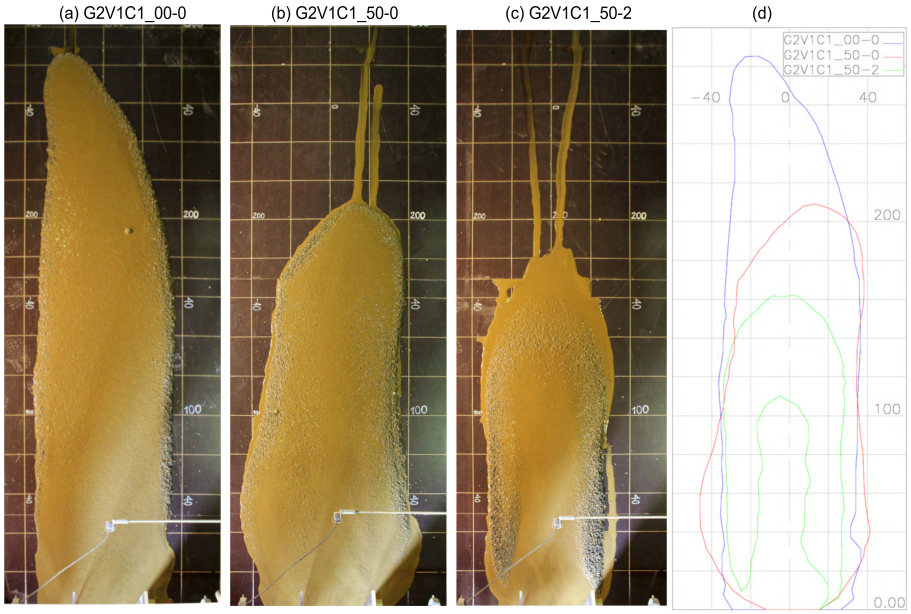

Fig. 6.5: Deposition shape of: (a) G2V1C1_00-0, (b) G2V1C1_50-0, (c) G2V1C1_50-2, and (d) compiled deposition shapes. (The lines in the photo represent $0.2m$ interval)

conducted to evaluate the topographical change due to the application of the screen and it is referred to as G2V1C1_50-0. In this scenario, a solid plate with the same length ($0.5cm$ long) as of the screen was placed in the same position as where the screen was intended to be placed. The third scenario was where the screen was used and it is referred to as G2V1C1_50-2. The $0.5cm$ long screen has $2mm$ wide gaps left between the $1cm$ thick grids giving an opening ratio of approximately 20%.

The deposition shapes obtained after conducting the respective tests on these three scenarios are presented in Figure 6.5. The L_{FL} of G2V1C1_00-0, G2V1C1_50-0, and G2V1C1_50-2, when measured from the beginning of the deposition, were $2.86m$, $2.08m$, and $1.61m$ respectively. The summary of L_{FL} and deposition areas along with their respective percentage reductions are presented in Table 6.2.

The L_{FL} percentage decreases were 27% by the solid plate and 44% by the screen from the reference test. The net contribution of L_{FL} reduction from screening out the fluid part can be determined by comparing the result form the screen with the plate and it was about 23%. The lateral spread and volume of material in the deposition area were not considered in evaluating the percentage reductions in L_{FL}. Therefore, comparison is also made based on the area of deposition. As seen in the compiled pictures of deposition

Table 6.2: Summary of the run-out distance, L_{FL}, and area depositions of the laboratory test results (given in Figure 6.5), and their respective percentage reductions

Test scenarios	L_{FL} [m]	Reduction w.r.t* 00-0 [%]	Reduction w.r.t 50-0 [%]	Area of deposition [cm^2]	Reduction w.r.t 00-0 [%]	Reduction w.r.t 50-0 [%]
00-0 (Reference)	2.86	—	—	17 300	—	—
50-0 (Plate)	2.08	27	—	13 800	20	—
50-2 (Screen)	1.61	44	23	5 900	66	57

**w.r.t = with respect to*

area and shape given by Figure 6.5(d), the shape when using screen was different from the other two. The debris material that jumped and pushed over the screen was then washed further by the filtered fluid in the deposition area. Its deposition shape shows that the area of deposited solids was small although the L_{FL} seen to be longer. The depositional areas were measured to be approximately 17 300 cm^2, 13 800 cm^2, and 5 900 cm^2 in the reference, the plate, and the screen tests, respectively (as seen in Table 6.2). The percentage decrease at the depositional area can be another suitable measure to describe the effect of the screen. The percentage decrease in area when the solid plate was used was around 20%, and when screen was used was around 66%. The net contribution of filtering out the fluid part from the debris-flow (by comparing the solid plate with the screen) was around 57%. Maximum deposition thicknesses in different locations of the depositional area for all the scenarios were observed to be around $2cm$ except in the washed out part of when using screen.

Photos of the debris mass accumulated over the solid plate and the screen were given in Chapter 5 by Figure 5.29 in Section 5.4.5. Although the topography alteration represented by the solid plate was seen to reduce the flow mobility as seen in both run-out and deposition area reductions, it could only accumulate a uniform $2cm$ thick debris mass over the plate. On the other hand, accumulation thickness on the screen was seen to vary between $5cm - 6cm$. The amount of mass remained over the screen explains the significant decrease in the deposition area and the high value of net percentage deposition area decrease.

The flow height reading in the channel and at the deposition area is plotted and given in Figure 6.6. The fh-1, fh-2, fh-3, and fh-4 were flow heights recorded by the flow height sensors (as seen in Figure 3.7). In the reference test, the flow height was seen to continuously decrease from ca. $55mm$ near the debris releasing area to ca. $20mm$ at the end of the flume channel and beginning of the deposition area. The location of fh-3 was ca. $0.5m$ away from the end of the plate or the screen. In Figure 6.6(b), it records a very high flow

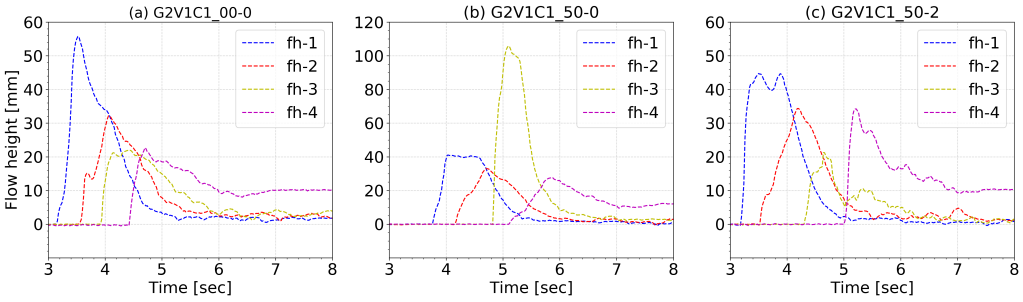

Fig. 6.6: Recorded flow heights: (a) for the reference test, (b) when using the $0.5m$ long plate, and (c) when using the $0.5m$ long screen

height (ca. $105mm$) because of the flow jump crossing the plate while in Figure 6.6(c), it captures the flow breaking effect of the screen as the flow height, fh-3, reduced in the contrary. In the next two sections, the 1D and 2D numerical simulation results of screen are presented based on the results presented in this section.

6.3.3 One-dimensional (1D) Simulation

In this section, the results of 1D simulation of the screen is presented. In order to evaluate the performance of the screen, the other two scenarios are also included. These scenarios are the reference test with no countermeasure and the test conducted with the solid plate. The simulation without any countermeasure used the DTM topography given by Figure 6.1 while the simulations for solid plate and the screen used the DTM shown by Figure 6.7.

The releasing volume representation was the same as what was described in Section 6.2.

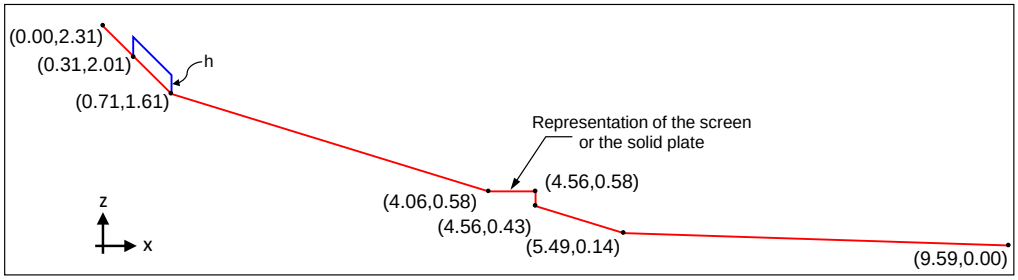

Fig. 6.7: The flume model DTM topography representation for tests with the screen or the solid plate

For this simulation, only the V1 tests were used and h was $0.2m$. In addition, to define the screen in the numerical model, a special geometry definition was designated in the input file of the DTM topography. One must specify the locations of the screen using the

coordinates (as seen in Figure 6.7) and assign the designated value to tell the numerical model that the location was a permeable surface. This permeable surface location was treated as a free surface that was in contact with the atmosphere with zero pore-water pressure. The Voellmy rheology basal shear strength equation (given by Equation 2.22) used in this model incorporates pore-water pressure term that reduces the shear resistance to the flow. This screen (permeable surface) was contributing to the increase of the shear resistance by reducing this pore-pressure term.

Few calibration simulations were conducted first on the reference test (G2V1C1_00-0) to check with the back-calculated parameters. The values of the governing parameters that reasonably replicate the L_{FL} and flow velocity were ξ of 500 m/s^2, $tan(\phi_b)$, of 0.27, and B_{fact} of $1E-3$. The flow velocity observed in the laboratory test, shown in Figure 6.8(a), as the flow front reaches at each flow height sensor coincides with the simulation flow front. The flow between fh-1 and fh-4 takes ca. $1.2sec$. However, the depth-averaged

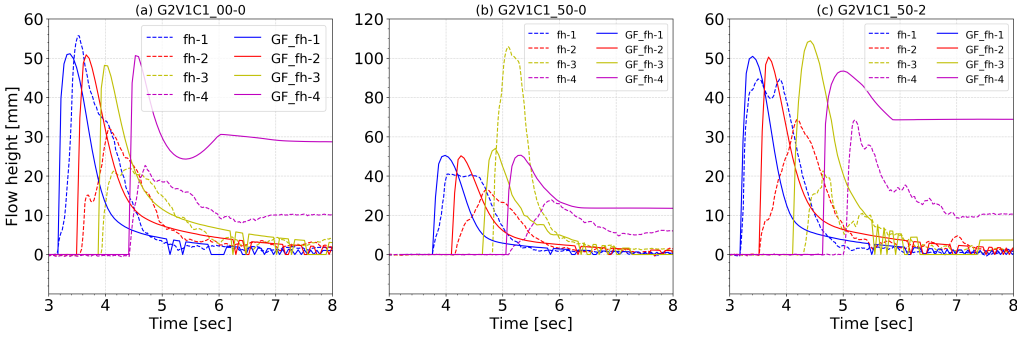

Fig. 6.8: Flow heights: laboratory results vs numerical simulation results (a) of the reference test, (b) when using the $0.5m$ long plate, and (c) when using the $0.5m$ long screen

flow height was seen to overestimate the flow height at around the end of the channel (fh-2 and fh-3) and the deposition area (fh-4). The numerical model was seen to result in higher flow heights and deposition thicknesses for the tests that suit with the L_{FL} and flow velocities. This looks like that the flow height was one of the laboratory debris-flow characteristic that could not be replicated fully by the numerical model.

Using the parameters that back-calculated the reference test, the other two scenarios of implementing the plate and the screen were simulated. The resulting flow height propagation is given in Figure 6.8(b) and (c). The arrival time of the flow front at each point fits with the laboratory result when using the plate with flow duration between fh-1 and fh-4 ca. $1.3sec$. The flow shows exception at fh-3 where the simulation looks to be faster than what was observed in the laboratory. This could be because of the jumping of the flow over the plate at this location that could not be replicated in the simulation as the SPH

points need to be connected with the DTM mesh points. In the case of simulating the screen, fh-3 and fh-4 arrive earlier than what was observed in the laboratory. However, the effect of screen in slowing down the flow was reasonably replicated when the flow duration between the fh-1 and fh-4 ($1.8sec$) was compared with the simulation case ($1.4sec$).

The final simulation values of the reference test at the deposition area is given in Figure 6.9. The relative excess pore-water pressure, $\overline{\Delta P}_{wp}$, is given in Figure 6.9(a) where the maximum value (full liquefaction, as seen in Figure 6.2) has dissipated to ca. 8%. This goes with what is seen in Figure 6.9(b) where the total pore-water pressure, P_{wp} showed comparable values to the hydrostatic pore-water pressure, $P_{wp,hyd}$ values. This can also be seen by comparing values from Figure 6.9(c) multiplied by water unit weight with values of Figure 6.9(b). The deposition heights on the screen/solid plate and on the

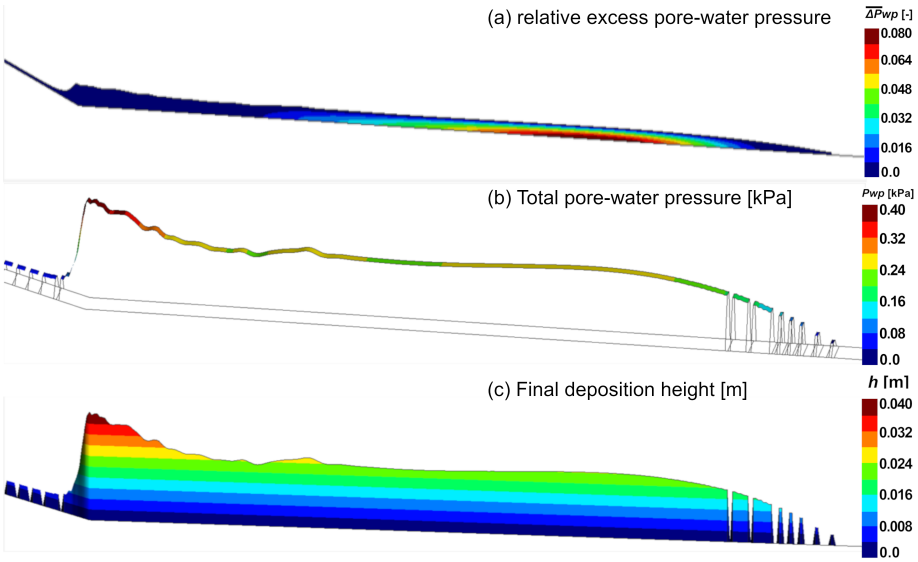

Fig. 6.9: End of simulation for G2V1C1_00-0 at deposition area: (a) relative excess pore-water pressure, $\overline{\Delta P}_{wp}$, [-], (b) Total pore-water pressure at the basal surface, P_{wp}, [kPa], and (c) deposition height, h, $[m]$.

deposition area is given in Figure 6.10. For a better visualization, the vertical scale is exaggerated five times. In addition, the simulation L_{FL} are given along with the laboratory results in Table 6.3.

The L_{FL} for the solid plate and screen were found to be longer by 38% and 34%, respectively, than what was observed in the laboratory tests (as seen in Table 6.3). However, the percentage decrease in the L_{FL} of the screen simulation with respect to the L_{FL} of the solid plate simulation was found to be 24% which was similar to the laboratory result,

Table 6.3: Summary of the run-out distances of the laboratory tests and the 1D simulation results along with their respective percentage reductions

Test scenarios	Laboratory run-out distance			Simulation run-out distance		
	L_{FL} [m]	Reduction w.r.t 00-0 [%]	Reduction w.r.t 50-0 [%]	L_{FL} [m]	Inc. w.r.t* Lab L_{FL} [%]	Reduction w.r.t 50-0 [%]
00-0 (Reference)	2.86	—	—	2.88	—	—
50-0 (Plate)	2.08	27	—	2.86	38	—
50-2 (Screen)	1.61	44	23	2.16	34	24

**Inc. w.r.t = Increase with respect to*

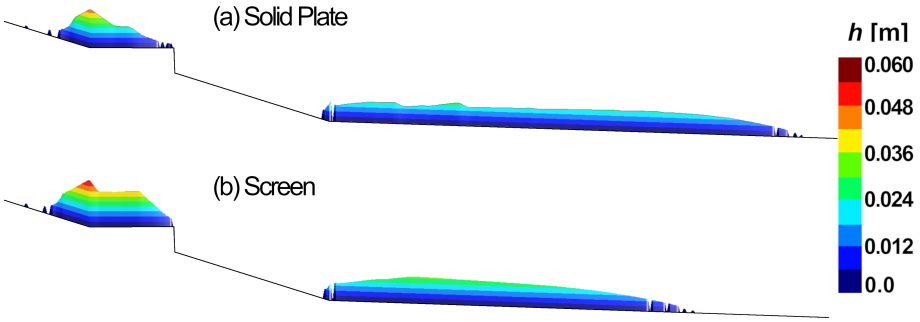

Fig. 6.10: Final flow height simulation result when using (a) the $0.5m$ long solid plate, and (b) the $0.5m$ long screen

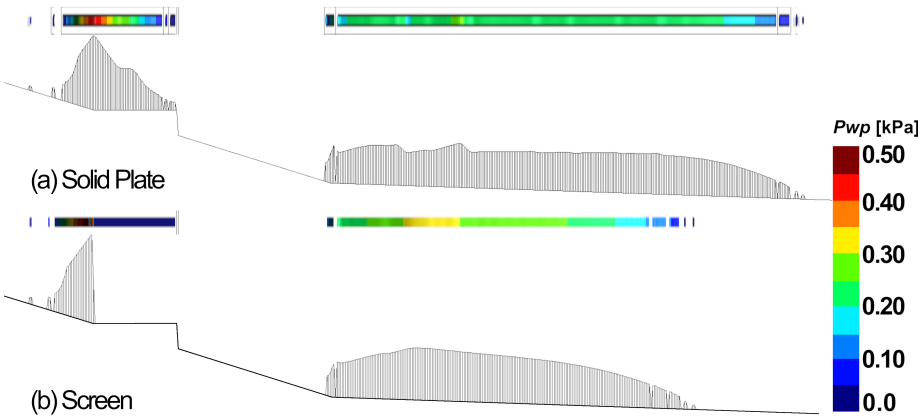

Fig. 6.11: Final total basal pore-water pressure, P_{wp}, result when using (a) the $0.5m$ long solid plate, and (b) the $0.5m$ long screen

i.e 23% (as seen in Table 6.2). The accumulated mass in the deposition area was seen to be around 2.5cm thick when using the solid plate and ca. 3.2cm thick when using the screen. This was due to the reduced flow energy that forces the flowing mass to accumulate in a short distance of the depositional area (as seen in Figure 6.10). The maximum accumulation thicknesses on the solid plate and the screen were found to be 4.5cm and 5.5cm, respectively. However, the shapes of these accumulations were not similar in which the screen has an average thickness of 4.5cm with a uniform level whereas the solid plate has an average thickness of 2.5cm with sloped shape. What was found when simulating the screen was comparable with what was observed in the laboratory test (ca. $5cm-6cm$).

The relative pore-water pressure, $\overline{\Delta P}_{wp}$, evolution over the plate and over the screen is given by Figure 6.12. For the assumed fully saturated ($S_r = 1.0$) flow, $\overline{\Delta P}_{wp}$ starts

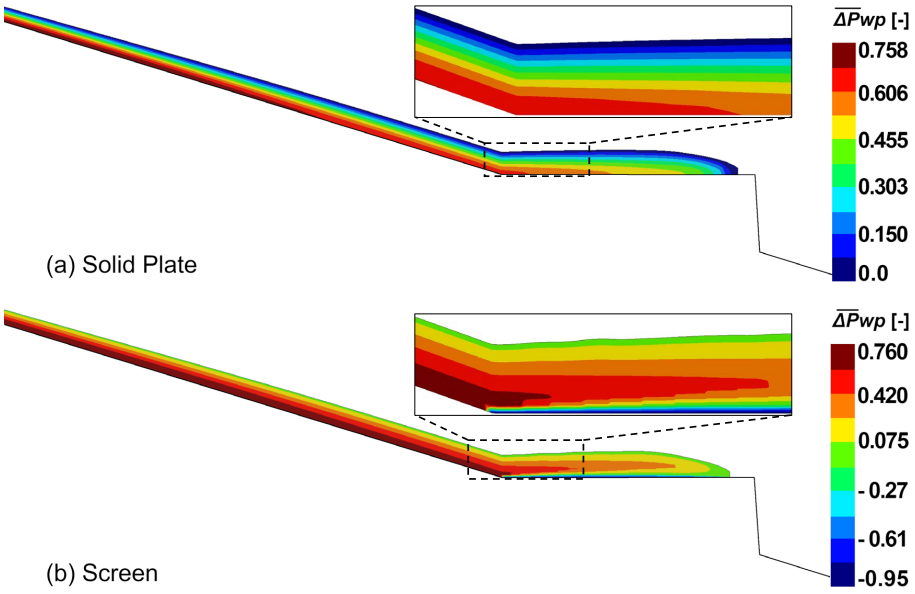

Fig. 6.12: (a) Relative pore-water pressure, $\overline{\Delta P}_{wp}$, over: (a) the 0.5m long solid plate, and (b) the 0.5m long screen

from unity and dissipates according to the consolidation coefficient value given when flowing on a solid surface. However, when it encounters with a permeable surface like the screen in this case, the total pore-water pressure, P_{wp}, at the basal level become zero (as seen in Figure 6.11). Therefore, the $\overline{\Delta P}_{wp}$ must be equal with the negative of the relative hydrostatic water pressure, $\overline{P}_{wp,hyd}$, only at the basal level. This relation was given by $\overline{\Delta P}_{wp} = -\frac{\rho_w}{\rho'}(\frac{h_{sat}}{h})$ which resulted in [-1000/(2050-1000) = - 0.95] (as seen in Figure 6.12(b)) as the lowest value of the relative excess pore-water pressure. For the rest of the flow height, the relative excess pore-water pressure values were evaluated on the

rest of finite difference (FD) nodes at each SPH point.

6.3.4 Two-dimensional (2D) simulation

In this section, 2D DTM models with basic DTM profile shapes as shown in Figure 6.1 and Figure 6.7 were used for the respective simulations. The boundary walls were given as segments specified by coordinate points as shown in Figure 6.13. These segments are given in the input file together with the source volume. The laboratory tests that were simu-

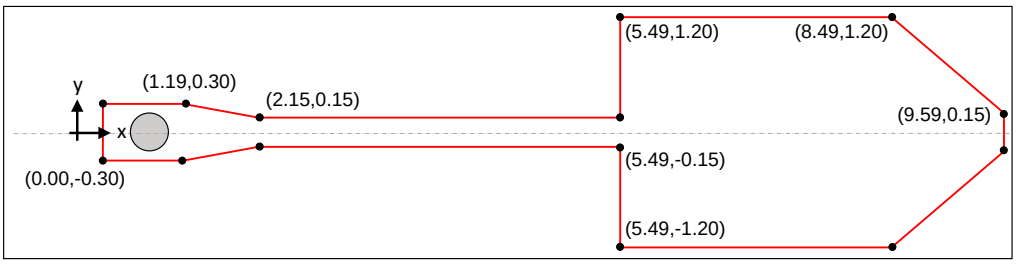

Fig. 6.13: Boundary wall representing coordinates to specify plan of the flume model: applicable to the reference, the solid plate, and the screen representation tests.

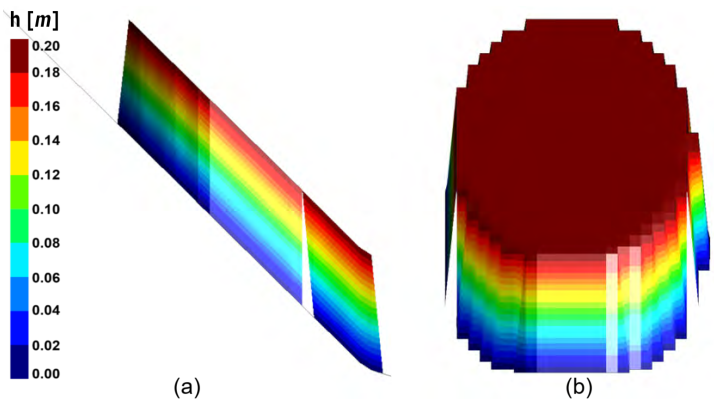

Fig. 6.14: The starting height condition and cylindrical representation of the release volume: (a) side view and (b) front view

lated here were those presented in Section 6.3.2. For this simulation, the back-calculated governing parameters in the previous sections were used as starting points. The release volume was represented by a cylindrical volume having a radius of $0.2m$ with uniform $0.2m$ thickness as shown in Figure 6.14 for V1 = $25L$.

The back-calculation of the three laboratory tests were evaluated based on L_{FL}, lateral spread, and area of deposition. In the simulation, a uniform spreading of the debris

mass was observed in both transverse and parallel flow directions of the deposition area as given in Figure 6.15(b). However, in the laboratory tests as given in Figure 6.15(a),

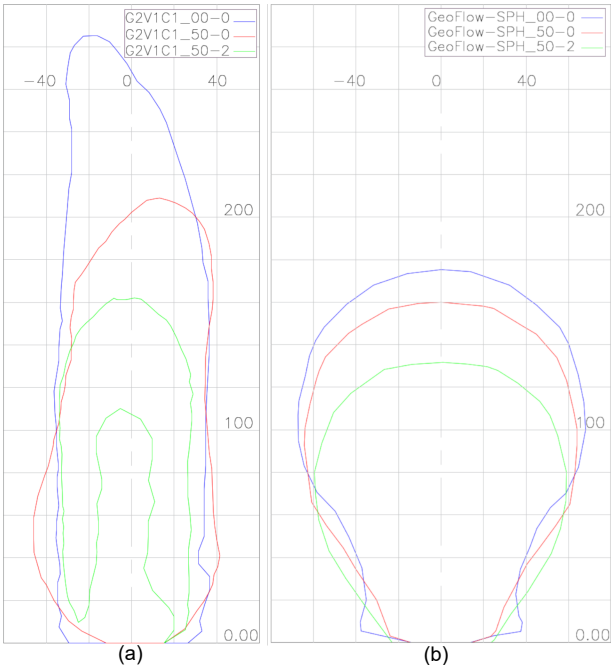

Fig. 6.15: Final deposition shapes of the reference, plate, and screen cases from: (a) the laboratory test results, and (b) the simulation results

the parallel flow direction was longer than the transverse direction. The effect of the natural process of levee making and segregation of the bigger particles in the deposition area, observed in the laboratory tests, could not be fully replicated in the simulation. The elongated flow was due to the relatively fully saturated part of the flow continues to progress while the relatively dry and granular part was accumulated sideways.

In general, in the 2D simulation case, the run-out distance could not be entirely replicated even for the reference test although There were possibilities to replicate the same run-out distance by reducing the basal friction angle of the deposition area. However, the spreading would comparably became widened giving a very large oval shape of deposition. Therefore, for now, it was focused on the area of deposition that was back-calculated in the reference test along with the relative decrease in the run-out distance with provision of the solid plate and screen. Summary of the run-out distances and depositional areas for both laboratory test and simulation are given in Table 6.4 and Table 6.5.

The percentage decrease in the simulated L_{FL} were 9% and 25% when providing the

plate and the screen, respectively. These values were 27% and 44% in the results of

Table 6.4: Summary of the run-out distances of the laboratory tests and the 2D simulation results along with their respective percentage reductions

Test scenarios	Laboratory run-out distance			Simulation run-out distance		
	L_{FL} [m]	Reduction w.r.t 00-0 [%]	Reduction w.r.t 50-0 [%]	L_{FL} [m]	Reduction w.r.t 00-0 [%]	Reduction w.r.t 50-0 [%]
00-0 (Reference)	2.86	—	—	1.76	—	—
50-0 (Plate)	2.08	27	—	1.60	9	—
50-2 (Screen)	1.61	44	23	1.32	25	17

Table 6.5: Summary of the area depositions of the laboratory test results and the 2D simulation results along with their respective percentage reductions

Test scenarios	Laboratory area of deposition			Simulation area of deposition		
	Area of deposition [cm^2]	Reduction w.r.t 00-0 [%]	Reduction w.r.t 50-0 [%]	Area of deposition [cm^2]	Reduction w.r.t 00-0 [%]	Reduction w.r.t 50-0 [%]
00-0 (Reference)	17 300	—	—	17 700	—	—
50-0 (Plate)	13 800	20	—	15 600	12	—
50-2 (Screen)	5 900	66	57	12 400	30	20

the laboratory tests. The net screen contribution in percentage reduction of the L_{FL} was 17%, which was 23% in the laboratory test. The area of deposition for the back-calculated reference test was around 17 700 cm^2, which was comparable with what was observed in the laboratory test of G2V1C1_00-0, i.e., 17 300 cm^2. The areas of deposition have been reduced to 15 600 cm^2 and 12 400 cm^2 when using the plate and the screen, respectively. This shows comparable result with the case of the plate while overestimating it in the case of screen. One reason why this percentage reduction, when using the screen, could not be replicated was that the area recorded in the laboratory does not include the fluid part while there was no distinction between the water and soil particles in the simulation as a one-phase flow mode was considered (as seen in Figure 6.15). However, if the fluid part was considered in the laboratory case, the wide gap in the area of deposition between the laboratory and the simulation results would narrow down.

The deposition thickness over the solid plate and the screen is given in Figure 6.16. For a better visualization, the vertical scale is exaggerated four times than the horizontal scale. In both cases, the thickness at the deposition area was approximately $2cm$. However, in the case of solid plate, this thickness was maintained in larger area while a slightly less

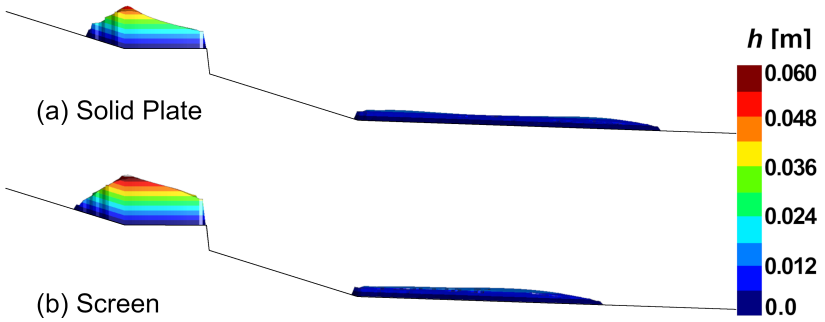

Fig. 6.16: Final accumulation and deposition thicknesses of (a) the $0.5m$ long solid plate simulation, and (b) the $0.5m$ long screen simulation.

thickness, ca. $1.8cm$, was seen to cover wide area of deposition in the case of screen. Lesser final deposition thickness in smaller area was accompanied by relatively higher average deposition height on the screen, i.e ca. $6cm$. Similar to the 1D case, more mass was observed to be accumulated on the plate (ca. $5cm$) than what was observed during the laboratory test ($2cm$).

In the laboratory test, the screen accumulates the debris layer-by-layer while filtering the fluid part out and also as a result of the damming effect. However, from the step-by-step simulation observation, the final mass over the screen was accumulated mainly after the flow has stopped on the screen. This looks like it was resulted from the damming effect of the already slowed down and deposited SPH points. The slowing down of these SPH points was a result of dissipation of basal pore-water pressure which increases the basal shear strength (friction force). This increase in basal shear strength makes the SPH points to get packed together closely to decrease the depth-averaged velocity and increase the depth-averaged flow height (accumulation thickness). Because of this depth-averaging simulation, the layer-by-layer accumulation process observed in the laboratory tests could not be simulated by the numerical model.

6.3.5 Summary

The 1D and 2D numerical studies made by GeoFlow_SPH-FD on the laboratory tests shows the potential in replicating the effect of screen in reducing the mobility of debris-flow by incorporating the pore-water pressure term in the basal shear strength equation of the Voellmy rheology. Filtering the fluid part out from a liquefied moving debris restores its shearing resistance. During the laboratory tests, two simultaneous flow behaviors were observed on the screen. While the fluid part was filtering out through the screen, a decrease in relative velocity from bottom to top leaving a growing frozen mass over the screen and a shifting of the shearing layer upward due to the growing frozen mass were

observed. This results in a reduction of a moving mass over a shearing layer and at the same time, the frozen mass on the screen serves as a dam for any subsequent flow coming behind. In the numerical simulations, the screen was observed in showing the damming effect along with the reduced averaged velocity where the behaviors of screen reasonably replicated. Therefore, due to such potential of the GeoFlow_SPH-FD model, it was used to back-calculate a real debris-flow case which happened in Mjåland, Norway as well as used for evaluation of size, number, and locations of screen(s).

6.4 Real debris-flow case

6.4.1 Description of the debris-flow case

The Mjåland debris-flow happen on 2^{nd} of June 2016 in Hunnedalen, Rogaland county in South-west of Norway. The national landslide registration database (NVE skredregistrering 2019) gives short description stating that around $150m$ long section of the road Fv.45 - Hunnedalsveien was covered by debris of rocks, sediments and tree logs with average height of around $2m$. It forced temporary closure of the road and power outage was occurred with no road accident, settlement damage or any causality. The report written after assessment of the event, (Multiconsult 2016) stated that there was deposit of moraines(till) throughout the mountainside and the slide source area of the flow was situated on approximately 40° inclination located in the upper part of the mountain where a weak and loosely packed soil mass was found. In addition, the initial slide was associated with a short and intense precipitation period in the area (Multiconsult 2016). The triggering cause was the large amount of rainfall and snow melting in the area (ca. $40mm$) on the previous days according to the meteorology database (NVE xgeo 2019). This high amount of water was accompanied by a continuous $20mm/day$ of precipitation in the area (NVE xgeo 2019). This phenomenon could have saturated and infiltrated through the weak and loose mass that was found on top of the mountain. Because of the presence of excess amount of water than usual, this debris-flow was believed to be facilitated by excess pore-water pressure.

6.4.2 Geology and Geo-hazard levels

From the terrain deposit map (NVE Atlas 2019), the area shows mainly a bare mountain overlain by thin layer of loose soil (as seen in Figure 6.17). This loose soil supports mountain trees up to elevation of $630m$ above mean sea level (AMSL). At the bottom of the valley where the road passes through, the soil formation map shows thick layer of material from previous sliding events. The stream channel where the debris-flow happened through is called Garbekksjuvet (Garbekken gorge). It starts from the top of the mountain near a small water pond and ends up in a small lake called Mjålandslona.

Both the debris-flow susceptible area zoning and the slide extent probability zoning

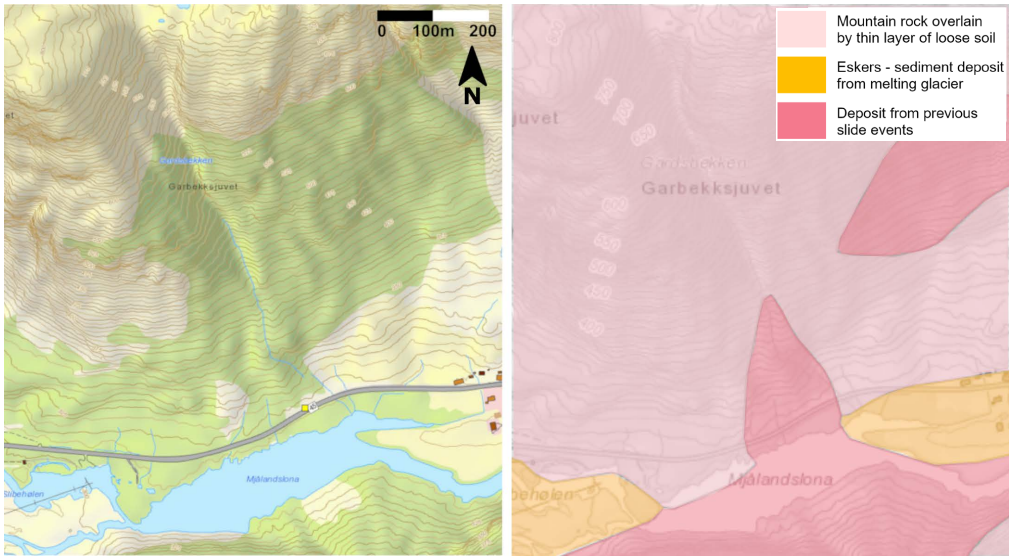

Fig. 6.17: Geological formation and geological cover map of the Mjåland debris-flow area (from NVE Atlas (2019)

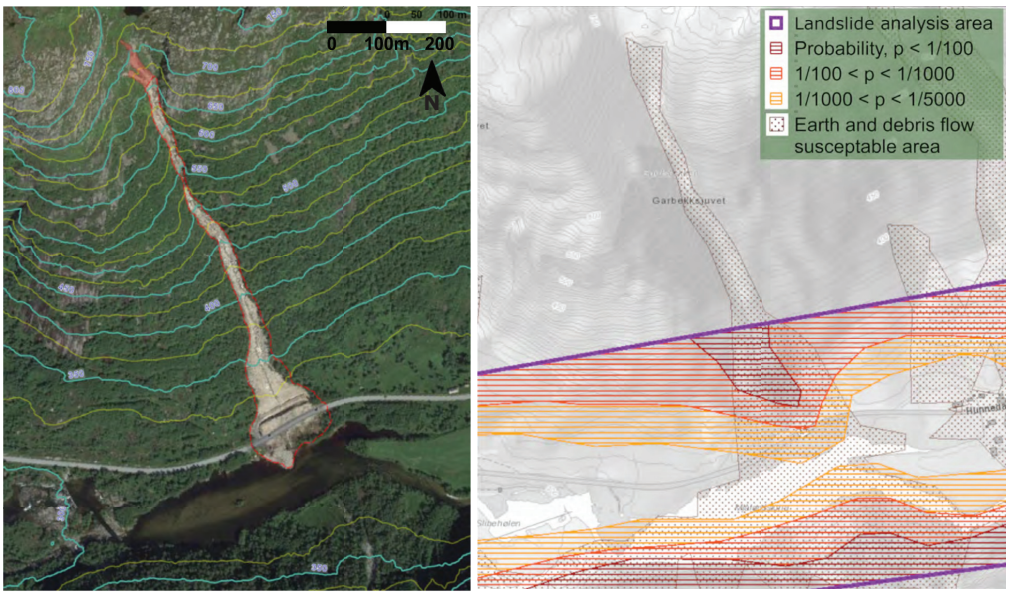

(a) (b)

Fig. 6.18: (a) Event map with AMSL elevations and (b) Susceptibility map and slide extent probability areas (from NVE Atlas (2019)

estimated and given in NVE Atlas (2019) seen to include the Mjåland debris-flow event as shown in Figure 6.18. This debris-flow event coincides with the lowest slide-extent-probability, which is 1/1000 - 1/5000.

The data preparation, the before and after topography with initial and final volume of the debris-flow are explained in Section 6.4.3. The back-calculation of the event using the GeoFlow_ SPH-FD model and implementation of the screen as mitigating measure is presented in the subsequent sections.

6.4.3 Terrain model preparation

Two input DTM files are required by the GeoFlow_SPH-FD numerical model to simulate large scale debris-flows. The first one is the original terrain topography without the slide volume that initiates the debris-flow. The second is a DTM file that represents only the source (slide volume). In order to prepare these two files of the Mjåland debris-flow, ArcGIS, QGIS, and Surfer software were used. In order to prepare these two DTM files, the pre- and post-slide DTM of the debris-flow location was required. However, neither the field report nor any of the mapping sources we looked up could provide the DTM of the after-slide topography. Therefore, the starting, the transition, and the deposition zones were estimated from the site photos taken immediately after the event happened and from the ortho-photos in google earth and norgeibilder.no as seen in Figure 6.19. These zones were, additionally, confirmed after the site visit made by a team that in-

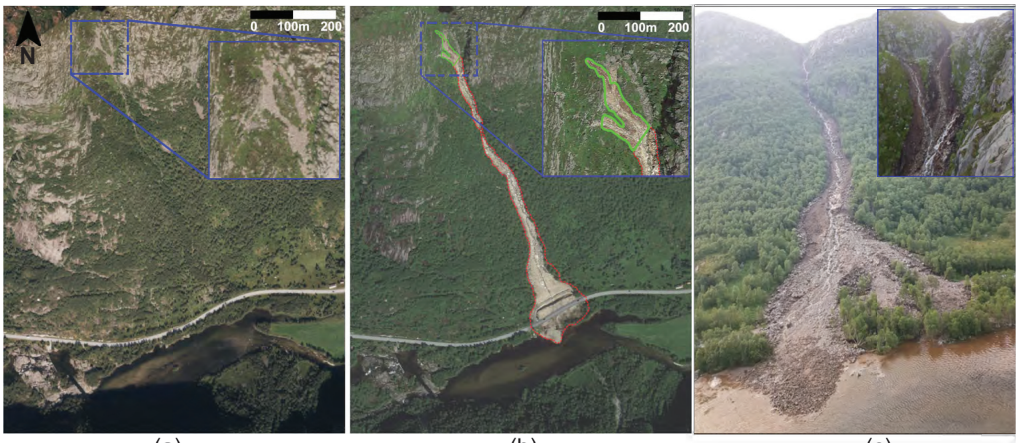

Fig. 6.19: The Mjåland debris-flow: (a) before the slide in 2014 (from norgeibilder.no), (b) after the slide (from Google Earth pro and QGIS), (c) photo of the event (from Multiconsult and NPRA)

cluded this author. Elevation of the starting zone was between $655m - 725m$ above mean sea level while the transposition (transportation) zone goes down until elevation of $370m$.

Then the deposition zone was the rest of the valley until the lake surface at $305m$ elevation.

For a better and more accurate result, we used a $2m$ grid DTM for the topography and a $0.5m$ grid DTM for defining the SPH source volume. In previous study by Pastor et al. (2004), it was shown that the numerical simulation result can be affected by grid spacing, which is considered as meshing space, by comparing $5m$ grid and $10m$ grid of a debris-flow cases.

After studying the photos taken from the report and the areal maps before and after the event, the initial slide area and volume was estimated to be 3 270 m^3 (as seen in Figure 6.19(c)). The final deposition area was similarly estimated to cover 13 500 m^2 which makes the final volume of deposition calculated to be approximately 20 000 m^3 with an average deposition thickness of $1.5m$.

This case study was chosen because it was representative for the E39 coastal highway and similar topographies in the Norwegian terrain which are inside the designated areas of national landslide susceptibility map. Moreover, during the site visit, it was observed that there was still sufficient material left in the channel and atop the mountain to trigger another potential debris-flow when met by favourable triggering conditions.

There are few assumptions that were considered in simplifying the complicated process of the debris-flow event for this numerical simulation. The assumptions are listed below:

- The starting mechanism, which possibly involved some retrogressive failure in the triggering area, was not replicated in the simulation. The entire starting volume at the estimated starting area was released at once.
- The DTM representing the terrain does not include trees. Therefore, their flow resisting contribution was not considered in the numerical study.
- The debris-flow portion that went into the lake was not considered.
- Erosion or entrainment was considered based on the McDougall and Hungr (2005) erosion rule which was given in Section 2.8.3 by Equation 2.24 and Equation 2.25. It uses the estimated initial and final volumes of the slides along with length of the flow path considered to have gone through the erosion process.
- Two sections, from elevation $650m$ to $550m$ and from elevation $520m$ to $370m$ were delineated to have contributed the major entrained volume after the site visit and study of the photos and maps available. The total length of these two sections becomes $L = 455m$.

Figure 6.20 gives contours produced using QGIS software from the DTM extracted from ArcGIS and QGIS. From Figure 6.20(b)-(e), the original DTM given in Figure 6.20(a)

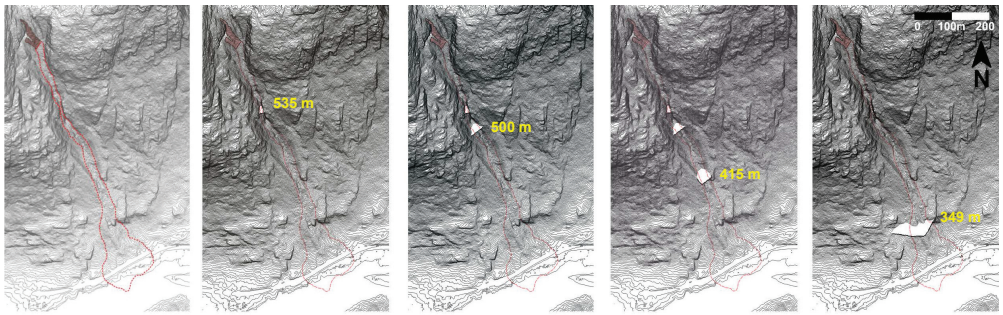

Fig. 6.20: The prepared DTMs of (a) the original debris-flow topography, and (b)-(e) different options of screen implementations

was modified in Surfer software to implement a horizontal surface that was used as either a solid surface or screen. The elevations these alterations provided were at $535m$, $500m$, $415m$, and $349m$ above mean sea level, respectively. There was a $90m$ wide and $5m$ high wall constructed from the debris deposit. This wall was evaluated using the numerical model and for that similar DTM topographical modifications were made on the original DTM given by Figure 6.20(a).

6.4.4 Back-calculation of the debris-flow case

Similar to the laboratory test case, back-calculation of the event was performed on the original DTM without any terrain modification. These simulations were performed to se-

Table 6.6: Back-calculated parameters for the Mjåland, debris-flow

Material and Rheological parameters	Calibrated values
Turbulence coefficient, ξ	100 m/s^2
Friction angle, ϕ_b	25°
$B_{fact} = \pi^2 C_v/4$	$1E-3$ m^2/s
Erosion growth factor, E_s	0.004 m^{-1}
Specific gravity of solids, ρ_s	2750 kg/m^3
Solids concentration, C_s	60%
Saturation, S_r	100%
Porosity, n	40%
Total average density, $\bar{\rho}$	2050 kg/m^3

lect the appropriate values of the governing parameters of the Voellmy rheology; $\tan(\phi_b)$,

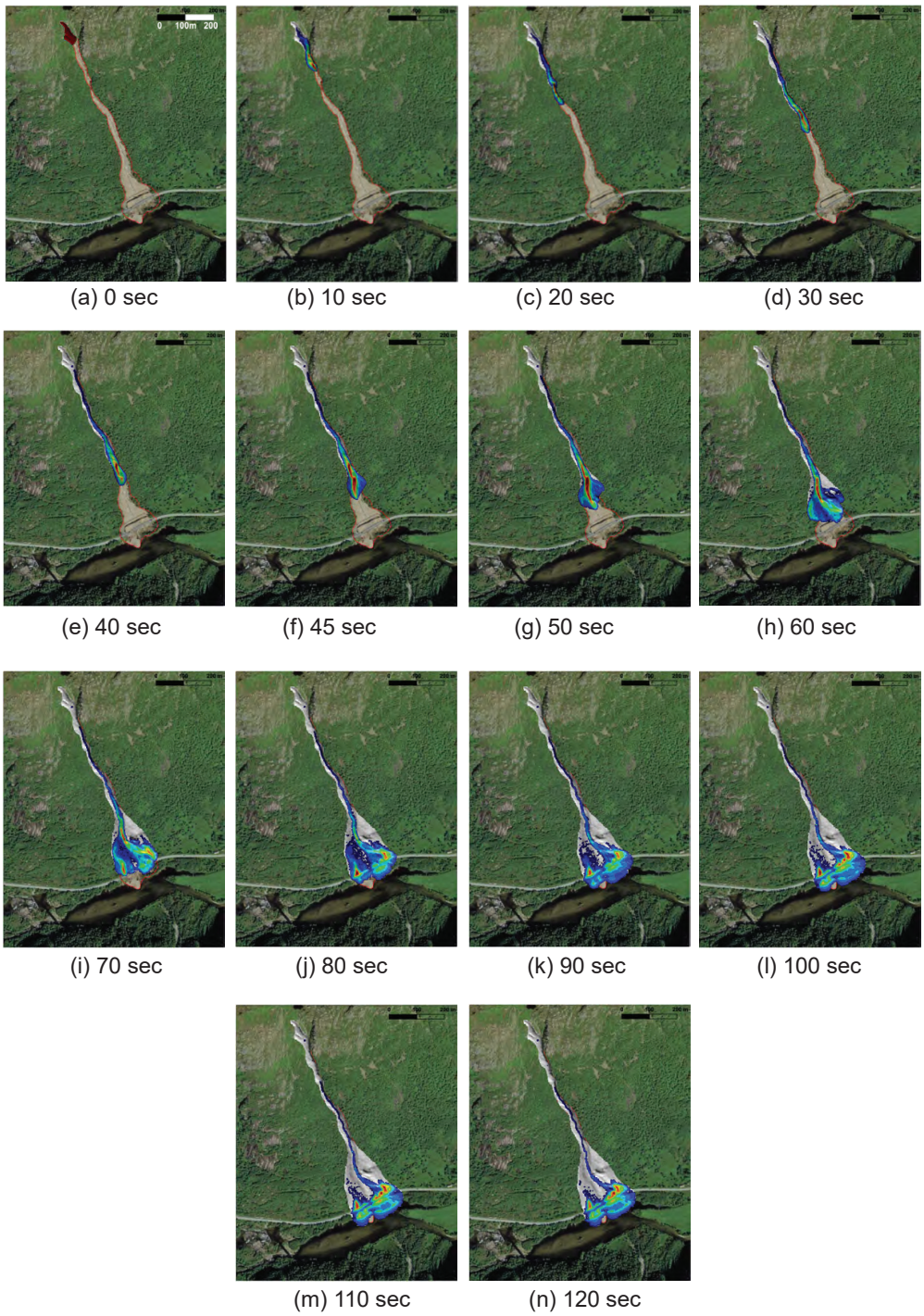

Fig. 6.21: Analysis simulation steps of the event using parameters given in Table 6.6

ξ, as well as the B_{fact} based on the run-out distance and area of deposition observed on site. In this simulations, partial liquefaction ($\overline{\Delta P}_{wp} = 0.7$) was considered at the start of the simulation as we assume some part of the slide will not be fully remolded. However, full saturation of the debris mass, $S_r = 1.0$, and a solid concentration of $C_s = 60\%$ by volume were assumed.

Several combinations of the governing parameters were run and evaluated according to the run-out distance and lateral spread at the deposition area. The major behaviors of the debris-flow were replicated when the following parameters given in Table 6.6 were used.The analysis steps are given in Figure 6.21. The run-out distance and the deposition area were replicated well although lateral spread beyond the actual flow boundary was observed, as shown by Figures 6.21(d) and (e). This lateral spread, that happened after the flow went out of the confining channel, could be a result of not considering the resistance offered from the vegetation.

After the back-calculation of the event, the embankment wall that was built after the slide and three options of implementing screen(s) are evaluated.

6.4.5 Evaluation of the countermeasures

There was an existing $5m$ high embankment wall made from the debris deposit. Its width was around $90m$ wide. This protective measure as well as applications of the screen-type countermeasure were evaluated using the GeoFlow_SPH-FD numerical model based on the back-calculated parameters given in Table 6.6.

Embankment walls

The existing countermeasure constructed after the debris-flow happened was $90m$ wide. Its height was $5m$ as measured during the field visit. Since the deposited debris material was used to construct the embankment wall, there was a dugout on the mountain side of the wall, which can serve as an accumulating space. The DTM was modified using a software called Surfer to create this existing wall on the pre-slide DTM. Then, the simulation was run using the calibrated parameters and the $5m$ high embankment wall was evaluated. The resulting final flow is presented in Figure 6.22. The wall was seen to be insufficient to contain the whole debris-flow. The dugout was seen to accumulate around $5m$ high debris. However, the width of this wall was seen to be unable to contain the wide debris-flow.

To exhaustively evaluate different embankment walls, two heights ($7.5m$ and $10m$) of embankment walls and extension of wall width were assessed. While varying the heights, options of extending the width of the wall was considered. The DTM was modified for each case and simulations were run on respective options. The results are given in Fig-

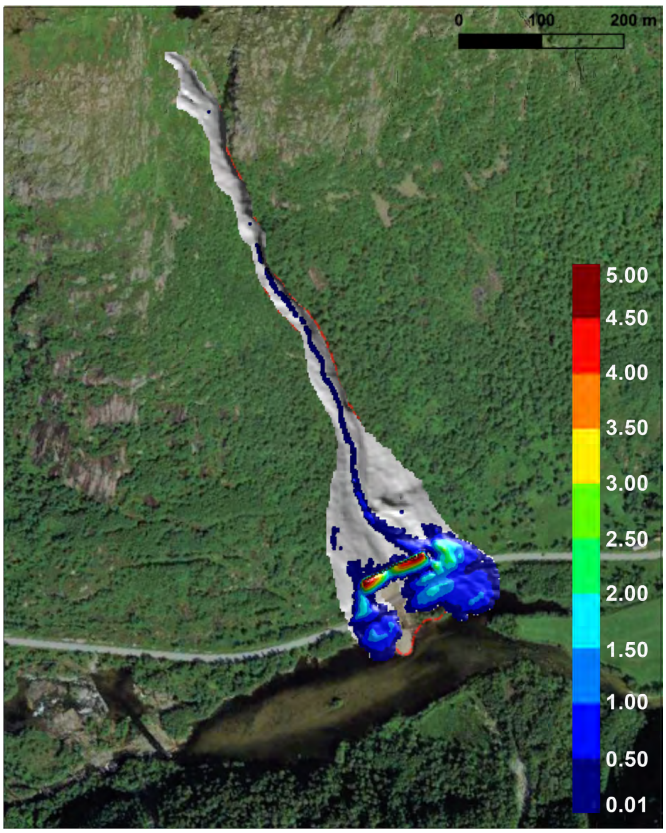

Fig. 6.22: Evaluation of the existing $5m$ tall wall, $90m$ wide embankment wall. (scale in $[m]$).

ure 6.23.

According to what the terrain allowed, the wall was extended by $60m$ on the left side and $70m$ on the right side giving it a total width of $220m$. The maximum accumulation thickness in case of $7.5m$ high wall was seen to be around $7.3m$ and there was no debris over-topping the wall. However, the debris-flow passed the wall on either sides requiring the need to lateral extension, Figure 6.23(a). The $7.5m$ high wall with the lateral extensions was then evaluated and its performance is given by Figure 6.23(b). It has almost contained the entire debris-flow except it was over-topped in few locations. This size looks to be the limiting embankment wall dimension with safety factor of unity. The final case was evaluation of the $10m$ high wall with the lateral extensions. Figure 6.23(c) shows that this wall option was able to contain the whole flow without allowing any debris to pass and rich at the road section. However, building a $10m$ high embankment wall would require a wide area and several cubic meters of material. In addition, the $10m$ high

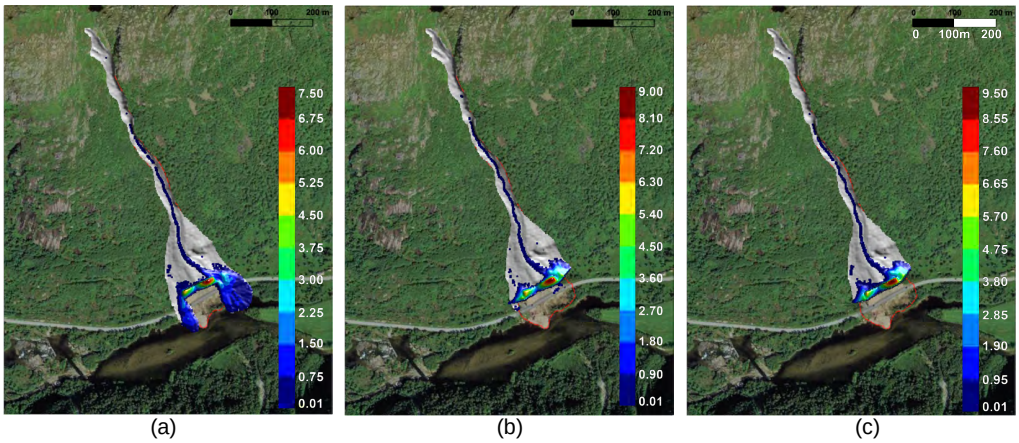

(a) (b) (c)

Fig. 6.23: Simulation result of embankment wall with: (a) 7.5m high wall, (b) 7.5m high, wide wall, and (c) 10m high, wide wall

wall safety and stability at normal time and during debris-flow impact must be carefully looked and evaluated.

Screen-type countermeasures

The screen-type debris-flow countermeasure which has been used in japan and china were placed as horizontal leveled terrain, as reported in, among others, Kim et al. (2012), Gonda (2009), and Liu et al. (2017). In addition, it was mentioned in Kim et al. (2012) that it is more effective and suitable to install the screen in a narrow section of the expected debris-flow channel. Therefore, the DTM of existing topography was edited and modified using Surfer software, QGIS, and ArcGIS, to horizontally place the screens at strategically chosen locations.

Four locations were selected and are shown in Figure 6.24. The first option to place

Table 6.7: The Screen sizes and implementation locations along with their combination options

Screen location	Screen area	Screen combination options			
at	$[m^2]$	CM-1	CM-2	CM-3	CM-4
535m AMSL	200	✓	✓	✓	—
500m AMSL	604	—	✓	✓	—
415m AMSL	1 000	—	—	✓	—
349m AMSL	3 025	—	—	—	✓

a screen was selected to be at a narrow section at elevation 535m AMSL, as shown in

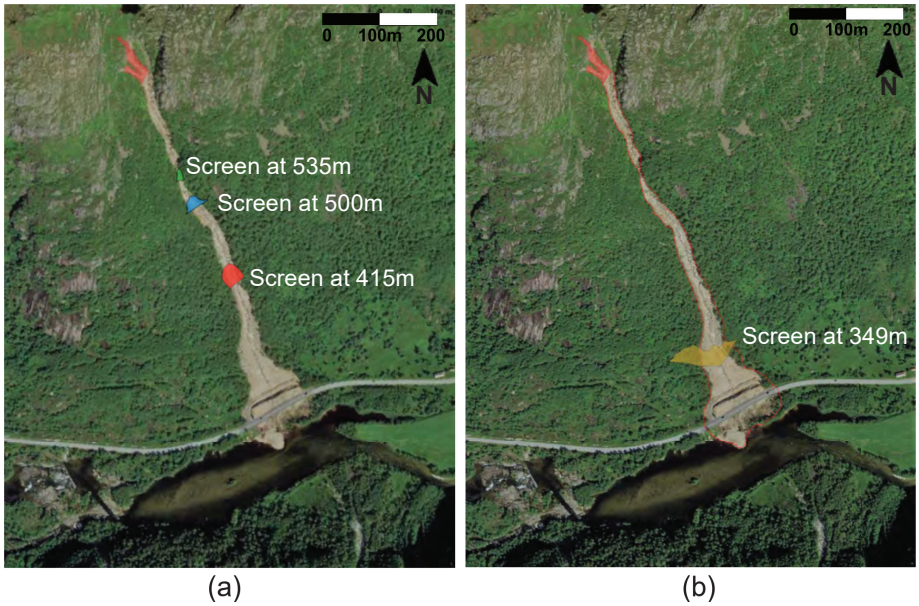

Fig. 6.24: Proposed locations of screens: (a) for CM-1, CM-2, and CM-3, (b) for CM-4 based on their combinations given in Table 6.7

Figure 6.24(a). It was approximately $20m$ long with an average width of $10m$ in the gully. The location has average slope of $30°$ at which it creates a vertical drop of $12m$ at the end of the screen. Similarly, other two screens were placed at elevations of $500m$ and $415m$ AMSL to evaluate them in combination to one another. Finally, a large screen near the deposition area was placed to evaluate the screen performance if placed near the road section (as seen in Figure 6.24(b)). Their dimensions and their combinations options as countermeasures (CM) is given in Table 6.7. The numerical simulation of each countermeasure option, as described in Table 6.7, was conducted using the back-calculated governing rheological and material parameters given in Table 6.6. The effectiveness of the options was evaluated based on the reduction of run-out distance, more specifically for not reaching at the road section. In addition, the deposition thickness on the road section was investigated along with the approach velocity of the flow near the road.

The simulation results at the flow end are given in Figure 6.25. Summary of approach velocity near the road, accumulation height, and width on the road are given in Table 6.8. CM-1 shows provision of a $200m^2$ screen $150m$ from the start of the flow at a selected narrow section. It was found inadequate to contain the flow and protect the road. Moreover, the steep location with $30°$ slope could not allow the material to accumulate upstream of the screen. The next option was to assist it by adding a subsequent screen at elevation $500m$.

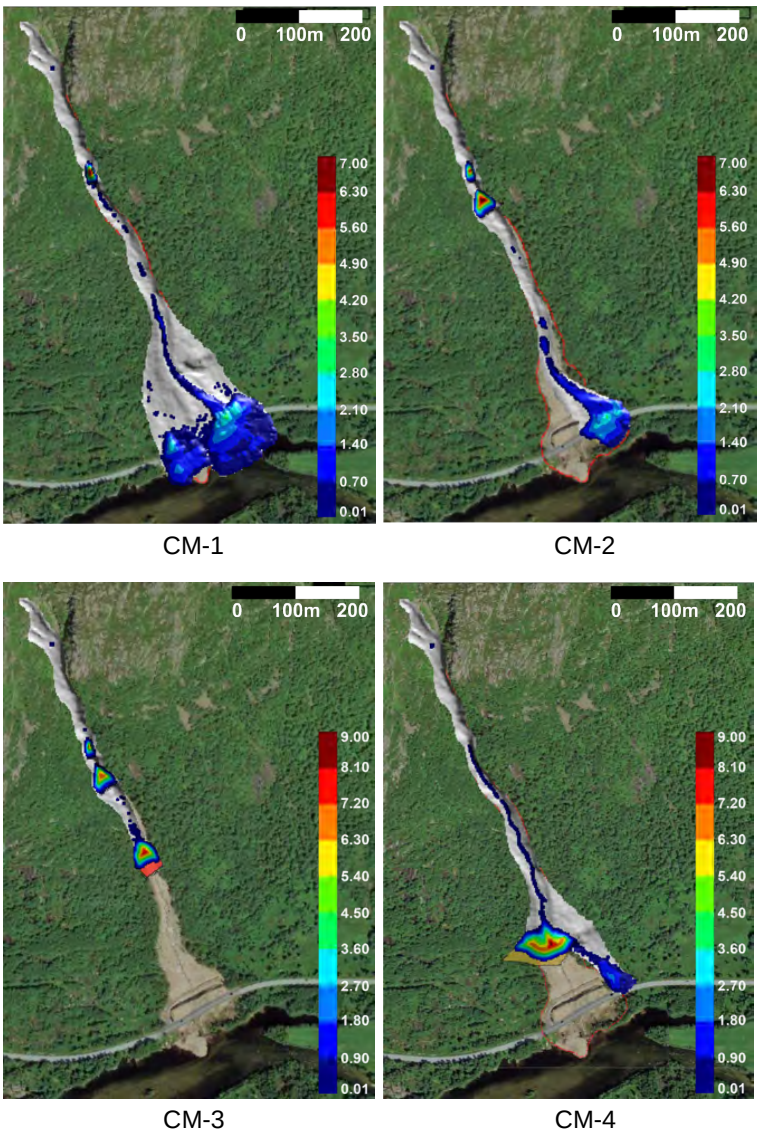

Fig. 6.25: Simulation results for different combinations options of the screen given in Table 6.7.

CM-2 was made by combining the first two screens. The second screen position was selected for an advantage of having a relatively gentler slope upstream of it. This helps in accumulating more material that supplemented effect of its wider fluid screening area. Combining the first two screens yield a satisfactory result as it reduces the affected road width by almost 53% and the approach velocity by 20% (from the values given in Table 6.8).

The third option, CM-3, was applied to see what it takes for the screen-type debris-

Table 6.8: Simulation results for different combinations of the screen-type countermeasure

		CM-1	CM-2	CM-3	CM-4
$v_{approach}$ $[m/s]$		3.65	2.9	0.0	1.0
h_{max} on the road $[m]$		2.3	2.65	0.0	0.5
h_{max} on screen(s) $[m]$	@535m	6.9	6.15	6.3	—
	@500m	—	6.93	7.2	—
	@415m	—	—	7.91	—
	@349m	—	—	—	8.4
Width on the road $[m]$		184	86.0	0.0	35.0

flow countermeasure to completely stop the flow before reaching to the road section. The location for the placement of the third screen was chosen to be near the second screen before the flow gains additional momentum. As seen from Figure 6.25(c), the area of the third screen is not fully utilized where it was possible to halt the flow even by half of the current size. CM-3 has effectively contained the flow before reaching the road and it is safe to say that three properly placed screens can be able to contain this debris-flow.

The fourth option, CM-4, shows that providing a wide screen near the deposition area might not be sufficient by itself to contain a debris-flow after the flow goes through an entrainment process with higher momentum. This screen was almost 15 times larger than the first, and 5 times larger than the second screen. Yet it was seen to allow part of the flow towards the road. This shows that screen-type countermeasure is mainly works in reducing the flow energy which is challenging to do at once, especially if placed near an infrastructure to protect.

To show the effect of filtering the water and dissipating the pore-water pressure in the debris-flow, the condition of CM-3 was simulated without assigning the three screen location as permeable. The simulation gave the effect of providing a horizontal topography in the downhill motion of the debris-flow. Figure 6.26 shows the comparison between providing the screens and providing only the topographical change. The maximum accumulation thickness observed was nearly $4m$ at location $415m$ which was only half of the maximum accumulation thickness seen when using the screen on the same location. Beyond this, the road could not be protected by these topographical changes only. Therefore, the road can be secured if this topographical change is complemented with filtering the water out by using screens. After the scaling-up study of screens using the numerical model as well as the different laboratory studies conducted in the laboratory, it is found vital to recommend how to implement the screen in actual debris-flow prone areas. In

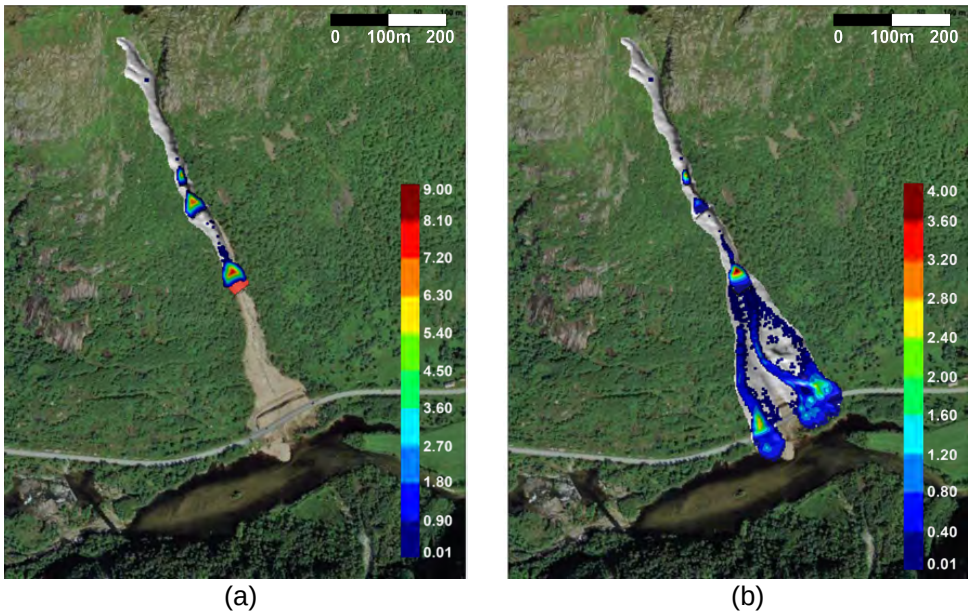

Fig. 6.26: Simulation results comparing between (a) the CM-3 screens and (b) the CM-3 topographical change contribution (solid surface)

this recommendation, implementation techniques in Kamikami Valley, Japan is also used.

A simple sketch is given in Figure 6.27 to show the implementation technique. Narrow sections are ideal places to install the screens. It is economical and can help trapping most part of the debris in a narrow section although faster flows are expected in narrow sections. In addition, it is best if the a screen can be placed near the expected triggering area with consideration to location's accessibility and working conditions. This will help in dissipating the flow energy before entraining more mass and developing into a larger one. The length, L and W can be determined according to site conditions and using the numerical tool. The grid cross-sectional sizes can be taken as $0.2m - 0.25m$ with similar screen opening width that has 50% opening ratio as seen in Kamikami Vally case (Gonda 2009, Yokota et al. 2012). The d_{50} of the expected debris material can also be considered as opening width of the screen according to the laboratory study and GSD reports from Kamikami Valley (Nisimoto et al. 1994). In addition, from the incidents seen during the laboratory tests, clogging of the grains with sizes similar to the opening width of the screens can be avoided by using grids with isosceles trapezoidal cross-sectional shape. This ensures the immediate functional availability of the screen after a debris-flow event happens as quick cleaning process facilitated.

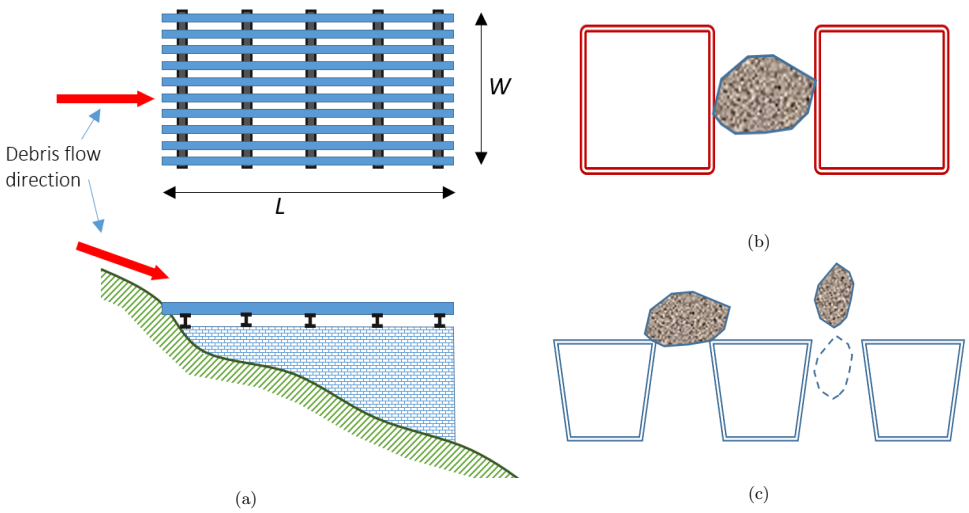

Fig. 6.27: Screen implementation sketch (a) plan and profile, (b) rectangular cross-section of screen grid with possible clogging, and (c) isosceles trapezoidal cross-section without clogging possibility.

6.4.6 Summary

In this numerical study of a real debris-flow case, it was shown that the GeoFlow_SPH-FD model was a promising tool which could capture the major behaviors of debris-flow in steep terrains. It was also able to reasonably replicate run-out distance, flow height, deposition height, and flow velocity. Its ability to simulate the evolution of pore-water pressure, which is deemed to be one of the important factors in the mobility of debris-flow, makes the flow propagation simulation more fitting to the reality. Moreover, the pore-water pressure evolution feature makes it suitable for investigating the screen-type debris-flow countermeasures. This was because the main purpose of the countermeasure is to dissipate pore-water pressure by filtering out the fluid part from a debris-flow mass.

By using this tool, the performance of the screen-type debris-flow countermeasure in real scale was evaluated using the Mjåland debris-flow case. The effectiveness and potential of screens in mitigating debris-flows in steep coastal terrains was demonstrated. It was shown that proper location, placement and combination of screens could be one and simple alternative to effectively mitigate such areas that are prone to debris-flow threats. Based on the studies conducted on screen and the capability of the numerical model, an implementation technique is also recommended.

7 Summary and conclusions

The mountainous terrains of Norway are exposed to debris-flow hazards due to extreme weather events with intense and prolonged rainfall. This hazard is expected to increase with the changing climate. The E39 coastal highway is a main corridor in the western part of Norway that is exposed to debris-flow hazards. In connection with a long-term goal to upgrade the E39 coastal highway, this work focuses on understanding debris-flows in steep coastal terrains and how to mitigate the highway from the debris-flow threats. Based on a broad pilot study, it was decided to concentrate the work on the screen countermeasure for its potential to mitigate debris-flows. The study was conducted using laboratory flume models and numerical simulations.

In this study, the overall behavior of debris-flow, its dependency on flow compositions like solids concentration, fines content, and water content were investigated using a laboratory flume model. The debris-flow composition was varied to investigate the flow regime by comparing it with other laboratory tests and real debris-flows using dimensionless parameters and dimensionless analyses. A screen-type debris-flow countermeasure (simply, a screen) was investigated for its capability and performance in reducing debris-flow mobility, using the variation of debris-flow compositions. The evaluation was made based on reductions of flow velocity, run-out distance, and the flow's impact force. Also, the screen performance in combination with a guide wall and an underpass was demonstrated. A focused and closer look at the working mechanism of screens was also performed using Particle Image Velocimetry (PIV) analyses. The position of shearing layer and the rate of up-ward shifting (rate of accumulation) due to the filtration of fluid was demonstrated. The performance of these screens was further back-calculated using the GeoFlow_SPH-FD numerical model. The model was capable of simulating debris-flows, including its pore-water pressure evolution. This model was also used for back-calculating a real, full-scale debris-flow case, as well as for up-scaling results from screen tests.

Debris-flow composition and flow regime study
Debris-flow behavior study was conducted in Model-2 by varying water and fines content along with the total volume, V. Varying these characteristics help determine to which extent the laboratory tests replicate the behavior and characteristics of real debris-flows by using scale-independent parameters that describe flow regimes. The tests with 5.4% fines content, $d < 0.06mm$, (G1) and solids concentrations, C_s of 60% and 55%, showed flow regimes dominated by frictional stresses that most real debris-flows probably fall in. In addition, some of the tests conducted with 14% fines content (G2) and $C_s = 60\%$

showed similar flow characteristics of frictional stress dominance.

The debris-flow composition affected the resulting mobility as well as the final run-out distance, L_{FL}. The changes in L_{FL} was observed to be primarily affected by the changes in C_s, followed by the changes in fines content. The higher the water content (lower C_s), the longer the L_{FL} while increasing the fines content also contribute in extending the L_{FL}. In addition, increase in the V resulted in almost a linear increase in the L_{FL}. It was observed that the L_{FL} was not linearly changing with C_s. With non-linear behavior change observed around $C_s = 55\%$, the $C_s = 50\%$ tests showed more fluid-like flow with turbulent behavior and longer L_{FL} whereas the $C_s = 60\%$ flows exhibited viscous behavior with relatively slower flow and shorter L_{FL}.

The screen countermeasure study

The potential of using a screen in order to reduce the mobility of debris-flow was studied. Its effect on the L_{FL}, flow velocity, v, and flow impact force was investigated. The first study was performed in Model-1 to investigate the effect of screen length and opening width. A general observation on the $0.5m$ and $1m$ long screens show that the L_{FL} and v decreases with an increase in screen length. However, among the three screen opening-widths, applying an opening equal to $2mm$, that was $\approx d_{50}$ of the debris material used, was found to be optimal regarding reducing both the L_{FL} and v.

Studies in Model-1 continued using the screen with $d_{50} \approx 2mm$ opening width. Two screens with $0.25m$ and $0.5m$ lengths were studied with and without the use of downstream underpass. The underpass represents a safe passage for debris-flows with elevated roads near the foot of a mountain. The tests were conducted by varying the V and the C_s. The L_{FL}, the downstream deposition thickness, t_d, the run-up height on the guide-wall of the underpass, and the flow impact force show progressive reduction with increasing screen length. The screens' performance was affected by the debris-flow composition that was varied by simultaneous change of V and C_s. Large V with smaller water content ($V = 50L$, $C_s = 60\%$) and small V with large water content ($V = 30L$, $C_s = 50\%$) resulted in similar effects while the intermediate V and C_s ($V = 40L$, $C_s = 55\%$) resulted in slightly higher values in L_{FL}, t_d, and run-up heights. However, the impact force increased with an increase of the V and vice versa.

The debris-flow composition variation test that was conducted in Model-2 on the screens showed the individual effects of changing the fines content, V, and C_s on their performance. Two screen lengths ($0.25m$ and $0.5m$) with a $2mm$ opening width were investigated. Debris accumulation thickness on each screen was decreased, and the L_{FL} was increased when using debris material with 14% fines content compared to the material with 5.4% fines content. The additional fines content was believed to affect the fluid separation

process when the flow passes over the screen. The L_{FL} increases when either V or water content increases. In addition, the accumulation thickness on the screens increased with an increase of V or with a decrease in water content.

To investigate the accumulation process on the screens, Particle Image Velocimetry (PIV) analyses were performed on the $0.5m$ long screen tests conducted using the material with 5.4% fines content in Model-2. The analyses showed how the screens function. An accumulation mechanism was observed, providing a layer-by-layer deposition over the screen. The process was facilitated by the filtering of the fluid, which, after a moment, was accompanied by a dam of deposited debris. During this layer-by-layer deposition process, the shearing layer was forced to shift upward. The rate at which this shift happens (rate of accumulation) indicates the performance of the screen. This rate was seen to be affected by debris-flow composition. The rate of accumulation was faster when V and water content decreased while it was seen to take a relatively longer duration for increasing V. However, the final accumulation thickness grows with an increase of V.

The numerical study
The GeoFlow_SPH-FD numerical model parameters and its Voellmy rheology parameters were calibrated for the debris-flow composition. The calibration showed a relation between turbulence coefficient, ξ, and the C_s. An increase in ξ was related to a decrease in C_s (or an increase in water content). This relation indicates that the flow turbulence was related to the amount of water in the debris-flow. Similarly, the consolidation factor, B_{fact}, relates with the fines content variation. A decrease in B_{fact} was related to an increase in fines content. This implies that decreasing B_{fact} slows down the dissipation of the pore-water pressure. This agrees with the laboratory findings showing that the debris material with more fines retain the water (fluid part) longer than those with less fines. The back-calculated basal friction angle, $\phi_b = 15°$, was found low and to be different from internal friction angles of the material expected to be about $\phi \approx 30°$. This basal friction angle expresses the friction in a turbulent debris-flow.

The capability of the GeoFlow_SPH-FD model in simulating the evolution of pore-water pressure was also demonstrated by back-calculating the results from the tests conducted with the screen countermeasure. Both the 1D and 2D simulations replicate the pore-water dissipation in the debris-flow resonably while flowing over the screen. Moreover, the accumulation thickness over the screen that was observed in the laboratory was replicated to a reasonable degree, which made the numerical model a promising tool for simulating the screens for real debris-flow cases.

The Mjåland debris-flow event that happened in the steep coastal terrains of Norway was evaluated using the GeoFlow_SPH-FD numerical model. Calibration of the model

and its parameters was done by back-calculating the event by incorporating pore-water pressure and entrainment. After reasonable replication of the event, different options of screen combinations were simulated. The options were combinations of screens in different locations of the debris-flow channel. The simulation showed that the option with three consecutive screens that were strategically placed in the flow channel was able to halt the debris-flow and protect the road located at the foot of the mountain. The result also showed the capability of the numerical model for evaluating and scaling-up of the screen performance.

The E39 coastal highway route and similar roads in steep terrain need effective countermeasures for the debris-flow threats. This study contributes insight and tools necessary to choose debris-flow countermeasures. The screen structure was shown to potentially reduce the mobility of the debris-flow through laboratory model investigations and numerical simulations. The knowledge obtained from the laboratory investigations together with the simulation capability of the GeoFlow_SPH-FD numerical model to capture screen performance can be beneficial in debris-flows mitigation process. As the performance in the laboratory and simulation capability of the numerical model have shown, strategically selected and placed screens (and perhaps combined with other countermeasure types) can mitigate road sections and settlements that are prone to debris-flow dangers. If need arises to mitigate an area with screen(s), the numerical model can help in scaling up the size (area) and effective locations of the required screen(s) while the screen opening width can be suggested to have percentage opening of 50% or opening width that relates with the d_{50} with grid sizes ranging between $0.20m$ and $0.25m$.

New developments during this study

A new and simple method of measuring flow impact force of debris-flow using a pillar (a passable structure) was developed. The method was evaluated by using existing analytical formulas and dimensionless parameters. From these flow mobility and impact pressure relationships, the hydro-dynamic power-function relationship between Froude number, $F_r = v/(\sqrt{gh})$ and the empirical pressure coefficient (normalized impact pressure, $\alpha = F/(A\rho v^2)$) looked to fit reasonably well with the test results. This relationship serves as a bridge between real debris-flows ($F_r \leq 3$) and results of the laboratory flume tests, where typically have $F_r > 3$. Moreover, the effects of debris-flow composition on F_r and α were studied. Increasing fines and water contents increase the F_r and slightly decrease the α. Increasing V reduces the variation (range) in F_r and reduces the α value. It was also demonstrated that this relationship was not affected by impact width variation. The impact force test results were also compared with another hydrodynamic relationship that related F_r with 2α. The relationship was developed from aggregates of granular flow data and it covers a wide range of F_r and 2α values. The impact force test data from this study (fluidized flow) seen to fit well in the intermediate flow region described by

$0.1 < F_r < 10$ where most real and fluidized laboratory debris-flows fall in.

Another simple pore-water pressure measurement device was developed and installed in the bed of both Model-1 and Model-2. The basal pore-water pressure of the flow was successfully measured on few tests. The result showed that, at the peak flow height, the liquefaction level (ratio of pore-water pressure to the total pressure) varies between 74% and 98%. In addition, the contribution of pore-water pressure to the flow mobility and its prolonged presence in debris deposit long after the debris-flow stops were demonstrated. Moreover, the challenges and limitations of measuring pore-water pressure in an open channel were also described.

A new flume model (Model-2) along with new debris-flow mixing and releasing cylinder was also developed during this study, which was done to improve repeatability and accuracy in relation to tests in Model-1. In addition, Model-2 was designed and built in such a way that the channel width and slope can be adjusted. The new mixing cylinder was designed to provide homogeneous well-mixed debris-flow material. The mixer was integrated into the data acquisition program, where mixing and releasing were controlled remotely.

8 Recommendation for future work

The following are recommended for future work:

- During this study, all the screen tests involve the use of only one screen at a time. As future work, investigating the performance of two consecutive screens as well as the performance of a screen with previously accumulated debris can expand the understanding further.
- Based on the existing hazard and susceptibility maps and the rainfall expectations, the screens can be applied in some selected sites by installing them in narrow sections where they can be more effective and economical. The numerical model can be used to estimate the number and location(s) of screens before applying them on site.
- In using the screens, it is recommended to use grids with an isosceles trapezoidal cross-sectional shape where the narrow edge is placed in the bottom, which can help in avoiding debris grains getting stuck in the opening gap after a debris-flow event. This phenomenon was observed while cleaning the screen after conducting tests in the laboratory and this cross-section can be used in the future suggested laboratory tests.
- To strengthen the database of debris-flows (in atlas.nve.no and skredregistrering.no), field assessments should be accompanied by a quick digital terrain model (DTM) scanning of the area after a landslide event. The DTM scanning can help to estimate and study the amounts of erosion, deposition, and locate the starting area along with its cause more accurately.
- For further development of the GeoFlow_SPH-FD numerical model, for one-phase and two-phase flows, it is recommended to use the result obtained from the PIV analyses. It is of particular interest to look further into flow over a permeable surface. The aim is to replicate the fluid-particle separation process and the progressive layer-by-layer accumulation of the debris.
- The flume Model-2 is well developed by integrating its operation with the data acquisition program, including starting the mixer, releasing the mass while mixing, and initiating the data logging. However, the video cameras are not integrated, and it is recommended to do so to develop the flume model further.

References

Arattano, M. and Franzi, L. (2003). On the evaluation of debris flows dynamics by means of mathematical models. *Natural Hazards and Earth System Science*, 3(6):539–544.

Armanini, A. (1997). On the dynamic impact of debris flows. In Armanini, A. and Michiue, M., editors, *Recent Developments on Debris Flows*, pages 208–226, Berlin, Heidelberg. Springer.

Armanini, A., Dalri, C., and Larcher, M. (2014). Slit-Check Dams for Controlling Debris Flow and Mudflow. In *Disaster Mitigation of Debris Flows, Slope Failures and Landslides*, pages 141–148, Tokyo. Universal Academy Press, Inc.

Armanini, A., Larcher, M., and Odorizzi, M. (2011). Dynamic impact of a debris flow front against a vertical wall. In *5th International Conference on Debris-Flow Hazards. Mitigation, Mechanics, Prediction and Assessment*, pages 1041–1049, Rome.

Ashwood, W. and Hungr, O. (2016). Estimating total resisting force in flexible barrier impacted by a granular avalanche using physical and numerical modeling. *Canadian Geotechnical Journal*, 53:1700–1717.

Atienza, E. F. and Hipolito, D. M. (2010). Challenges on Risk Management of Sediment-Related Disasters in the Philippines. *International Journal of Erosion Control Engineering*, 3(1):85–91.

Bagnold, R. A. (1954). Experiments on a gravity-free dispersion of large solid spheres in a Newtonian fluid under shear. *Proceedings of the Royal Society of London. Series A.*, 225:49–63.

Beguería, S., W. J. Van Asch, T., Malet, J. P., and Gröndahl, S. (2009). A GIS-based numerical model for simulating the kinematics of mud and debris flows over complex terrain. *Natural Hazards and Earth System Science*, 9(6):1897–1909.

Bowman, E. T., Laue, J., Imre, B., and Springman, S. M. (2010). Experimental modelling of debris flow behaviour using a geotechnical centrifuge. *Canadian Geotechnical Journal*, 47(7):742–762.

Breien, H., De Blasio, F. V., Elverhøi, A., and Høeg, K. (2008). Erosion and morphology of a debris flow caused by a glacial lake outburst flood, Western Norway. *Landslides*, 5(3):271–280.

Brown, D. (2019). Tracker Video Analysis and Modeling Tool v. 5.0.6. URL: https://physlets.org/tracker/.

Bugnion, L., Boetticher, A. V., and Wendeler, C. (2012). Large Scale Field Testing of Hillslope Debris Flows Resulting in the Design of Flexible Protection. In *12th Congress Interpraevent 2012*, pages 59–66, Grenoble.

Canelli, L., Ferrero, A. M., Migliazza, M., and Segalini, A. (2012). Debris flow risk mitigation by the means of rigid and flexible barriers - Experimental tests and impact analysis. *Natural Hazards and Earth System Sciences*, 12(5):1693–1699.

Cascini, L., Cuomo, S., Pastor, M., and Rendina, I. (2016). SPH-FDM propagation and pore water pressure modelling for debris flows in flume tests. *Engineering Geology*, 213:74–83.

Chen, N. S., Zhou, W., Yang, C. L., Hu, G. S., Gao, Y. C., and Han, D. (2010). The processes and mechanism of failure and debris flow initiation for gravel soil with different clay content. *Geomorphology*, 121(3-4):222–230.

Choi, C., Ng, C., Song, D., Kwan, J., Shiu, H., Ho, K., and Koo, R. (2014). Flume investigation of landslide debris-resisting baffles. *Canadian Geotechnical Journal*, 51(5):540–553.

Christen, M., Kowalski, J., and Bartelt, P. (2010). Ramms: Numerical simulation of dense snow avalanches in three-dimensional terrain. *Cold Regions Science and Technology*, 63(1):1–14.

Christiansen, L. F. (2013). Flomskred: Litteraturstudie go modellforsæk med voller som sikringstiltak [in norwegian]. Msc thesis, NTNU, Trondheim, Norway.

Costa, J. E. (1984). Physical Geomorphology of Debris Flows. In *Developments and Applications of Geomorphology*, pages 268–317. Springer, Berlin, Heidelberg.

Coussot, P. and Meunier, M. (1996). Recognition, classification and mechanical description of debris flows. *Earth-Science Reviews*, 40(3-4):209–227.

Cui, P., Zeng, C., and Lei, Y. (2015). Experimental analysis on the impact force of viscous debris flow. *Earth Surface Processes and Landforms*, 40(12):1644–1655.

Cuomo, S., Moretti, S., and Aversa, S. (2019). Effects of artificial barriers on the propagation of debris avalanches. *Landslides*, 16(6):1077–1087.

Cuomo, S., Moretti, S., D'Amico, A., Frigo, L., and Aversa, S. (2020a). Modelling of geosynthetic-reinforced barriers under dynamic impact of debris avalanche. *Geosynthetics International*, 27(1):65–78.

Cuomo, S., Moretti, S., Frigo, L., and Aversa, S. (2020b). Deformation mechanisms of deformable geosynthetics-reinforced barriers (DGRB) impacted by debris avalanches. *Bulletin of Engineering Geology and the Environment*, 79(2):659–672.

D'Agostino, V., Cesca, M., and Marchi, L. (2010). Field and laboratory investigations of runout distances of debris flows in the Dolomites (Eastern Italian Alps). *Geomorphology*, 115(3-4):294–304.

Daido, A. (1993). Impact force of mud debris flows on structures. In *XXV IAHR congress proceedings, the international association for hydraulic research*, volume 3, pages 211–211.

de Haas, T., Braat, L., Leuven, J. R. F. W., Lokhorst, I. R., and Kleinhans, M. G. (2015). Effects of debris flow composition on runout, depositional mechanisms, and deposit morphology in laboratory experiments. *Journal of Geophysical Research: Earth Surface*, 120(9):1949–1972.

Faug, T. (2015). Macroscopic force experienced by extended objects in granular flows over a very broad Froude-number range. *The European Physical Journal E*, 38(5):1–10.

Fink, J. H., Malin, M. C., D'Alli, R. E., and Greeley, R. (1981). Rheological properties of mudflows associated with the spring 1980 eruptions of Mount St. Helens Volcano, Washington. *Geophysical Research Letters*, 8(1):43–46.

Fiskum, E. (2012). Flomskred: Testing av ulike sikringstiltak i modellforsøk [in norwegian]. Msc thesis, NTNU, Trondheim, Norway.

Frauenfelder, R., Solheim, A., Isaksen, K., Romstad, B., Dyrrdal, A. V., Ekseth, K. H. H., Gangstø Skaland, R., Harbitz, A., Harbitz, C. B., Haugen, J. E., Hygen, H. O., Haakenstad, H., Jaedicke, C., Jónsson, Á., Klæboe, R., Ludvigsen, J., Meyer, N. K., Rauken, T., and Sverdrup-Thygeson, K. (2016). Impacts of extreme weather events on transport infrastructure in norway. In *EGU General Assembly - Geophysical Research Abstracts*, volume 18, pages 15407–3.

Golden Software, Inc. (2014). Grapher - Version 10.5.1011.

Gonda, Y. (2009). Function of a debris-flow brake. *International Journal of Erosion Control Engineering*, 2(1):15–21.

He, S., Liu, W., and Li, X. (2016). Prediction of impact force of debris flows based on distribution and size of particles. *Environmental Earth Sciences*, 75(4):298.

Heller, P. and Jenssen, L. (2009). Modellforsøk med flomskred mot bruer virkning av bruåpning og ledevoller [in norwegian]. Report TeknologiRapport No. 2582, Norwegian University of Science and Technology (NTNU) and Norwegian Public Roads Administration (NPRA), Trondheim, Norway.

Huang, H.-P., Yang, K.-C., and Lai, S.-W. (2007). Impact force of debris flow on filter dam. *momentum*, 9:3218.

Huebl, J. and Fiebiger, G. (2005). Debris-flow mitigation measures. In Jakob, M. and Hungr, O., editors, *Debris-flow Hazards and Related Phenomena*, book section 18, pages 445–487. Springer, Berlin Heidelberg.

Huebl, J. and Holzinger, G. (2003). Development of design basis for crest open structures for debris flow [in German]. Technical report, University of Natural Resources and Applied Life Sciences, Vienna.

Huebl, J., Suda, J., Proske, D., Kaitna, R., and Scheidl, C. (2009). Debris flow impact estimation. In *International Symposium on Water Management and Hydraulic Engineering*, pages 137–148, Macedonia.

Hungr, O. (1995). A model for the runout analysis of rapid flow slides, debris flows, and avalanches. *Canadian Geotechnical Journal*, 32(4):610–623.

Hungr, O. (2005). Classification and terminology. In Jakob, M. and Hungr, O., editors, *Debris-flow hazards and related phenomena*, pages 9–23. Springer, Berlin Heidelberg.

Hungr, O. and McDougall, S. (2009). Two numerical models for landslide dynamic analysis. *Computers & Geosciences*, 35(5):978–992.

Hungr, O., Morgan, G. C., and Kellerhals, R. (1984). Quantitative analysis of debris torrent hazards for design of remedial measures. *Canadian Geotechnical Journal*, 21(4):663–677.

ICHARM (2008). Debris-flow dewatering brakes: a promising tool for disaster management in developing countries. Newsletter 3, Public Works Research Institute, Japan.

ICHARM (2009). Testing and demonstrating a technology to cope with debris flows in mountain regions. Report, International Centre for Water Hazard and Risk Management, The Philippines.

Imai, K., Miyamoto, N., and Mizuyama, T. (1989). Test of a Debris-Flow Breaker at the Kamikamihori Valley, Mt. Yakedake (Part-2) [in Japanese]. *Journal of the Japan Society of Erosion Control Engineering*, 42(2):16–20.

Ishikawa, N., Inoue, R., Hayashi, K., Hasegawa, Y., and Mizuyama, T. (2008). Experimental Approach on measurement of impulsive fluid force using debris flow model. *Conference proceedings interpraevent*, 1:343–354.

Ishikawa, Y., Kusano, S., Kakimoto, T., and Morita, A. (1994). Experimental Study on Impact Effects of Debris-flow Breaker Screen [in Japanese]. *Journal of the Japan Society of Erosion Control Engineering*, 47(4):23–27.

Iverson, R. M. (1997). The physics of debris flows. *Reviews of Geophysics*, 35(3):245–296.

Iverson, R. M. (2015). Scaling and design of landslide and debris-flow experiments. *Geomorphology*, 244:9–20.

Iverson, R. M., Costa, J. E., and LaHusen, R. G. (1992). Debris-flow flume at H.J. Andrews Experimental Forest, Oregon. *USGS Open-File Report 92-483*, pages 2–3.

Iverson, R. M. and Denlinger, R. P. (2001). Flow of variably fluidized granular masses across three-dimensional terrain: 1. Coulomb mixture theory. *Journal of Geophysical Research: Solid Earth*, 106:537–552.

Iverson, R. M. and Lahusen, R. G. (1989). Dynamic pore-pressure fluctuations in rapidly shearing granular materials. *Science*, 246:796–9.

Iverson, R. M., Logan, M., LaHusen, R. G., and Berti, M. (2010). The perfect debris flow? Aggregated results from 28 large-scale experiments. 115(F3):F03005.

Iverson, R. M. and Vallance, J. W. (2001). New views of granular mass flows. *Geology*, 29(2):115–118.

Jaeggi, M. N. R. and Pellandini, S. (1997). In Armanini, A. and Michiue, M., editors, *Recent Developments on Debris Flows*, pages 186–207. Springer Berlin Heidelberg, Berlin, Heidelberg.

Jakob, M. and Hungr, O. (2005). *Debris-flow hazards and related phenomena*. Springer, Berlin; New York.

Kailey, P., Bowman, E. T., Laue, J., and Springman, S. M. (2011). Modelling debris flow processes with a geotechnical centrifuge. *Italian Journal of Engineering Geology*, pages 339–349.

Kaitna, R., Palucis, M. C., Yohannes, B., Hill, K. M., and Dietrich, W. E. (2016). Effects of coarse grain size distribution and fine particle content on pore fluid pressure and shear behavior in experimental debris flows. *Journal of Geophysical Research: Earth Surface*, 121(2):415–441.

Kim, Y. (2013). *Study on hydraulic characteristics of debris flow breakers and sabo dams with a flap*. Phd thesis, Kyoto University, Japan.

Kim, Y., Nakagawa, H., Kawaike, K., and Zhang, H. (2012). Numerical and Experimental Study on Debris-flow breaker. *Annuals of Disas. Prev. Res. Inst., Kyoto Univ.*, (55B):471–481.

Laache, E. (2016). Model testing of the drainage screen type debris flow breaker. Msc thesis, Norwegian University of Science and Technology (NTNU), Trondheim, Norway.

Le, T. M. H., Christensen, S. O., Watn, A., Christiansen, L., Emdal, A., and Norem, H. (2016). Effects of deflection wall on run-up height of debris flow. In Aversa, editor, *Landslides and Engineered Slopes. Experience, Theory and Practice - Aversa et al. (Eds)*, pages 1237–1244, Rome. Associazione Geotecnica Italiana.

Lichtenhahn, C. (1973). Die Berechnung von Sperren in Beton und Eisenbeton [in German]. Technical report, Mitt Forstl Bundes Versuchsanst Wein, Wein.

Lien, H.-P. (2003). Design of slit dams for controlling stony debris flows. *International Journal of Sediment Research*, 18(1):74–87.

Liu, F., Xu, Q., Dong, X., Yu, B., Frost, J., and Li, H. (2017). Design and performance of a novel multi-function debris flow mitigation system in Wenjia Gully, Sichuan. *Landslides*, 14(6):2089–2104.

Major, J. J. and Iverson, R. M. (1999). Debris-flow deposition: Effects of pore-fluid pressure and friction concentrated at flow margins. *Bulletin of the Geological Society of America*, 111(10):1424–1434.

Maricar, F., Hashimoto, H., Ikematsu, S., and Miyoshi, T. (2011). Effect of Two Successive Check Dams on Debris Flow Deposition. *Italian Journal of Engineering Geology and Environment*, pages 1073–1082.

McArdell, B. W., Bartelt, P., and Kowalski, J. (2007). Field observations of basal forces and fluid pore pressure in a debris flow. *Geophysical Research Letters*, 34(7):L07406.

McDougall, S. (2006). *A new continuum dynamic model for the analysis of extremely rapid landslide motion across complex 3D terrain*. Phd thesis.

McDougall, S. and Hungr, O. (2005). Dynamic modelling of entrainment in rapid landslides. *Canadian Geotechnical Journal*, 42(5):1437–1448.

Mergili, M., Fischer, J.-T., Krenn, J., and Pudasaini, S. P. (2017). r.avaflow v1, an advanced open-source computational framework for the propagation and interaction of two-phase mass flows. *Geoscientific Model Development*, 10(2):553–569.

Meyer, N. K., Dyrrdal, A. V., Frauenfelder, R., Etzelmüller, B., and Nadim, F. (2012). Hydrometeorological threshold conditions for debris flow initiation in Norway. *Natural Hazards and Earth System Science*, 12(10):3059–3073.

Milne, F., Brown, M., Knappett, J., and Davies, M. (2012). Centrifuge modelling of hillslope debris flow initiation. *CATENA*, 92:162–171.

Mizuyama, T. (1979). Computational method and some considerations on impulsive force of debris flow acting on sabo dams [in Japanese]. *Journal of the Japan Society of Erosion Control Engineering*, 32(1):40–43.

Mizuyama, T. (2008). Structural Countermeasures for Debris Flow Disasters. *International Journal of Erosion Control Engineering*, 1(2):38–43.

Moriwaki, H., Inokuchi, T., Hattanji, T., Sassa, K., Ochiai, H., and Wang, G. (2004). Failure processes in a full-scale landslide experiment using a rainfall simulator. *Landslides*, 1(4):277–288.

Multiconsult (2016). Vurdering av skredløp - Fv 45 Hunnendalsveien Mjåland [in Norwegian]. Technical report.

Ng, C. W. W., Choi, C. E., Song, D., Kwan, J. H. S., Koo, R. C. H., Shiu, H. Y. K., and Ho, K. K. S. (2014). Physical modeling of baffles influence on landslide debris mobility. *Landslides*, 12(1):1–18.

Nisimoto, H., Ishikura, K., Mizuyama, T., and Santosa, U. B. (1994). Behavior of a debris-flow on the debris-flow breaker at Mount Yake-dake [in Japanese]. *Journal of the Japan Society of Erosion Control Engineering*, 46(6(191)):21–24.

NPRA (2014). Flom- og sørpeskred [debris flows and slush avalanches (in norwegian)]. Report 139, Norwegian Public Roads Administration (NPRA).

NPRA (2016). Debris flows and slush avalanches. Handbook V139, Norwegian Public Roads Administration (NPRA), Norway.

NPRA (2019). The E39 Coastal Highway Route | Statens vegvesen.

NVE (2011). Plan for skredfarekartlegging - delrapport jordskred og flomskred [in norwegian]. Report No. 16/2011, NVE - Norwegian Water Resources and Energy Directorate.

NVE (2014). Preliminary regionalization and susceptibility analysis for landslide early warning purposes in norway. Report No. 37/2014, NVE - Norwegian Water Resources and Energy Directorate, Norway.

NVE (2017). Årsrapport for utførte sikrings-og miljøtiltak 2016 - Nr. 58/2017 [in Norwegian]. Technical report.

NVE (2018). Årsrapport for utførte sikrings-og miljøtiltak 2017 - Nr. 65/2018 [in Norwegian]. Technical report.

NVE (2019a). Årsrapport for sikrings-og miljøtiltak 2018 - Nr. 30/2019 [in Norwegian]. Technical report.

NVE (2019b). Sikrings- og miljøtiltak - Norges Vassdrags- og Energidirektorat (NVE).

NVE Atlas (2019). Noregs vassdrags- og energidirektorat (NVE) geografiske temadata, URL: https://www.atlas.nve.no/.

NVE skredregistrering (2019). Noregs vassdrags- og energidirektorat (NVE) Skredregistrering database, URL: https://www.skredregistrering.no/Forsiden.

NVE xgeo (2019). Noregs vassdrags- og energidirektorat (NVE) overvåking og varsling av flom, jordskred og snøskred, URL: https://www.xgeo.no/.

O'Brien, J. S., Julien, P. Y., and Fullerton, W. T. (1993). TwoDimensional Water Flood and Mudflow Simulation. *Journal of Hydraulic Engineering*, 119(2):244–261.

Ochiai, H., Okada, Y., Furuya, G., Okura, Y., Matsui, T., Sammori, T., Terajima, T., and Sassa, K. (2004). A fluidized landslide on a natural slope by artificial rainfall. *Landslides*, 1(3):211–219.

Ochiai, H., Sammori, T., and Okada, Y. (2007). Landslide Experiments on Artificial and Natural Slopes. In Sassa, K., Fukuoka, H., Wang, F., and Wang, G., editors, *Progress in Landslide Science*, pages 209–226. Springer, Berlin, Heidelberg.

Parsons, J. D., Whipple, K. X., and Simoni, A. (2001). Experimental Study of the Grain-Flow, Fluid-Mud Transition in Debris Flows. *The Journal of Geology*, 109:427–447.

Pastor, M., Blanc, T., Haddad, B., Drempetic, V., Morles, M. S., Dutto, P., Stickle, M. M., Mira, P., and Merodo, J. A. F. (2015). Depth Averaged Models for Fast Landslide Propagation: Mathematical, Rheological and Numerical Aspects. *Archives of Computational Methods in Engineering*, 22(1):67–104.

Pastor, M., Haddad, B., Sorbino, G., Cuomo, S., and Drempetic, V. (2009). A depth-integrated, coupled SPH model for flow-like landslides and related phenomena. *International Journal for Numerical and Analytical Methods in Geomechanics*, 33(2):143–172.

Pastor, M., Quecedo, M., Gonzalez, E., Herreros, M. I., Merodo, J. A. F., and Mira, P. (2004). Modelling of Landslides: (II) Propagation. In *Degradations and Instabilities in Geomaterials*, pages 319–367. Springer Vienna, Vienna.

Pierson, T. (1986). Flow behavior of channelized debris flows mount st. helens washington. In Abrahams, A., editor, *Hillslope processes*, pages 269–296. Boston, Allen & Unwin.

Poudyal, P., Choi, C. E., Song, D., Zhou, G. G. D., Yune, C. Y., Cui, Y., Leonardi, A., Busslinger, M., Wendeler, C., Pitoni, G., Moase, E., and Strouth, A. (2019). Review of the mechanisms of debris-flow impact against barriers. In Kean, J. W., Coe, J. A., Santi, P. M., and Guillen, B. K., editors, *7th International Conference on Debris-Flow Hazards Mitigation*, pages 1027–1034, Golden, Colorado. the Association of Environmental and Engineering Geologists.

Proske, D., Suda, J., and Huebl, J. (2011). Debris flow impact estimation for breakers. *Georisk: Assessment and Management of Risk for Engineered Systems and Geohazards*, 5(2):143–155.

Rickenmann, D. (1999). Empirical Relationships for Debris Flows. *Natural Hazards*, 19(9):47–77.

Sandersen, F. (1997). The influence of meteorological factors on the initiation of debris flows in Norway. In Matthews, J., Brunsden, D., Frenzel, B., Glaser, B., and Weib, M., editors, *Rapid Mass Movement as a Source of Climatic Evidence for the Holocene: Palaeoclimate Research*, pages 321–332. Gustav Fischer Verlag, Stuttgart.

Savage, S. and Iverson, R. (2003). Surge dynamics coupled to pore-pressure evolution in debris flows. In Rickenmann, D. and Chen, C., editors, *Proc. 3rd Int. Conf. on Debris-Flow Hazards Mitigation: Mechanics, Prediction, and Assessment*, volume 1, pages 503–514, Davos, Switzerland. Millpress, Rotterdam.

Savage, S. B. (1984). The mechanics of rapid granular flows. volume 24 of *Advances in Applied Mechanics*, pages 289 – 366. Elsevier.

Savage, S. B. and Hutter, K. (1989). The motion of a finite mass of granular material down a rough incline. *Journal of Fluid Mechanics*, 199:177–215.

Scheidl, C., Chiari, M., Kaitna, R., Müllegger, M., Krawtschuk, A., Zimmermann, T., and Proske, D. (2013). Analysing Debris-Flow Impact Models, Based on a Small Scale Modelling Approach.

Scheidl, C., McArdell, B. W., and Rickenmann, D. (2015). Debris-flow velocities and superelevation in a curved laboratory channel. *Canadian Geotechnical Journal*, 52(3):305–317.

Scotton, P. and Deganutti, A. M. (1997). Phreatic line and dynamic impact in laboratory debris flow experiments. In *Debris-Flow Hazards Mitigation: Mechanics, Prediction, and Assessment*, pages 777–786. ASCE.

Song, D., Choi, C. E., Ng, C. W., and Zhou, G. G. (2018). Geophysical flows impacting a flexible barrier: effects of solid-fluid interaction. *Landslides*, 15(1):99–110.

Song, D., Ng, C. W. W., Choi, C. E., Zhou, G. G. D., Kwan, J. S. H., and Koo, R. C. H. (2017). Influence of Debris Flow Solid Fraction on Rigid Barrier Impact. *Canadian Geotechnical Journal*, 54:1421–1433.

Stalsberg, K., Fischer, L., Rubensdotter, L., and Sletten, K. (2012). Approaches to shallow landslide and debris flow assessments in Norway. In Eberhardt, editor, *Landslides and Engineered Slopes: Protecting society through improved understanding*, pages 737–740. Taylor & Francis Group, London.

Stortingsmelding_nr.15 (2012). How to live with the dangers - of flooding and landslide [in norwegian]. Report, Det Kongelige Olje- og Energidepartment.

Suwa, H., Okano, K., and Kanno, T. (2009). Behavior of debris flows monitored on test slopes of Kamikamihorizawa Creek, Mount Yakedake, Japan. *International Journal of Erosion Control Engineering*, 2(2):33–45.

Takahashi, T. (2009). A review of japanese debris flow research. *International Journal of Erosion Control Engineering*, 2(1):1–14.

Takahashi, T. (2014). *Debris Flow - Mechanics, Prediction and countermeasures*. CRC Press, London, 2nd edition.

Tayyebi, S. M., Pastor, M., Yifru, A. L., Thakur, V., and Stickle, M. M. (). Two-phase

SPH-FD depth integrated model for debris flows: application to basal grid brakes. *Géotechnique*. Submitted manuscript.

The GIMP Development Team (2019). GNU Image Manipulation Program (GIMP 2.10.14). URL: https://www.gimp.org/.

Thielicke, W. and Stamhuis, E. J. (2014). PIVlab – towards user-friendly, affordable and accurate digital particle image velocimetry in MATLAB. *Journal of Open Research Software*, 2.

Thomas, D. G. (1965). Transport characteristics of suspension: VIII. A note on the viscosity of Newtonian suspensions of uniform spherical particles. *Journal Of Colloid Science*, 20(3):267–277.

Tiberghien, D., Laigle, D., Naaim, M., Thibert, E., and Ousset, F. (2007). Experimental investigations of interaction between mudflow and an obstacle. In Chen, C. L. and Major, J., editors, *Debris-flow Hazards Mitigation: Mechanics, Prediction and Assessment*, pages 681–687. Millpress.

Vagnon, F. and Segalini, A. (2016). Debris flow impact estimation on a rigid barrier. *Natural Hazards and Earth System Sciences*, 16(7):1691–1697.

Vallance, J. W. and Savage, S. B. (2000). Particle Segregation in Granular Flows Down Chutes. In Rosato, A. D. and Blackmore, D. L., editors, *IUTAM Symposium on Segregation in Granular Flows. Solid Mechanics and Its Applications*, volume 81, pages 31–51. Springer, Dordrecht.

VanDine, D. (1996). Debris flow control structures for forest engineering. *Res. Br., BC Min. For., Victoria, BC, Work. Pap*, 08.

Varnes, D. J. (1978). Slope movement types and processes. *Special report*, 176:11–33.

Volkwien, A. W., Wendeler, C. G., and Guasti, G. G. (2011). Design of Flexible Debris Flow Barriers. *Italian Journal of Engineering Geology and Environment*, page 7.

Wang, D., Chen, Z., He, S., Liu, Y., and Tang, H. (2018). Measuring and estimating the impact pressure of debris flows on bridge piers based on large-scale laboratory experiments. *Landslides*, 15(7):1331–1345.

Wang, G. and Sassa, K. (2001). Factors affecting rainfall-induced flowslides in laboratory flume tests. *Géotechnique*, 51(7):587–599.

Wang, G. and Sassa, K. (2007). On the pore-pressure generation and movement of rainfall-induced landslides in laboratory flume tests. *Progress in Landslide Science*, 69:167–181.

Wendeler, C., Mcardell, B. W., Rickenmann, D., Roth, A., and Denk, M. (2006). Field testing and numerical modeling of flexible debris flow barriers. In Ng, C. W., Wang, Y., and Zhang, L., editors, *Physical Modelling in Geotechnics - 6th ICPMG '06.*, volume 2, pages 1573–1578, London, UK.

Wendeler, C. and Volkwein, A. (2015). Laboratory tests for the optimization of mesh size for flexible debris-flow barriers. *Natural Hazards and Earth System Sciences*, 15(12):2597–2604.

Wu, C.-C. and Chang, Y.-R. (2003). Debris-trapping efficiency of crossing-truss open-type check dams. In Rickenmann, D. and Chen, C.-L., editors, *Debris-Flow Hazards Mitigation: Mechanics, Prediction and Assessment*, pages 1315–1325. Millpress.

Xie, T., Yang, H., Wei, F., Gardner, J. S., Dai, Z., and Xie, X. (2014). A new water-sediment separation structure for debris flow defense and its model test. *Bulletin of Engineering Geology and the Environment*, 73(4):947–958.

Yifru, A. L., Laache, E., Norem, H., Nordal, S., and Thakur, V. (2018). Laboratory investigation of performance of a screen type debris-flow countermeasure. *HKIE Transactions*, 25(2):129–144.

Yokota, H., Yoshida, K., Furuyama, T., and Handa, K. (2012). Motion analysis of debris flows monitored on the float-board debris-flow breaker [in Japanese]. *Journal of the Japan Society of Erosion Control Engineering*, 65(4):45–49.

Zanuttigh, B. and Lamberti, A. (2006). Experimental analysis of the impact of dry avalanches on structures and implication for debris flows. *Journal of Hydraulic Research*, 44(4):522–534.

Zhou, G. G. and Ng, C. W. (2010). Dimensional analysis of natural debris flows. *Canadian Geotechnical Journal*, 47(7):719–729.

Zhou, G. G. D., Li, S., Song, D., Choi, C. E., and Chen, X. (2019). Depositional mechanisms and morphology of debris flow: physical modelling. *Landslides*, 16(2):315–332.

Papers

Paper I

Yifru, A. L., Laache, E., Norem, H., Nordal, S., and Thakur, V. (2018). Laboratory investigation of performance of a screen type debris-flow countermeasure. *HKIE Transactions*, 25(2):129–144

Laboratory investigation of performance of a screen type debris-flow countermeasure

A. L. Yifru[a], E. Laache[b], H. Norem[c], S. Nordal[a] and V. Thakur[a]

[a]Geotechnical Division, Department of Civil and Environmental Engineering, NTNU, Trondheim, Norway; [b]Rambøll Norge AS, Kristiansand, Norway; [c]Professor Emeritus at the Department of Civil and Environmental Engineering, NTNU, Trondheim

ARTICLE HISTORY
Compiled May 9, 2018

ABSTRACT
Debris-flows are forms of landslides in mountainous regions that can potentially cause significant damage. Structural countermeasures to mitigate an entire debris-flow may become unrealistically large and expensive. If the flow cannot be stopped completely, one may alternatively consider reducing the impact and velocity of the flow using energy dissipating structures. A debris-flow screen is such countermeasure designed to dissipate energy. A screen is made by parallel grids, with some gap, placed in the direction of the debris-flow on an elevated foundation. This structure acts as a filter for separating water from the saturated debris-flow to reduce its flow energy.

This work presents a laboratory model test investigating the effect of screen length (0.5 m and 1.0 m) and opening width (2 mm, 4 mm and 6 mm) in dissipating the debris-flow energy. The effectiveness of the screens was determined in terms of reductions in the run-out distance and flow velocity. The importance of the screen length and opening width is demonstrated. A hypothesis that the optimum opening size should be close to d_{50} of the solid material seems to be validated. The application of the laboratory observations to the field is indicated based on the energy line and scaling principles.

KEYWORDS
debris-flow, debris-flow screen, countermeasure, laboratory testing, physical modelling

1. Introduction

A debris-flow is a destructive natural hazard that occur in regions with steep or mountainous terrain. Depending on the place and time, debris-flows place human lives and infrastructure in danger. Figure 1 shows a debris-flow that occurred by a steep mountain with an average slope of $\sim 35^\circ$ and an initiation location 425 m above the road level. The total run-out distance is estimated to be 750 m, with a maximum deposition width of 150 m and a thickness of 2 m at the road section. The volume of such a debris-flow is in the order of tens of thousands of cubic metres.

A debris-flow involves a rapid to extremely rapid downhill movement of a mixture of water, soil, gravel and organic matter in a relatively long and steep channelled terrain. Debris-flows significantly affect countries like Norway, which have abundant

CONTACT A. L. Yifru. Email: ashenafi.yifru@ntnu.no

Figure 1. Example of a debris-flow in the coastal areas of Norway [Hunnedalen, Norway - occurred on 2 June 2016]. (Courtesy: Multiconsult and NPRA).

precipitation or water sources and such terrains. These vulnerable countries include Austria, Canada, the Caribbean, China, Colombia, France, Indonesia, Italy, Japan, Nepal, the Philippines, Taiwan, Switzerland, and Venezuela [1].

Because of the constituents of a debris-flow and the irregularity of the terrain where it occurs, its flow mechanism is highly complex and is not fully understood. The existing literature contains numerous studies that attempt to understand the mechanism and behaviours of debris-flow, e.g. ([2–6]); empirical or analytical approaches to quantify the mobility of debris-flow, e.g. ([7–12]); mapping of debris-flow hazard zones, e.g. ([13–18]; investigation of debris-flow triggering causes, e.g. ([19–21]); debris-flow countermeasures, e.g. ([9,22–30]).

Debris-flow countermeasures are preventive methods designed to reduce the existing risk of debris-flows to an acceptable level of residual risk, and they are generally classified into two main categories: structural and non-structural countermeasures [22]. Structural countermeasures are physical barriers or partial obstacles to completely or partly stop the debris-flow. However, non-structural countermeasures are mostly methods focusing on reducing the damage and loss by setting up early warning systems, hazard mapping and land-use zoning.

Structural countermeasures focus on reducing the probability of debris-flow occurrence or their damaging consequences by manipulating their flow course. These types of countermeasures can be applied at the initiation, transportation or even deposition zones of expected debris-flow locations. The potential, working mechanism, and design principles of structural countermeasures such as barriers, baffle and deflection walls have been extensively studied and reported in the literature, i.e. open and closed check dams or generally rigid and flexible barriers [24,25,28,29,31–38], baffle walls [26–28,39,40], deflection and channel-side walls [9,22,41], and debris-flow screens [42–45].

Rigid barriers are those countermeasures designed to fully or partially stop a debris-flow. A sabo dam with a sediment basin is a complete debris-flow stopping counter-

measure that is designed according to peak debris-flow discharge and total volume [23]. The possibility of the sediment storage basin being filled during a single debris-flow event is high. Maintenance of this countermeasure requires excavation of several cubic metres of debris, which is impractical. A closed check dam is a similar kind of countermeasure but smaller in size and it only helps breaking the flow velocity while storing part of the debris-flow at its back. This type of countermeasure is usually designed and constructed sequentially along a stream to prevent bed erosion and to raise the channel bed and reduce the stream gradient [22], which can control debris-flow energy.

Open check dams with steel grids are designed to trap larger-sized boulders from the debris-flow, allowing the rest to pass through with a reduced flow velocity. Open check dams are designed to be self-cleaning from the subsequent stream flows, although most exhibit the deposition of finer sediments at the upstream due to boulders and woody debris interlocking at the grid opening [22,23]. However, open check dams takes approximately 3–10 times longer time to be filled by sediment than the fully blocking dams [22]. A slit dam is another type of open dam that is designed to temporarily retain bed-load, allowing some smaller-sized particles to pass while retaining large boulders with high destructive potential [22]. A channel-side wall and a deflection wall are similar structures that are implemented at different situations and locations. A channel-side wall is implemented to protect stream banks from further erosion and debris overflow. A deflection wall, however, is constructed to direct the debris-flow out of its course and towards areas of low consequence [22].

Another energy-dissipating structure is a baffle wall, which is usually used in combination with rigid barriers and is implemented in several rows, with a systematic staggered arrangement to reduce the debris-flow's impacting force on the downstream rigid barrier. The empirical-approach design of baffle walls is improved using flume model studies that provide the optimum spacing between baffles and between rows of baffles, as well as the ideal baffle height with respect to the flow height of the expected debris-flows [26,27,39]. A debris-flow screen is another countermeasure designed to reduce debris-flow energy [46], and it is usually located at the most upstream position in a system of debris-flow countermeasures, and it has a capacity to retain at least the volume of a debris-flow surge wave [22]. Unlike debris-flow screen that is implemented horizontally across a debris-flow channel, flexible barrier that is made of steel rope is placed vertically and is designed to trap major part of a debris-flow while allowing the water and some of the fine soil particles. Due to successful application of flexible barrier in mitigating rock fall hazards, it has been implemented and tested for its potential in mitigating debris-flows, mainly in Switzerland and Hong Kong [19,24,32,33].

Not many structural countermeasures are used in Norway to mitigate debris-flows; however, deflection walls are widely used for guiding snow avalanches to protect downstream infrastructures and inhabitants. Flexible barriers have also been used to mitigate rock falls in some parts of Norway. In recent years, the destruction of road infrastructures and the interruption of traffic by debris-flow events in Norway have been increasing due to the rapidly changing climate, according to the report from the Norwegian Water Resources and Energy Directorate, NVE [47]. The report explains the strong relation between the changing climate and an increased frequency of debris-flow events in Norway. This gives rise to the need to study and implement appropriate countermeasures for such debris-flows. Check dams and baffle walls are studied for their potential in reducing the run-out distance of debris-flows in a laboratory model [40]. Different combinations of deflection and inclination angles of deflection walls are also tested in the same laboratory model to investigate the run-up height potential of debris-flows [41]. A general guideline in application of various countermeasures to

mitigate debris-flow hazards is given by the Norwegian Public Roads Administration [48].

The south-western and northern parts of Norway are highly susceptible regions for debris-flow-related hazards [49]. These regions have highways that run under the feet of mountains and by the sides of fjords or lakes. Occasionally, debris-flows interrupt traffic, as shown in Figure 1. For such relatively small volume debris-flows, mitigation measures, like energy-dissipating structures and/or guide walls with an underpass at the road section, can be more suitable. At a known location of debris-flow hazard, it might be more economical and easier to implement an energy-dissipating structure to prohibit stream erosion or a small landslide from developing into a debris-flow, assuming the area is accessible for installation and maintenance.

A debris-flow screen is one of such flow energy-dissipating structures, and it can be made from one-directional arrangement of a certain length of steel rods or wooden logs, with a specified gap to separate the water and fine-grained soil from the saturated debris-flow. This study attempts to investigate the applicability of debris-flow screens. As a first step in this direction, physical model tests were conducted to investigate the potential and effectiveness of debris-flow screens. Two screen lengths (0.5 m and 1.0 m) and three opening widths (2 mm, 4 mm and 6 mm) were used to study the flow energy and the run-out distance reductions of a 50 litre ($0.05\,m^3$) debris-flow in a 9 m long and 0.6 m wide flume model. The experiment investigates the optimal opening width and length of debris-flow screen in relation to the d_{50} of the debris(soil) material property.

2. Debris-flow screen

The idea of the debris-flow screen was conceived in Japan in the 1950s to reduce the energy in debris-flows and, thus, contribute to mitigating damage in downstream areas [50]. The main purpose of the debris-flow screen is to separate water from the moving debris. As a result, the pore-water pressure will dissipate from the shearing zone and the rest of the debris-flow mass. In return, the soil particles regain their contact friction and thereby increase shearing resistance of the moving debris [42,45,51]. A schematic representation of a debris-flow screen is illustrated in Figure 2.

Numerous researchers have tested debris-flow screens, and a field trial in the Kamikami-Horisawa Valley, Japan has also been reported in the literature (e.g.[23, 42,43]). The debris-flow screen in the field trial was 20 m long and 10 m wide. The screen grids are made from 0.2 m × 0.2 m square steel tubes that were 8 mm thick and resting on 0.4 m × 0.4 m wide flange beams at a spacing of 0.2 m [42].

Due to their simple construction and cost effectiveness, debris-flow screens have been implemented and used in other countries, including China [44,52] and the Philippines [50,53]. Debris-flow screens have been used to protect mountain roads by installing them in narrow sections of streams where recurrent debris-flows occur.

To study the performance and effectiveness of debris-flow screens, Gonda [42] conducted a small-scale model study with different opening widths on the debris-flow run-out distance, using three different uniform-sized materials of $700\,cm^3$ volume. The study found that the reduction in run-out distance increases with an increase in the opening width of up to approximately 2 mm. Kim [43], however, investigated three different bed sediments of $13\,300\,cm^3$ volume with three different blocking and opening widths of debris-flow screens. The study showed the effect of opening width percentage in reducing the run-out distance. However, the above two studies used the debris-flow

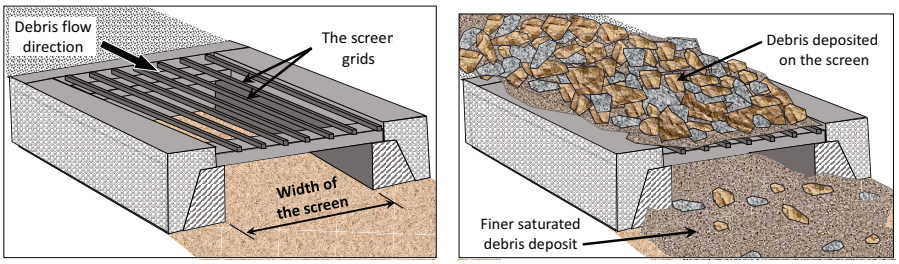

(a) A debris-flow screen structure prior to a debris-flow event.

(b) The debris-flow screen after stopping a granular part of the debris-flow.

Figure 2. Schematic representation of a debris-flow screen's performance.

screen as a deposition area and in all the tests, the debris-flow's mass was retained on the screen.

In real debris-flow cases (as shown in Figure 2), the entire debris-flow volume might not be deposited on the debris-flow screen. Therefore, in the current study, it is interesting to look into the run-out and velocity reduction potential of different screen lengths in combination with different opening widths. The details of the debris-flow's working mechanism are discussed in Section 2.1.

2.1. Working mechanism of a debris-flow screen

The body of a debris-flow surge consist of a water-saturated, muddy, granular slurry liquefied by high pore-water pressure, whereas the front of a debris-flow surge consists of unsaturated, coarse-grained, granular rubble that is pushed from behind by the liquefied slurry [3]. The high pore-water pressure in excess of the hydrostatic water pressure facilitates the high mobility of the debris-flow and is maintained through the entire course of the flow. Savage and Iverson [54] expressed the components of the total normal stress, σ, as a sum of the effective stress between grains, the hydrostatic water pressure and the excess pore-water pressure. A schematic representation of this total normal stress distribution of debris-flow on a solid surface is seen in section A in Figure 3(a) and (b).

Widespread natural decay of pore-water pressure in the flow margin does not contribute to debris-flow deposition, rather it is the grain-contact friction and bed friction concentrations [55]. Major and Iverson [55] showed that the pore-water pressure persisted until the debris-flow was deposited, and then it dissipated significantly during post-depositional sediment consolidation. Therefore, one can introduce a debris-flow screen that helps facilitate the dissipation of pore-water pressure. This results in increasing of the grain-contact friction and grain-bed friction concentration by the sudden removal of the liquid, i.e. dissipation of the pore-water pressure, as schematically shown in Figure 3(a) and (b) in section B.

The energy grade line (energy line) of debris-flow in section A and B can be expressed as the total energy in terms of head, H, which can be given by the Bernoulli equation. Considering an open channel flow situation, the Bernoulli equation of debris-flow just before the beginning of the screen, in section A, can be expressed as:

$$H_A = z_A + h_A + \frac{(v_A)^2}{2g} \tag{1}$$

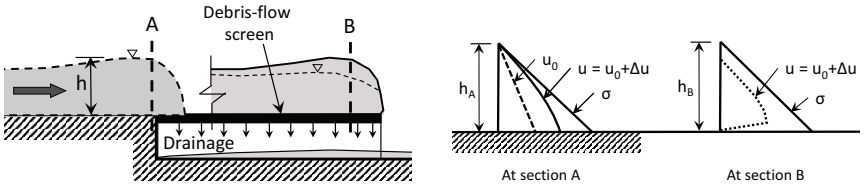

(a) Schematic representation of a debris-flow on a solid surface and on a debris-flow screen.

(b) Total normal stress distribution in solid-liquid mixture: Section A is on a solid surface, and Section B is on a debris-flow screen.

Figure 3. Pore-water pressure development during debris-flow and its dissipation when it hits a screen-type countermeasure.

where H_A is the total head in m; z_A is the elevation of a point from a reference datum in m; h_A is the flowing debris pressure head, which is equal to σ_A/γ in m; σ_A is the total normal stress in kN/m^2; γ is the unit weight of the debris kN/m^3; v_A is the flow velocity and g is the gravitational acceleration. Similarly, the energy head at the end of the screen, in section B, can be expressed as:

$$H_B = z_B + h_B + \frac{(v_B)^2}{2g} \tag{2}$$

The effectiveness of debris-flow screen can be shown by the energy-dissipation factor, E_D, which is expressed as:

$$E_D = 1 - \frac{H_B}{H_A} \tag{3}$$

where $E_D = 0$ represents no energy dissipation, while $E_D = 1$ represents the maximum possible energy dissipation.

2.2. Scaling aspects of the physical modelling

In spite of the disproportionately large effects of viscous shear resistance and cohesion, as well as disproportionately small effects in pore-water pressure in small-scale laboratory model tests, it is also important to systematically study debris-flow by simplifying the complex natural processes in scaled-down laboratory models. The mechanism of dissipation of the pore-water pressure and the hydrostatic water pressure while a debris-flow travels over a screen is yet to be fully understood.

To illustrate the working mechanism and effect of the debris-flow screen, either a field experiment or physical modelling in a laboratory is required. Therefore, this study uses physical modelling in a laboratory to systematically study the effects of a debris-flow screen in reducing a debris-flow run-out distance and flow velocity. Monitoring fluid pressure inside a moving debris can be demanding. Therefore, in this study, the energy dissipation of the debris-flow over a given debris-flow screen will be studied by comparing the energy in the moving debris when entering and leaving the debris-flow screen.

The correct scaling is required when setting up a laboratory physical model to maintain the geometric, kinematic and dynamic similarities of the debris-flow terrain and behaviour. The geometric similarity can be achieved by maintaining the shape by

a linear factor, λ, which can be given as:

$$\lambda = \frac{L_M}{L_F} \tag{4}$$

where λ can be referred to as the linear model scale, which is approximately 1/20 for this study; L_F is any linear dimension in the field (nature); and L_M is any linear dimension on the model.

The kinematic similarity, which is based on velocities, should also have a certain scaling factor to relate between the field and model velocities. To estimate this factor, geometric and dynamic similarities are required. A dimensionless number, called the Froude number (F_r), is used in relating model tests with field cases. It is given by the square root of the ratio between the inertia and gravitational forces of the flow, and it is simplified and shown in Equation 5.

$$F_r = \frac{v}{\sqrt{gh}} \tag{5}$$

where v is the velocity of the moving debris in m/s; g is the gravitational acceleration in m/s^2; and h is the flow height of the moving debris. To conduct a laboratory experiment on debris-flow, the Fr value should be equal to that of the field. However, the resulting Fr for most model tests is observed to be higher than that of a typical debris-flow at the field. From data collected from the field and miniaturised model test measurements, an Fr value less than 2 is seen in real debris-flow cases, while a range of 1.2–12 has been observed in small-scale model tests [56].

Debris-flows generally have velocities between 5 m/s and 10 m/s where the terrain slope angle is close to 20° [48]. NPRA [48] assumes the slope of the energy line to have a gradient between 0.2:1 and 0.3:1 in the run-out zone after the 20° point. The slope angle is an important parameter to fulfil the model-scale laws, which should be maintained when building a laboratory model for debris-flow study.

3. Physical Modelling

3.1. The model set-up

The flume model used for this study is 9 m long and has two parts: a run-out channel and a deposition area. The run-out channel has two inclinations, 23° and 14° slopes, and it is 0.6 m wide and 0.3 m high. The deposition area is 3.6 m long and 2.5 m wide, with a 2° inclination. Figure 4 provides a schematic representation of the model.

Two identical wooden crates (boxes), measuring 0.9 m × 0.6 m × 0.8 m, were used for containing the debris-flow material. One crate was used for releasing the debris, and the other is used for collecting it before and after each test. The debris-flow screen was placed at the end of the run-out channel. The flume model was instrumented with two flow-height sensors before and after the debris-flow screen. The first sensor was used to measure the flow height in the run-out channel, while the second measured the deposition thickness at the deposition area. Three video cameras were used to capture the flow behaviour, in which Cam-1 was placed above the run-out channel, Cam-2 was placed above the deposition area and Cam-3 was placed at the front of the flume model. Cam-1 was used to record the debris-flow's behaviour when it interacted with the debris-flow screen.

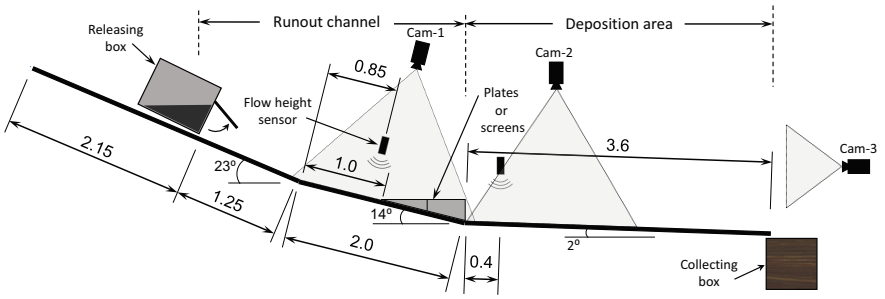

Figure 4. The flume model, placement of debris-flow screens and instrumentation. All linear dimensions are in metres.

3.2. Methodology

A 100 kg soil-water mixture was prepared by mixing 80 kg of soil and 20 kg of water to simulate a saturated debris-flow. These weighted amounts of soil and water were added to the releasing box and were then thoroughly mixed. The soil–water mixture corresponded to a total of 50 litres (0.05 m^3) of fully saturated debris material with a solid concentration of $C_s = 60\%$ by volume. This saturated debris represents well-developed and fast-moving debris-flow material upon release. In the experiments, the releasing mechanism simulated a dam break by releasing the whole mass at once, as the focus of the study was to investigate the behaviour of a well-developed debris-flow interaction with different debris-flow screen types.

To conduct a given test, the releasing box with the saturated debris material was lifted by crane and placed on the top end of the run-out channel, as shown in Figure 4. Before releasing the debris mass from the box, video recording started in all cameras, and the flow-height sensors were checked. The debris material was then thoroughly mixed using a hand mixer to create a well-mixed, less-segregated debris-flow upon release. Finally, the gate was opened, and the saturated debris was released.

Two debris-flow screen lengths (0.5 m and 1.0 m) and three screen opening widths (2 mm, 4 mm and 6 mm) were chosen to be tested. The screens were made by the systematic arrangement of rectangular steel rods with a cross-section of 10 mm × 15 mm, using spacers 2 mm, 4 mm and 6 mm in size (see Figure 5(b)). Figure 5(a) shows the placements and starting point of these screens. The starting point of the screens, which is considered as a reference point for measuring the debris-flow's run-out distance, is 2.25 m away from the releasing box and 1.0 m before the start of the deposition area (see Figure 4). In addition, two scenarios that represent only the terrain alteration of the screens are included and used as reference tests, and they are made from 0.5-m- and 1.0-m-long solid plates in which their opening widths are referred to as zero.

After each test, the run-out distance (with reference point 'x' in Figure 5(a)), maximum deposition width and maximum deposition thickness of the soil in the deposition area were recorded. In addition, the maximum deposition thickness on the debris-flow screen was recorded. After taking all the important measurements and representative photos, soil samples from selected tests were taken from different parts of the flow area to evaluate how the grain size distribution of the debris material changed from the original released material. Finally, the model was cleaned and made ready for the

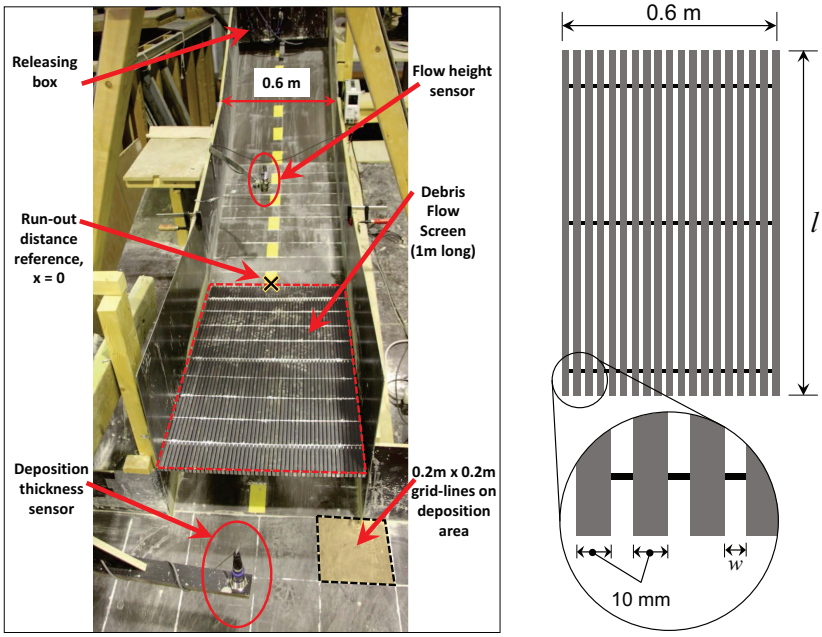

(a) The run-out channel and partial view of the deposition area (photo from Laache [57]).

(b) A schematic detail of the debris-flow screen: l is 0.5 m or 1.0 m and w is 2 mm, 4 mm and 6 mm.

Figure 5. Details and measurements of the run-out channel, the screens and the deposition area.

next test.

3.3. Test plan

The test plan is given in Table 1. The 24 tests are named based on the various scenarios and are given the code *'s-l-w-n'*, where s is scenario, l is the length of a screen in m, w is the width of a single opening on a screen in mm, and n is the scenario repetition number. Each scenario was repeated three times and numbered as $n = 1$, 2 and 3. The opening percentage is the percentage ratio of the cumulative opening and the width of the screen.

3.4. The test material

The debris material used for this test is a sandy soil with a grain size property of $d_{max} = 8.0\,\text{mm}$, $d_{90} = 6.0\,\text{mm}$, $d_{50} = 1.8\,\text{mm}$ and $d_{10} = 0.11\,\text{mm}$. The grain size distribution (GSD) of the sand is given by Figure 6. The coefficient of uniformity is $C_u = 25$, and the coefficient of curvature is $C_c = 1.96$, which indicates a well-graded material. The specific gravity of the soil is 2.71 at $20°c$. This GSD was maintained without any significant variation throughout the tests.

Table 1. Test plan and description of dimensions of the debris-flow screens used.

		Screen					Screen		
Test Number	Test Name	length [m]	opening [mm]	opening [%]	Test Number	Test Name	Length [m]	opening [mm]	opening [%]
T1	S-0.5-0-1				T13	S-0.5-4-1			
T2	S-0.5-0-2	0.5	0	0	T14	S-0.5-4-2	0.5	4	29
T3	S-0.5-0-3				T15	S-0.5-4-3			
T4	S-1-0-1				T16	S-1-4-1			
T5	S-1-0-2	1.0	0	0	T17	S-1-4-2	1	4	29
T6	S-1-0-3				T18	S-1-4-3			
T7	S-0.5-2-1				T19	S-0.5-6-1			
T8	S-0.5-2-2	0.5	2	17	T20	S-0.5-6-2	0.5	6	38
T9	S-0.5-2-3				T21	S-0.5-6-3			
T10	S-1-2-1				T22	S-1-6-1			
T11	S-1-2-2	1	2	17	T23	S-1-6-2	1	6	38
T12	S-1-2-3				T24	S-1-6-3			

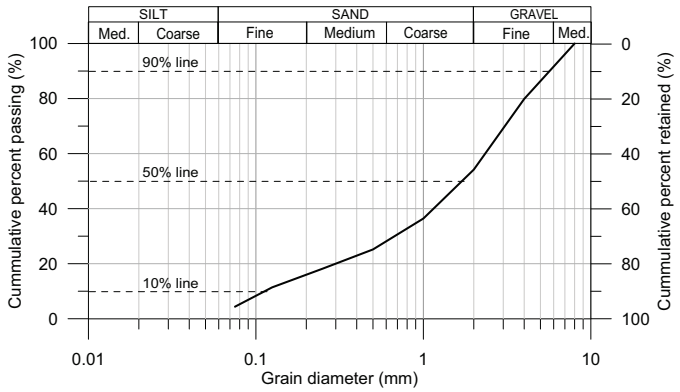

Figure 6. Grain size distribution of the test material.

4. Results

These results are from the experiment made for a Master's thesis by Laache [57], and are re-analysed by the first author. The run-out distance (L_{FL}), maximum width of deposition (B), maximum upstream flow height (h_{Max}), maximum deposition thickness on the screen (t_u) and downstream at the deposition area (t_d), and average front-flow velocity at the beginning (v_A) and the end (v_B) of a screen were recorded for all 24 tests and are summarised in Table 2. Tests T1 to T6 are the reference tests without debris-flow screens, where solid plates of 0.5-m- and 1.0-m-long were used. Tests T7-T24 were conducted using 0.5-m- and 1.0-m-long screens with three opening sizes, i.e. 2 mm, 4 mm and 6 mm. The reference tests were used as the benchmark to evaluate the performance of the debris-flow screens. The model geometry was identical in each test. Therefore, changes in the debris-flow run-out distance and flow velocity are attributed to the debris-flow screen.

The flow-front velocity was measured by analysing the Cam-1 video using Tracker (Tracker v4.11.0), a video processing software. Due to the homogeneous-looking flow of the debris-flow's body and tail, only the flow-front was tracked to compute velocity. In

Table 2. Summary of the test results (Based on data from Lacche [57]).

Test Number	Test Name	L_{FL} [m]	B [m]	h_{Max} [cm]	t_u [cm]	t_d [cm]	v_A [m/s]	v_B [m/s]
T1	S-0.5-0-1	2.35	0.90	3.20	3.35	1.90	2.63	2.23
T2	S-0.5-0-2	2.60	0.87	3.40	2.49	1.70	2.28	1.73
T3	S-0.5-0-3	3.05	1.12	5.40	1.44	1.60	2.00	1.80
T4	S-1-0-1	2.65	1.08	3.50	4.39	1.00	2.63	1.97
T5	S-1-0-2	2.75	1.08	4.90	2.61	0.90	2.47	1.97
T6	S-1-0-3	2.10	0.98	4.00	3.83	1.40	2.87	2.80
T7	S-0.5-2-1	1.95	0.66	3.50	7.71	1.20	3.13	2.57
T8	S-0.5-2-2	1.80	0.98	4.00	5.64	1.30	2.63	1.65
T9	S-0.5-2-3	2.28	0.90	3.20	3.81	1.30	2.93	2.37
T10	S-1-2-1	0.95	0.60	3.60	6.78	0.80	3.03	0.00
T11	S-1-2-2	0.90	0.60	3.40	5.62	0.30	-	-
T12	S-1-2-3	0.90	0.60	3.70	5.89	0.40	2.67	0.43
T13	S-0.5-4-1	2.25	1.18	3.90	5.20	2.00	3.10	2.27
T14	S-0.5-4-2	2.50	1.08	3.50	3.75	1.70	2.90	2.43
T15	S-0.5-4-3	2.95	1.02	3.90	5.36	1.60	2.77	1.83
T16	S-1-4-1	0.75	0.60	3.70	5.40	0.40	-	-
T17	S-1-4-2	1.00	0.60	3.10	4.22	0.70	2.82	0.57
T18	S-1-4-3	1.00	0.60	3.20	5.07	0.30	3.08	1.10
T19	S-0.5-6-1	2.40	0.85	4.90	6.34	1.20	2.23	1.53
T20	S-0.5-6-2	3.00	1.00	3.60	3.70	1.10	3.20	2.17
T21	S-0.5-6-3	2.50	0.70	3.40	6.17	1.30	2.77	1.63
T22	S-1-6-1	0.90	0.60	4.30	4.86	0.80	2.77	0.10
T23	S-1-6-2	0.90	0.60	3.50	4.39	0.70	2.87	0.40
T24	S-1-6-3	0.90	0.60	4.30	5.85	0.90	2.90	0.50

many of the model test cases, the flow-front velocity was non-uniform across the width of the flow channel because of flow surges. As a result, the average flow-front velocity is computed by considering velocities at the left, centre and right of the flow. The values presented in Table 2 as v_A and v_B are the average approach and the average exit-velocities to and from a debris-flow screen, respectively. Figure 7 presents the flow-front velocities of six representative tests from each scenario group, except for the two reference test scenarios. This is due to limitations of the output video recordings that only the v_A and v_B values were computed and given in Table 2.

Two distinguishing parts of the debris deposit are observed. The first is water mixed with very fine soil particles that continued to flow and ended up in the collecting box. The second is the solid debris that accumulated in the deposition area or on the screen. The L_{FL} and B measurements given in Table 2 are for the solid debris. The photos showing the final deposition shape, along with L_{FL} and B of the four representative tests, are presented in Figure 8. This figure illustrates how the debris material flowed, spread and segregated in the deposition area when using the 0.5-m-long plate and screens.

From the upstream flow-height sensor, variations in the average flow heights with time for all the tests are given in Figure 9. For each test, two peak values were extracted from a respective plot. The first peak represents the h_{Max} while the second, stabilized and horizontal line represents t_u, which are given in Table 2.

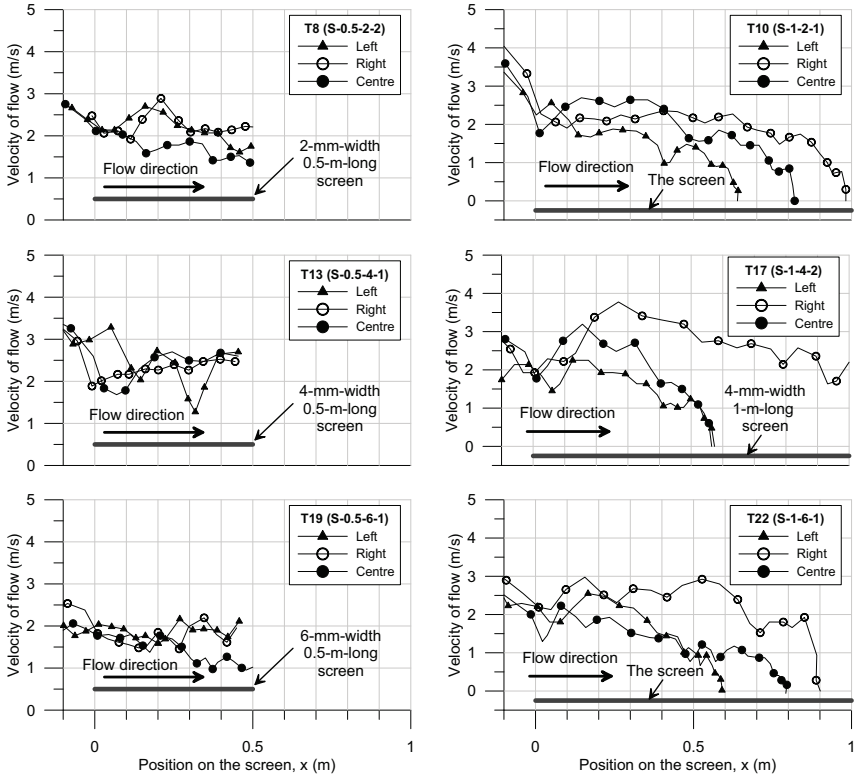

Figure 7. Representative plots showing the flow-front velocities at the left, centre and right sections of the run-out channel over the 0.5-m- and 1-m-long screens; for 2 mm, 4 mm and 6 mm opening widths from top to bottom.

5. Discussion

The reference test results from T1 to T6 will be used as a benchmark for discussing the performance of the debris-flow screens. The average run-out distance, L_{FL}, for the 0.5-m-long reference test (T1–T3) is 2.67 m, with a standard deviation of 0.35 m, while for the 1.0-m-long reference test (T4–T6), the average L_{FL} became 2.5 m, with a standard deviation of 0.35 m. As expected, the resulting L_{FL} is found to be shorter for the longer slope-alteration length than the shorter.

The average value of the maximum deposition width, B for the 1.0-m-long reference test, is found to be slightly wider than that of the 0.5-m-long reference test. A wider B can be an indication of slower flow-front in the deposition area, which forced the flow-tail to spread side ways, causing a shorter L_{FL}. Similarly, a lower average upstream deposition, t_u, and a higher average downstream deposition, t_d, were observed in the case of the 0.5-m-long plate than for the 1.0-m-long plate. The average t_u for both reference tests can be seen in Figure 9 between $t = 4s$ and $t = 5s$.

In both cases, the flow velocities were decreased at the end of the plates when compared to the velocity at the beginning of the plates. The average flow-front velocity decrease was observed to be in the order of 15%, which can be considered as a channel

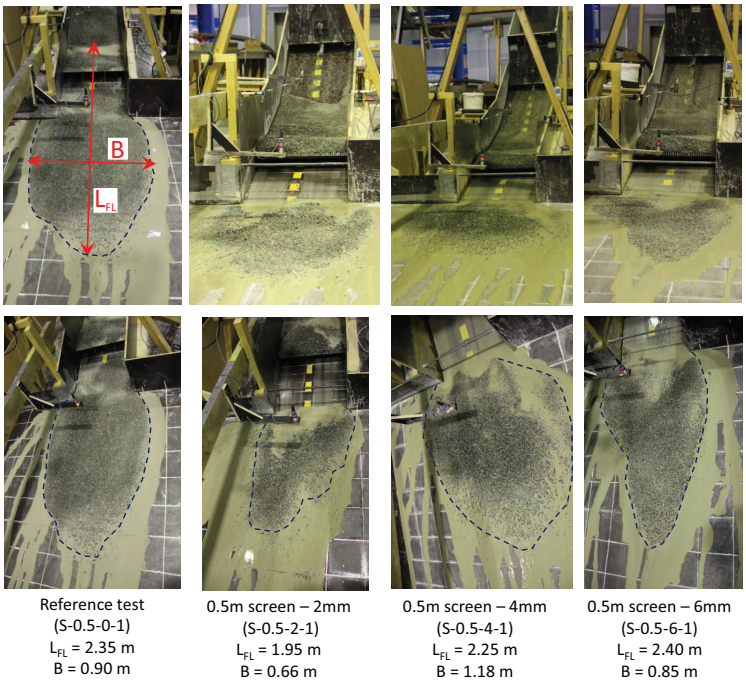

Figure 8. Photos showing deposition pattern and run-out distance of selected tests from 0.5-m-long cases (Photos from Laache [57]).

alteration contribution.

5.1. The run-out distance

The recorded L_{FL} are plotted against the opening width of the screen for each length in Figure 10. The plot shows the average L_{FL} along with the lower- and upper-bound values represented by error bars. The lower- and upper-bound values are those given in Table 2.

The average L_{FL} when using the 0.5-m-long screen is observed to decrease to 2.01 m with the provision of a 2 mm opening width. However, the average L_{FL} showed no significant change from the reference test when using 4 mm and 6 mm screen opening widths (T13–T15 and T19–T21). The respective average L_{FL} were 2.57 m and 2.63 m, which are not far from the reference average of $L_{FL} = 2.70$ m. One possible reason for these relatively longer L_{FL} values may be the mixing of the sufficiently fast liquid and solid fractions filtered through the screen with the material that jumped over the screen.

The 1.0-m-long screen is observed to be sufficient for the debris-flow volume, as it retains almost the entire granular part of the test material. The L_{FL} were also found to be relatively consistent, with an average value of around 0.9 m for all the three opening widths. All were less or equal to the total screen length. However, some solid fractions that had filtered through the 4 mm and 6 mm screens were observed in the

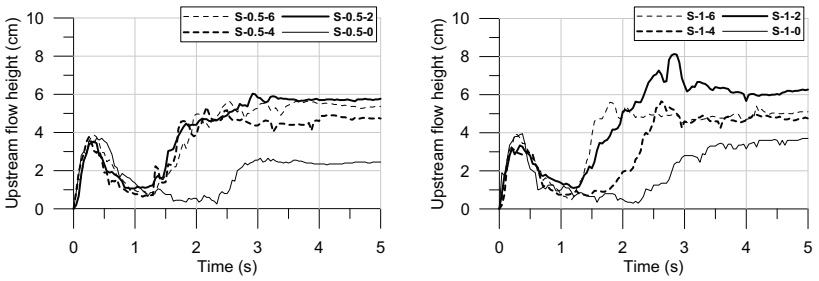

(a) Average flow heights when using a 0.5-m-long plate and screen.

(b) Average flow heights when using a 1.0-m-long plate and screen.

Figure 9. Average flow height variation with time at the upstream of the countermeasures.

deposition area. In addition, for test T17 and T18 of the 4 mm opening screens in particular, a saturated surge on one side of the channel was observed to travel the whole length of the screen, which produced a 1-m-long L_{FL}.

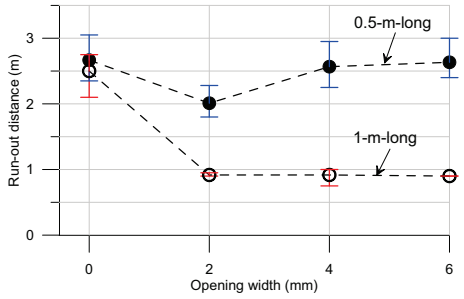

Figure 10. Run-out distance with respect to the opening widths of the 0.5-m- and 1-m-long screens

5.2. Flow velocity

The average flow velocities recorded approaching, v_A, and exiting, v_B, the respective plate or screen are given in Table 2. As expected, the average v_A is consistent and between 2.65 m/s and 2.95 m/s, except some outliers were observed in T3 and T20 with very low and very high velocities. This variation is a result of different surges observed in different sections of the flow channel, as shown in Figure 7.

Although average velocity reductions are observed due to the terrain alteration in the reference tests and the water-draining effect in the screens, the value of v_B was affected by small surges of highly-saturated debris mass. Some of the v_B values of the 1-m-long screen shown in Table 2 are non-zero; this is the effect of a small flow-front part, either in the left or right of the channel, which shoots until the end of the screen. In the cases of T17 and T18, the average exit-velocity value was as high as 1.1 m/s. However, the average exit velocities when using 0.5-m-long screen vary, and more will be discussed based on the energy dissipation.

5.3. Maximum flow height and deposition thickness

Like the approach flow velocity, v_A, the maximum flow height, h_{Max}, recorded at the upstream sensor was expected and observed to be uniform. The average h_{Max} was around 3.5 cm (see Figure 9). Some outliers were observed in T3, T5 and T19 that gave h_{Max} between 4.9 cm and 5.4 cm. These thick flow heights are due to some saturated frozen (lumped) masses that were not fully mixed with the rest of the fluidized debris.

In discussing the upstream deposition thickness, t_u, Figure 9 shows that the flow height increases after the $t \approx 1.5s$ mark. This is due to the damming effect from the decelerating flow-front, which is the first to lose its water content. As the flow proceeds, the amount of dry flow-front increases, as well as the grains' resistance through grain-contact friction and grain-bed friction, while the flow-tail still pushes. However, after a short time ($\sim 1s$), the major part of the flow-front stops completely and acts as a dam to halt the entire flow-tail, including the remaining liquid. After the debris mass was deposited on the debris screen, the liquid held at the back of the debris-dam continued to drain slowly through the mass and the screen. In some tests, a turbulent flow behind the debris-dam was observed, and one of them is visible on the plot of (S-1-2) in Figure 9(b).

The resulting average t_u vary between 4.7 cm and 6.1 cm for both screen lengths, whereas for the reference tests, the average t_u was recorded as 2.5 cm and 3.6 cm for the 0.5-m- and 1-m-long plates, respectively. The average t_u almost doubled from their respective reference test results when using the 2 mm opening width (T7–T12), while a relatively lesser increase was seen when using 4 mm and 6 mm opening widths.

In comparing the downstream deposition thickness t_d, the 1-m-long screens gave an average t_d thickness of less than 1 cm, as there is no significant debris mass in the deposition area. When using the 0.5-m-long screen, the lowest average t_d were observed during the 2 mm and 6 mm opening widths, while a similar average t_d was recorded as that of the reference test when using the 4 mm opening width. This can also be considered as a measure for the decrease in the amount of the debris passing the screen. Therefore, all opening widths from the 1-m-long screen, and the 2 mm and 6 mm opening widths from the 0.5-m-long screen were found to reduce the downstream deposition thickness by up to 33%.

5.4. Effectiveness of the screens

5.4.1. Run-out distance reduction

Effectiveness of the screens can be evaluated using the percentage decrease in average L_{FL} in comparison with the average L_{FL} of the respective reference test. This calculated effectiveness is presented in Figure 11 and plotted against the opening width for each screen length.

The 2 mm opening width reduced the average L_{FL} observed in the reference tests of 1 m and 0.5 m by 63% and 25%, respectively. For the 0.5-m-long screen, this is the highest percentage reduction on average L_{FL}, while the 1-m-long screen keeps almost the same percentage reduction for all opening widths. However, the percentage decrease in average L_{FL} for the 4 mm and 6 mm opening widths in the 0.5-m-long screen case are less than 4% and 1.3%, respectively. The reason for these small percentage reductions is the result of the fast-moving water and soil fractions passing through the screen and mixing with the debris that jumped over the screen to travel longer. The resulting percentage reduction when using the 2 mm opening width for both screen

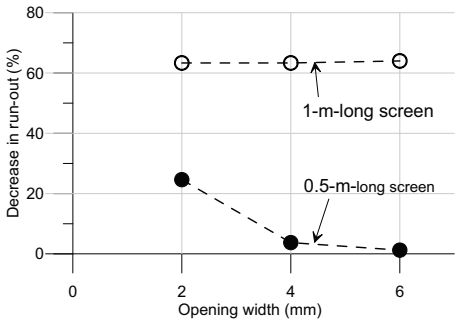

Figure 11. Percentage run-out distance reduction of the debris-flow screen based on length and opening width, with respect to the reference run-out distances.

lengths can be an indication of an interesting relationship between the opening width and the $d_{50} = 1.8\,\text{mm}$ of the testing material used.

A similar experiment done in Kyoto, Japan, by Kim [43], showed assessment of the effectiveness of the screen-type debris-flow countermeasure based on the percentage of the ratio between the cumulative opening width and the total width of the screen. The screen was, at the same time, used as a deposition area for the tested material, which makes it suitable to compare it with the 1-m-long screen used in this study. Therefore, the data from Kim [43] with $d_{50} = 1.78\,\text{mm}$ is plotted against the data from the present study and given in Figure 12. The blocking width of the screens, in the present study, is a constant 10 mm, while Kim [43] varied it along with the opening widths, which might explain the slight variations in the results when it comes to the low-percentage openings of 17% and 29%. The 0.5-m-long screen case is not comparable, as the debris material run beyond the screen.

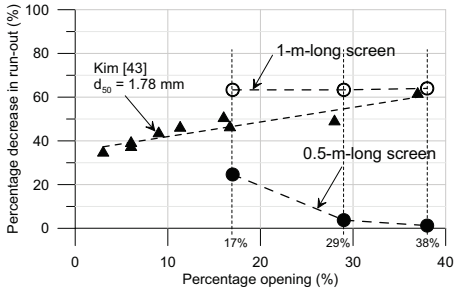

Figure 12. Comparison of percentage opening versus percentage run-out distance reductions with data from Kim [43].

5.4.2. Energy dissipation

Energy dissipation potential is another aspect for evaluating the effectiveness of a countermeasure. Because of the horizontally aligned provision of the debris-flow screens and an extremely low-pressure head compared to the velocity head, the energy dissipation between the beginning and end of each screen will be assessed by the velocity head

term only i.e. $v^2/(2g)$, (from Equation 1 and 2). Then Equation 3 is simplified as:

$$E_D \approx 1 - (\frac{v_B}{v_A})^2 \tag{6}$$

where v_A and v_B represent the average velocities given in Table 2.

Figure 13 shows the average percentage energy dissipated in each case. In both the 0.5-m- and 1.0-m-long screen cases, the major amount of energy is dissipated when using the 2 mm opening width. When using the 4 mm and 6 mm opening widths, no significant increase in energy dissipation beyond what is obtained by the 2 mm opening width is observed in the case of the 1.0-m-long screen. However, a gradual increase in energy dissipation is observed when using the 0.5-m-long screen. In the case of the 4 mm opening width and 1-m-long screen, the energy dissipation is seen to be small and out of the data trend. This might be attributed to the high flow velocity observed at the end of the screen by some small portion of the debris-flow front.

Generally, the average percentage energy dissipation presented in Figure 13(b) implies that, without the contribution of the terrain alteration, the 1-m-long debris-flow screen can reduce the flow energy up to 70%, while the 0.5-m-long screen is able to reduce the flow energy between 25% and 50%.

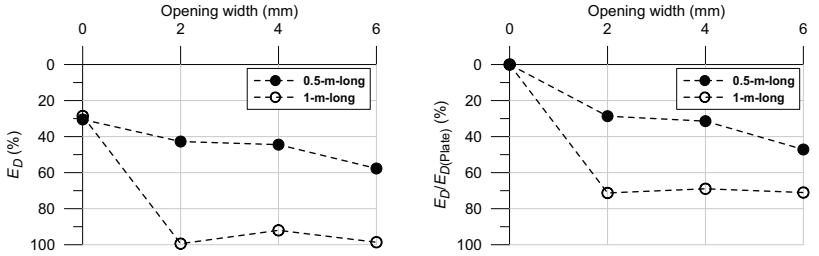

(a) Percentage of energy-dissipation factor with opening width.

(b) Percentage energy-dissipation with respect to energy-dissipation factor by terrain alteration (from reference tests).

Figure 13. Illustration of energy-dissipation factor for evaluating effectiveness of debris-flow screen-types.

5.5. Segregation of the debris material

Soil samples from the deposition area and from the top of the countermeasures were collected to study the segregation or change in grain size distribution of the original debris-flow material. The selected tests are T7 (S-0.5-2-1), T13 (S-0.5-4-1) and T19 (S-0.5-6-1).

The samples that are taken from the top of the screen were collected from the end of the screens because the material deposited in the middle or at the back of the screen is affected by the debris-tail (subsequent flow surges), while the front material is interacted fully with the screen to show the effect of the screen.

A sample GSD plot (Figure 14) from T7 (S-0.5-2-1) shows that the material accumulated on the screen was coarser than the original material, while finer materials were observed in the deposition area. Table 3 shows a comparison using the d_{50} values of the tested samples. The values given in the table demonstrate that the screens can

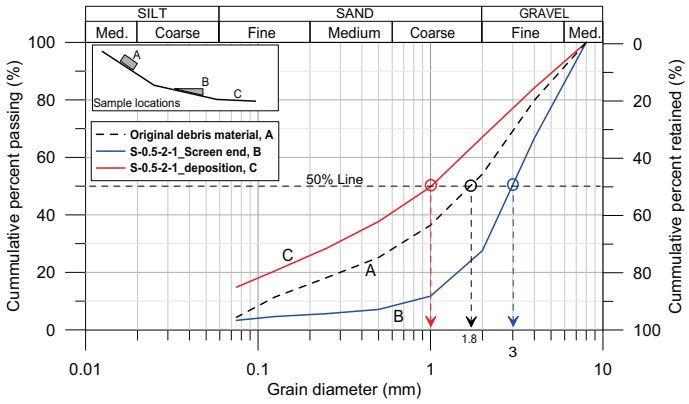

Figure 14. Change in grain size distribution (GSD) of the debris-flow material on the screen and at the deposition area.

retain the major coarse part of the debris-flow. This also shows that debris-flow screens are not only breaking the flow but also have the potential to retain coarser debris that might have significant destructive powers.

Table 3. Values of d_{50} for the samples at deposition and on the 0.5-m-long screen

Test number	Scenario	d_{50} screen end	d_{50} deposition area
T7	S-0.5-2-1	3.0	1.0
T13	S-0.5-4-1	4.2	1.4
T19	S-0.5-6-1	2.7	1.6

In general, the performance of the debris-flow screen with respect to the opening width can be discussed in light of the soil material grain size property, d_{50}. The d_{50} of the test material is 1.8 mm. In the case of the 4 mm and 6 mm opening widths, the d_{50} values in the deposition area are found to be greater than that of the 2 mm cases. This indicates that the mass in the deposition area is not only the soil that is pushed over the screen but also the soil that is filtered through the openings along with the muddy liquid. This phenomenon is observed in the case of the 1-m-long screen as well, where some soil grains escaped through the 4 mm and 6 mm screens.

If not for the frictional force between the soil grains, 6 mm and 4 mm opening widths could allow 94% and 80% of the debris solids, respectively, while the 2 mm opening width could allow 54% of the debris solids through the openings of the screen. This gives another perspective on why the first two allowed some soil fractions and were less effective than the latter. This might be an interesting observation that relates the debris material property, d_{50}, with the opening width on the performance of debris-flow screens. Thus, this observation during the use of the 2 mm opening width in both screen lengths may contribute to the possible use of d_{50} as a design criterion for the optimal opening of debris-flow screens.

5.6. Scaling effect

In laboratory model studies of debris-flows, the slope of the energy line is one of the important model scale laws that must be maintained. According to NPRA [48], the slope of the energy line is expected to fall between 0.2:1 and 0.3:1. Three model calibration tests, without any structure in the flume channel and deposition area, were carried out, and the slope of the average energy line was 0.22:1, satisfying the requirement [57].

From the recorded maximum flow heights and flow velocities, the Fr values were calculated, and the maximum and minimum values were 5.5 and 2.75 for test numbers T3 and T18, respectively. This ensures that the Fr of the model test results are with in the range given as $1.2 < Fr < 12$ by Huebl et al. [56]. However, a typical debris-flow in nature has an Fr value around 2.

The scaling effect can be discussed in terms of the geometric linear scale λ. The model is assumed to have an approximate linear scale of $\lambda = 1/20$. According to the linear scale factor, the initial volume used in the model, i.e. $0.05\,\mathrm{m}^3$, will give an approximate scaled-up volume of around $400\,\mathrm{m}^3$. Such volume can be related to a small debris-flow, which can be said that a 20-m-long debris-flow screen could dissipate a major part of the debris-flow energy. The Kamikami-Horisawa Valley field experience on debris-flow screen [23,43,58] can give an overview of the size and volume of flow along with the tested screen length.

Encouraging results are found in the model tests. A comparison of these results with field trial in a controlled condition will consolidate the findings. The optimal length of debris-flow screen with different opening widths shall be tested with different flow discharges and volumes. The effect of multiple surges on debris-flow screen performance should also receive close attention.

6. Conclusion

This work attempts to investigate the debris-flow screen on a laboratory model for its potential to dissipate the flow energy of debris-flows. The assessment was done by comparing the effects of different lengths and opening widths of the debris-flow screen on the resulting run-out distances, flow velocities, flow heights and deposition thicknesses.

The 1-m-long debris-flow screen is found to be sufficient to halt the flow of the entire debris-flow volume regardless of the opening width. However, the 4 mm and 6 mm opening widths, which are widths greater than the d_{50} size of the debris-flow material, are found to allow some solid fractions through their openings along with the draining water.

A general observation about the 0.5-m- and 1-m-long debris-flow screens is that the run-out distance and flow velocity decreases with an increase in screen length. However, among the three screen opening widths, the 2 mm ($\approx d_{50}$) opening width was found to be optimal regarding reducing both the run-out distance and flow velocity of the debris-flow. A further increase in the opening width exhibits a relatively small improvement in the reduction of run-out distance and flow velocity.

Further study on different screen lengths and opening widths with varying debris-flow volume will add to this result and consolidate the interesting relationship found between d_{50} and the screen opening width in flow mobility reduction. In addition, validation from a field experiment will be vital to develop robust design criteria for an

effective debris-flow screen.

Acknowledgement

The Norwegian Public Roads Administration, NPRA, financially supported this study under the E39 ferry-free highway project, and the study was conducted in close cooperation with the Klima2050 project. The authors would like to thank Frank Stæhli and Tage Westrum, for building the screens and the plates, and Geir Tesaker for operating the crane during the experiment.

References

[1] Takahashi T. Debris flow: mechanics, prediction and countermeasures. London (UK): CRC Press; 2014.

[2] Takahashi T. A review of japanese debris flow research. Int J of Eros Cont Eng. 2009; 2(1):1–14.

[3] Iverson RM. The physics of debris flows. Rev Geophys. 1997;35(3):245–296.

[4] Iverson RM. Debris-flow mechanics. In: Jakob M, Hungr O, editors. Debris-flow hazards and related phenomena. Berlin, Heidelberg: Springer; 2005. p. 105–134.

[5] Iverson RM, Logan M, LaHusen RG, et al. The perfect debris flow? aggregated results from 28 large-scale experiments. J Geophys Res-earth. 2010;115.

[6] Viccione G, Genovese M, Rossi F, et al. Physical modelling of laboratory debris flows by using the sodium carboxymethylcellulose (na-cmc). WSEAS Trans Fluid Mech. 2015; 10:163–173.

[7] Hungr O, Morgan GC, Kellerhals R. Quantitative-analysis of debris torrent hazards for design of remedial measures. Can Geotech J. 1984;21(4):663–677.

[8] Rickenmann D. Empirical relationships for debris flows. Nat Hazards. 1999;19(1):47–77.

[9] VanDine D. Debris flow control structures for forest engineering. Victoria (BC): Res Br BC Min For.; 1996. Work Pap. 08/1996.

[10] Scheidl C, Rickenmann D. Empirical prediction of debris flow mobility and deposition on fans. Earth Surf Proc Land. 2010;35(2):157–173.

[11] Federico F, Cesali C. An energy-based approach to predict debris flow mobility and analyze empirical relationships. Can Geotech J. 2015;52(12):2113–2133.

[12] Devoli G, De Blasio FV, Elverhi A, et al. Statistical analysis of landslide events in central america and their run-out distance. Geotech Geol Eng. 2009;27(1):23–42.

[13] Sandersen F. The influence of meteorological factors on the initiation of debris flows in norway. In: Matthews JA, Brunsden D, Frenzel B, et al., editors. Rapid mass movement as a source of climatic evidence for the Holocene: Palaeoclimate Research; Vol. 19; Gustav Fischer Verlag, Stuttgart; 1997. p. 321–332.

[14] Glade T. Linking debris-flow hazard assessments with geomorphology. Geomorphology. 2005;66(1):189–213.

[15] Fischer L, Rubensdotter L, Sletten K, et al. Debris flow modeling for susceptibility mapping at regional to national scale in norway. In: Proceedings of the 11th International and 2nd North American Symposium on Landslides; 2012 Jun 03-08; Alberta, Canada; 2012. p. 3–8.

[16] Meyer NK, Dyrrdal AV, Frauenfelder R, et al. Hydrometeorological threshold conditions for debris flow initiation in norway. Nat Hazard Earth Syst. 2012;.

[17] Meyer NK, Schwanghart W, Korup O, et al. Estimating the topographic predictability of debris flows. Geomorphology. 2014;207:114–125.

[18] Devoli G, Strauch W, Chvez G, et al. A landslide database for nicaragua: a tool for landslide-hazard management. Landslides. 2007;4(2):163–176.

[19] Wang G, Sassa K. Factors affecting rainfall-induced flowslides in laboratory flume tests. Geotechnique. 2001;51(7):587–599.
[20] Blijenberg HM. Application of physical modelling of debris flow triggering to field conditions: Limitations posed by boundary conditions. Eng Geol. 2007;91(1):25–33.
[21] Bacchini M, Zannoni A. Relations between rainfall and triggering of debris-flow: case study of cancia (dolomites, northeastern italy). Nat Hazard Earth Syst. 2003;3(1-2):71–79.
[22] Huebl J, Fiebiger G. Debris-flow mitigation measures. In: Jakob M, Hungr O, editors. Debris-flow hazards and related phenomena. Berlin, Heidelberg: Springer; 2005. p. 445–487.
[23] Mizuyama T. Structural countermeasures for debris flow disasters. Int J Eros Control Eng. 2008;1(2):38–43.
[24] Ashwood W, Hungr O. Estimating total resisting force in flexible barrier impacted by a granular avalanche using physical and numerical modeling. Can Geotech J. 2016; 53(10):1700–1717.
[25] Bugnion L, Bötticher A, Wendeler C. Large scale field testing of hill slope debris flows resulting in the design of flexible protection barriers. In: Koboltschning G, Hübl J, Braun J, editors. 12th Congress Interpraevent; 2012 Apr 23-26; Grenoble; 2012. p. 59–66.
[26] Choi CE, Ng CWW, Song D, et al. Flume investigation of landslide debris-resisting baffles. Can Geotech J. 2014;51(5):540–553.
[27] Ng CWW, Choi CE, Song D, et al. Physical modeling of baffles influence on landslide debris mobility. Landslides. 2015;12(1):1–18.
[28] Ng CWW, Choi CE, Su AY, et al. Large-scale successive boulder impacts on a rigid barrier shielded by gabions. Can Geotech J. 2016;53(10):1688–1699.
[29] Wendeler C, McArdell B, Rickenmann D, et al. Field testing and numerical modeling of flexible debris flow barriers. In: Ng CWW, Zhang LM, Wang YH, editors. 6th ICPMG; 2006 Aug 4-6; Hong Kong; 2006.
[30] Scheidl C, Chiari M, Kaitna R, et al. Analysing debris-flow impact models, based on a small scale modelling approach. Surv Geophys. 2013;34(1):121–140.
[31] Canelli L, Ferrero A, Migliazza M, et al. Debris flow risk mitigation by the means of rigid and flexible barriers-experimental tests and impact analysis. Nat Hazard Earth Syst. 2012; 12(5):1693–1699.
[32] Volkwein A, Wendeler C, Guasti G. Design of flexible debris flow barriers. In: Genevois R, Hamilton DL, Prestininzi A, editors. 5th International Conference on Debris-flow Hazard Mitigation: Mech Predic Assess; 2011 Jun 14-17; Padua, Italy; 2011. p. 1093–1100.
[33] Song D, Choi C, Ng C, et al. Geophysical flows impacting a flexible barrier: effects of solid-fluid interaction. Landslides. 2017;15(1):99–110.
[34] Vagnon F, Segalini A. Debris flow impact estimation on a rigid barrier. Nat Hazard Earth Syst. 2016;16(7):1691–1697.
[35] Moriguchi S, Borja RI, Yashima A, et al. Estimating the impact force generated by granular flow on a rigid obstruction. Acta Geotech. 2009;4(1):57–71.
[36] Jiang YJ, Towhata I. Experimental study of dry granular flow and impact behavior against a rigid retaining wall. Rock Mech Rock Eng. 2013;46(4):713–729.
[37] Choi CE, Ng C, Goodwin G, et al. Flume investigation of the influence of rigid barrier deflector angle on dry granular overflow mechanisms. Can Geotech J. 2016;53(10):1751–1759.
[38] Armanini A, Dalri C, Larcher M. Slit-check dams for controlling debris flow and mudflow. In: Marui H, Mikos M, editors. Disaster mitigation of debris flows, slope failures and landslides: proceedings of the interpraevent international symposium; 2006 Sept 25-26; Tokyo, Japan; 2006. p. 141–148.
[39] Choi CE, Law RPH. Performance of landslide debris-resisting baffles. HKIE Transactions. 2015;22(4):235–246.
[40] Fiskum E. Flomskred - testing av ulike sikringstiltak i modellforsøk [master's thesis]. Trondheim, Norway: Norwegian University of Science and Technology (NTNU); 2012.

[41] Le TMH, Christensen SO, Watn A, et al. Effects of deflection wall on run-up height of debris flow. In: Aversa S, Cascini L, Picarelli L, et al., editors. Landslides and Engineered Slopes. Experience, Theory and Practice. CRC Press; 2016. p. 1237–1244.
[42] Gonda Y. Function of a debris-flow brake. Int J of Eros Cont Eng. 2009;2(1):15–21.
[43] Kim Y. Study on hydraulic characteristics of debris flow breakers and sabo dams with a flap [dissertation]. Japan: Kyoto University; 2013.
[44] Xie T, Yang H, Wei F, et al. A new watersediment separation structure for debris flow defense and its model test. B Eng Geol Environ. 2014;73(4):947–958.
[45] Cascini L, Cuomo S, Pastor M, et al. Sph-fdm propagation and pore water pressure modelling for debris flows in flume tests. Eng Geol. 2016;213:74–83.
[46] Fiebiger G. Structures of debris flow countermeasures. In: Chen Cl, editor. Debris-Flow Hazards Mitigation: Mechanics, Prediction, and Assessment; 1997 Aug 7-9; San Francisco (CA). ASCE; 1997. p. 596–605.
[47] NVE. Plan for skredfarekartlegging - delrapport jordskred og flomskred. Norway: NVE - Norwegian Water Resources and Energy Directorate; 2011. Report No. 16/2011.
[48] NPRA. Debris flows and slush avalanches. Norway: Norwegian Public Roads Administration (NPRA); 2016. Handbook V139.
[49] NVE. Preliminary regionalization and susceptibility analysis for landslide early warning purposes in norway. Norway: NVE - Norwegian Water Resources and Energy Directorate; 2014. Report No. 37/2014.
[50] ICHARM. Debris-flow dewatering brakes: a promising tool for disaster management in developing countries. Japan: Public Works Research Institute; 2008. Newsletter 3.
[51] Ochiai H, Sammori T, Okada Y. Landslide experiments on artificial and natural slopes. In: Sassa K, Fukuoka H, Wang F, et al., editors. Progress in landslide science. Berlin, Heidelberg: Springer; 2007. p. 209–226.
[52] Lien HP. Design of slit dams for controlling stony debris flows. Int J Sediment Res. 2003; 18(1):74–87.
[53] ICHARM. Testing and demonstrating a technology to cope with debris flows in mountain regions. The Philippines: International Centre for Water Hazard and Risk Management; 2009. Report.
[54] Savage SB, Iverson RM. Surge dynamics coupled to pore-pressure evolution in debris flows. Debris-Flow Hazards Mitigation: Mech Predict Assess. 2003;1-2:503–514.
[55] Major JJ, Iverson RM. Debris-flow deposition: Effects of pore-fluid pressure and friction concentrated at flow margins. Geol Soc Am Bull. 1999;111(10):1424–1434.
[56] Huebl J, Suda J, Proske D, et al. Debris flow impact estimation. In: Popovska C, editor. International symposium on water management and hydraulic engineering: 2009 Sept 1-5; Ohrid, Macadonia; 2009. p. 137–148.
[57] Laache E. Model testing of the drainage screen type debris flow breaker [master's thesis]. Trondheim, Norway: Norwegian University of Science and Technology (NTNU); 2016.
[58] Watanabe M, Mizuyama T, Uehara S. Review of debris flow countermeasure facilities. J Japan Eros Control Eng Soc. 1980;115:40–45.

Paper II

Tayyebi, S. M., Pastor, M., Yifru, A. L., Thakur, V., and Stickle, M. M. (). Two-phase SPH-FD depth integrated model for debris flows: application to basal grid brakes. *Géotechnique*. Submitted manuscript

This paper is awaiting publication and is not included in NTNU Open

Appendices

Appendix A

Results from Model-1

A1 Additional results from screen and underpass tests on Model-1

Table A1: Down-stream deposition thickness, t_d, and run-up height results from screen and underpass tests

Set-up description	Test Name	V1 = 49.4L, C1 = 50%			V2 = 40.1L, C2 = 55%			V3 = 29.4L, C3 = 60%		
		Test Nr.	t_d	run-up	Test Nr.	t_d	run-up	Test Nr.	t_d	run-up
			[mm]	[cm]		[mm]	[cm]		[mm]	[cm]
No countermeasure	S1_r1	V1T1	27.52	-	V2T1	9.95	-	V3T1	8.59	-
	S1_r2	V1T2	18.13	-	V2T2	22.89	-	V3T2	12.62	-
	S1_r3	V1T3	12.46	-	V2T3	18.24	-	V3T3	13.22	-
0.3m wide underpass	S2_r1	V1T4	22.98	25.0	V2T4	37.98	13.0	V3T4	29.54	9.0
	S2_r2	V1T5	30.85	20.0	V2T5	34.51	23.0	V3T5	25.91	8.0
	S2_r3	V1T6	29.90	25.0	V2T6	30.04	17.0	V3T6	24.90	9.0
0.5 m long solid plate	S3-50-0_r1	V1T7	10.60	-	V2T7	19.75	-	V3T7	11.23	-
	S3-50-0_r2	V1T8	14.03	-	V2T8	18.53	-	V3T8	7.17	-
	S3-50-0_r3	V1T9	9.27	-	V2T9	12.89	-	V3T9	13.89	-
0.25 m long screen	S3-25-2_r1	V1T10	8.15	-	V2T10	11.71	-	V3T10	10.06	-
	S3-25-2_r2	V1T11	5.48	-	V2T11	11.77	-	V3T11	8.03	-
	S3-25-2_r3	V1T12	14.72	-	V2T12	15.25	-	V3T12	11.11	-
0.5 m long screen	S3-50-2_r1	V1T13	19.30	-	V2T13	6.14	-	V3T13	5.88	-
	S3-50-2_r2	V1T14	14.02	-	V2T14	8.84	-	V3T14	7.37	-
	S3-50-2_r3	V1T15	13.02	-	V2T15	12.88	-	V3T15	7.81	-
0.5 m solid plate and underpass	S4-50-0_r1	V1T16	27.06	11.0	V2T16	31.82	17.0	V3T16	28.18	8.0
	S4-50-0_r2	V1T17	27.35	20.0	V2T17	25.41	16.0	V3T17	25.42	12.0
	S4-50-0_r3	V1T18	26.41	5.0	V2T18	27.55	17.0	V3T18	29.74	14.0
0.25 m screen & underpass	S4-25-2_r1	V1T19	22.98	10.0	V2T19	30.14	10.0	V3T19	20.22	7.0
	S4-25-2_r2	V1T20	21.10	10.0	V2T20	23.57	12.0	V3T20	28.82	8.0
	S4-25-2_r3	V1T21	21.76	8.0	V2T21	26.50	15.0	V3T21	22.55	8.0
0.5 m screen & underpass	S4-50-2_r1	V1T22	26.95	13.0	V2T22	17.63	7.0	V3T22	20.53	6.0
	S4-50-2_r2	V1T23	25.53	5.0	V2T23	18.63	7.0	V3T23	14.82	6.0
	S4-50-2_r3	V1T24	25.91	7.0	V2T24	13.36	7.0	V3T24	13.96	7.0

A2 All impact force measurement plots for V1C1, V2C2, and V3C3

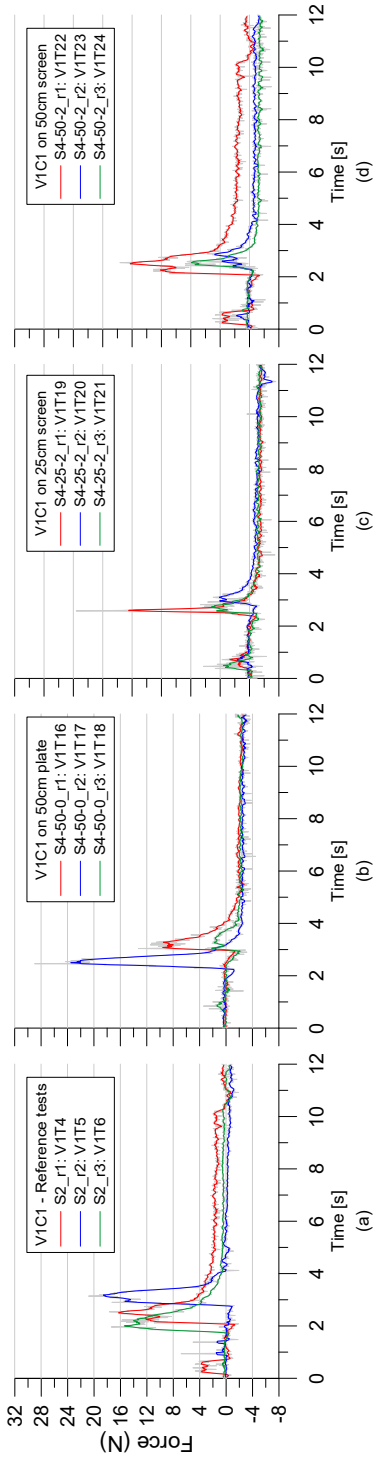

Fig. A1: All impact force plots from material V1C1 for: (a) reference, (b) 50cm long plate, (c) 25cm long screen, and (d) 50cm long screen tests

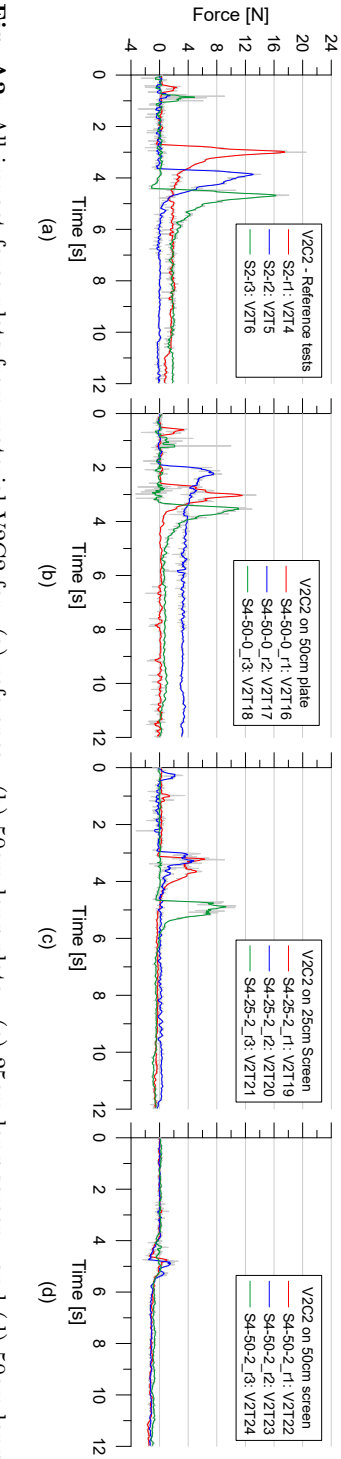

Fig. A2: All impact force plots from material V2C2 for: (a) reference , (b) 50cm long plate , (c) 25cm long screen , and (d) 50cm long screen tests

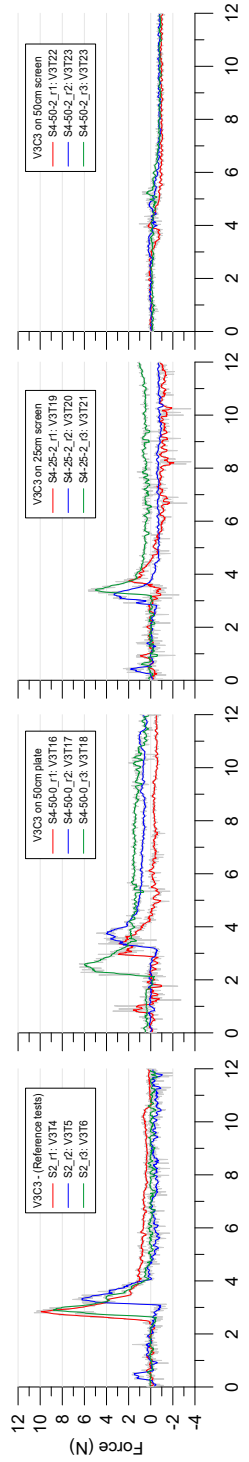

Fig. A3: All impact force plots from material V3C3 for: (a) reference, (b) 50cm long plate, (c) 25cm long screen, and (d) 50cm long screen tests

A3 Pore-water pressure measured on Model-1

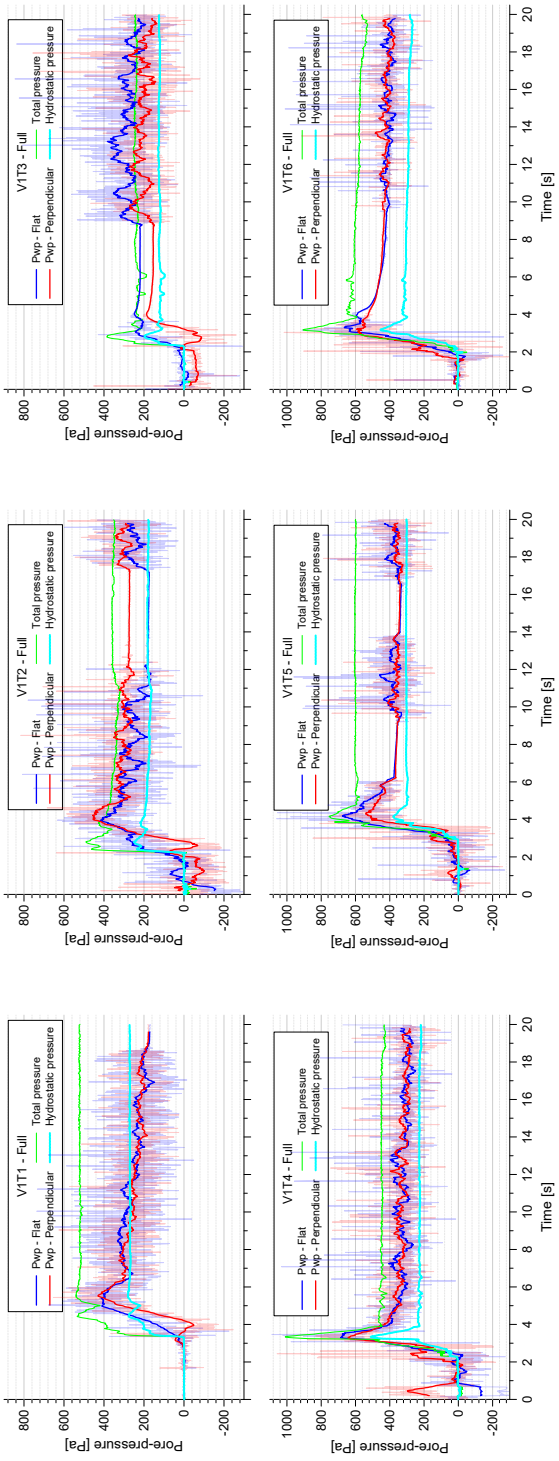

Fig. A4: Measured pore-water pressures along with calculated total normal stress and hydrostatic pore-water pressure

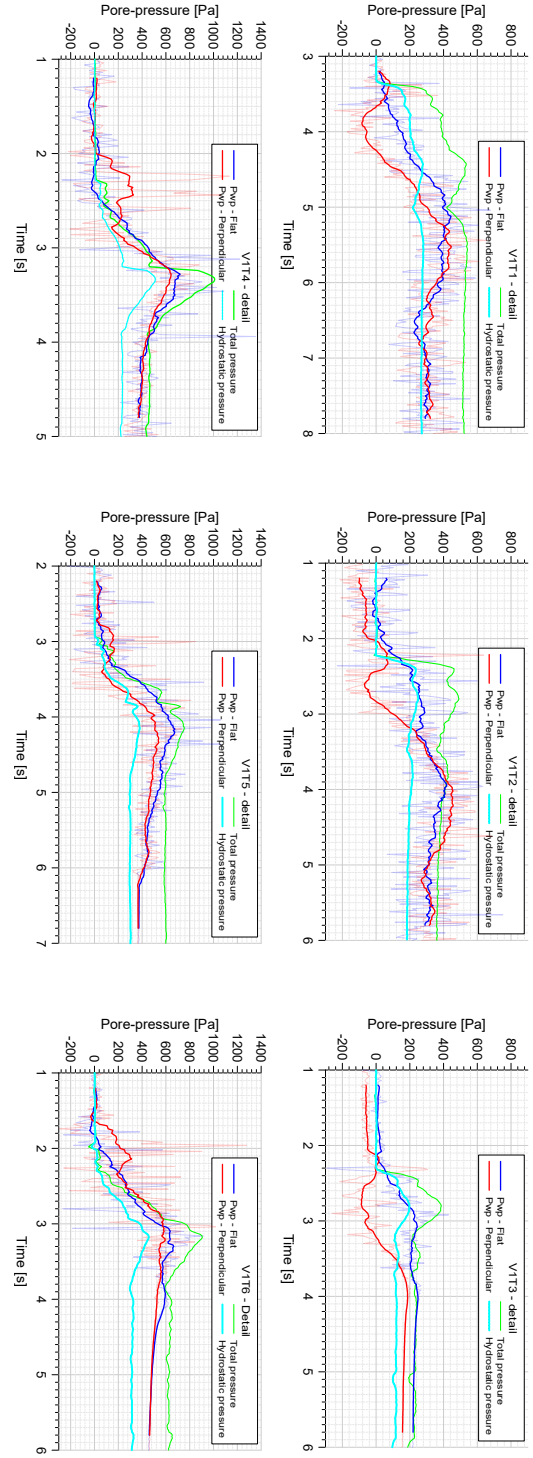

Fig. A5: Measured pore-water pressures along with calculated total normal stress and hydrostatic pore-water pressure: With detail at peak flow height and peak pore-water pressure values

Appendix B

Results from Model-2

B1 Full result of the dimensionless analyses of the Model-2 debris-flow characterization tests

Table B1: Physical and dimensionless parameters for all tests using flow front tracked velocity

Test Name	v m/s	h m	C_s [-]	C_f [-]	ρ_f $[kg/m^3]$	μ $[pa \cdot s]$	$\dot{\gamma}$ $[1/s]$	N [-]	N_{Sav} [-]	N_{Bag} [-]	N_{mass} [-]	N_{Dar} [-]	N_{Rey} [-]	N_{fric} [-]
G1V1C1-r3	2.60	0.029	0.57	0.43	1 131	0.0013	90.61	42.20	0.04	121	3	295	38	3 041
G1V1C2-r3	3.25	0.026	0.52	0.48	1 108	0.0012	124.98	38.24	0.08	144	3	224	53	1 747
G1V1C3-r3	3.5	0.022	0.47	0.53	1 090	0.0012	157.83	32.61	0.15	155	2	188	69	1 022
G1V2C1-r3	3.1	0.034	0.57	0.43	1 131	0.0013	92.27	49.41	0.04	123	3	290	39	3 497
G1V2C2-r3	3.0	0.026	0.52	0.48	1 108	0.0012	114.53	38.52	0.07	132	3	244	49	1 921
G1V2C3-r3	3.6	0.024	0.47	0.53	1 090	0.0012	151.27	35.00	0.13	149	2	197	66	1 144
G1V3C1-r3	3.3	0.038	0.57	0.43	1 131	0.0013	85.78	56.58	0.03	114	3	312	36	4 308
G1V3C2-r3	3.4	0.032	0.52	0.48	1 108	0.0012	107.09	46.69	0.05	123	3	261	46	2 490
G1V3C3-r3	3.8	0.027	0.47	0.53	1 090	0.0012	140.18	39.87	0.10	138	2	212	61	1 406
G2V1C1-r3	2.4	0.027	0.52	0.48	1 304	0.0018	89.39	31.59	0.07	106	2	704	47	1 469
G2V1C2-r3	2.9	0.021	0.47	0.53	1 256	0.0016	140.24	24.33	0.22	155	2	441	79	695
G2V1C3-r3	4.0	0.027	0.43	0.57	1 215	0.0015	147.40	31.93	0.18	149	2	424	87	816
G2V2C1-r3	2.7	0.024	0.52	0.48	1 304	0.0018	110.88	28.65	0.12	132	2	567	59	1 074
G2V2C2-r3	4.1	0.026	0.47	0.53	1 256	0.0016	159.71	30.20	0.23	177	2	388	90	758
G2V2C3-r3	4.0	0.034	0.43	0.57	1 215	0.0015	117.40	40.09	0.09	119	2	533	70	1 287
G2V3C1-r3	3.45	0.034	0.52	0.48	1 304	0.0018	100.12	40.54	0.07	119	2	628	53	1 684
G2V3C2-r3	3.75	0.035	0.47	0.53	1 256	0.0016	106.39	41.47	0.08	118	2	582	60	1 563
G2V3C3-r3	4.15	0.037	0.43	0.57	1 215	0.0015	112.04	43.57	0.08	114	2	558	66	1 465
G3V1C1-r3	3.0	0.022	0.47	0.54	1 442	0.0025	138.60	20.61	0.17	149	2	1 383	90	863
G3V1C2-r3	3.6	0.019	0.43	0.57	1 377	0.0021	188.82	18.16	0.36	202	1	951	136	555
G3V1C3-r3	4.2	0.019	0.39	0.61	1 321	0.0019	218.76	18.28	0.49	226	1	796	172	466
G3V2C1-r3	3.5	0.027	0.47	0.54	1 442	0.0025	127.94	26.05	0.12	138	2	1 498	83	1 181
G3V2C2-r3	3.8	0.021	0.43	0.57	1 377	0.0021	183.46	19.73	0.32	196	1	979	132	621
G3V2C3-r3	4.0	0.022	0.39	0.61	1 321	0.0019	178.71	21.32	0.28	185	1	975	140	665
G3V3C1-r3	3.6	0.020	0.47	0.54	1 442	0.0025	175.76	19.51	0.29	189	2	1 090	114	644
G3V3C2-r3	3.85	0.024	0.43	0.57	1 377	0.0021	161.16	22.75	0.21	172	1	1 114	116	815
G3V3C3-r3	4.0	0.028	0.39	0.61	1 321	0.0019	145.38	26.20	0.15	150	1	1 198	114	1 005
Max	2.40	0.019	0.39	0.43	1 090	0.0012	85.78	18.16	0.03	106	1	188	36	466
Min	4.20	0.038	0.57	0.61	1 442	0.0025	218.76	56.58	0.49	226	3	1 498	172	4 308

Appendix B

Table B2: Physical and dimensionless parameters for all tests using average velocity

Test Name	v m/s	h m	C_s [-]	C_f [-]	ρ_f $[kg/m^3]$	μ $[pa \cdot s]$	$\dot{\gamma}$ $[1/s]$	N [-]	N_{Sav} [-]	N_{Bag} [-]	N_{mass} [-]	N_{Dar} [-]	N_{Rey} [-]	N_{fric} [-]
G1V1C1-r1	2.59	0.030	0.568	0.43	1 131	0.00125	86.58	43.93	0.03	115	3	309	36	3 314
G1V1C1-r2	2.78	0.033	0.568	0.43	1 131	0.00125	84.94	48.09	0.03	113	3	315	35	3 697
G1V1C1-r3	2.59	0.029	0.568	0.43	1 131	0.00125	90.13	42.20	0.04	120	3	297	38	3 057
G1V1C2-r1	3.00	0.025	0.520	0.48	1 108	0.00120	120.38	36.65	0.08	138	3	232	51	1 738
G1V1C2-r2	2.78	0.027	0.520	0.48	1 108	0.00120	103.86	39.33	0.06	119	3	269	44	2 163
G1V1C2-r3	2.68	0.026	0.520	0.48	1 108	0.00120	103.00	38.24	0.06	118	3	272	44	2 120
G1V1C3-r1	4.17	0.027	0.473	0.53	1 090	0.00116	152.68	40.13	0.12	150	2	195	66	1 300
G1V1C3-r2	3.13	0.023	0.473	0.53	1 090	0.00116	133.90	34.32	0.10	132	2	222	58	1 267
G1V1C3-r3	3.00	0.022	0.473	0.53	1 090	0.00116	135.28	32.61	0.11	133	2	220	59	1 192
G1V2C1-r1	3.13	0.027	0.568	0.43	1 131	0.00125	115.33	39.85	0.07	154	3	232	48	2 256
G1V2C1-r3	2.78	0.034	0.568	0.43	1 131	0.00125	82.68	49.41	0.03	110	3	324	35	3 902
G1V2C2-r2	3.33	0.031	0.520	0.48	1 108	0.00120	107.68	45.52	0.05	124	3	260	46	2 414
G1V2C2-r3	3.26	0.026	0.520	0.48	1 108	0.00120	124.49	38.52	0.08	143	3	225	53	1 767
G1V2C3-r1	3.41	0.024	0.473	0.53	1 090	0.00116	143.26	35.00	0.12	141	2	208	62	1 208
G1V2C3-r3	3.41	0.024	0.473	0.53	1 090	0.00116	143.25	35.00	0.12	141	2	208	62	1 208
G1V3C1-r1	2.88	0.038	0.568	0.43	1 131	0.00125	75.38	56.28	0.02	100	3	355	31	4 876
G1V3C1-r3	2.78	0.038	0.568	0.43	1 131	0.00125	72.20	56.58	0.02	96	3	371	30	5 117
G1V3C2-r1	3.26	0.026	0.520	0.48	1 108	0.00120	126.20	38.00	0.08	145	3	222	54	1 719
G1V3C2-r3	3.26	0.032	0.520	0.48	1 108	0.00120	102.70	46.69	0.05	118	3	272	44	2 596
G1V3C3-r1	3.85	0.028	0.473	0.53	1 090	0.00116	138.74	40.77	0.09	136	2	214	60	1 453
G1V3C3-r3	3.57	0.027	0.473	0.53	1 090	0.00116	131.74	39.87	0.09	130	2	226	57	1 496
G2V1C1-r1	2.50	0.026	0.516	0.48	1 304	0.00179	95.77	30.71	0.09	114	2	657	51	1 333
G2V1C1-r2	2.63	0.023	0.516	0.48	1 304	0.00179	113.75	27.22	0.14	135	2	553	60	995
G2V1C1-r3	2.38	0.027	0.516	0.48	1 304	0.00179	88.68	31.59	0.07	105	2	709	47	1 481
G2V1C2-r1	3.13	0.025	0.473	0.53	1 256	0.00161	126.71	29.02	0.15	140	2	489	71	918
G2V1C2-r2	3.85	0.027	0.473	0.53	1 256	0.00161	144.88	31.23	0.19	160	2	427	82	864
G2V1C2-r3	3.41	0.021	0.473	0.53	1 256	0.00161	164.86	24.33	0.31	183	2	376	93	592
G2V1C3-r1	4.17	0.033	0.430	0.57	1 215	0.00148	126.11	38.87	0.11	128	2	496	75	1 161
G2V1C3-r3	3.85	0.027	0.430	0.57	1 215	0.00148	141.73	31.93	0.17	144	2	441	84	849
G2V2C1-r1	2.50	0.030	0.516	0.48	1 304	0.00179	84.64	34.75	0.06	100	2	743	45	1 707
G2V2C1-r2	2.78	0.032	0.516	0.48	1 304	0.00179	87.21	37.47	0.06	103	2	721	46	1 786
G2V2C1-r3	2.50	0.024	0.516	0.48	1 304	0.00179	102.67	28.65	0.10	122	2	613	54	1 160
G2V2C2-r1	3.33	0.028	0.473	0.53	1 256	0.00161	117.41	33.40	0.11	130	2	527	66	1 140
G2V2C2-r2	3.13	0.026	0.473	0.53	1 256	0.00161	120.28	30.57	0.13	133	2	515	68	1 019
G2V2C2-r3	3.13	0.026	0.473	0.53	1 256	0.00161	121.73	30.20	0.14	135	2	509	69	995
G2V2C3-r1	3.85	0.033	0.430	0.57	1 215	0.00148	117.63	38.47	0.10	119	2	532	70	1 232
G2V2C3-r3	3.57	0.034	0.430	0.57	1 215	0.00148	104.82	40.09	0.07	106	2	597	62	1 441
G2V3C1-r1	2.94	0.030	0.516	0.48	1 304	0.00179	96.82	35.74	0.07	115	2	650	51	1 535
G2V3C1-r3	3.13	0.034	0.516	0.48	1 304	0.00179	90.69	40.54	0.06	108	2	694	48	1 859
G2V3C2-r1	3.13	0.033	0.473	0.53	1 256	0.00161	96.03	38.29	0.07	106	2	645	54	1 598
G2V3C2-r3	3.33	0.035	0.473	0.53	1 256	0.00161	94.57	41.47	0.06	105	2	655	53	1 758
G2V3C3-r1	4.17	0.040	0.430	0.57	1 215	0.00148	104.56	46.88	0.06	106	2	598	62	1 689
G2V3C3-r3	3.85	0.037	0.430	0.57	1 215	0.00148	103.84	43.57	0.07	105	2	602	62	1 581
G3V1C1-r1	2.94	0.025	0.465	0.54	1 442	0.00245	116.85	23.97	0.22	126	2	1 640	76	566
G3V1C1-r2	3.13	0.027	0.465	0.54	1 442	0.00245	113.98	26.11	0.19	123	2	1 681	74	632
G3V1C1-r3	2.68	0.022	0.465	0.54	1 442	0.00245	123.75	20.61	0.29	133	2	1 549	80	460
G3V1C2-r1	3.57	0.032	0.426	0.57	1 377	0.00210	110.56	30.77	0.15	118	1	1 624	80	802
G3V1C2-r2	3.85	0.027	0.426	0.57	1 377	0.00210	143.84	25.47	0.30	154	1	1 248	104	510
G3V1C2-r3	3.75	0.019	0.426	0.57	1 377	0.00210	196.69	18.16	0.79	210	1	913	142	266
G3V1C3-r1	4.17	0.039	0.388	0.61	1 321	0.00186	107.60	36.88	0.11	111	1	1 619	84	993
G3V1C3-r3	3.26	0.019	0.388	0.61	1 321	0.00186	169.85	18.28	0.56	176	1	1 025	133	312
G3V2C1-r1	3.57	0.028	0.465	0.54	1 442	0.00245	126.56	26.88	0.23	136	2	1 514	82	586
G3V2C1-r2	3.57	0.029	0.465	0.54	1 442	0.00245	121.65	27.96	0.21	131	2	1 576	79	634
G3V2C1-r3	3.00	0.027	0.465	0.54	1 442	0.00245	109.66	26.05	0.18	118	2	1 748	71	656
G3V2C2-r1	3.57	0.029	0.426	0.57	1 377	0.00210	122.14	27.85	0.20	131	1	1 470	88	657
G3V2C2-r2	3.85	0.027	0.426	0.57	1 377	0.00210	140.40	26.09	0.28	150	1	1 279	101	535
G3V2C2-r3	3.57	0.021	0.426	0.57	1 377	0.00210	172.43	19.73	0.56	185	1	1 041	124	330
G3V2C3-r1	3.57	0.030	0.388	0.61	1 321	0.00186	118.80	28.63	0.18	123	1	1 466	93	698
G3V2C3-r3	3.95	0.022	0.388	0.61	1 321	0.00186	176.35	21.32	0.52	182	1	988	138	350
G3V3C1-r1	3.33	0.035	0.465	0.54	1 442	0.00245	96.16	33.01	0.11	103	2	1 993	62	947
G3V3C1-r2	2.94	0.021	0.465	0.54	1 442	0.00245	141.23	19.83	0.39	152	2	1 357	92	388
G3V3C1-r3	3.00	0.020	0.465	0.54	1 442	0.00245	146.47	19.51	0.43	157	2	1 308	95	368
G3V3C2-r1	3.85	0.028	0.426	0.57	1 377	0.00210	138.59	26.43	0.27	148	1	1 296	100	549
G3V3C2-r3	3.75	0.024	0.426	0.57	1 377	0.00210	156.97	22.75	0.40	168	1	1 144	113	418
G3V3C3-r1	3.85	0.031	0.388	0.61	1 321	0.00186	123.41	29.68	0.18	128	1	1 411	97	697
G3V3C3-r3	3.95	0.028	0.388	0.61	1 321	0.00186	143.47	26.20	0.28	148	1	1 214	113	529

– – – represents tests that are not conducted.

B2 Result plots of dimensionless numbers from Table B1

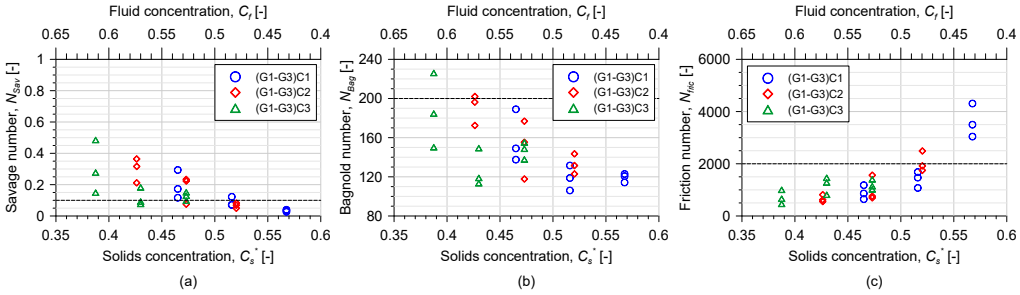

Fig. B1: Dimensionless numbers variations with GSD and C_s from Table B1: (a) Savage number, (b) Bagnold number, and (c) friction number

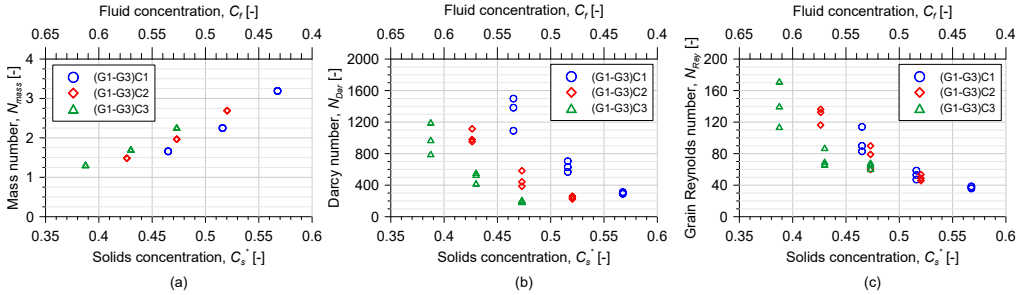

Fig. B2: Dimensionless numbers variations with GSD and C_s from Table B1: (a) mass number, (b) Darcy number, and (c) grain Reynolds number

Appendix C

Result from numerical parametric study

C1 1D sensitivity simulation result from V1

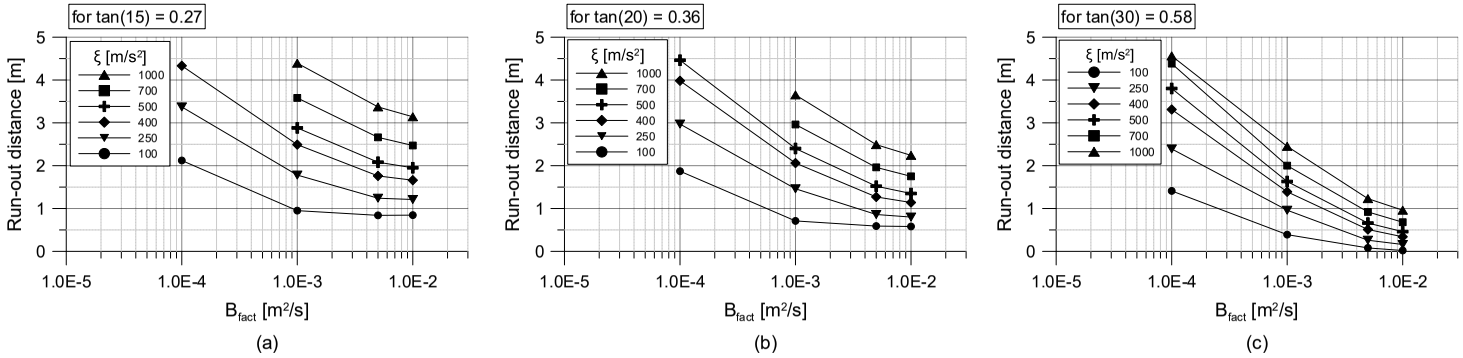

Fig. C1: The simulation run-out distance Vs B_{fact}: (a) for $tan(\phi_b) = 0.27$, (b) for $tan(\phi_b) = 0.36$, and (c)for $tan(\phi_b) = 0.58$

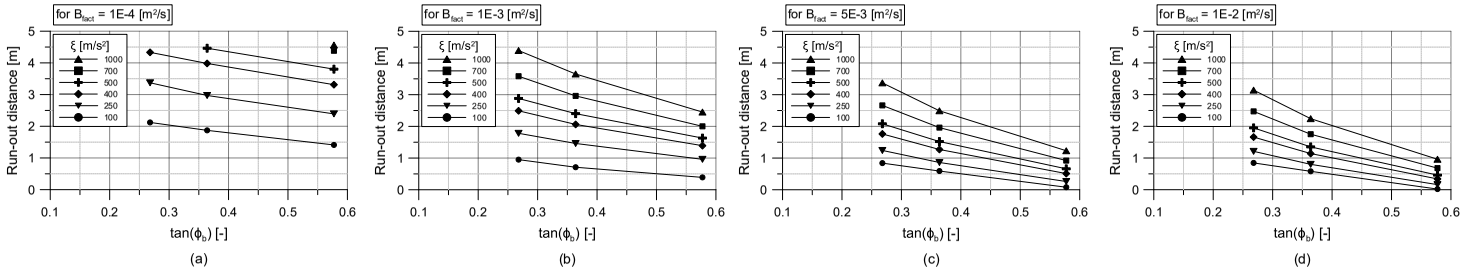

Fig. C2: The simulation run-out distance Vs $tan(\phi_b)$: (a) for $B_{fact} = 1E{-}4m^2/s$, (b) for $B_{fact} = 1E{-}3m^2/s$, (c) for $B_{fact} = 5E{-}3m^2/s$, (d) for $B_{fact} = 1E - 2m^2/s$

Appendix D

Design of Model-2

D1 The working drawing of Model-2

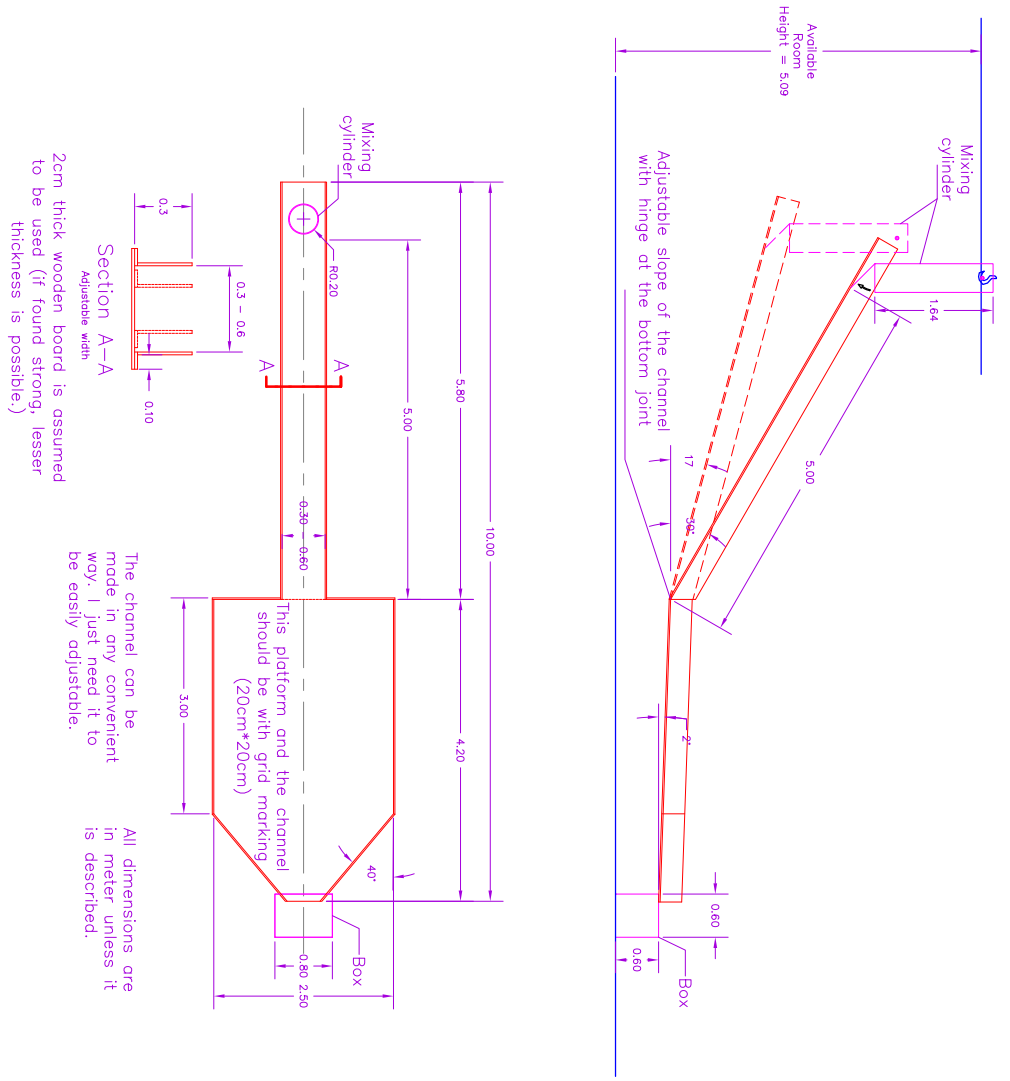

Fig. D1: Design and working drawing of Model-2

Appendix E

Raw data from Model-2 tests and sequential results from PIV analyses

E1 Raw data plots of the Model-2 debris-flow tests

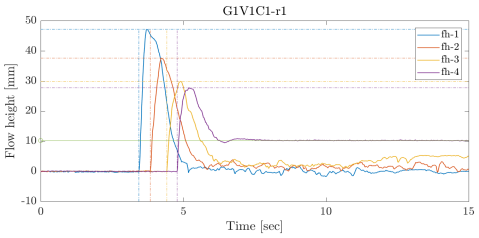
G1V1C1-r1
fh-1
fh-2
fh-3
fh-4
Flow height [mm]
Time [sec]

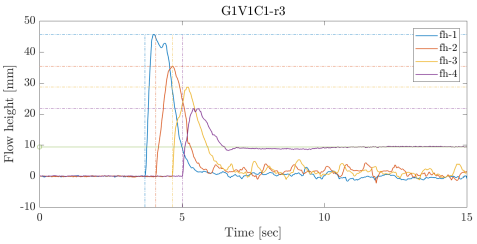
G1V1C1-r3
fh-1
fh-2
fh-3
fh-4
Flow height [mm]
Time [sec]

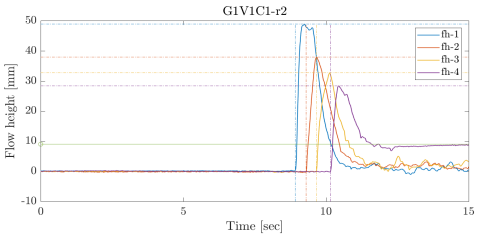
G1V1C1-r2
fh-1
fh-2
fh-3
fh-4
Flow height [mm]
Time [sec]

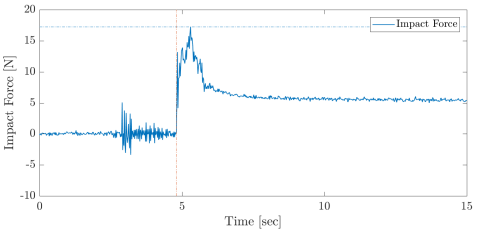
Impact Force
Impact Force [N]
Time [sec]

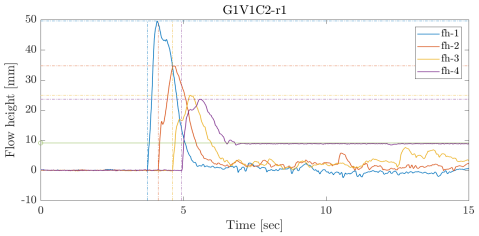
G1V1C2-r1
fh-1
fh-2
fh-3
fh-4
Flow height [mm]
Time [sec]

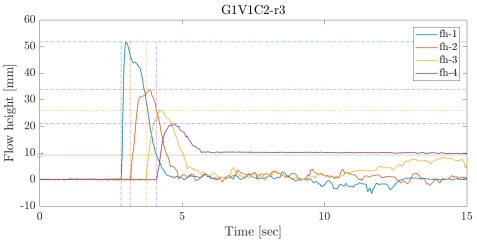
G1V1C2-r3
fh-1
fh-2
fh-3
fh-4
Flow height [mm]
Time [sec]

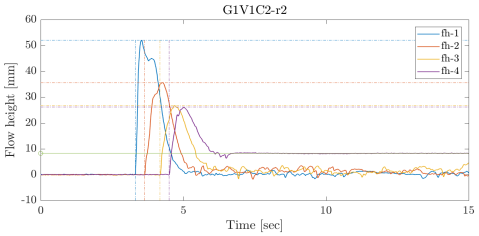
G1V1C2-r2
fh-1
fh-2
fh-3
fh-4
Flow height [mm]
Time [sec]

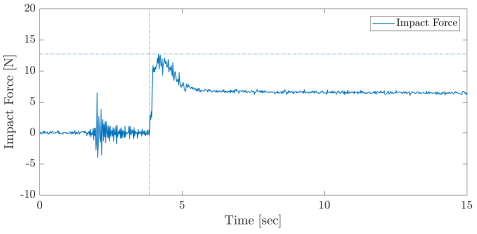
Impact Force
Impact Force [N]
Time [sec]

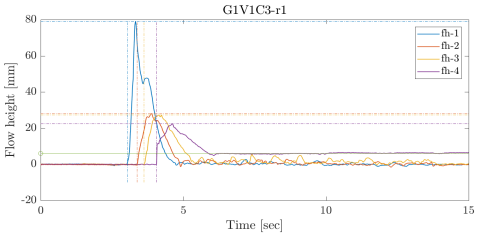
G1V1C3-r1
fh-1
fh-2
fh-3
fh-4
Flow height [mm]
Time [sec]

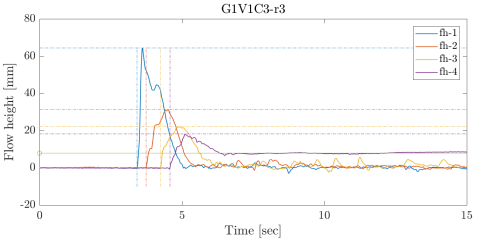
G1V1C3-r3
fh-1
fh-2
fh-3
fh-4
Flow height [mm]
Time [sec]

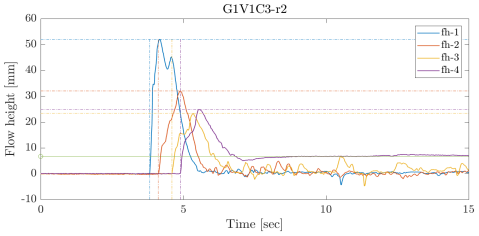
G1V1C3-r2
fh-1
fh-2
fh-3
fh-4
Flow height [mm]
Time [sec]

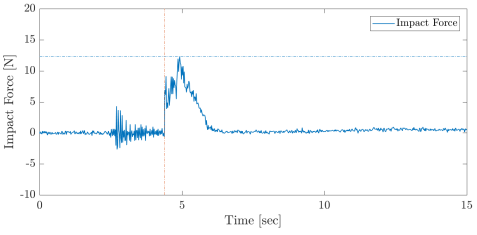
Impact Force
Impact Force [N]
Time [sec]

G1V2C1-r1

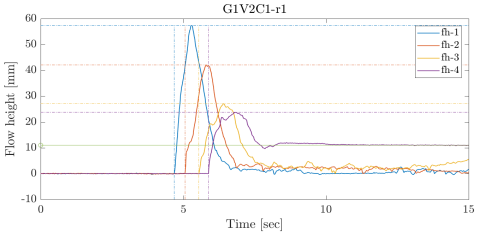

G1V2C1-r3

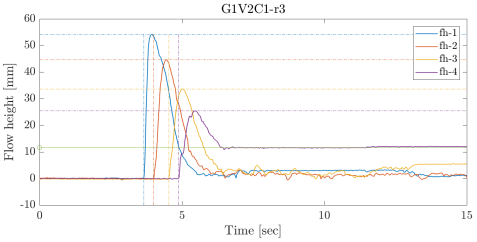

G1V2C1-r2
No data

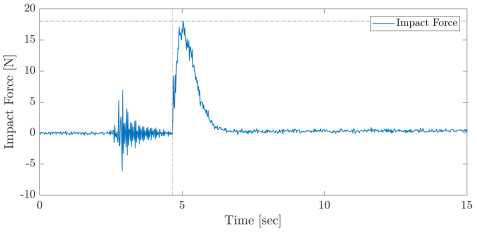

G1V2C2-r1
No data

G1V2C2-r3

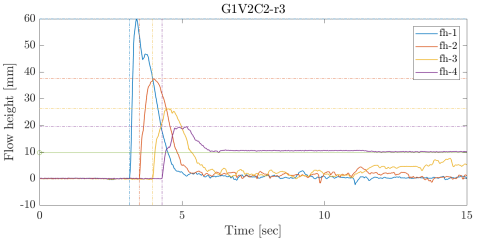

G1V2C2-r2

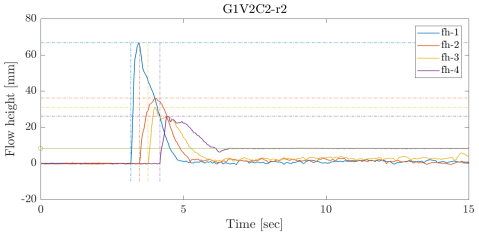

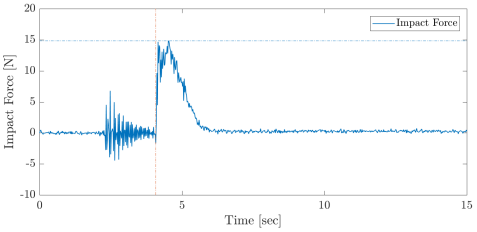

G1V2C3-r1

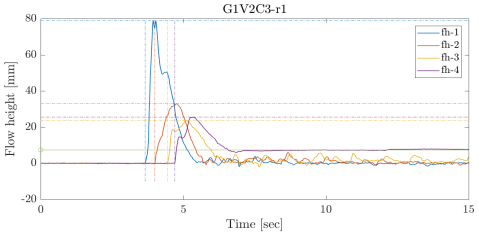

G1V2C3-r3

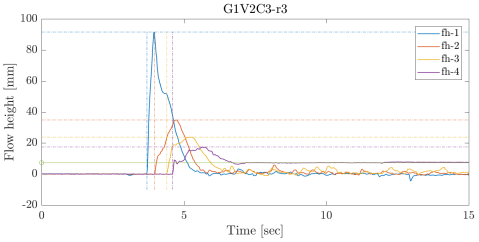

G1V2C3-r2
No data

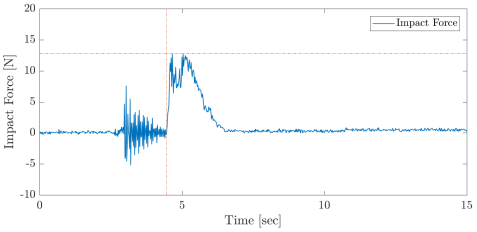

G1V3C1-r1

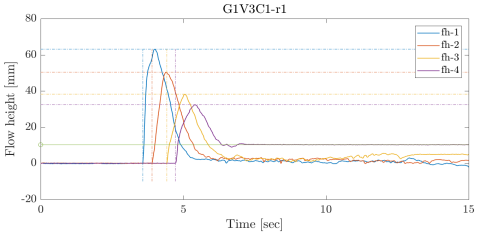

G1V3C1-r3

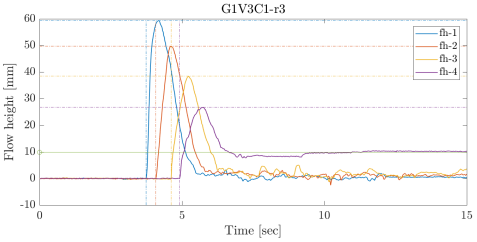

G1V3C1-r2
No data

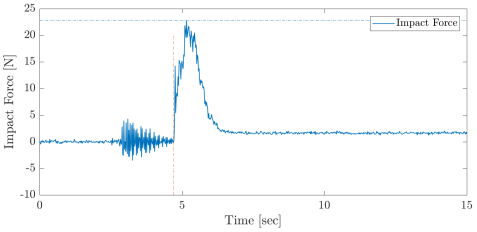

G1V3C2-r1

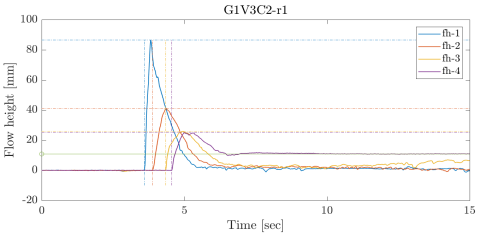

G1V3C2-r3

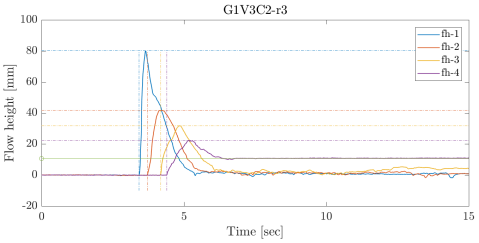

G1V3C2-r2
No data

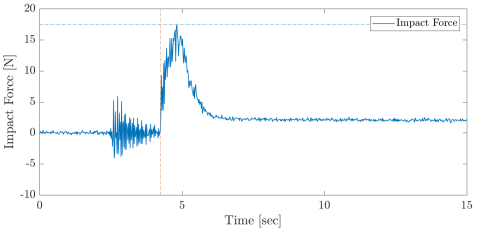

G1V3C3-r1

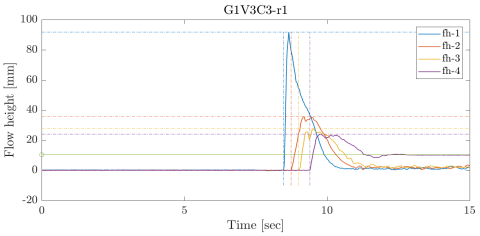

G1V3C3-r3

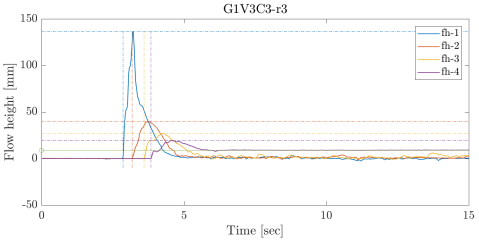

G1V3C3-r2
No data

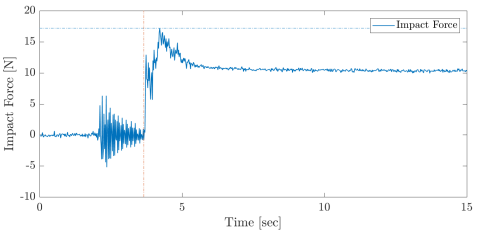

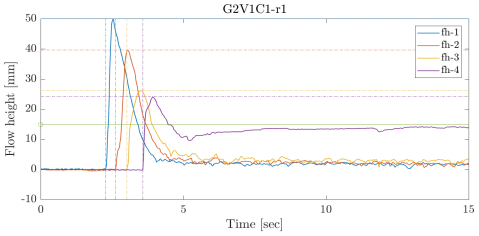

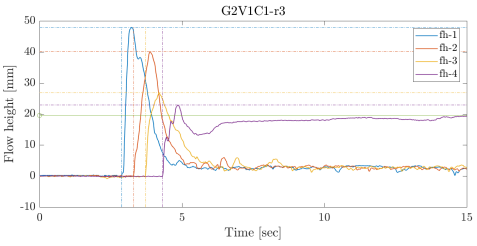

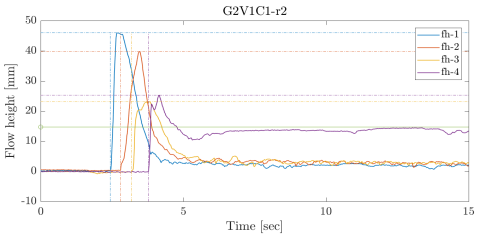

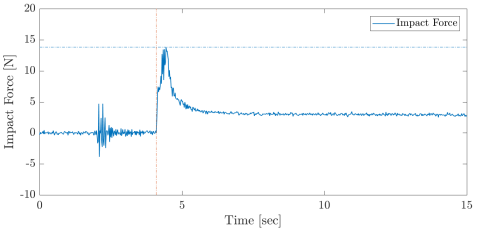

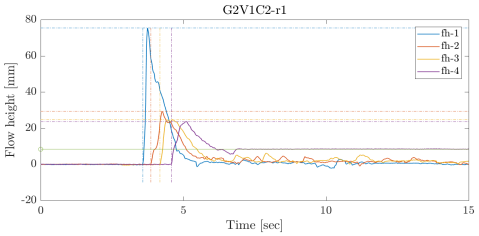

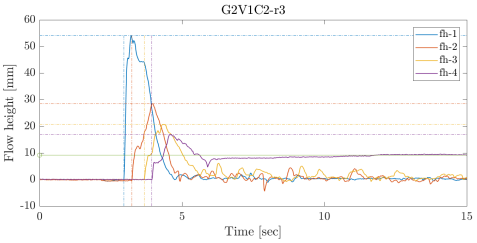

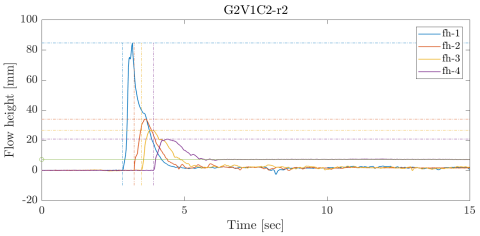

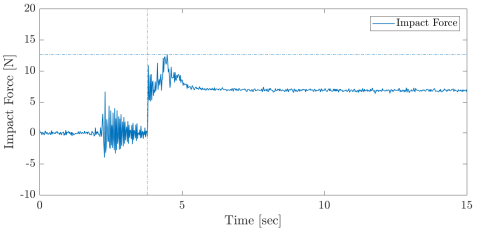

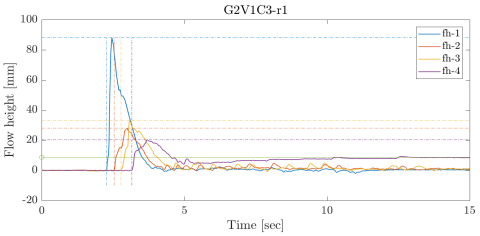

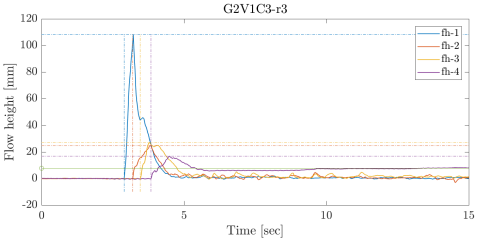

G2V1C3-r2
No data

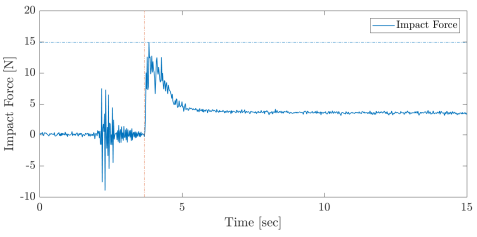

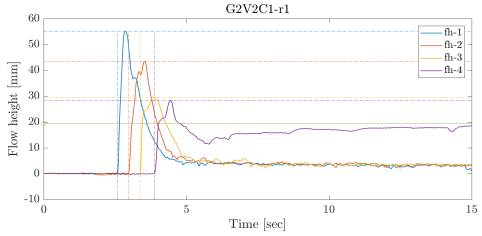

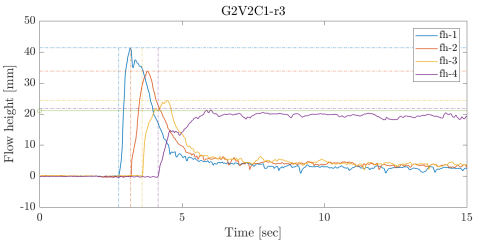

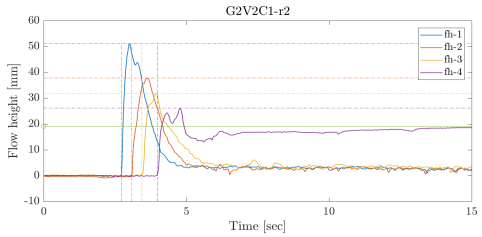

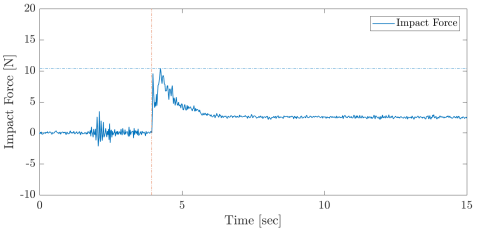

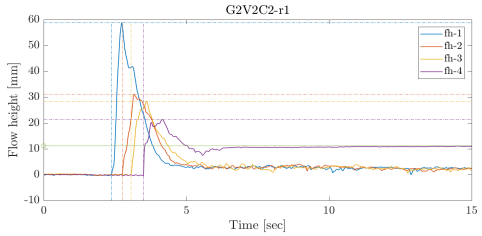

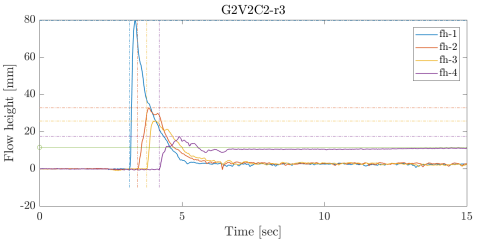

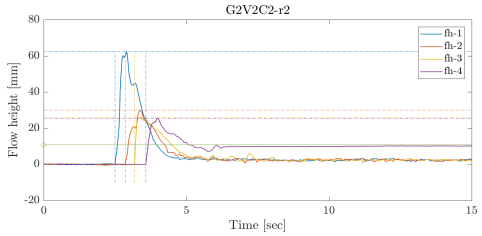

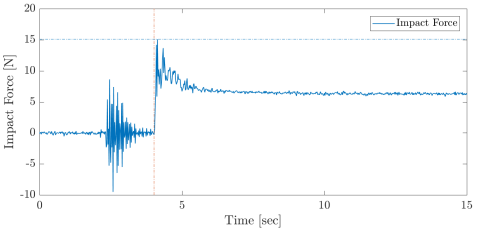

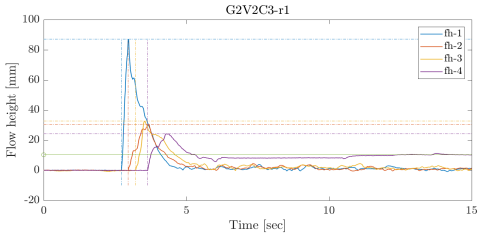

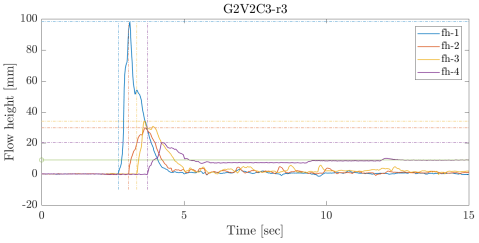

G2V2C3-r2
No data

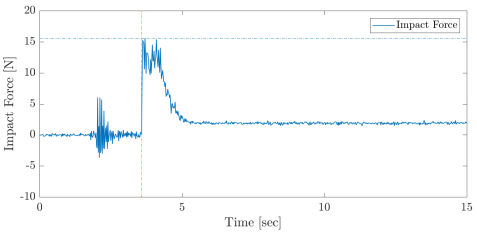

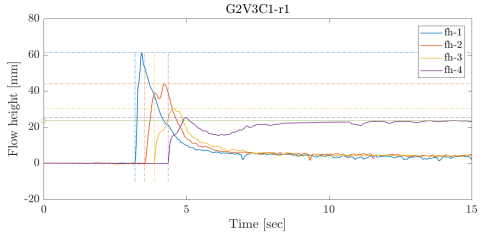

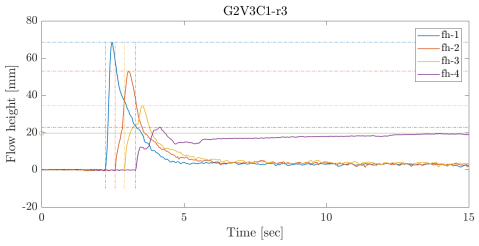

G2V3C1-r2
No data

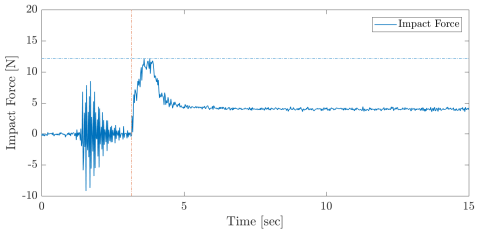

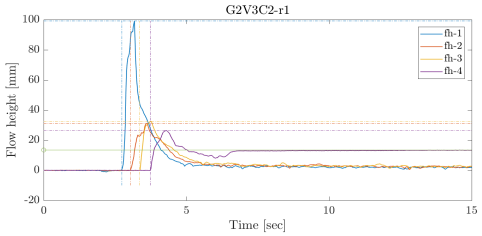

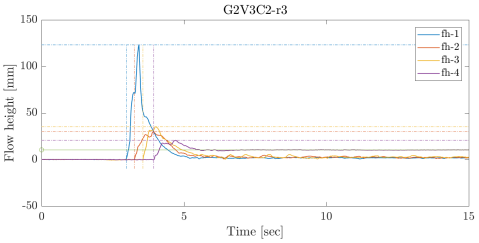

G2V3C2-r2
No data

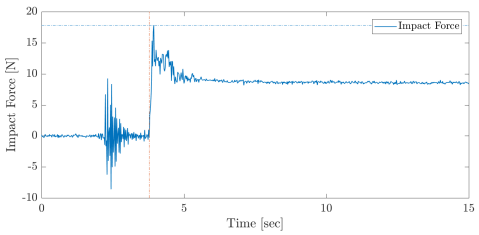

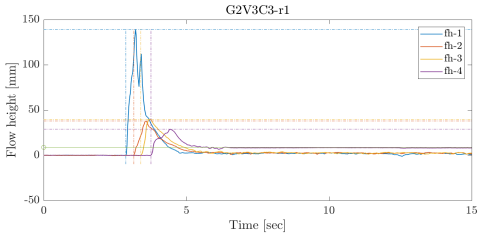

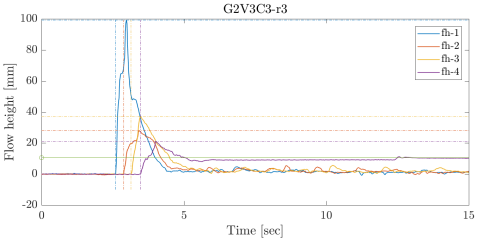

G2V3C3-r2
No data

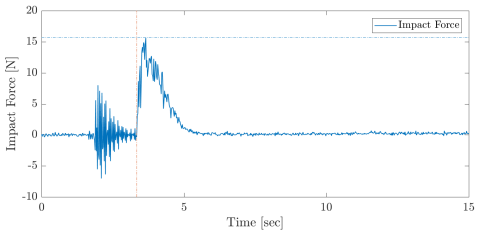

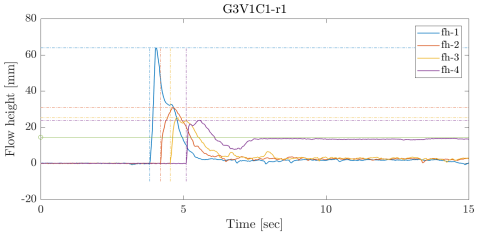

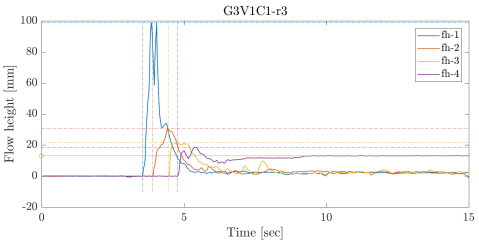

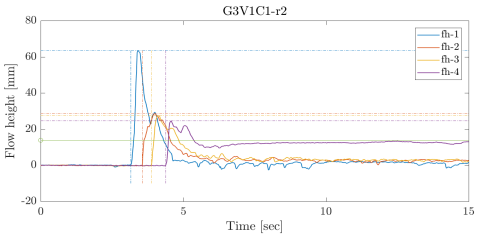

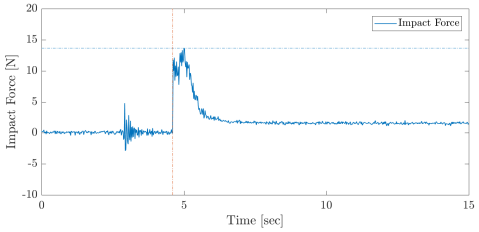

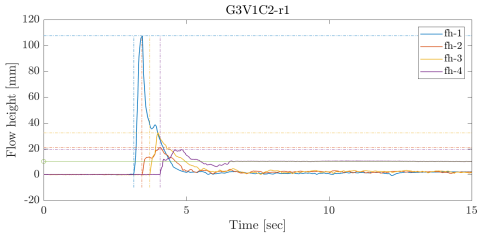

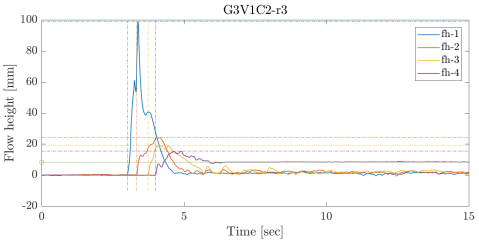

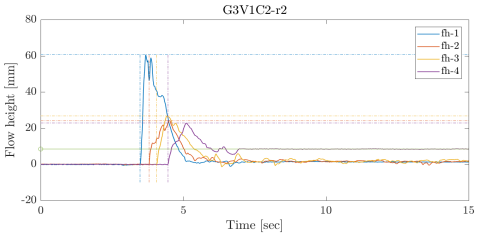

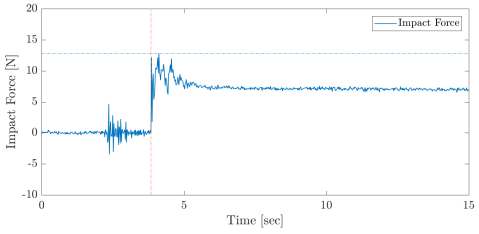

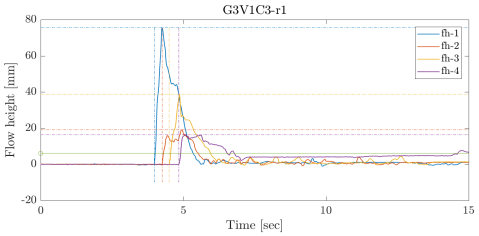

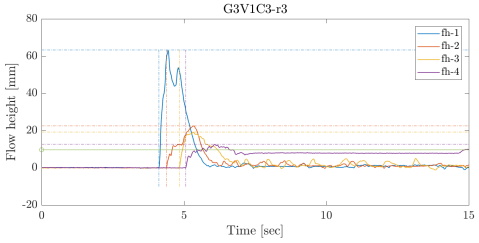

G3V1C3-r2
No data

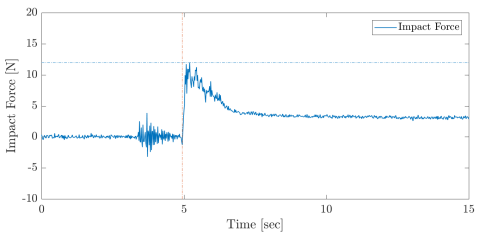

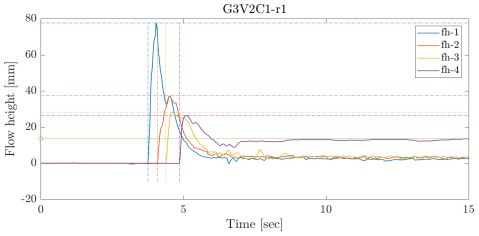

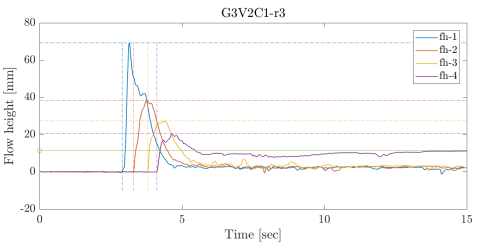

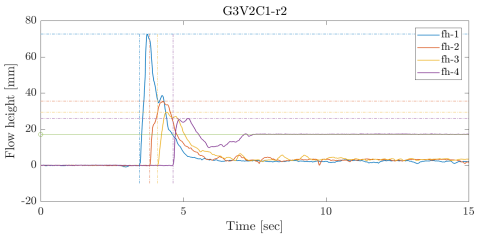

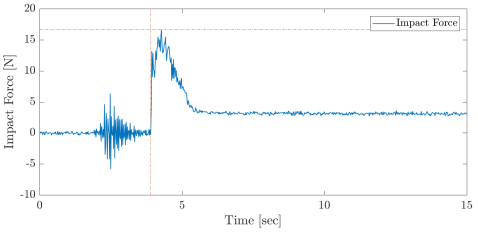

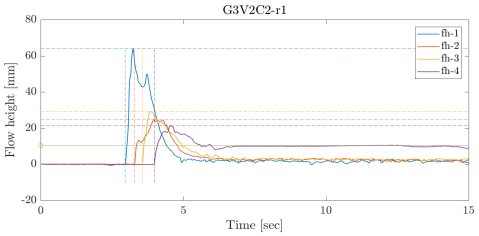

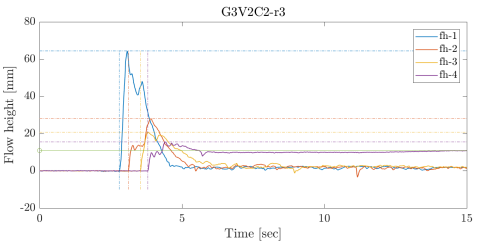

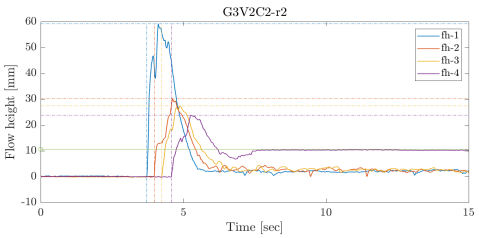

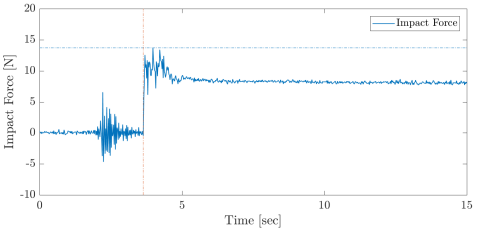

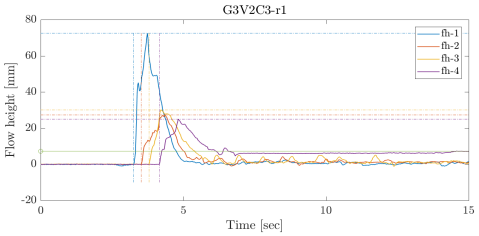

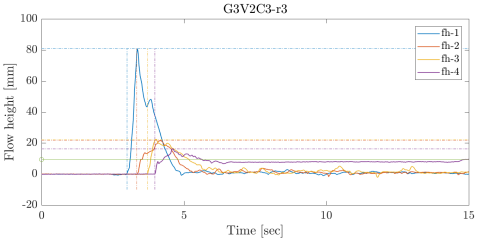

G3V2C3-r2
No data

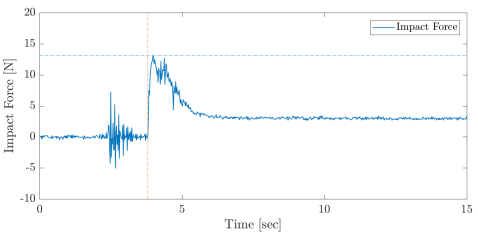

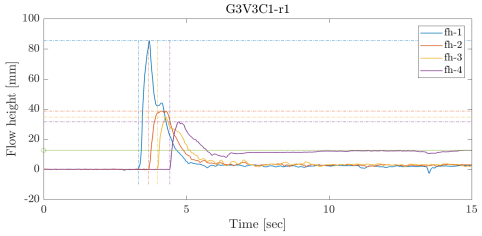

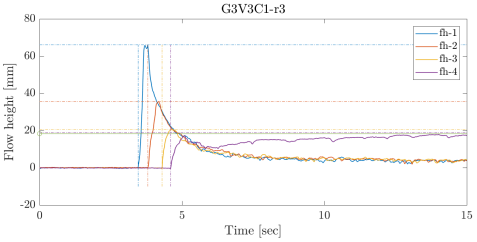

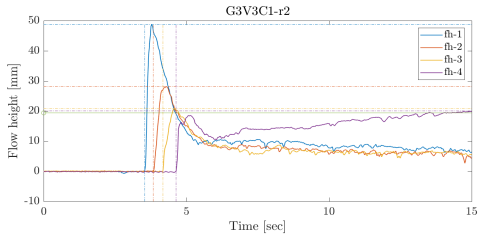

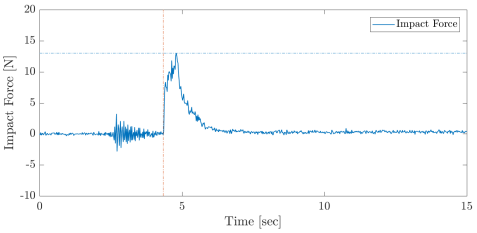

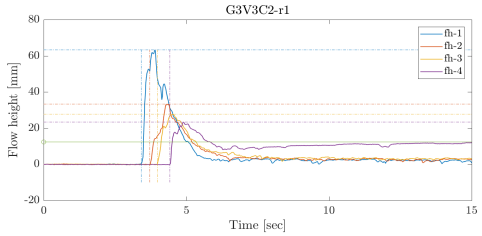

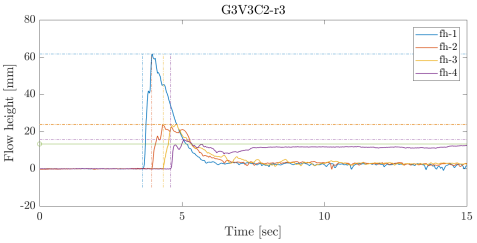

G3V3C2-r2
No data

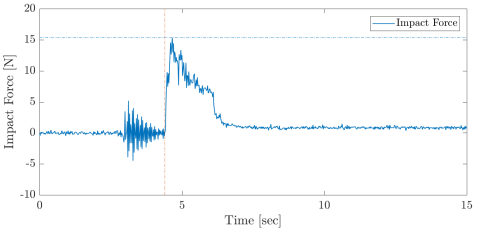

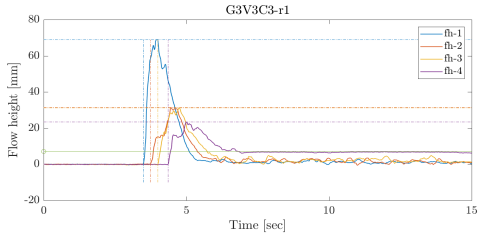

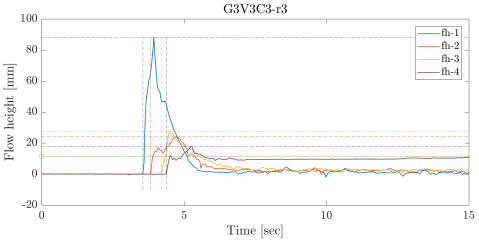

G3V3C3-r2
No data

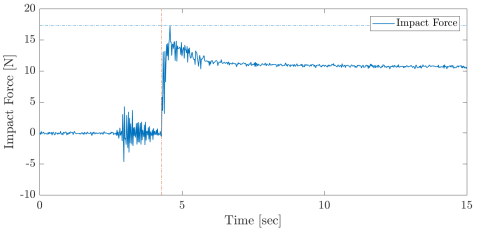

E2 Sequential PIV simulation pictures from G1V1C1_50-2 test

Sequential pictures from PIV simulation of the G1V1C1_50-2 test

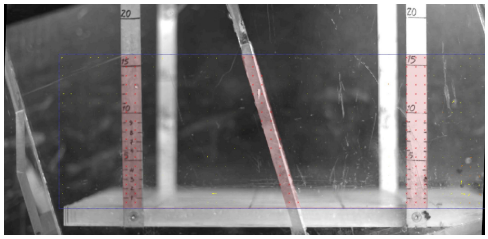

0.0 sec

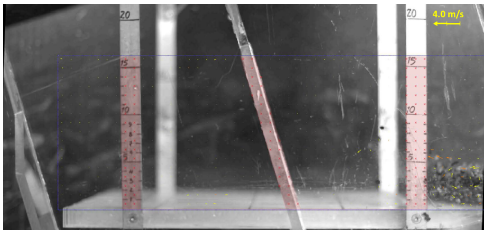

0.020 sec

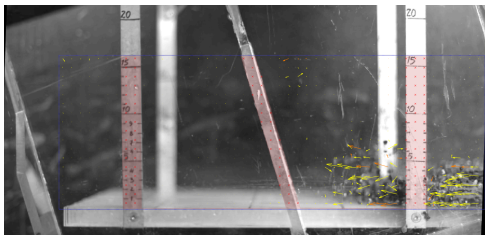

0.040 sec

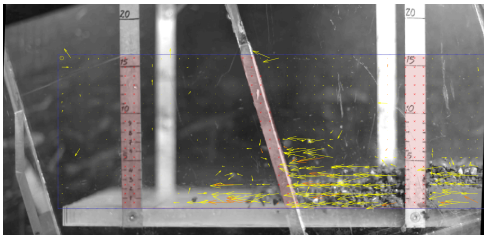

0.060 sec

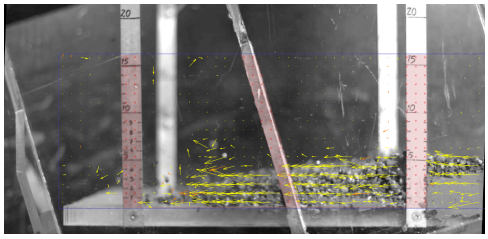

0.080 sec

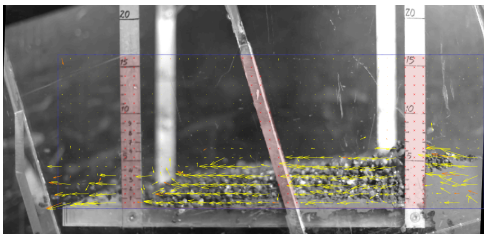

0.100 sec

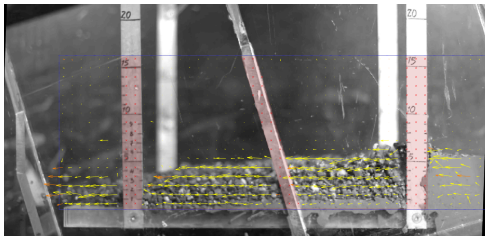

0.120 sec

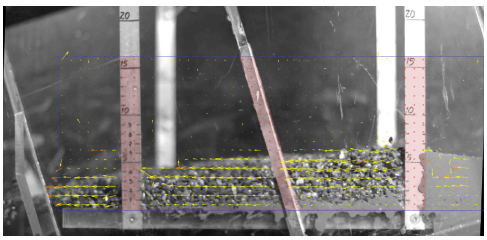

0.140 sec

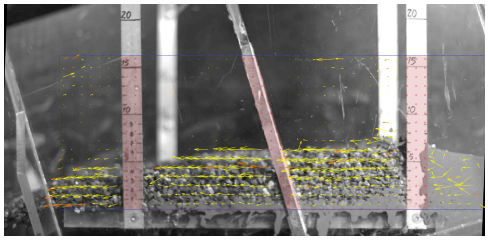

0.160 sec

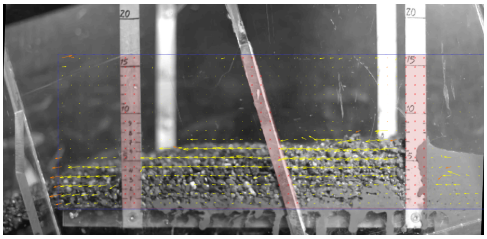

0.180 sec

G1V1C1_50-2

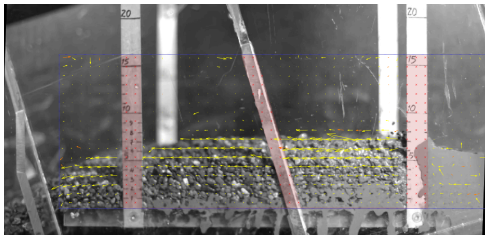

0.200 sec

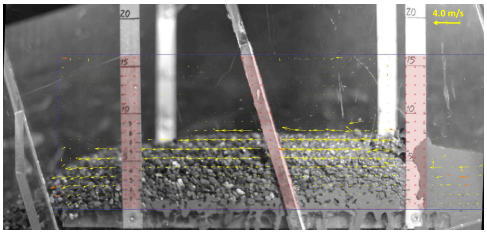

0.220 sec

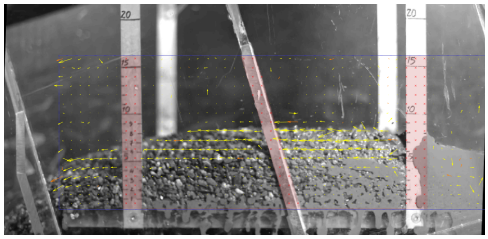

0.240 sec

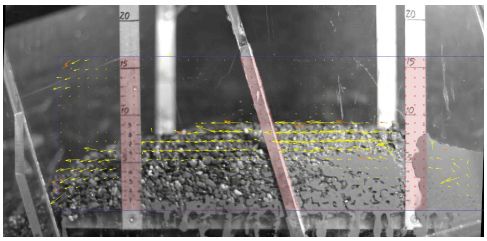

0.260 sec

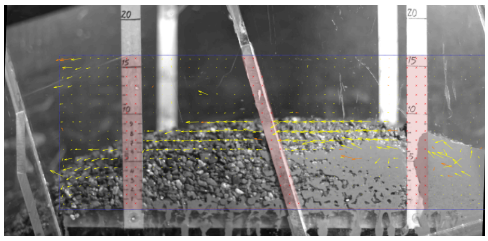

0.280 sec

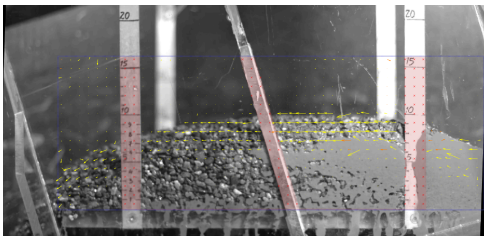

0.300 sec

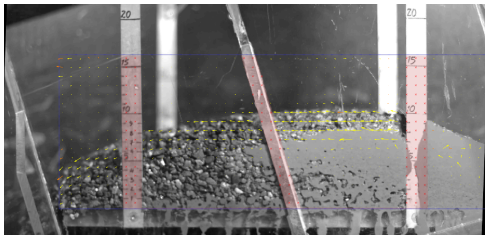

0.320 sec

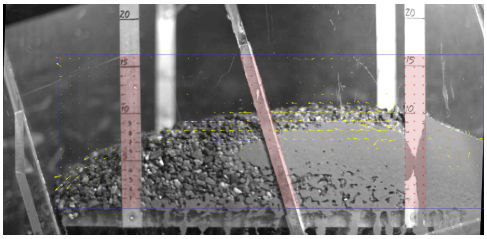

0.340 sec

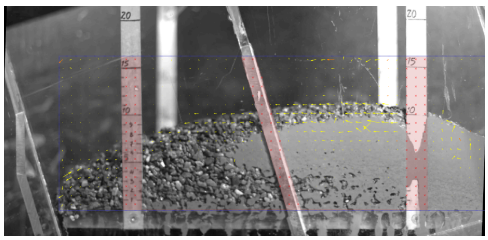

0.360 sec

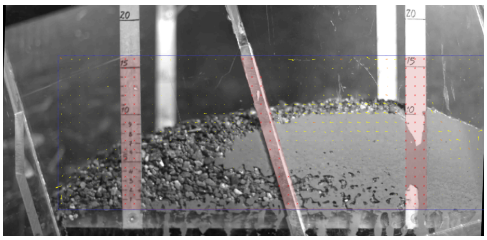

0.380 sec

E3 Sequential PIV simulation pictures from G1V1C2_50-2 test

Sequential pictures from PIV simulation of the G1V1C2_50-2 test

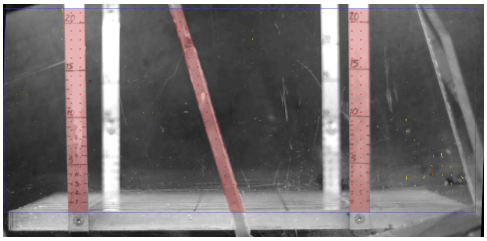

0.0 sec

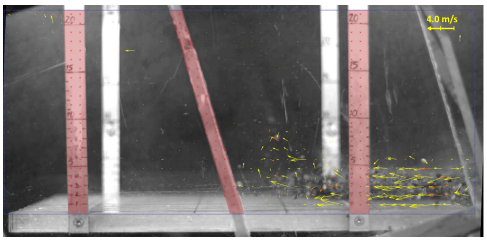

0.040 sec

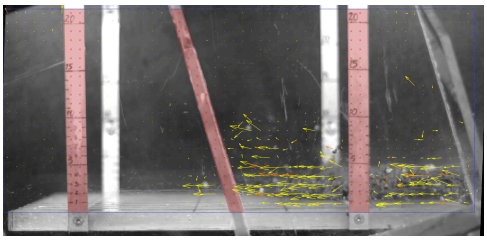

0.048 sec

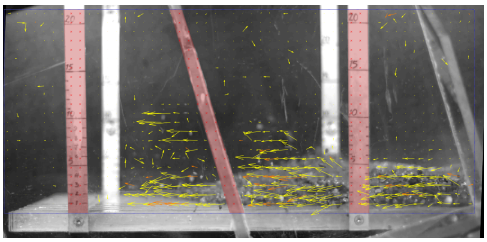

0.072 sec

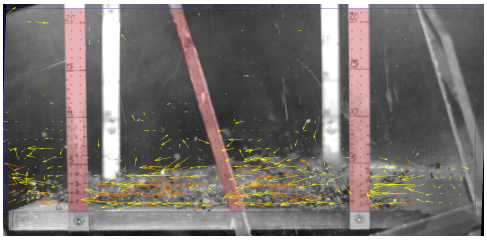

0.100 sec

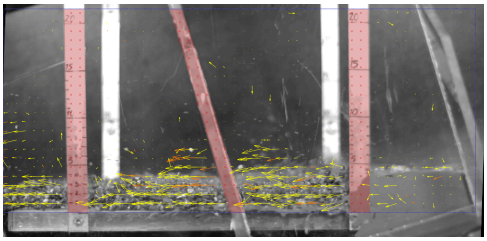

0.128 sec

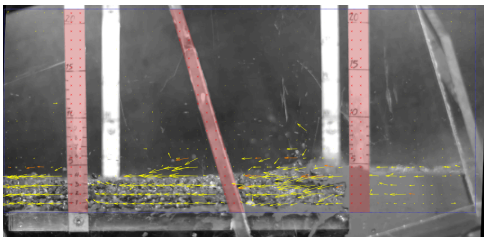

0.148 sec

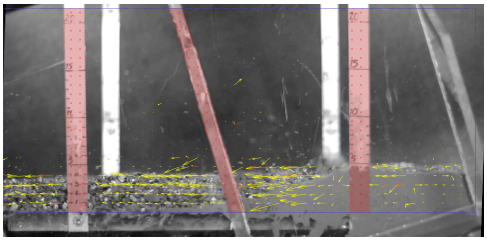

0.172 sec

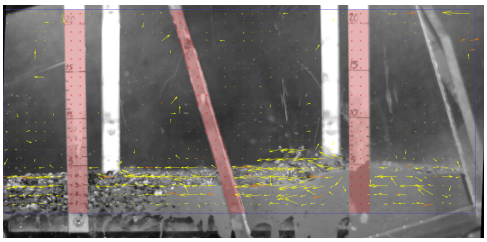

0.196 sec

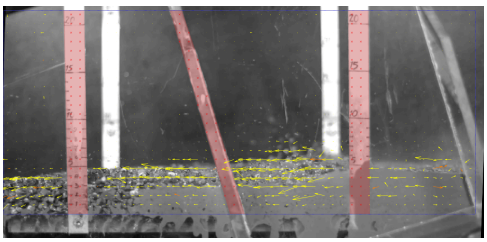

0.216 sec

G1V1C2_50-2

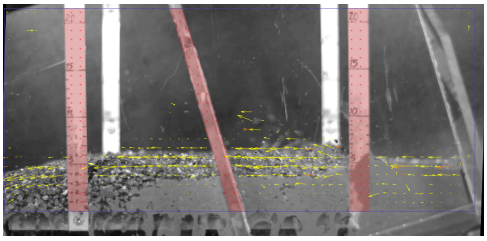

0.260 sec

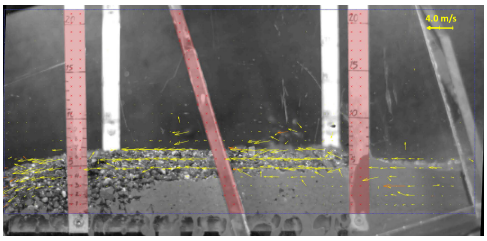

0.280 sec

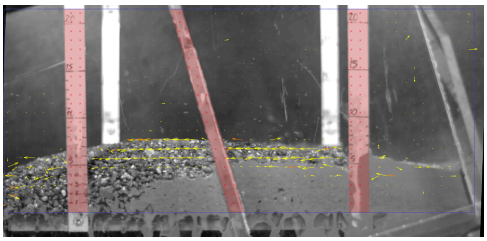

0.304 sec

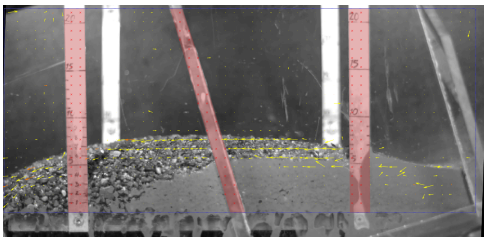

0.320 sec

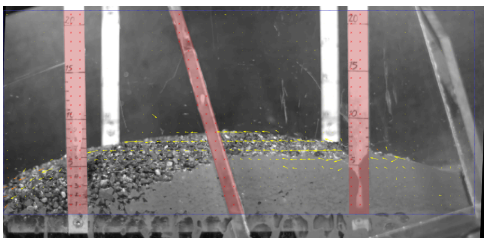

0.340 sec

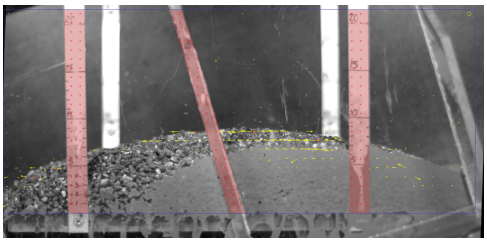

0.364 sec

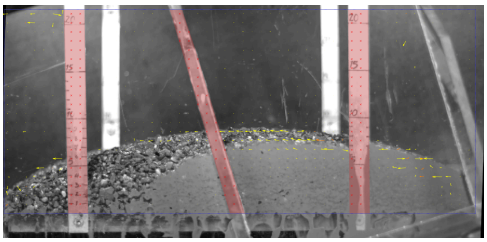

0.380 sec

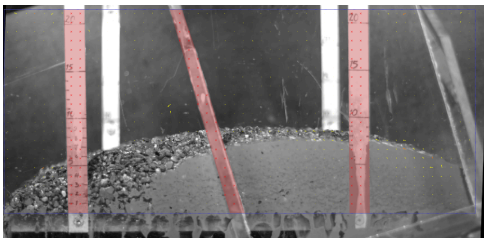

0.400 sec

E4 Sequential PIV simulation pictures from G1V2C1_50-2 test

Sequential pictures from PIV simulation of the G1V2C1_50-2 test

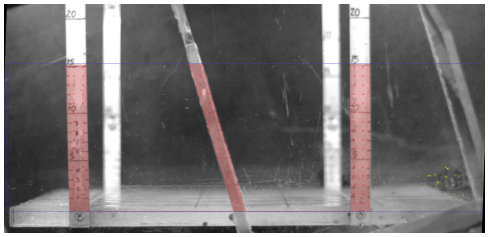

0.0 sec

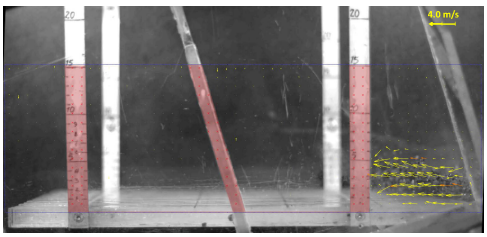

0.020 sec

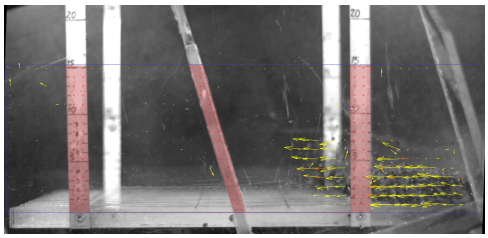

0.04 sec

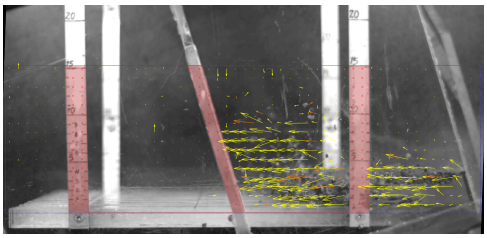

0.060 sec

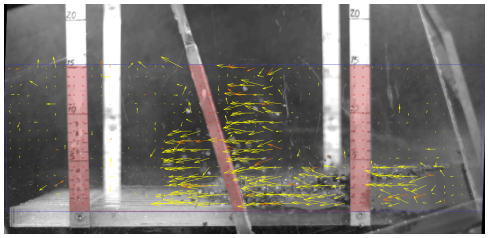

0.080 sec

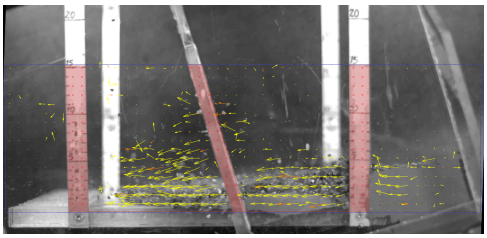

0.100 sec

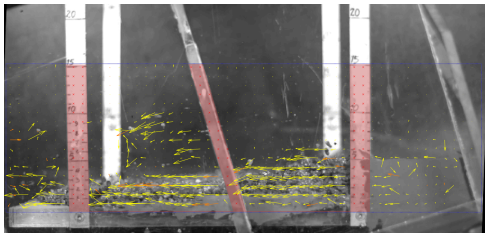

0.120 sec

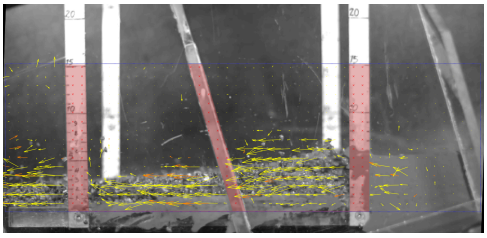

0.140 sec

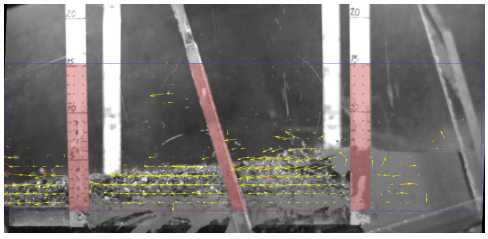

0.160 sec

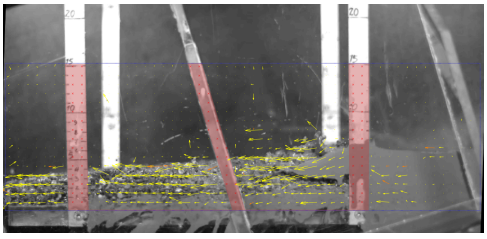

0.180 sec

G1V2C1_50-2

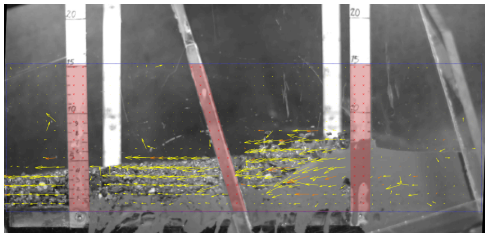

0.200 sec

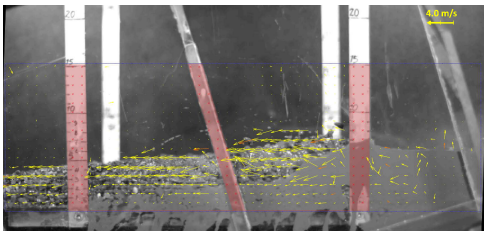

0.220 sec

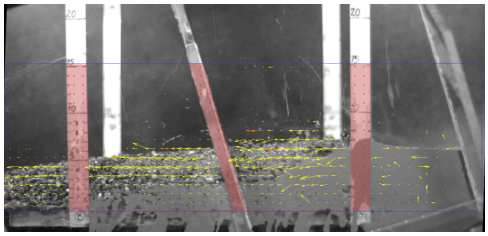

0.240 sec

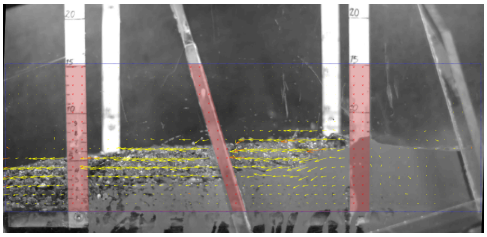

0.260 sec

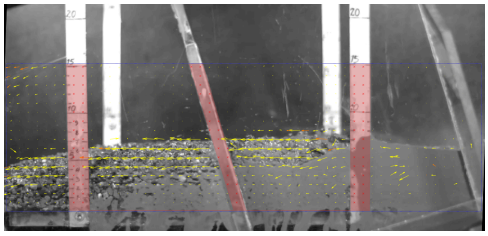

0.280 sec

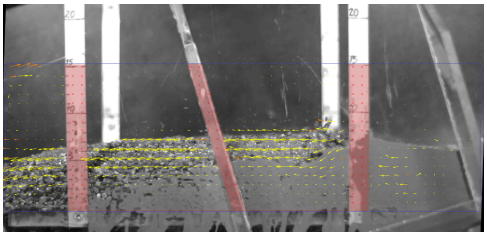

0.300 sec

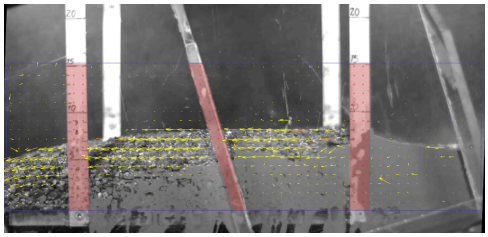

0.320 sec

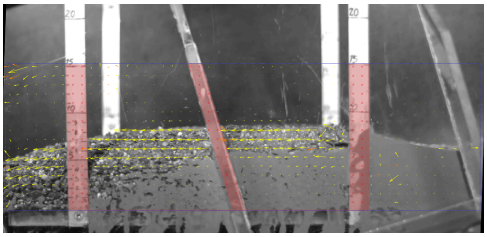

0.340 sec

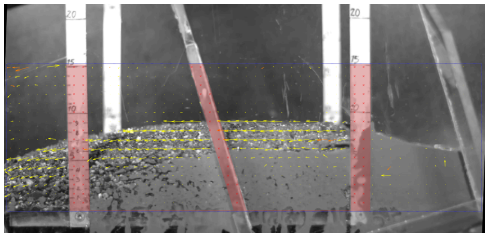

0.360 sec

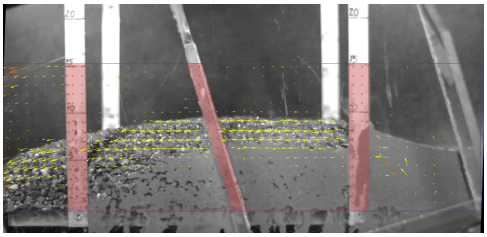

0.380 sec

G1V2C1_50-2

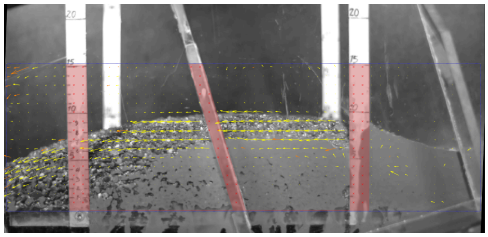

0.400 sec

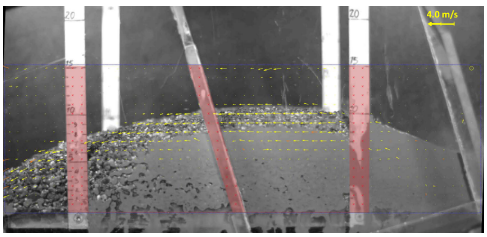

0.450 sec

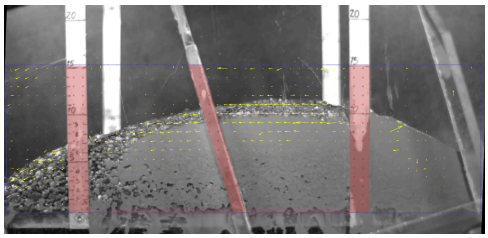

0.500 sec

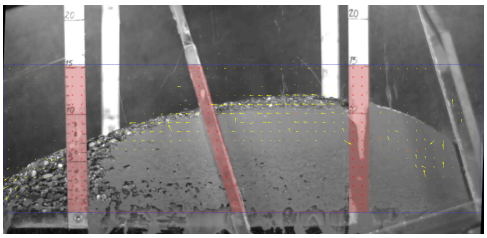

0.550 sec

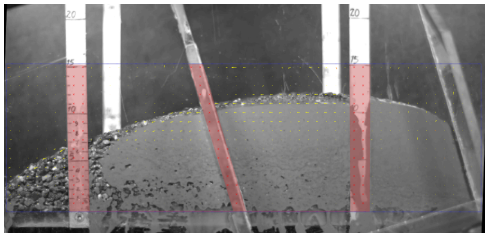

0.600 sec

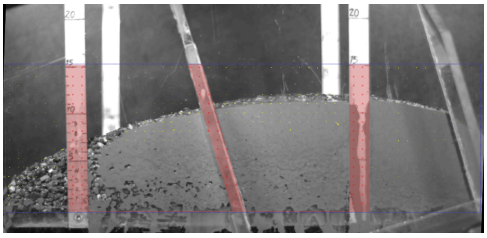

0.650 sec

E5 Sequential PIV simulation pictures from G1V3C1_50-2 test

Sequential pictures from PIV simulation of the G1V3C1_50-2 test

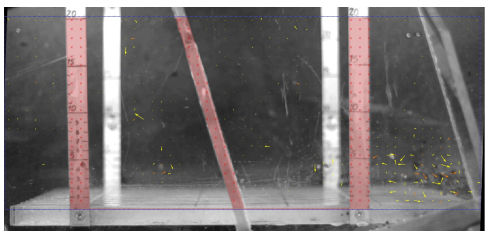

0.0 sec

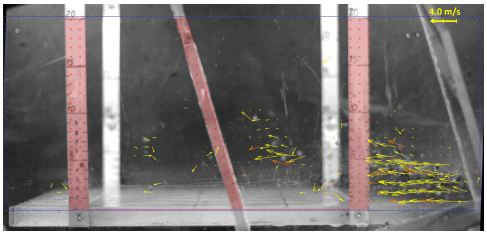

0.020 sec

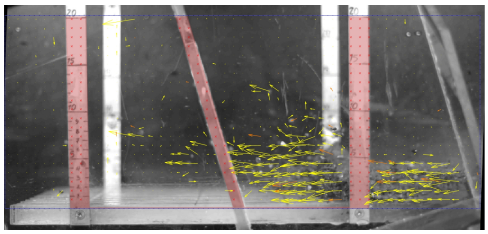

0.040 sec

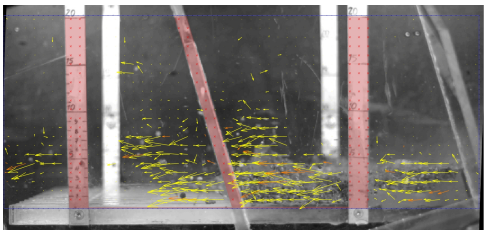

0.060 sec

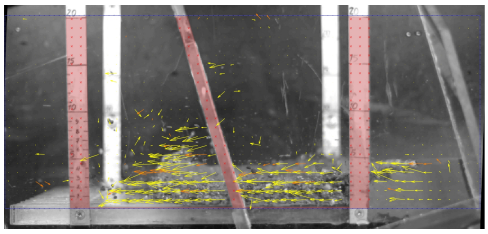

0.080 sec

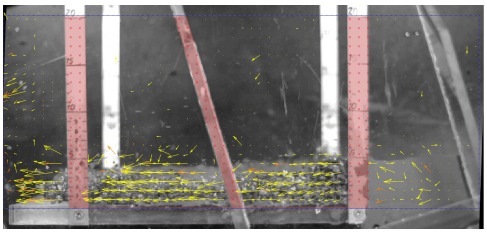

0.100 sec

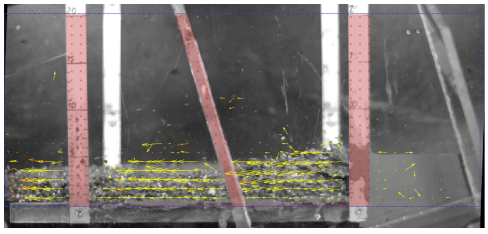

0.120 sec

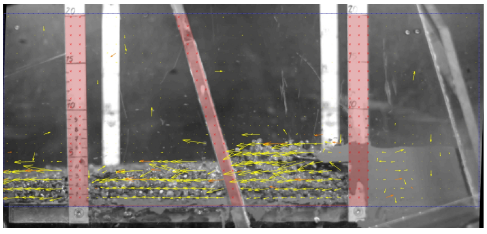

0.140 sec

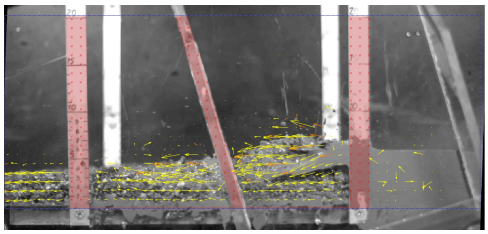

0.160 sec

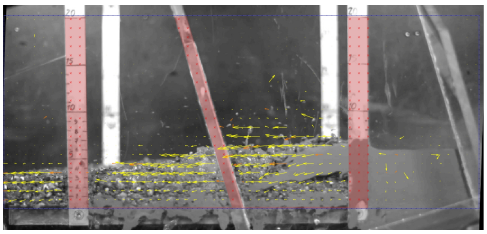

0.180 sec

G1V3C1_50-2

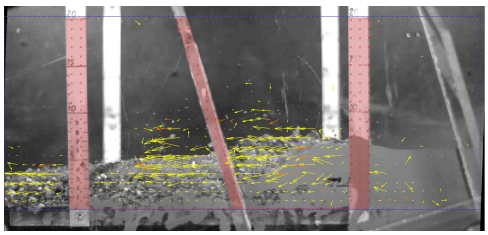

0.200 sec

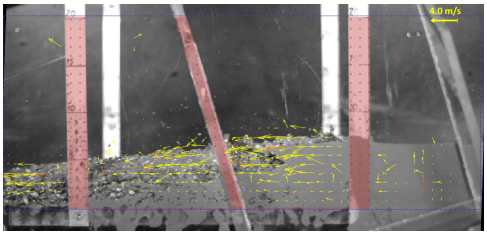

0.220 sec

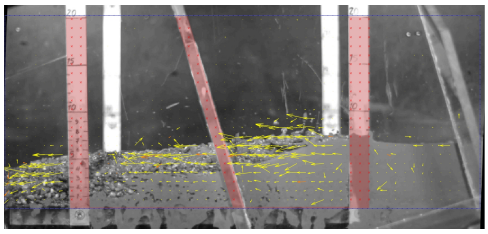

0.240 sec

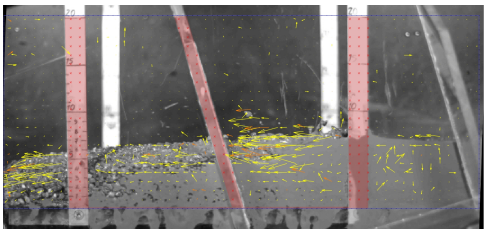

0.260 sec

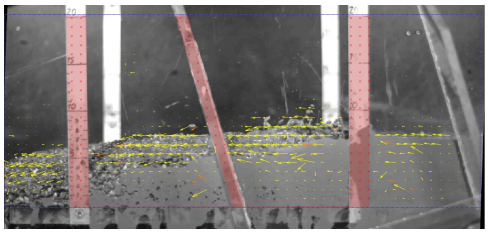

0.280 sec

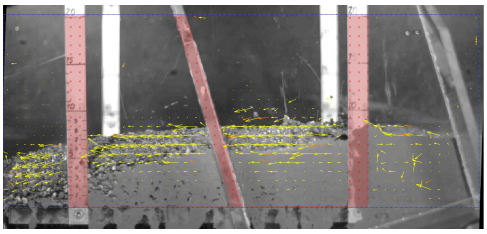

0.300 sec

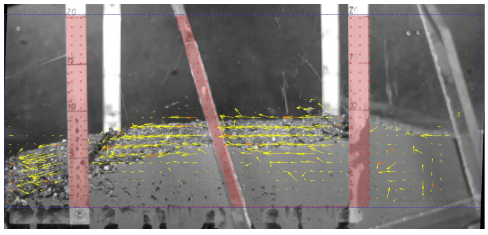

0.320 sec

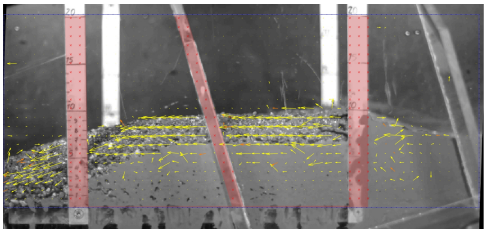

0.340 sec

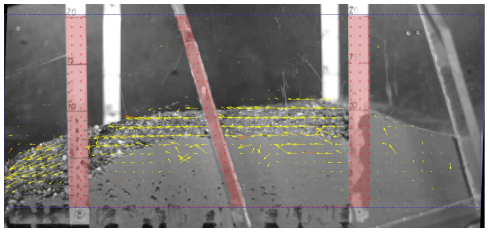

0.360 sec

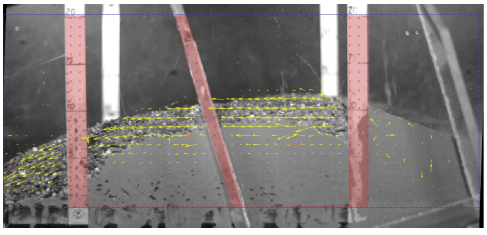

0.380 sec

G1V3C1_50-2

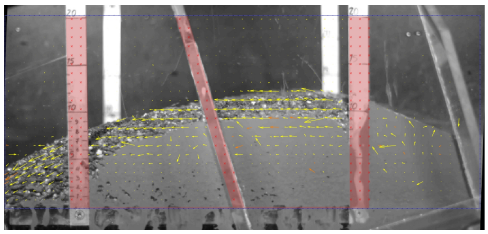

0.400 sec

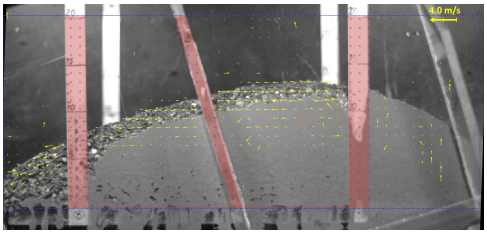

0.420 sec

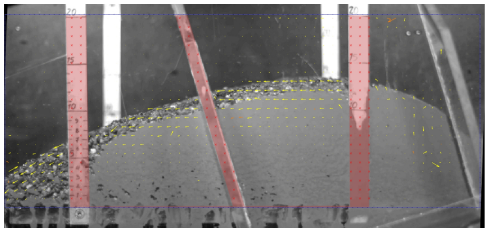

0.440 sec

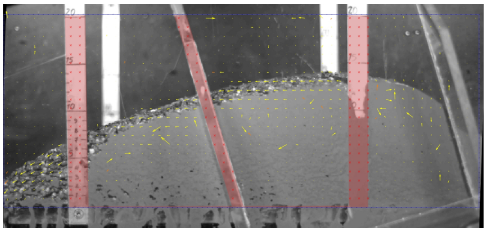

0.460 sec

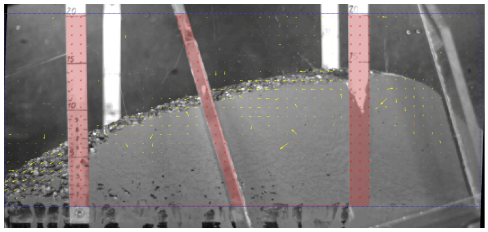

0.480 sec

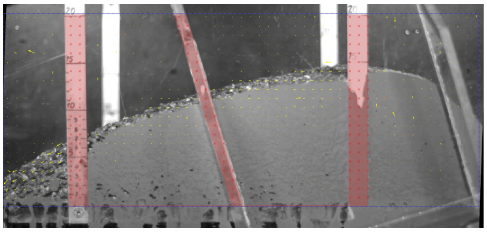

0.500 sec

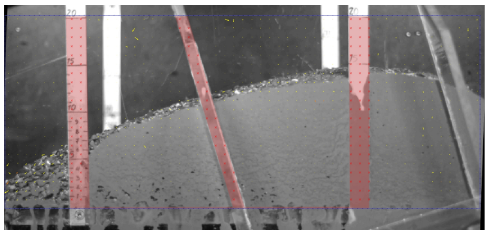

0.540 sec

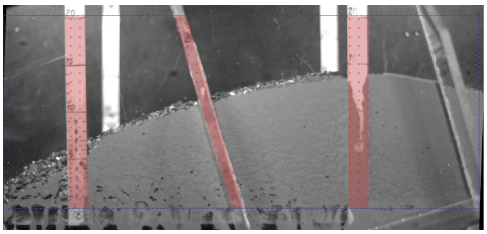

0.580 sec

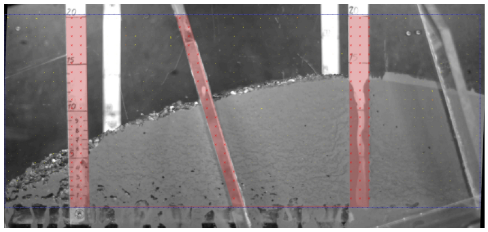

0.620 sec

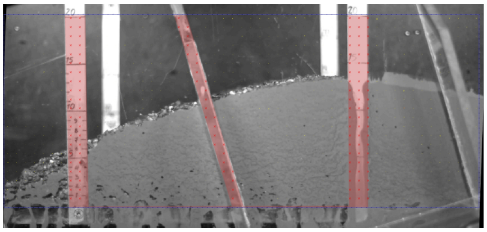

0.650 sec

Appendix F

F1 Instrument specification of the flow height sensor

mic+35/IU/TC

scale drawing

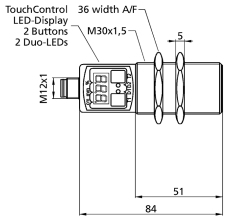

detection zone

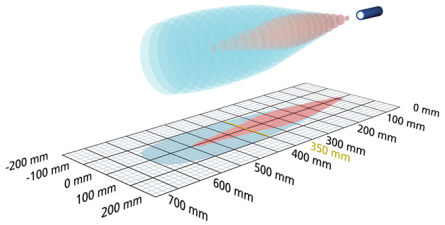

1 x analogue 4-20 mA + 0-10 V

600 mm

measuring range	65 - 600 mm
design	cylindrical M30
operating mode	analogue distance measurements
particularities	Display UL Listed

ultrasonic-specific

means of measurement	echo propagation time measurement
transducer frequency	400 kHz
blind zone	65 mm
operating range	350 mm
maximum range	600 mm
resolution/sampling rate	0.025 mm to 0.17 mm, depending on the analogue window
reproducibility	± 0.15 %
accuracy	± 1 % (temperature drift internally compensated)

electrical data

operating voltage U_B	9 - 30 V d.c., reverse polarity protection
voltage ripple	± 10 %
no-load current consumption	≤ 80 mA
type of connection	5-pin M12 initiator plug

mic+35/IU/TC

outputs	
output 1	analogue output current: 4-20 mA / voltage: 0-10 V (at $U_B \geq 15$ V), short-circuit-proof switchable rising/falling
response time	64 ms
delay prior to availability	< 300 ms

inputs	
input 1	com input synchronisation input

housing	
material	brass sleeve, nickel-plated, plastic parts, PBT, TPU
ultrasonic transducer	polyurethane foam, epoxy resin with glass contents
class of protection to EN 60529	IP 67
operating temperature	-25°C to +70°C
storage temperature	-40°C to +85°C
weight	150 g
further versions	stainless steel cable connection (on request)
further versions	mic+35/IU/TC/E

technical features/characteristics	
temperature compensation	yes
controls	2 push-buttons + LED display (TouchControl)
scope for settings	Teach-in and numeric configuration via TouchControl LCA-2 with LinkControl
Synchronisation	yes
multiplex	yes
indicators	3-digit LED display, 2 x three-colour LED
particularities	Display UL Listed

mic+35/IU/TC

pin assignment

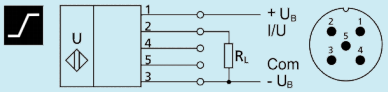

order no.	**mic+35/IU/TC**

The content of this document is subject to technical changes.
Specifications in this document are presented in a descriptive way only. They do not warrant any product features.

F2 Instrument specification of the pore-water pressure sensor

Pressure Sensors

Gage and Differential/Unamplified-Compensated

Temperature Compensated Sensors

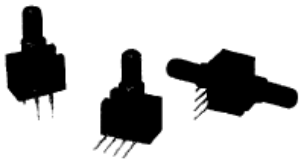

FEATURES

- Lowest priced sensor with temperature compensation and calibration
- Variety of gage pressure port configurations - easily and quickly modified for your special needs
- Choice of termination for gage sensors
- Calibrated Null and Span
- Temperature compensated for Span over 0 to 50°C
- Provides interchangeability
- Can be used to measure with vacuum or positive pressure

26PC SERIES PERFORMANCE CHARACTERISTICS at 10.0 ±0.01 VDC Excitation, 25°C

	Min.	Typ.	Max.	Units
Excitation	---	10	16	VDC
Null Offset	–1.5	0	+1.5	mV
Null Shift, 25° to 0°, 25° to 50°C	---	---	±1.0	mV
Linearity, P2 > P1, BFSL	---	±0.25	---	%Span
Sensitivity Shift, 25° to 0°, 25° to 50°C	---	---	±1.0	%Span
1 psi Sensitivity Shift	---	---	±2.0	%Span
Repeatability & Hysteresis	---	±0.20	---	%Span
Response Time	---	---	1.0	msec
Input Resistance	---	7.5 K	---	ohms
Output Resistance	---	2.5 K	---	ohms
Stability over One Year	---	±0.5	---	%Span
Weight	---	2	---	grams

Total error calculation, see page 66

ENVIRONMENTAL SPECIFICATIONS

Operating Temperature	–40° to 85°C (–40° to +185°F)
Storage Temperature	–55° to +100°C (–67° to +212°F)
Compensated Temperature	0° to +50°C (32° to +122°F)
Shock	Qualification tested to 150 g
Vibration	MIL-STD-202. Method 213 (150g halfsine, 11 msec)
Media (P1 & P2)	Limited only to those media which will not attack polyetherimide, silicon and fluorosilicone seal

26PC SERIES ORDER GUIDE

Catalog Listing	Pressure Range psi	Span, mV			Sensitivity mV/psi Typ.	Overpressure psi Max.	Linearity, %Span P2 > P1 Max.
		Min.	Typ.	Max.			
26PCA Type	1	14.7	16.7	18.7	16.7	20	±1.0
26PCB Type	5.0	47	50	53	10	20	±1.0
26PCC Type	15	97	100	103	6.67	45	±1.0
26PCD Type	30	97	100	103	3.33	60	±1.0

Pressure Sensors

26PC Series

Gage and Differential/Unamplified-Compensated

SENSOR SELECTION GUIDE

2 Product Family	6 Circuit Type	PC Pressure Transducer	B Pressure Range	F* Type of Seal	A Type of Port	2 Termination Style	G Pressure Measurement
2 20PC family	**6** Compensated Calibrated		**A** 1 psi **B** 5 psi **C** 15 psi **D** 30 psi	**F** Fluorosilicone	**A** Straight **B** Barbed **C** Luer **D** Modular **H** M5 Thread **I** 90° Port **J** Needle **M** ¼ - 28 UNF Thread	**1** 1 x 4 **2** 2 x 2	**G** Gage **D** Differential

Example: 26PCBFA2G
Compensated and calibrated 5 psi sensor with fluorosilicone seal, straight port, 2 x 2 terminals, and Gage pressure measurement.
*Other media seal materials may be available.

ACCESSORIES SELECTION GUIDE

Catalog Number	Description
PC10182	Steel lockring (Included with Port Style A, 1 x 4 terminals only)
PC10949	Single hole plastic bracket (Must be separately ordered)

Not all combinations are established. Contact 800 number before final design. The following listings are typically stocked in small quantities.

26PC ORDER GUIDE

Catalog Listing
26PCBFA1D
26PCBFA1G **26PCCFA1D**
26PCCFA1G
26PCDFA1D
26PCDFA1G

Gage and Differential/Unamplified

MOUNTING DIMENSIONS (for reference only)

GAGE SENSOR
Pressure is applied to port P2.
Port P1 vents to ambient pressure.

"1 x 4" Termination (Style 1), Port Style A, Straight
Pin 1 is notched, and is shown at the right of the package.
Pin 2 is next to pin 1, etc.

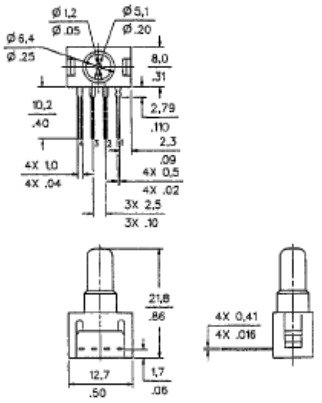

DIFFERENTIAL SENSOR
Straight Port, 1 x 4 termination (Style 2) ONLY
Port P1 is near terminals.

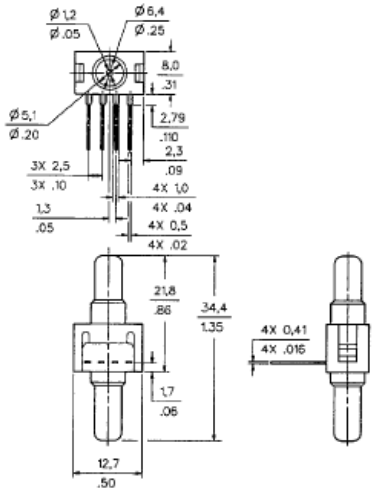

"2 x 2" Termination (Style 2), Port Style A, Straight
Pin 1 is notched, and is shown at lower right corner.
Pins 2, 3 and 4 are clockwise.

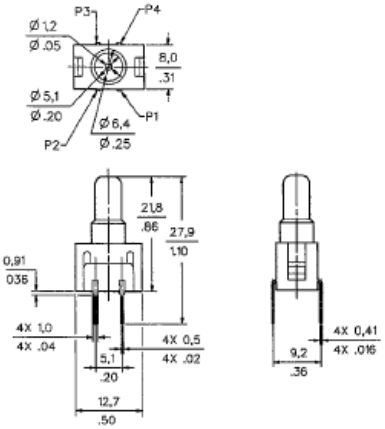

ACCESSORIES
Lockring (included with A port)
PC10182

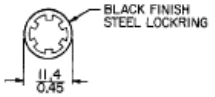

Single hole Plastic Bracket (purchase separately)
PC10949

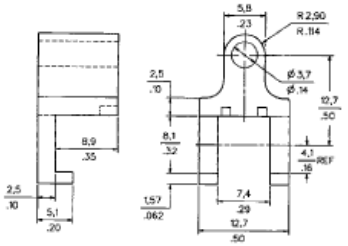

Dual Port Plastic Bracket (purchase separately)
PC15015

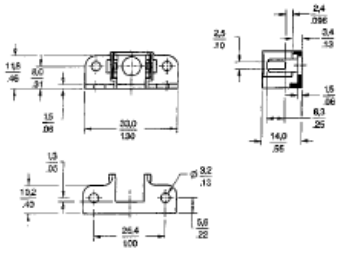

OTHER GAGE SENSOR PORT STYLES
(2 x 2 or 1 x 4 Termination)

B Barbed

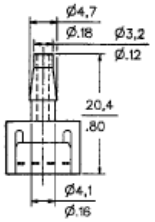

C Luer

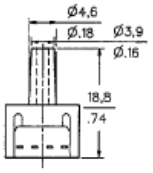

D Modular

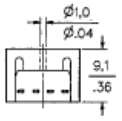

H M5 Thread

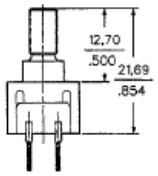

O-Ring
Size .007
O-Ring Counterbore
.40" deep ±.005 × .30 ±.003"

90°

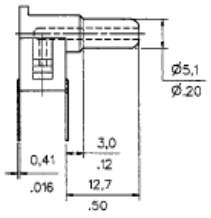

I Needle

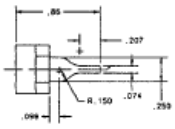

¼–28 UNF Thread

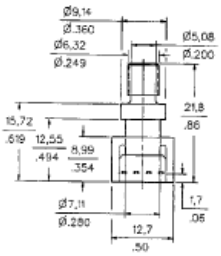

O-Ring
Size .009
O-Ring Counterbore
.40" deep ±.002 × .360" ±.003"

20PC SERIES CIRCUIT - NOTES

1. Circled numbers refer to Sensor Terminals (interface pins).
2. V_O increases with pressure change.
3. $V_O = V_2 - V_4$
4. Pin 1 designated with a notch.

Pin Designation
Styles 1 and 2

Pin 1	V_S (+)
Pin 2	Output (+)
Pin 3	Ground (–)
Pin 4	Output (–)

EXCITATION
Styles 1 and 2

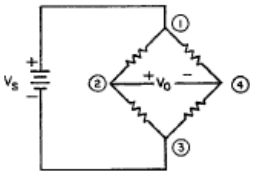

20PC Construction

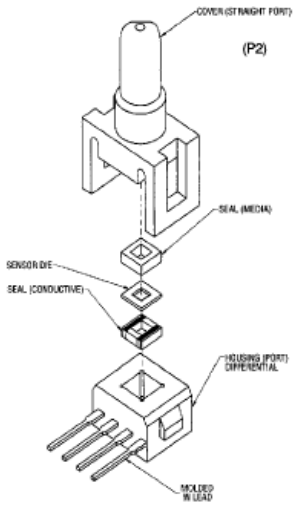

F3 Instrument specification of the load cell

Data sheet

S2M

Force Transducer

Special features

- Tensile/compressive force transducer
- Accuracy class 0.02
- Nominal (rated) forces: 10 N ... 1000 N
- High protection class (IP67)
- High lateral force stability
- Six-wire circuit

Principle of the S2M force transducer

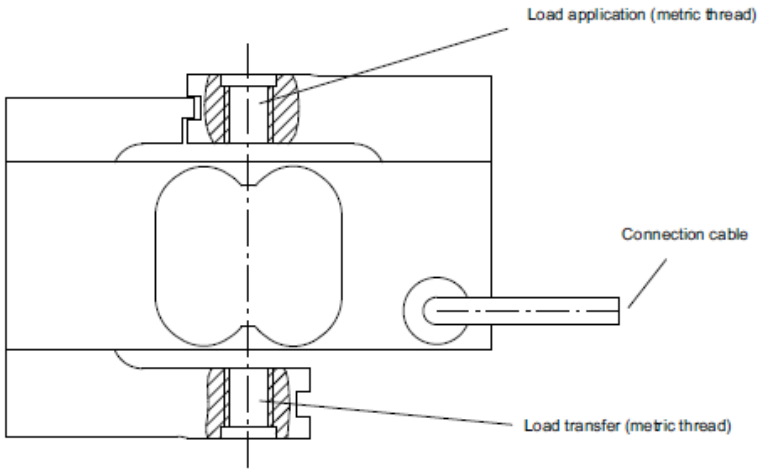

HBM

Dimensions

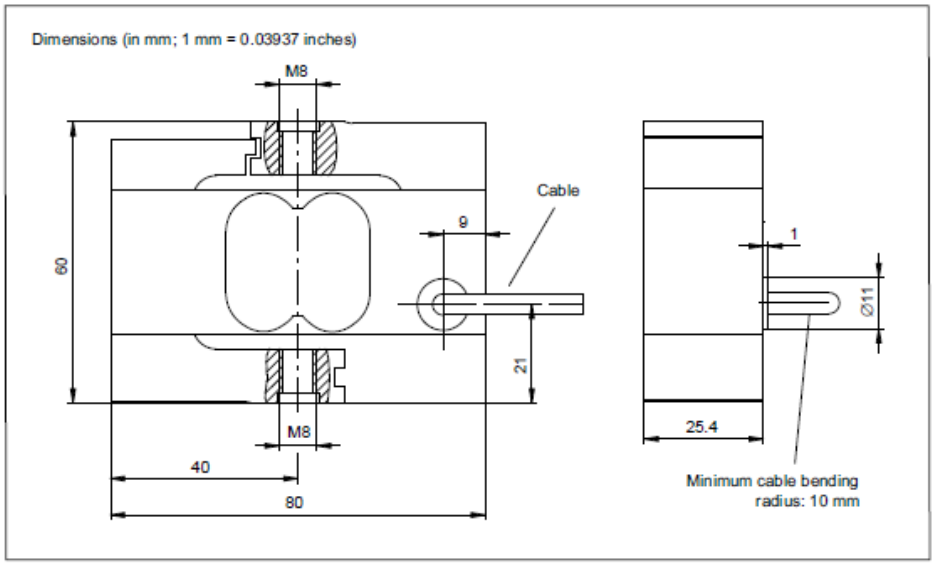

Cable assignment (six-wire configuration)

With this cable assignment, the output voltage at the measuring amplifier is positive in the pressure direction when the transducer is loaded.

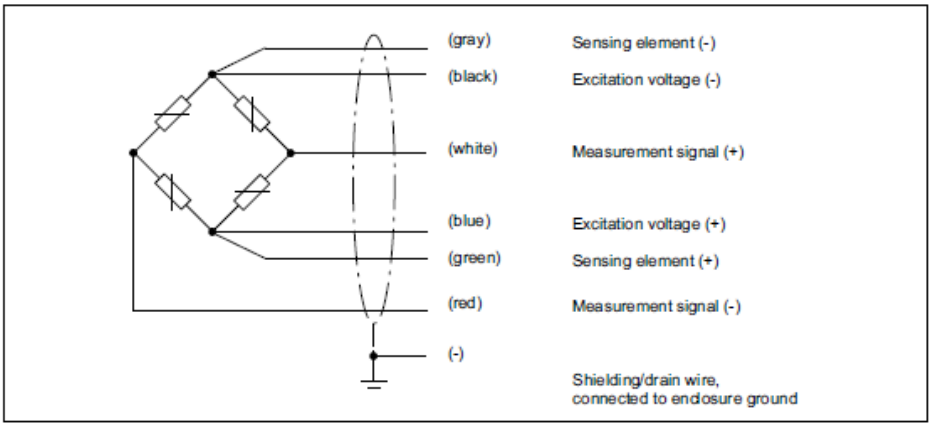

Mounting accessories (to be ordered separately)

Dimensions (in mm; 1 mm = 0.03937 inches)

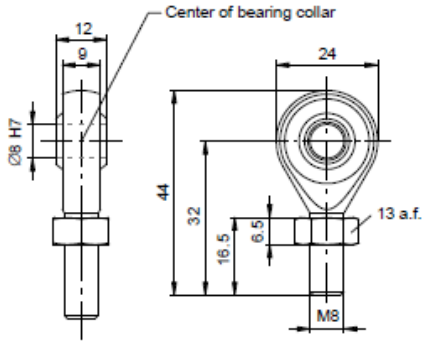

ZGW knuckle eye
Order no. 1-U1R/200KG/ZGW

Material: Tempered steel, galvanized
roller bearing steel
PTFE/bronze corrugated foil

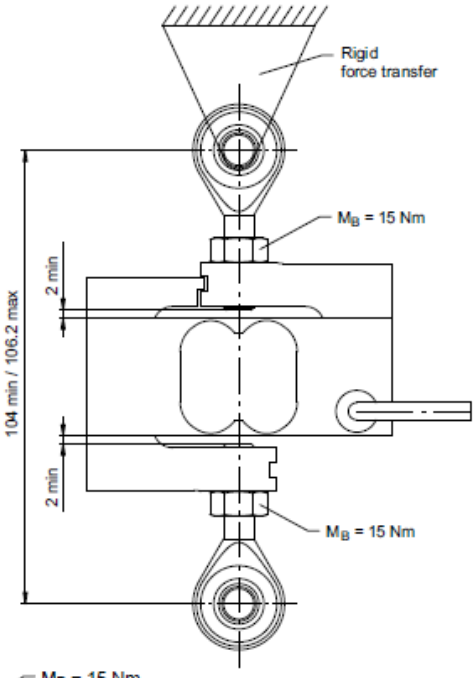

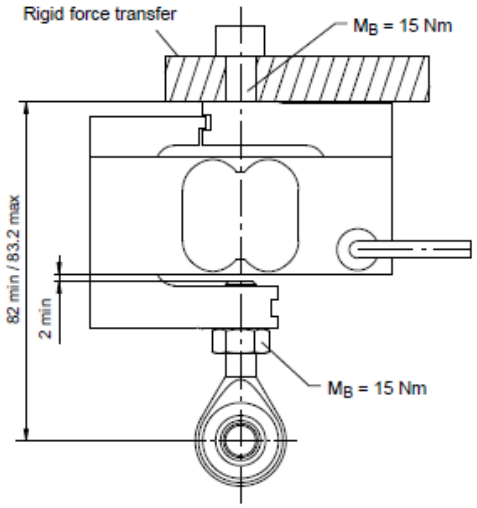

Specifications (data per VDI/VDE/DKD 2638 standards)

Type			S2M						
Nominal (rated) force	F_{nom}	N	10	20	50	100	200	500	1000
Accuracy									
Accuracy class			0.02						
Relative reproducibility and repeatability errors without rotation	b_{rg}	%	0.02						
Relative reversibility error	v		0.02						
Non-linearity	d_{lin}		0.02						
Relative creep over 30 min.	$d_{cr,\ F+E}$		0.02						
Effect of the bending moment at 10% F_{nom} * 10 mm	d_{Mb}		0.02						
Effect of lateral forces (lateral force = 10% F_{nom})	d_Q		0.02						
Effect of temperature on sensitivity	TK_C	% / 10 K	0.02						
Effect of temperature on zero signal	TK_0		0.02						
Electrical characteristic values									
Nominal (rated) sensitivity	C_{nom}	mV/V	2						
Relative zero signal error	$d_{S,\ 0}$	%	5						
Relative sensitivity error	d_c		0.25						
Rel. tensile/compression sensitivity variation	d_{ZD}		0.1						
Input resistance	R_i	Ω	> 345						
Output resistance	R_o		350 ± 50						
Insulation resistance	R_{is}	GΩ	> 2						
Operating range of the excitation voltage	$B_{U,\ G}$	V	0.5 ... 12						
Reference excitation voltage	U_{ref}		5						
Connection			Six-wire circuit						
Temperature									
Nominal (rated) temperature range	$B_{T,\ nom}$	°C	−10 ... +45						
Operating temperature range	$B_{T,\ G}$		−10 ... +70						
Storage temperature range	$B_{T,\ S}$		−10 ... +85						
Mechanical characteristic quantities									
Max. operating force	F_G	%	150						
Limit force	F_L		1000						
Breaking force	F_B		1000						
Limit torque	M_L	Nm	4	8	25	28			
Limit bending moment	$M_{b\ perm}$		6	25	34	50	71	95	125
Static lateral limit force	F_Q	% of F_{nom}	100						
Nominal (rated) displacement	s_{nom}	mm	0.27	0.21	0.18	0.15	0.13	0.12	0.13
Fundamental resonance frequency	f_G	Hz	94.4	146	243	358	475	582	618
Relative permissible oscillatory stress	F_{rb}	% of F_{nom}	140						
General data									
Degree of protection per EN 60529			IP 67						
Measuring body material			Aluminum						
Potting material			Silicone						
Cable			Six-wire circuit, PUR insulation, drag chain compliant						
Cable length		m	6						
Mass (with cable)	m	kg	0.5						

Versions and ordering numbers

Code	Measuring range	Stock item ordering number	The ordering numbers shown in gray are preferred types, they can be delivered rapidly. All force transducers with 6 m cable, open ends and without TEDS. The ordering number for the preferred types is 1-S2M.. The ordering number for customer-specific designs is K-S2M-MONT…
010N	10 N	1-S2M/10N-1	
020N	20 N	1-S2M/20N-1	
050N	50 N	1-S2M/50N-1	
100N	100 N	1-S2M/100N-1	
200N	200 N	1-S2M/200N-1	
500N	500 N	1-S2M/500N-1	
001K	1000 N	1-S2M/1000N-1	

Cable length	Plug version	Transducer identification
01M5 1.5 m	**Y** Free ends	**S** without TEDS
03M0 3 m	**F** D-Sub	**T** With TEDS
06M0 6 m	**Q** D-Sub HD	
	N ME3106PEMV	
	P CON P1016	

Example

K-S2M-MONT	010N	03M0	Q	T

The example shows an S2M with 10 N capacity, 3 m cable, a fitted plug for the Quantum system, and TEDS.

TEDS is only possible when a plug is fitted, TEDS and open ends cannot be combined.